CERN-ACC-Note-2019-XXX
Geneva, December 21, 2019

The Large Hadron-Electron Collider at the HL-LHC

From resolving the partonic structure of matter to Higgs and BSM physics

LHeC Collaboration

Submitted to J.Phys. G

Abstract

This is our abstract.

Foreword [Herwig Schopper]

This is the 2019 CDR of the LHeC. Thumbs up!

Preface

This is the 2019 CDR of the LHeC.

Contents

Space for ‘back of the envelope’ calculations.

Chapter 1

Executive Summary [Oliver Bruening, Max Klein]

Put your text here! this goes up to Q^2.

Chapter 2

Introduction [Max Klein]

SJB. The collisions of 60 GeV electrons with the 7 TeV protons of the high energy LHC collider at CERN can provide a new testing ground for fundamental hadronic physics, as well as novel tests of the Standard Model. The tests include electroweak theory, precision QCD, lepto-quark phenomenology, and supersymmetric extensions of the Standard Model.

A footnote from SJB [1]

[1] The center-of-mas energy at the proposed LHeC of $\sqrt{s} \simeq 1.3\,\mathrm{TeV}$ – equivalent to an electron laboratory energy $E_e^{lab} \simeq 1700\,\mathrm{TeV}$ – would require a 17 000 mile-long fixed-target accelerator based on the technology of the 50 GeV two-mile SLAC linear accelerator.

Chapter 3

Main Characteristics of the LHeC [Oliver Bruening, Max Klein]

3.1 Kinematics and Reconstruction of Final States [Max Klein]

3.1.1 Nominal Beam Energies

3.1.2 Reduced Electron or Proton Beam Energy

3.2 A Summary of the LHeC Configuration and Parameters [Max Klein]

3.2.1 Introduction

The Conceptual Design Report (CDR) of the LHeC was published in 2012 [1]. The CDR default configuration uses a 60 GeV energy electron beam derived from a racetrack, three-turn, intense energy recovery linac (ERL) achieving a cms energy of $\sqrt{s} = 1.3\,\text{TeV}$, where $s = 4E_pE_e$ is determined by the electron and proton beam energies, E_e and E_p. In 2012, the Higgs boson, H, was discovered which has become a central topic of current and future high energy physics. The Higgs production cross section in charged current (CC) deep inelastic scattering (DIS) at the LHeC is roughly 100 fb. The Large Hadron Collider has so far not led to the discovery of any exotic phenomenon. This forces searches to be pursued, in pp but as well in ep, with highest achievable precision in order to access a maximum range of phase space and possibly rare channels. The DIS cross section at large x roughly behaves like $(1-x)^3/Q^4$ demanding very high luminosities for exploiting the unknown regions of Bjorken x near to 1 and very high Q^2, the negative four-momentum transfer squared between the electron and the proton. For the current update of the design of the LHeC this has set a luminosity goal in excess of the $10^{33}\,\text{cm}^{-2}\text{s}^{-1}$ as had been adopted for the CDR. There arises the potential, as will be detailed in Sect.**??**, to transform the LHC into a high precision electroweak, Higgs and top quark physics facility.

The ep Higgs production cross section rises approximately with E_e. New physics may be related to the heaviest known elementary particle, the top quark, the ep production cross section of which rises stronger than linear with E_e in the LHeC kinematic range which is not very far from the $t\bar{t}$ threshold. Searches for heavy neutrinos, SUSY particles etc. are the more promising the higher the energy is. Access in DIS to very low Bjorken x requires high energies because of $x = Q^2/s$, for inelasticity $y = 1$. In DIS, one needs $Q^2 > M_p^2 \simeq 1\,\text{GeV}^2$. Physics therefore requires a maximally large energy. However, cost and effort set realistic limits such that twice the HERA electron beam energy, of about 27 GeV, appeared as a reasonable and affordable target value.

In the CDR the default electron energy was chosen to be 60 GeV. This can be achieved with an ERL

circumference of 1/3 of that of the LHC [1]. Recently the cost was estimated. This has defined a new default configuration of $E_e = 50\,\text{GeV}$ and a circumference of 5.4 km which is 1/5 of the LHC length. The decision on E_e is not taken now. This paper comprises studies with different energy configurations, mainly $E_e = 50$ and 60 GeV, which are close in their cms energy values of 1.2 and 1.3 TeV, respectively.

Given the non-linear dependence of the cost on E_e, for energies larger than about 60 GeV, significantly larger electron beam energy values may only be justified by overriding arguments, such as, for example, the existence of leptoquarks [1]. Higher values of $\sqrt{s}$ are also provided with enlarged proton beam energies by the High Energy LHC ($E_p = 13.5\,\text{TeV}$) and the FCC-pp with E_p between 20 and possibly 150 TeV, depending on the dipole magnet technology.

3.2.2 Cost Estimate, Default Configuration and Staging

In 2018 a detailed cost estimate has been performed [2] following the guidance and practice of CERN accelerator studies. The assumptions were also compared with the DESY XFEL cost. The result was that for the 60 GeV configuration about half of the total cost was due to the two SC linacs. The cost of the arcs decreases stronger than linear with decreasing energy, about $\propto E^4$ for synchrotron radiation losses and $\propto E^3$ when emittance dilution is required to be preserved [3]. It was therefore considered to set a new default of 50 GeV with a circumference of 1/5 of that of the LHC, see Sect. **??**, compared to 1/3 for 60 GeV. Furthermore, an initial phase at 30 GeV was considered, within the 1/5 configuration but with less equipped linacs. The HERA electron beam energy was 27 GeV. The main results, taken from [2] are reproduced in Tab. 3.1.

Item Mode	60 GeV CDR	30 GeV stage 1	50 GeV default
SRF System	805	402	670
SRF R+D and Prototyping	31	31	31
Injector	40	40	40
Arc Magnets and Vacuum	215	103	103
SC IR Magnets	105	105	105
Source and Dump System	5	5	5
Cryogenic Infrastructure	100	41	69
General Infrastructure and Installation	69	58	58
Civil Engineering	386	289	289
Total Cost	1756	1075	1371

Table 3.1: Summary of cost estimates, in MSF, from [2]. The 60 GeV configuration is built with a 9 km triple racetrack configuration as was considered in the CDR [1]. It is taken as the default configuration for FCC-eh, with an additional CE cost of 40 MSF due to the larger depth on point L (FCC) as compared to IP2 (LHC). Both the 30 and the 50 GeV assume a 5.4 km configuration, i.e. the 30 GeV is assumed to be a first stage of LHeC upgradeable to 50 GeV ERL. Whenever a choice was to be made on estimates, in [2] the conservative number was chosen.

The choice of a default of 50 GeV at 1/5 of the LHC circumference results, as displayed, in a total cost of 1.075 MSF for the initial 30 GeV configuration and an additional, upgrade cost to 50 GeV of 296 MSF. If one restricted the LHeC to a non-upgradeable 30 GeV only configuration one would, still in a triple racetrack configuration, come to roughly a 1 km long structure with two linacs of about 500 m length, probably in a

[1] If these existed with a mass of say $M = 1.5\,\text{TeV}$ this would require, at the LHC with $E_p = 7\,\text{TeV}$, to choose E_e to be larger than 90 GeV, and to pay for it. Leptoquarks would be produced by ep fusion and appear as resonances, much like the Z boson in e^+e^- and would therefore fix E_e (given certain E_p which at the FCC exceeds 7 TeV). The genuine DIS kinematics, however, is spacelike, the exchanged four-momentum squared $q^2 = -Q^2$ being negative, which implies that the choice of the energies is less constrained than in an e^+e^- collider aiming at the study of the Z or H bosons.

single linac tunnel configuration. The cost of this version of the LHeC is roughly 800 MSF, i.e. about half the 60 GeV estimated cost. However, this would essentially reduce the LHeC to a QCD and electroweak machine, still very powerful but accepting substantial losses in its Higgs, top and BSM programme.

Choices on the final energy will be made later. They not only depend on a budget but also on the future development of particle physics at larg. For example, it may turn out that the community for a foreseeable future may not find the O(10) GSF required to build any of the e^+e^- colliders currently considered. Then the only way to improve on the Higgs measurements beyond HL-LHC substantially is the high energy (50-60 GeV), high luminosity ($\int L = 1\,\mathrm{ab}^{-1}$) LHeC. Obviously, physics and cost are intimately related. Based on such considerations, but also taking into account technical constraints as resulting from the amount of synchrotron radiation losses in the interaction region and the arcs, we have chosen 50 GeV in a 1/5 of U(LHC) configuration as the new default. This economises about 400 MSF as compared to the CDR configuration.

If the LHeC ERL was built, it may later be transferred, with some reconfiguration and upgrades, to the FCC to serve as the FCC-eh. The FCC-eh has its own location, L, for the ERL which requires a new accelerator tunnel. It has been decided to keep the 60 GeV configuration for the FCC, as described in the recently published CDR of the FCC [4]. The LHeC ERL configuration may be used later as a top-up injector for the Z and possibly WW phase of the FCC-ee, should the FCC-ee indeed preceed the FCC-hh/eh phase.

3.2.3 Configuration Parameters

A possible transition from the 60 GeV to the 50 GeV configuration of the LHeC has been envisaged already in 2018, as considered in the paper submitted to the European strategy [5]. The machine layout shown in that paper is reproduced in Fig. 3.1. It is a rough sketch illustrating the reduction from a 60 GeV to a 50 GeV configuration, which results not only in a reduction of capital costs, as discussed above, but also of efforts.

The ERL configuration has been recently revisited [3] considering its dependence on the electron beam energy. Applying a dimension scaling which preserves the emittance dilution, the results have been obtained as are summarised in Tab. 3.2. The 1/5 configuration is chosen as the new LHeC default while the CDR

item circumference [U(LHC)]	1/3	1/4	1/5	1/6
Energy [GeV]	61.1	54.2	49.1	45.2
Linac length [m] x 2	1025	909	829	758
Arc radius [m] x 2 π	1058	737	536	427
Spreader and Recombiner length [m] x 4	76	76	76	76
Circumference [m]	9000	6750	5332	4500

Table 3.2: Scaling of the electron beam energy, linac and further accelerator element dimensions with the choice of the total circumference in units $1/n$ of the LHC circumference. For comparison, the CERN SPS has a circumference of 1/4 of that of the LHC.

on the LHeC from 2012 and the recent CDR on FCC-eh have used the 1/3 configuration. The energy and configuration may be decided as physics, cost and effort dictate when a decision is taken eventually.

3.2.4 Luminosity

The luminosity L for the LHeC in its linac-ring configuration is determined as

$$L = \frac{N_e N_p f \gamma_p}{4\pi\epsilon_p \beta^*} \cdot \prod_{i=1}^{3} H_i,$$

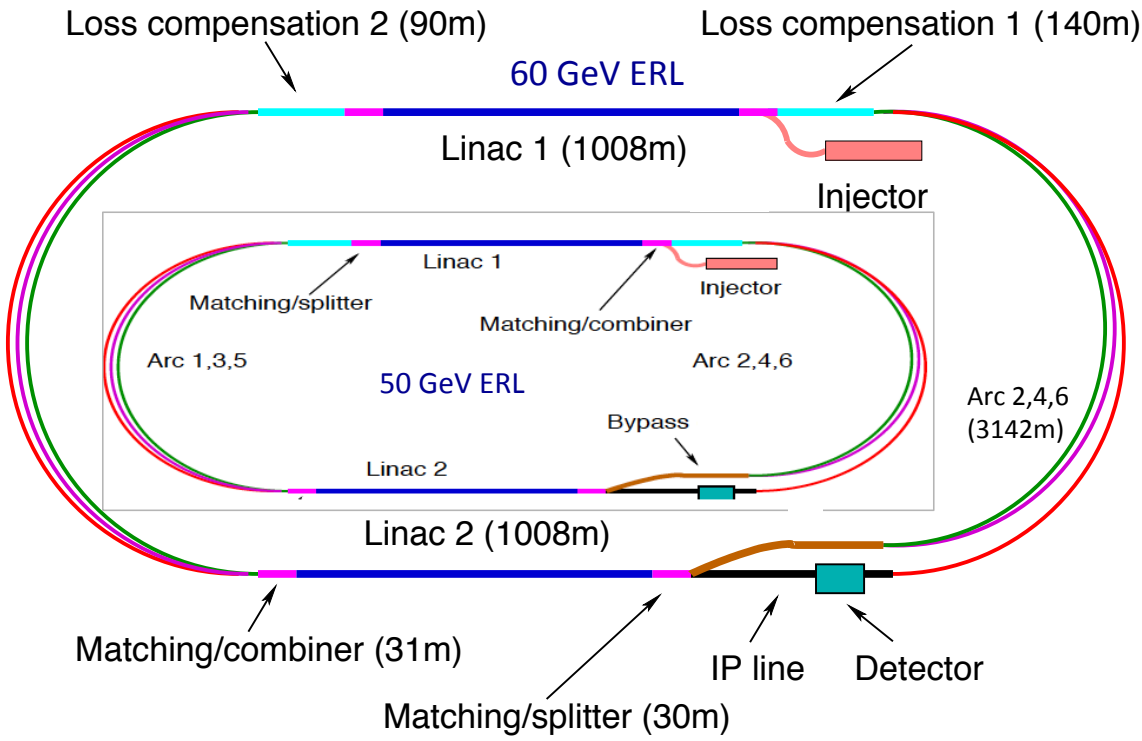

Figure 3.1: Schematic view of the three-turn LHeC configuration with two oppositely positioned electron linacs and three arcs housed in the same tunnel. Two configurations are shown: Outer: Default $E_e = 60\,\text{GeV}$ with linacs of about 1 km length and 1 km arc radius leading to an ERL circumference of about 9 km, or 1/3 of the LHC length. Inner: Sketch for $E_e = 50\,\text{GeV}$ with linacs of about 0.8 km length and 0.55 km arc radius leading to an ERL circumference smaller than the SPS size, i.e. 5.4 km or 1/5 of the LHC length. The 1/5 circumference configuration is flexible: it entails the possibility to stage the project as funds of physics dictate by using only partially equipped linacs, and it also permits upgrading to somewhat higher energies if one admits increased synchrotron power losses and operates at higher gradients.

where $N_{e(p)}$ is the number of electrons (protons) per bunch, $f = 1/\Delta$ the bunch frequency with the bunch distance Δ, equal to 25 ns at the LHC, and γ_p the relativistic factor E_p/M_p of the proton beam. Further, ϵ_p denotes the normalized proton transverse beam emittance and β^* the proton beta function at the IP, assumed to be equal in x and y. The luminosity is moderated by the hourglass factor, $H_1 = H_{geo} \simeq 0.9$, the pitch or beam-beam correction factor, $H_2 = H_{b-b} \simeq 1.3$, and the filling factor $H_3 = H_{coll} \simeq 0.8$. The product of these factors is estimated to be one and the factors are therefore not listed in the subsequent tables.

The electron beam current is given as

$$I_e = eN_e f.$$

The current for the LHeC is limited by the charge delivery of the source. In the new default design we have $I_e = 20\,\text{mA}$ which results from a charge of 500 pC for the bunch frequency of 40 MHz. It is one of the tasks of the PERLE facility to investigate the stability of the 3-turn ERL configuration in view of the challenge for each cavity to hold the sixfold current due to the simultaneous acceleration and deceleration of 3 bunches.

Electron-Proton Collisions

The design parameters of the luminosity have been recently provided in a note describing the FCC-eh configuration [**?**], including the LHeC. The following table, Tab. 3.3, represents an update comprising in

addition the initial 30 GeV configuration and the lower energy FCC-pp version based on the LHC magnets [2]. For the LHeC, as noted above, we assume $E_e = 50\,\text{GeV}$ while for FCC-eh we stick to 60 GeV. Since the source limits the electron current, the peak luminosity may be assumed not to depend on E_e. Studies of the interaction region design, presented in this paper, show that one may be confident in reaching a β^* of 10 cm, while it will be a challenge to reach values below. Similarly, it will be quite a challenge to operate with a current beyond 20 mA. That has yet been considered in the dedicated operation mode, in which, it has been assumed [6] that the LHeC would possibly operate for a few years when the *pp* program has ended.

E_p [TeV]	7	7	7	7	20	50
E_e [GeV]	60	30	50	50	60	60
mode	CDR	initial	default	dedicated	design	design
N_p [10^{11}]	1.7	2.2	2.2	2.2	1	1
ϵ_p [μm]	3.7	2.5	2.5	2.5	2.2	2.2
I_e [mA]	6.4	15	20	50	20	20
N_e [10^9]	1	2.3	3.0	7.8	3.0	3.0
β^* [cm]	10	10	7	7	12	15
Luminosity [$10^{33}\,\text{cm}^{-2}\text{s}^{-1}$]	1	5	9	23	8	15

Table 3.3: Summary of luminosity parameter values for the LHeC and FCC-eh. Left: CDR from 2012; Middle: LHeC in three stages, an initial low energy run, the default 50 GeV, both concurrently with the LHC, and a final, dedicated, stand-alone *ep* phase ; Right: FCC-eh with a 20 and a 50 TeV proton beam, in synchronous operation.

The peak luminosity values exceed those at HERA by 2-3 orders of magnitude. The operation of HERA in its first, extended running period, 1992-2000, provided an integrated luminosity of about $0.1\,\text{fb}^{-1}$ for the collider experiments H1 and ZEUS. This may now be expected to be taken in a day of initial LHeC operation.

Electron-Ion Collisions

The design parameters of the luminosity have recently been also provided [**?**] for the electron-lead ion scattering. The following table, Tab. 3.4, is a slight update of the numbers presented in there also introducing the $E_p = 20\,\text{TeV}$ FCC-hh configuration. A year of eA operation, possibly distributed over some smaller bits of operation thus has the potential to provide an integrated data set of about 5 (25) fb^{-1} for the LHeC (FCC-eh), resp. This exceeds the HERA *ep* luminosity values about tenfold and the fixed target nuclear DIS experiment kinematics by about $3-4$ orders of magnitude. These energy frontier electron-ion configurations therefore have the potential to establish a much different view on nuclear structure and parton dynamics as the current one. This is discussed in Sect.XX.

3.2.5 Linac Parameters

The brief summary of the main LHeC characteristics here concludes with the main ERL parameters, for the novel default of 50 GeV. Tab. 3.5, which are discussed in much detail in Sect.YY.

3.3 Operation Schedule [Oliver Bruening]

[2] The low energy FCC-pp collider, as of today, uses a 6 T LHC magnet in a 100 km tunnel. If within decades ahead high field magnets may become available based on HTS technology, then a 20 TeV proton beam energy may also be achievable in the LHC tunnel. To this extent the here considered low energy FCC and an HTS based HE-LHC represent much comparable options in terms of their energy reach.

parameter [unit]	LHeC	FCC-eh	FCC-eh
E_p [TeV]	7	20	50
E_{Pb} [PeV]	0.574	1.64	4.1
E_e [GeV]	50	50	50
$\sqrt{s_{eN}}$ electron-nucleon [TeV]	0.8	1.4	2.2
bunch spacing [ns]	50	100	100
no. of bunches	1200	2072	2072
ions per bunch [10^8]	1.8	1.8	1.8
$\gamma\epsilon_A$ [μm]	1.5	0.9	0.9
electrons per bunch [10^9]	6.2	12.5	12.5
electron current [mA]	20	20	20
IP beta function β^*_A [cm]	7	10	15
luminosity [$10^{32}\mathrm{cm}^{-2}\mathrm{s}^{-1}$]	10	18	54

Table 3.4: Baseline parameters of future electron-ion collider configurations based on the electron ERL, in concurrent eA and AA operation mode with the LHC and the two versions of a future hadron collider at CERN.

item	dimension	value
Frequency	MHz	801.58
Bunch charge	pC	499
Bunch spacing	ns	24.95
Electron current	mA	20
Injector energy	MeV	500
Gradient	MV/m	19.73
Cavity length, active	m	0.918
Cavity length, flange-to-flange	m	1.5
Cavities per cryomodule		4
Length of cryomodule	m	7
Acceleration per cryomodule	MeV	72.45
Total number of cryomodules		112
Acceleration energy per pass	GeV	8.1

Table 3.5: Basic LHeC ERL characteristics for the default configuration using two such linacs located opposite to each other in a racetrack of 5.3 km length. Each linac is passed three times.

Chapter 4

Precision Standard Model Physics with LHeC [Daniel Britzger, Fred Olness]

Introduction In this section we discuss the aspects of Standard Model precision measurements at the LHeC with $e^{\pm}p$ data. This includes measurement of the strong and the electroweak sector. First, precision measurements of the structure of the proton and the determination of parton distribution functions (PDFs) are discussed, due the extraordinary role of this QCD aspect in deep-inelastic scattering. In sect. **??** further aspects of precision QCD measurements are discussed. Then electroweak, and then top-quarks. Measurements of the Higgs sector is discussed in chapter 6.

4.1 Resolving the Parton Substructure of the Proton
[Daniel, Claire, Mandy, Paul, Anna, Fred]

Fred: I've inserted draft text from the previous version into the individual subsections. Please feel free to edit/delete as you like.

4.1.1 Open Questions on the QCD of PDFs [Fred, Pavel]

- collinear approximation
- further PDFs
- current techniques
- Compatibility of data (LHC in particular)
- pion, D, nuclear corr's

The LHeC provides the opportunity to push our Standard Model (SM) measurements to unprecedented precision. This also provides an opportunity to search for deviations from the SM predictions which may signal the presence of an undiscovered "new physics" channel.

In the near future, new physics searches will be driven by precision measurements which are sensitive to admixtures of new physics signals which distort the "vanilla" Standard Model (SM) measurements.

While direct production of new physics is limited by the energy ($\sqrt{s}$) of the machine, indirect precision measurements can probe scales may times larger than the CMS energy; this is an area where the LHeC excells. While the LHeC can directly probe the TeV scale, it offers the most promising avenue to search for

new physics signals at multi-TeV scales, and gather clues as how to design the next-generation of accelerator experiments such as the FCC program.

An essential step in advancing this precision program is improving our knowledge of the PDFs. For many precision measurements and "standard candle" observables, the element that limits our sensitivity to the highest energy scales is the PDF uncertainty.

In this section, we will explore specific processes by which the LHeC can significantly improve our determination of PDFs.

4.1.2 PDFs and the LHC [Fred, Lucien]

PDF4LHC Update:

- PDF4LHC
- update 19 (Lucien)

to cite:[7, 8]

Prospects with the HL-LHC

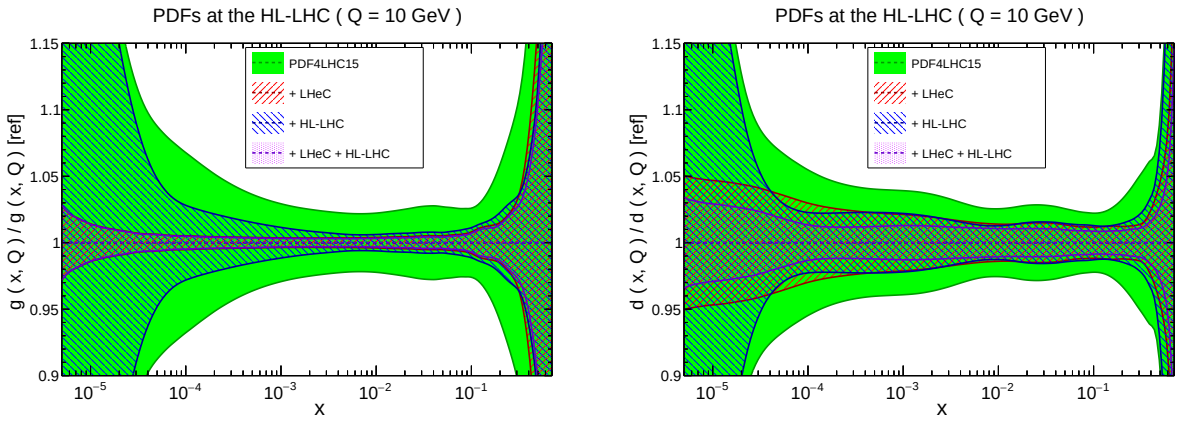

Figure 4.1: Projected PDF precision of HL-LHC and LHeC using pseudodata as outlined in Ref. [9].

PDF Sensitivity: Comparing LHC and LHeC:

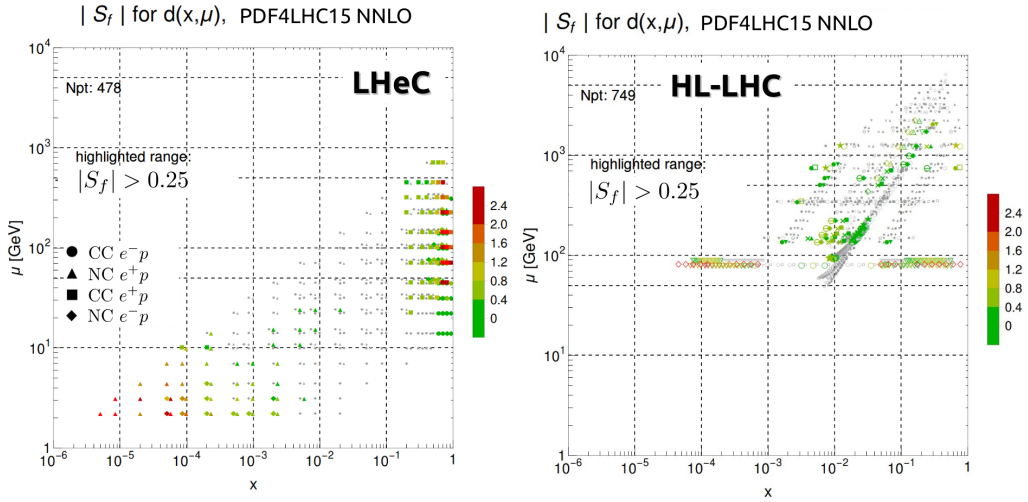

Figure 4.2: Sensitivity for a sample flavor ($d(x, Q)$) in the $\{x, Q^2\}$ kinematic plane for the LHeC (left) and the HL-LHC (right) calculated with pseudodata [10]. We observe the LHeC is particularly sensitive in both the high and low x regions, and the HL-LHC covers the intermediate x region out to large Q scales.

While experimental reach of each facility in the $\{x, Q^2\}$ kinematic plane of Fig. 4.3 [*** cite to the figure; no yet included ***] provides a useful comparison, there are more factors to consider–especially when we are striving for ultra-high precision measurements.

One measure that provides a dimension beyond the $\{x, Q^2\}$ plane is the *sensitivity*; this is a combination of the correlation coefficient times a scaled residual [11, 10]. In Fig. 4.2 we display this sensitivity for a sample PDF flavor. This gives us an extra dimension of information compared to Fig. 4.3, and provides a measure of the impact of the data. In particular, we observe the LHeC provides strong sensitivity in the high-x region (which is important for BSM searches), and also in the low-x region (which is relevant for saturation). The HL-LHC provides constraints coming from W/Z production ($Q \sim M_{W/Z}$) as well as from jets at high Q scales. The combination of these measurements can provide very strong constraints on the various PDF flavors across the broad $\{x, Q^2\}$ kinematic plane.

While the kinematic plots of Fig. 4.3 provide a valuable overview, we must be caution to consider other "dimensions" to ascertain the complementary aspects when comparing the separate facilities.

4.1.3 The Role of DIS/ep Colliders in the Determination of PDFs [Mandy, Max]

- Reasons for ep - Max
- HERA data and HERA2.0 Mandy
- The Role of LHeC Mandy

The Kinematic Landscape:

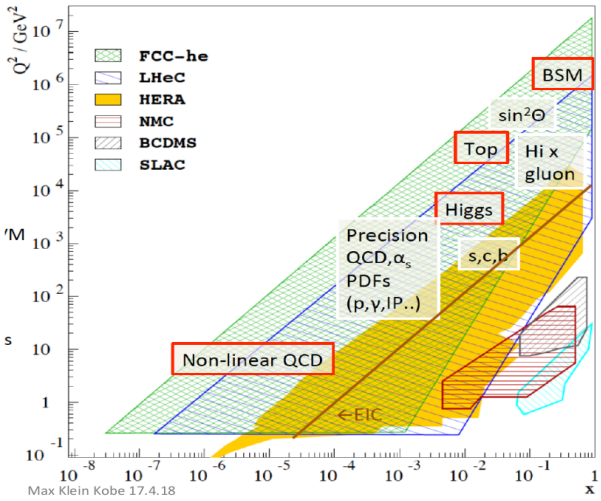

Figure 4.3: Comparison of $\{x, Q^2\}$ kinematic reach of various facilities. FIGURE TO BE UPDATED

In Fig. 4.3 we display the kinematic reach in $\{x, Q^2\}$ space for past, present, and future machines. We highlight the separate regions that impact specific processes such as BSM, top-quark production, Higgs production, and non-linear QCD.

The fixed-target measurements (SLAC, BCDMS, NMC) cover the high-x low-Q^2 region (bottom right portion of the figure). HERA ($\sqrt{s} \sim 313$ GeV) significantly extended the $\{x, Q^2\}$ reach. The proposed Electron Ion Collider (EIC) ($\sqrt{s} \sim 140 * **???$ GeV) will study both proton and nuclei in the high-x and low-Q^2 extremes.

The LHeC will extend the x reach by *** and the Q^2 reach by *** with a $\sqrt{s} \sim 1.2$ TeV an a luminosity 1000× that of HERA. In the farther future, an FCC-he will then push the kinematic limits to an unprecedented $\sqrt{s} \sim ***$ TeV.

4.1.4 Simulation and Default Fit [Mandy, Max]

- Data, Syst errors, L profile, energy sets. (Max)
- Fit ansatz and its motivation (Mandy)

The Pseudo-Data Sets:

To make quantitative comparisons such as those displayed in Figs. 4.3 and 4.2, we have used a set of LHeC pseudo-data computed as outlined in Ref.******** and shown in Fig. 4.4. [9]

The figure highlights the broad kinematic reach of the LHeC using electrons and positron beams, and also with a High Energy (HE) and Low Energy (LE) configuration in both Charged Current (CC) and Neutral Current (NC) channels. Additionally, we can include neutral current (NC) heavy quark production ($F_2^{c\bar{c}}$, $F_2^{b\bar{b}}$) which helps constrain the gluon PDF, as well as charged current production of charm (F_2^c) which can constrain the strange PDF.

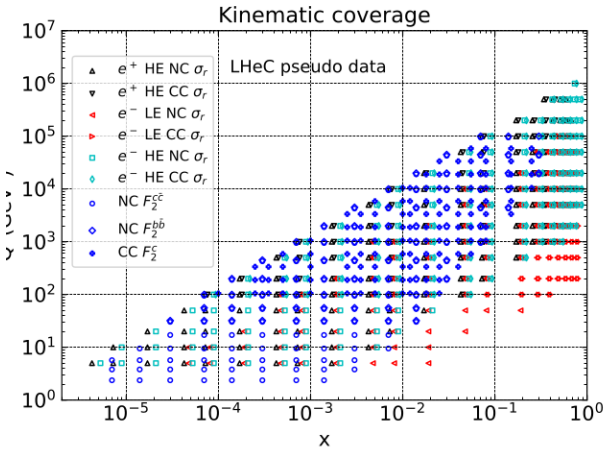

Figure 4.4: Pseudo-Data used for studies

4.1.5 PDF Prospects with the LHeC [... , Claire]

- Quarks (valence)
- Light sea, lifting dbar=ubar condition
- Gluon

Overview: PDF Improvements from LHeC:

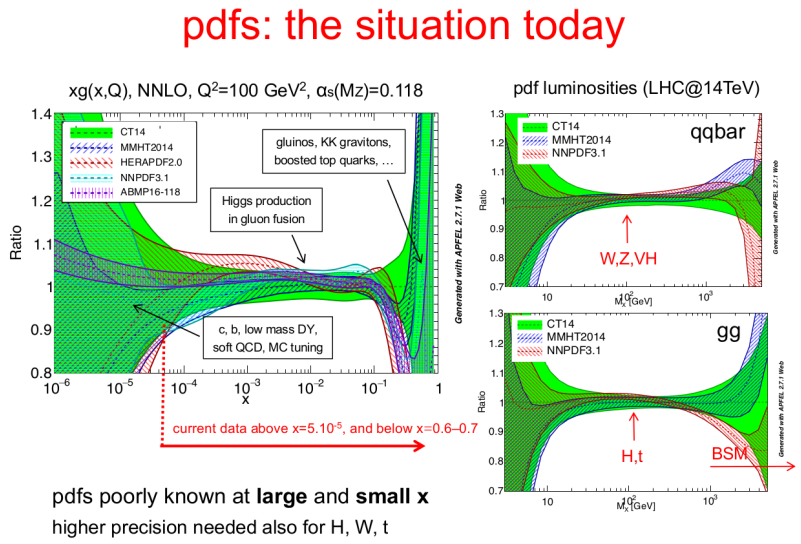

Figure 4.5: Current PDF uncertainties: this limits BSM searches

The extraction of PDFs in global analyses has an extensive history. At present, there are many group actively working on improving the PDFs. [*** Cite current PDF groups ***]

In Fig. 4.5 we display some sample PDF uncertainties and luminosities. In all these figures, we see the general pattern that the PDFs are reasonably constrained in the central x region, but poorly know in both

the large and small x region. The LHeC will greatly expand the kinematic coverage in the $\{x, Q^2\}$ plane, and offer an increased luminosity of 1000× that of HERA.

In the small x region, much of the PDF constraints came from the HERA data which extends down to a few 10^{-5} (depending on the Q^2 cuts); the LHeC will extend these limits by more than a decade.

The high x region is crucial for precision measurements of both SM and BSM processes (as discussed in the previous section); here the large luminosity of the LHeC together with an increase of the Q^2 reach by an order of magnitude ($\sim 15\times$) will allow for significant improvement in this region.

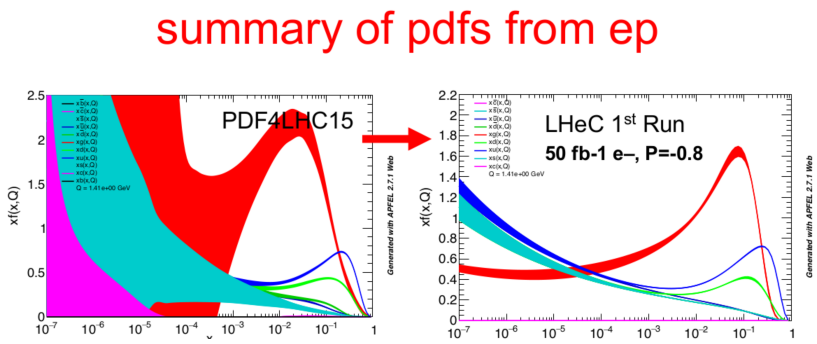

Figure 4.6: Improvements of PDFs from LHeC

The integrated luminosity for the LHeC across the full program is expected to be $1\,ab^{-1}$; however, in just the first three years of running an integrated luminosity of just 50 fb^{-1} will provide a dramatic reduction of the PDF uncertainties illustrated in Fig. 4.6. This improvement in the PDF uncertainties would presumably be in parallel with the running of the HL-LHC (and well before the end of the HL-LHC operation); hence, these improved PDFs would also be available to benefit improved HL-LHC analyses.

Improved PDFs from LHeC: High-x

We first focus on the high-x kinematic region, which is a particular strength of the LHeC; this advantage arises from primarily two factors: i) the increased energy of the LHeC machine ($Q^2 \sim 15$ times HERA), and ii) the fact that the initial state (ep) only has one composite object as compared to hadron-hadron processes.

In Figs. 4.7 and 4.8 we display the improvement of the LHeC PDF constraints as compared to current limits for the valence and gluon distributions, respectively. The broader (yellow) band represents the constraints from the initial run ($50\,pb^{-1}$), and the narrower (blue) band represent the constraints from the full inclusive run ($1\,ab^{-1}$). The improvements are dramatic for both the quark and gluon channels. Additionally, these measurements offer the opportunity to resolve the long-standing issue of the d/u ratio at large x as demonstrated in Fig. 4.9. Because these measurements are performed in the large Q^2 region on proton beams, they are insensitive to higher twist effects and nuclear corrections. As discussed previously, the high x region is key for constraining BSM physics signatures.

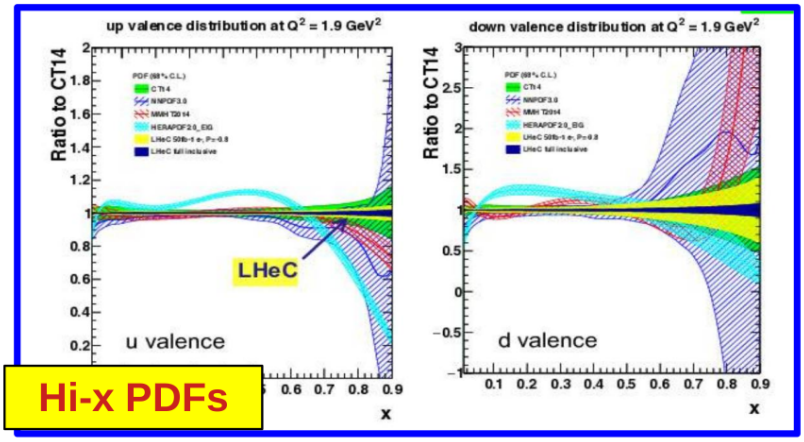

Figure 4.7: PDF constraints from LHeC at for quarks at hi-x.

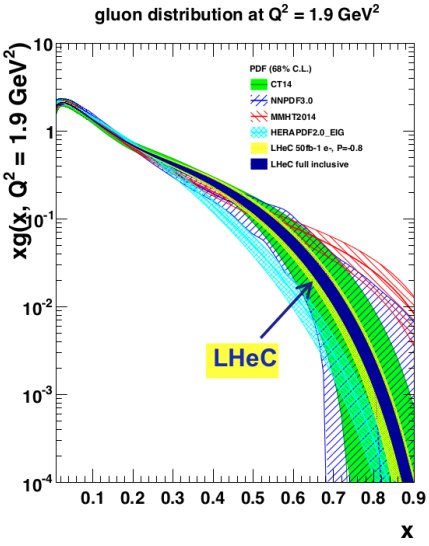

Figure 4.8: PDF constraints from LHeC for gluon at hi-x.

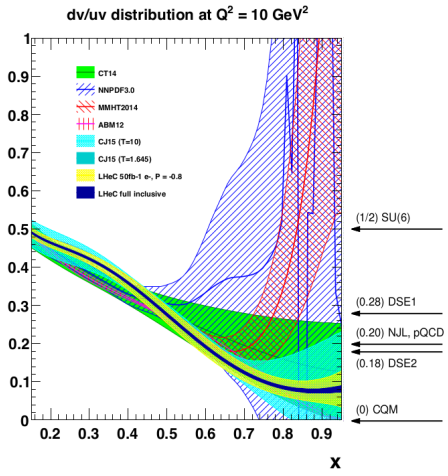

Figure 4.9: PDF constraints on the ratio d_v/u_v at hi-x.

Improved PDFs from LHeC: Low-x

The LHeC kinematics also enables us to probe the small x region of the kinematic plane with exceedingly high statistics. This allows us to address questions about parton saturation, recombination, and DGLAP vs. BFKL evolution and non-linear dynamics. This low x region is also relevant for ultra-high-energy neutrino cross sections as measured in cosmic ray experiments.

In Fig. 4.10 we display the comparative improvement of the up and down PDFs from the LHeC pseudo-data vs. the HERA constraints. Some care must be exercised when making comparisons at small x as parametrization effects can influence the interpretation [9]. In this particular case, we have used the same framework to compare the LHeC and HERA constraints.

Current data extends down to $x \sim 5{\times}10^{-5}$, while the LHeC provides a single precise data set down to $\sim 10^{-6}$, and the FCC-he can go down to $\sim 10^{-7}$. Evidence for the onset of BFKL dynamics has been investigated in a number of recent studies [12, 13, 14]. These simulations show that the LHeC has significant constraining power to discriminate between theoretical scenarios of small x dynamics. Additionally, the measurement of F_L has a critical role to play as this is sensitive to both the gluon PDF and higher order effects. [15]

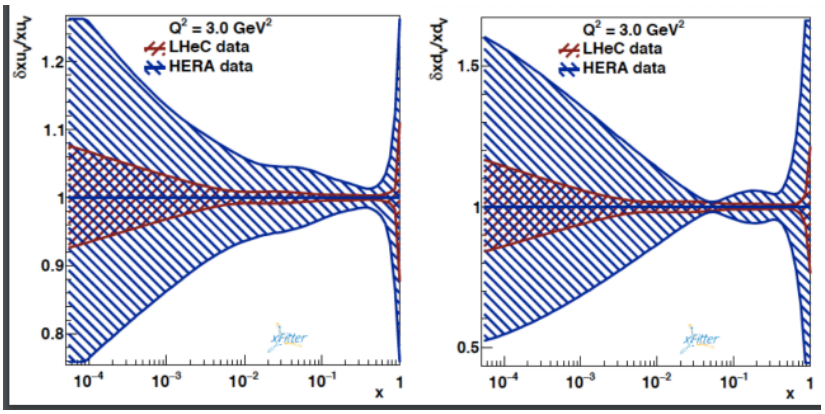

Figure 4.10: Constraints at small x.

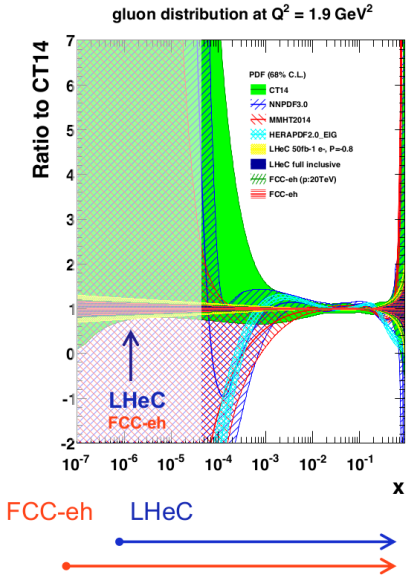

Figure 4.11: PDF constraints from LHeC for gluon at low-x.

Luminosity: Impact for LHC

Finally, we examine the impact of the LHeC precision measurements on the LHC proceses. As a sample, in Fig. 4.12 we display the gluon-gluon and quark-quark luminosities for the LHC ($\sqrt{s} = 14$ TeV) as compared with current estimates from the PDF4LHC15 benchmarks. The outer (yellow) band shows the improvement for the initial ($50\,pb^{-1}$) run, and the inner (blue) band shows the improvement for the full ($1\,ab^{-1}$) run. In either case, the LHeC data will allow us to make high precision measurements (on order of a few percent) well into the multi-TeV region.

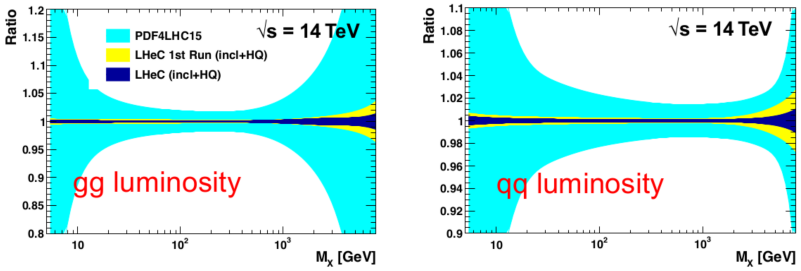

Figure 4.12: Current PDF luminosities.

LHeC PDF Sensitivity: Light Sea Quarks:

LHeC PDF Sensitivity: Gluons:

In Depth Investigations:

Within the working group on PDFs and Low x physics, there were a number of detailed studies examining the impact of parameterizations, tolerance factors, correlated errors, and other various factors that can influence the resulting PDF.

The result of one such study [16] is presented in Fig. 4.13 which shows the differing impacts due to different input assumptions.

It is for this reason that the PDF uncertainty limits have been re-calculated using multiple frameworks with different programs. For example, in Fig. 4.14 we display the improvements of selected PDF flavors using a different program (xFitter) in addition to a different parameterization. Recent efforts within the PDFs and Low x study group have reduced the final differences among the various calculations, and work is ongoing. Nevertheless, in all cases we see a dramatic improvement of the PDF uncertainties with the LHeC data included.

This study also highlights the point that many of these studies are implicitly assuming a specific framework (parameterization, tolerance level, ...). Should we encounter "new physics" signals that do not fit neatly into this framework, obviously the assumptions will need to be revised; this is an example where having complementary input from, for example, an HL-LHC and an LHeC would be crucial in discerning whether an anomalous signature arose from an uncertain SM process or could definitively be identified as a true BSM source.

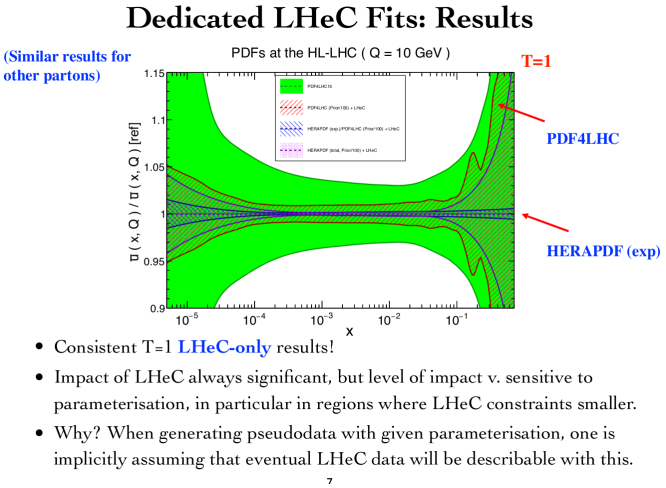

Figure 4.13: Parametrization and Pseudo-data issues.

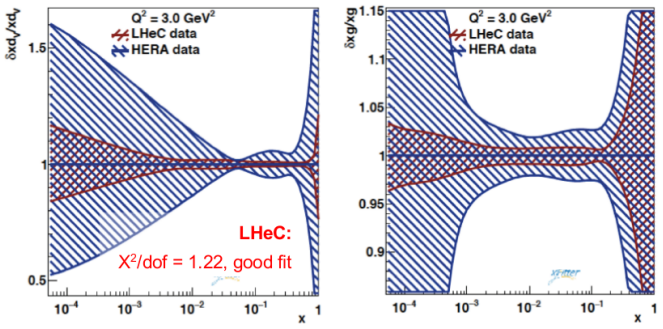

Figure 4.14: Marco & Fra studies:

4.1.6 Heavy Quarks [Mandy, Olaf, Fred, ...]

- Strange (tagged, flavour democracy?) Mandy,Fred

- c and b (and their role for LHC, parameters..) Olaf,
- Top PDF - NNPDF

Heavy Quarks: Strange:

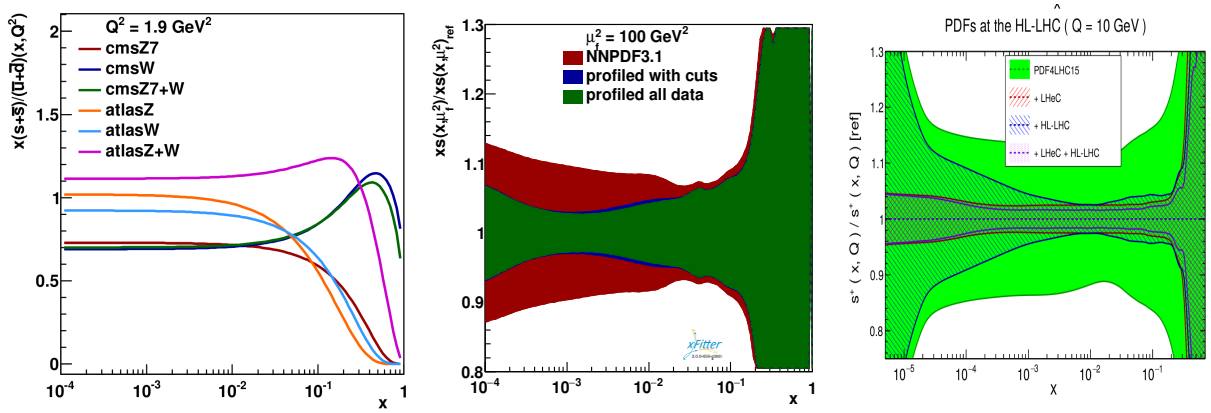

Figure 4.15: a) The fits to the PDF ratio $(s+\bar{s})/(\bar{u}+\bar{d})$ for various subsets of the ATLAS and CMS W and Z data sets from Ref. [17]. b) Constraints on the strange quark PDF using charged-current production of charm at the LHeC from Ref. [18]. c) Constraints on the strange quark PDF from Ref. [9].

Determination of the strange PDF has generated significant controversy in the literature for more than a decade. The older fixed-target neutrino DIS measurements typically prefer a strange PDF that is roughly half of the up and down sea distribution; $\kappa = (s+\bar{s})/(\bar{u}+\bar{d}) \sim 0.5$, while recent measurements from the LHC suggest a larger strange quark distribution.. The LHeC provides the opportunity to resolve many of these outstanding issues and greatly improved the precision of $s(x)$. The strange quark provides a significant contribution to "standard candle" measurements such as W/Z production, and influences the the W mass determination.

The high precision measurements of the inclusive W and Z boson cross section at the LHC provide new constraints on the strange quark density in the low-x regime. One of the earlier LHC analyses to study the strange quark PDF used the ATLAS inclusive W/Z data [19, 20]. In contrast to the results from the fixed-target experiments, the LHC analysis suggested the strange quark could be as large, or larger, than the up and down sea quarks ($\bar{u}$ and $\bar{d}$). This observation was supported by analysis of the ATLAS $W+c$ data [21]

However, the CMS $W+c$ data [22] favor a somewhat smaller strangeness. Since the analysis of the $W+c$ data involve assumptions on charm jet fragmentation and hadronisation it is interesting to investigate if this disagreement is present for the inclusive Drell-Yan (DY) data of ATLAS and CMS.

A combined analysis was done by performing a parton distribution function analysis in NNLO QCD using the inclusive deep inelastic scattering data from HERA jointly with the ATLAS and CMS inclusive Drell-Yan data [17]. This study found that while there was no tension between the HERA data and the LHC data, or between the LHC data sets, the LHC data support unsuppressed strangeness in the proton at low x at both low and high scales. The result is dominated by the ATLAS data but is not in contradiction with the CMS data. Figure 4.15-a displays the preferred value of the ratio $(s+\bar{s})/(\bar{u}+\bar{d})$ for the individual measurements.

The LHeC has the potential to significantly improve the precision of the strange quark PDF, and this may provide additional insight into the above analyses. To investigate this possibility, the xFitter collaboration used LHeC pseudodata for charged current production of charm final states to constrain the initial strange

quark PDF; at leading-order, the subprocess is $Ws \to c$. Additionally, the charged current process allows us to use the electron and positron beams to separately probe the strange and anti-strange PDFs individually; this provides another level of flavor discrimination.

This study found that the LHeC can provide strong constraints on the strange-quark PDF, especially in the previously unexplored small-x region. Figure 4.15-b displays the improved constraints on the strange PDF using the LHeC pseudo-data for the charged current charm production channel ($sg \to Wc$) as obtained using xFitter profiling tools [18]. A large reduction of uncertainties is observed also when restricting the input data (profiled with cuts, Fig. 4.15-b) to the kinematic range where the differences between the different heavy flavor schemes (VFNS and FFNS) are not larger than the present PDF uncertainties, indicating that the obtained PDF constraints are stable and independent of the particular heavy-flavor scheme. A reduction of the strange-PDF uncertainties influences the W/Z production, and thus the Higgs production; hence, the LHeC CC DIS charm production data represent a valuable addition for the future global PDF fits.

A separate study [9] also looked at constraints on $s(x)$ using a variety of channels. The results of the improved PDF limits are displayed in Fig. 4.15-c which shows the constraints from the LHeC, the HL-LHC,and the combination.

In summary, we find that CC DIS charm production at the LHeC can provide strong constraints on the strange PDF which are complementary to the current data sets. As the PDF uncertainty is the dominant factor for many precision analyses, a reduction of these uncertainties will allow for more accurate predictions which can be used to constrain both SM and BSM physics processes.

Heavy Quarks: Charm & Bottom:

The production of heavy quarks at HERA (charm and bottom) was an especially interesting process as the quark mass introduced a new scale ($m_{c,b}$) which was neither heavy or light. Such multi-scale problems are particularly difficulty, and numerous techniques were developed to cope with this challenging problem.

At the LHeC, the increased CMS energy allows us to extend to very large Q^2 values. Thus, the LHeC can comprehensively explore the high energy limit where $m^2_{c,b}/Q^2 \to 0$, as well as low energy region $m^2_{c,b}/Q^2 \sim 1$.

In Fig. 4.16 we display the kinematic reach of $F_2^{c\bar{c}}$ and $F_2^{b\bar{b}}$, and contrast this with the HERA combined data. The extended reach is dramatic.

These channels can also help improve the determination of the charm and bottom quark masses and bring these uncertainties into the range of $\lesssim 10$ MeV. *** Need refs here.

Additionally, the production of heavy quarks is closely tied to the gluon distribution ($g \to Q\bar{Q}$), so can also contribute to reducing this uncertainty, c.f., Fig. 4.17. In Fig. 4.17 we display the impact of the LHeC heavy quark data on the gluon PDFs. ********** needs a bit more discussion here **********8

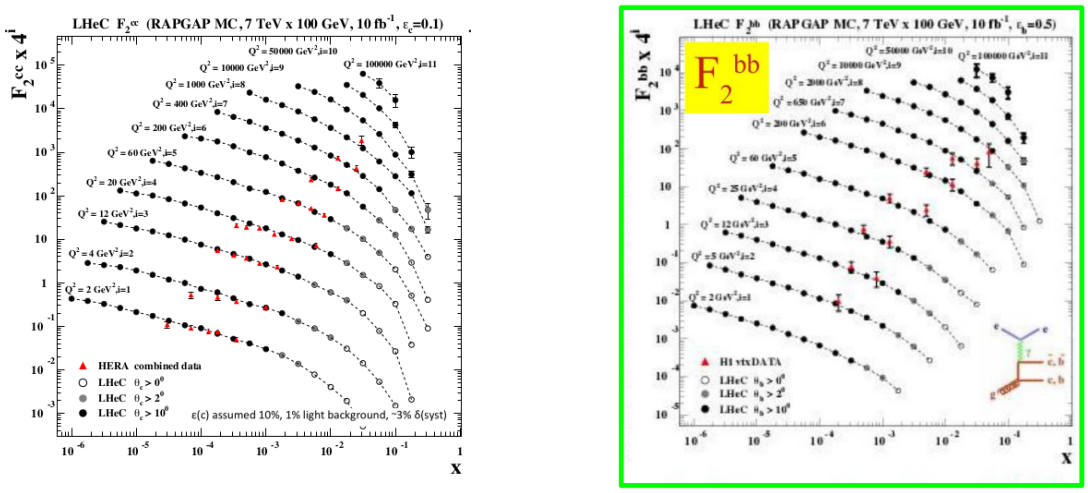

Figure 4.16: Heavy quark structure functions $F_2^{c\bar{c}}$ and $F_2^{b\bar{b}}$. Olaf has updated figures for this!!!

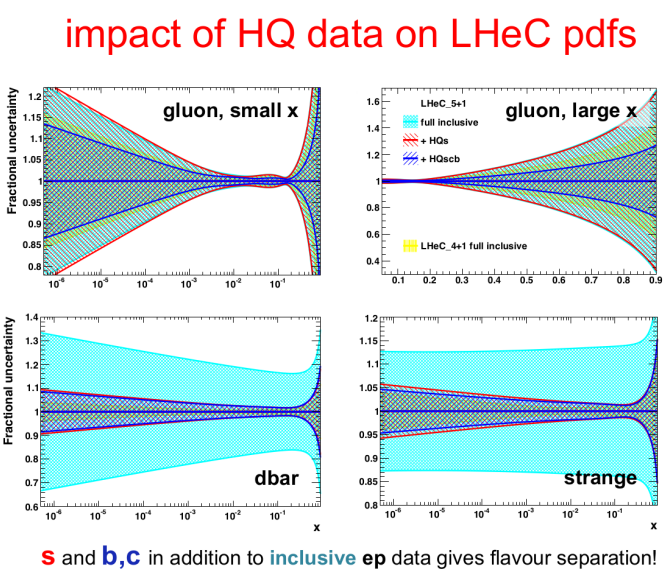

Figure 4.17: Impact of HQ data on LHeC PDFs Do we show just gluon, or also include dbar and strange???

Heavy Quarks: Top:

4.1.7 Jets and PDFs [Daniel]

joint inclusive + jet fit

- ...

4.1.8 Summary: [Fred, Daniel]

- Reasons for ep - Max
- HERA data and HERA2.0 Mandy

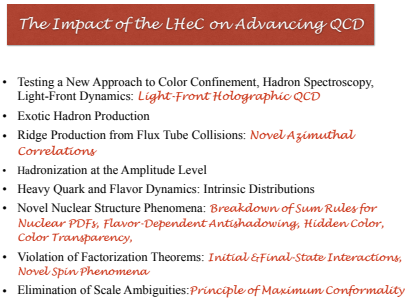

Figure 4.18: @ this should become text and go into SJB specials section. Tests of QCD at the LHeC

- The Role of LHeC Mandy

Conclusions:

Key points for summary. Edits/suggestions welcome.

- Precision determination of quark and gluon distributions of the proton are of fundamental importance for future studies of both SM processes and BSM discoveries.
- Substantial recent activity on both LHeC and FCC studies; work is still ongoing.
- New PDF studies for LHeC demonstrates critical improvements of the PDF uncertainty can be obtained from the inital 3-year run of $50\,pb^{-1}$; this is $50\times$ the total HERA integrated luminosity.
- The LHeC will provide a complete unfolding of the quark and gluon PDFs in both the large and small x regions.
- The precision LHeC measurements, when combined with the concurrently operating HL-LHC, will provide the most accurate extrapolation into the large energy region; this information can provide crucial clues as to the optimal design energy for a future FCC facility.

4.2 Pushing the limits of QCD with high precision measurements

SJB. The QCD tests at the LHeC involve many fundamental aspects of QCD: The LHeC extends tests of QCD to a new domain, particularly in deep inelastic electron-proton and lepton-nucleus reactions. The DIS events measure not only structure functions but also generalized structure observables such as the transverse momentum distributions (TMDs). These processes measure fundamental hadronic properties described by the light-front wavefunctions of the proton or nucleus, the frame-independent eigensolutions of the QCD light-front Hamiltonian, as illustrated in Fig. 4.19. The impact of the LHeC on tests of QCD is summarized in Fig. 4.18.

4.2.1 Determination of the strong coupling constant [Daniel Britzger]

Quantum Chromodynamics (QCD) has been established as the theory of strong interactions within the Standard Model of particle physics. While there are manifold aspects both from the theoretical and from the experimental point-of-view, by far the most important parameter of QCD is the coupling strength which is most commonly expressed at the mass of the Z boson, M_Z, as $\alpha_s(M_Z)$. Its (renormalisation) scale

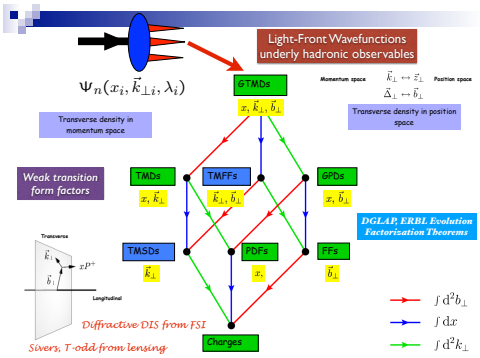

Figure 4.19: Light-Front wavefunctions encode hadron structure and underlie hadron observables such as the Drell-Yan-West Formula for elastic and inelastic form factors, structure functions, generalized parton distribution, etc. Observables with complex phases, such as diffractive deep inelastic scattering $ep \to e'p'X$ and the Sivers pseudo-T-odd spin correlation [23] $\vec{S}_p \cdot \vec{q} \times \vec{p}_q$, shadowing and antishadowing of nuclear structure function, incorporate the Wilson lines which involve final and/or initial state interactions, as well as the LFWFs. Adopted from an illustration by B. Pasquini and C. Lorcé [24, 25].

dependence is given by the QCD gauge group SU(3). Predictions for numerous processes in e^+e^-, pp or ep collisions are then commonly performed in the framework of perturbative QCD, and (the lack of) higher-order QCD corrections often represent limiting aspects for precision physics. Therefore, the determination of the strong coupling constant $\alpha_s(M_Z)$ constitutes one of the most crucial tasks for future precision physics, while at the same time the study of the scale dependence of α_s provides an inevitable test of the validity of QCD as the theory of strong interactions and the portal for GUT theories.

Different processes and methodologies can be considered for a determination of $\alpha_s(M_Z)$. Since QCD is an asymptotically free theory, with free behaviour at high scales but confinement at low scales, a high sensitivity to the value of $\alpha_s(M_Z)$ is naturally obtained from low-scale measurements. However, the high-scale behaviour must then be calculated by solving the renormalisation group equation, which implies the strict validity of the theory and an excellent understanding of all subleading effects, such as the behaviour around quark-mass thresholds.

Precision measurements at the LHeC offer the unique opportunity to exploit many of these aspects. Measurements of jet production cross sections or inclusive NC and CC DIS cross sections provide a high sensitivity to the value of $\alpha_s(M_Z)$, since these measurements can be performed at comparably low scales and with high experimental precision. At the same time, the LHeC provides the opportunity to test the running of the strong coupling constant over a large kinematic range. In this section, the prospects for a determination of the strong coupling constant with inclusive jet cross sections and with inclusive NC and CC DIS cross sections are studied.

Strong coupling from inclusive jet cross sections: The measurement of inclusive jet or di-jet production cross sections in NC DIS provides a high sensitivity to the strong coupling constant and to the gluon PDF of the proton. This is because jet cross sections in NC DIS are measured in the Breit reference frame, where the virtual boson γ^* or Z collides head-on with the struck parton from the proton and the outgoing jets are required to have a non-zero transverse momentum in that reference frame. The leading order QCD diagrams are QCD Compton and boson-gluon fusion and are both $\mathcal{O}(\alpha_s)$, see Fig. 4.20.

At HERA, jets are most commonly defined by the longitudinally invariant k_t jet algorithm with a distance parameter $R = 1.0$. This provides an infrared safe jet definition and the chosen distance parameter guarantees a small dependence on non-perturbative effects, such as hadronisation. Differently than in pp at the LHC, jet algorithms at the LHeC do not require any pile-up subtraction and any reduction of the dependence

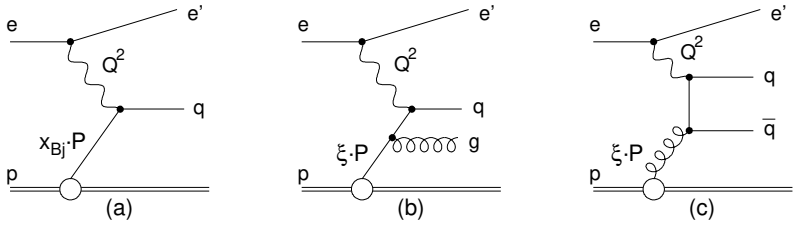

Figure 4.20: Leading order diagrams for inclusive DIS (a) and jet production (b,c) in the Breit frame (taken from Ref. [26]).

on minimum bias, due to the absence of such effects. Therefore, for this study we adopt the choices made at HERA.

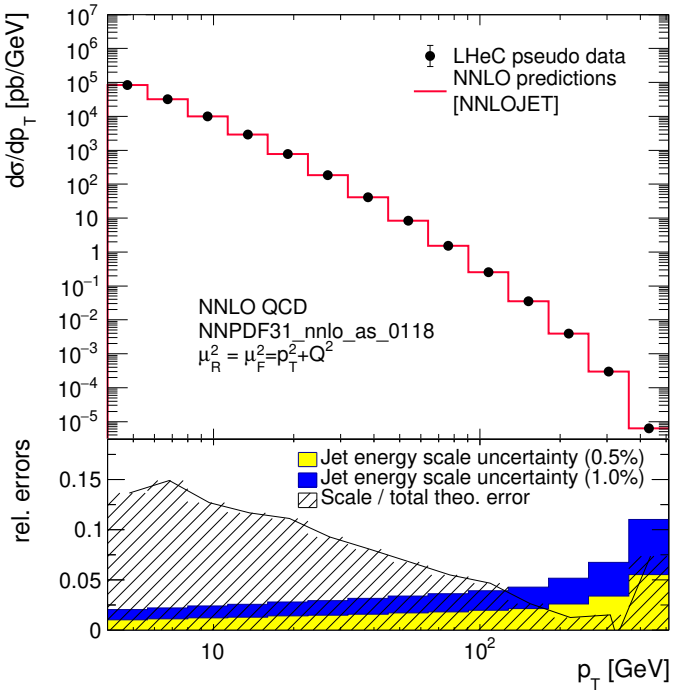

Figure 4.21: Inclusive jet cross sections calculated in NNLO QCD as a function of the jet transverse momentum in the Breit frame, p_{T}. The shaded area indicates NNLO scale uncertainties and the yellow band shows the estimated experimental jet energy scale uncertainty.

In Fig. 4.21 the next-to-next-to-leading order QCD (NNLO) predictions for cross sections for inclusive jet production in NC DIS as a function of the transverse momentum of the jets in the Breit frame are displayed. The calculations are performed for $E_e = 60\,\mathrm{GeV}$ and include γ/Z and Z exchange terms and account for the electron beam polarisation $P_e = -0.8$. The NC DIS kinematic range is set to $Q^2 > 4\,\mathrm{GeV}^2$.

The kinematically accessible range in jet-P_{T} ranges over two orders of magnitude, $4 < P_{\mathrm{T}} \lesssim 400\,\mathrm{GeV}$. The size of the cross section extends over many orders in magnitude, thus imposing challenging demands on LHeC experimental conditions, triggers and DAQ bandwidth, calibration, and data processing capabilities. The scale uncertainty of the NNLO predictions is about 10 % at low values of P_{T} and significantly decreases with increasing values of P_{T}. Future improved predictions will further reduce these theoretical uncertainties.

For the purpose of estimating the uncertainty of $\alpha_{\mathrm{s}}(M_{\mathrm{Z}})$ in a determination from inclusive jet cross sections at the LHeC, double-differential cross sections as a function of Q^2 and P_{T} with a full set of experimental uncertainties are generated. Altogether 509 cross section values are calculated in the kinematic range

$8 < Q^2 < 500\,000\,\mathrm{GeV}^2$ and $4 < P_\mathrm{T} < 512\,\mathrm{GeV}$, and the bin grid is similar to the ones used by CMS, H1 or ZEUS [27, 28, 29, **?**] . The various error sources considered are summarised in Table 4.1. The uncertainties related to the reconstruction of the NC DIS kinematic variables, Q^2, y and $x_{\mathrm{b}j}$, are similar to the estimates for the inclusive NC DIS cross sections (see Sec. **??**). For the reconstruction of hadronic final state particles which are the input to the jet algorithm, jet energy scale uncertainty (JES), calorimetric noise and the polar angle uncertainty are considered. The size of the uncertainties is gauged with achieved values by H1, ZEUS, ATLAS and CMS. The size of the dominant JES one is assumed to be 0.5 % for reconstructed particles in the laboratory rest frame, yielding an uncertainty of 0.2–4.4 % on the cross section after the boost to the Breit frame. A JES uncertainty of 0.5 % is well justified by improved calorimeters, since already H1 reported uncertainties of 1 %, and ATLAS and CMS achieved 1 % over a wide range in P_T, albeit the presence of pile-up and the considerably more complicated definition of a reference object for the in-situ calibration. The size of the JES uncertainty is also displayed in Fig. 4.21. The calorimetric noise of ±20 MeV on every calorimeter cluster, as reported by H1, yields an uncertainty of up to 0.7 % on the jet cross sections. A minimum size of the statistical uncertainty of 0.15 % is imposed for each data point. An overall normalisation uncertainty of 1.0 % is assumed, which will be mainly dominated by the luminosity uncertainty. In addition, an uncorrelated uncertainty component of 0.6 % collects various smaller error sources, such as for instance radiative corrections, unfolding or model uncertainties. Studies on the size and the correlation model of these uncertainties are performed below.

Exp. uncertainty	Shift	Size on σ [%]
Statistics with $1\,\mathrm{ab}^{-1}$	min. 0.15 %	0.15 –5
Electron energy	0.1 %	0.02 –0.62
Polar angle	2 mrad	0.02 –0.48
Calorimeter noise	±20 MeV	0.01 –0.74
Jet energy scale (JES)	0.5 %	0.2 –4.4
Uncorrelated uncert.	0.6 %	0.6
Normalisation uncert.	1.0 %	1.0

Table 4.1: Anticipated uncertainties of inclusive jet cross section measurements at the LHeC.

The value/uncertainty of $\alpha_\mathrm{s}(M_\mathrm{Z})$ is obtained in a χ^2-fit of NNLO predictions [**?**] to the simulated data with $\alpha_\mathrm{s}(M_\mathrm{Z})$ being a free fit parameter. The methodology follows closely analyses of HERA jet data [27, 28] and the χ^2 quantity is calculated from relative uncertainties, i.e. those of the right column of Table 4.1. The predictions account for both α_s-dependent terms in the NNLO calculations, i.e. in the DGLAP operator and the hard matrix elements, by using

$$\sigma = f_{\mu_0} \otimes P_{\mu_0 \to \mu_F}(\alpha_s(M_z)) \otimes \hat{\sigma}(\alpha_s(M_z), \mu)\,,$$

where f_{μ_0} are the PDFs at a scale of $\mu_0 = 30\,\mathrm{GeV}$. The α_s uncertainty is obtained by linear error propagation and is validated with a separate study of the $\Delta\chi^2 = 1$ criterion.

In the fit of NNLO QCD predictions to the simulated double-differential LHeC inclusive jet cross sections an uncertainty of

$$\Delta\alpha_\mathrm{s}(M_\mathrm{Z})(\mathrm{jets}) = \pm 0.00013_{(\mathrm{exp})} \pm 0.00010_{(\mathrm{PDF})}$$

is found. The PDF uncertainty is estimated from a PDF set obtained from LHeC inclusive DIS data. These uncertainties promise a determination of $\alpha_\mathrm{s}(M_\mathrm{Z})$ with the highest precision and would represent a considerable reduction of the current world average value with a present uncertainty of ±0.00110 [**?**].

The uncertainty of α_s is studied for different values of the experimental uncertainties for the inclusive jet measurement and for different assumption on bin-to-bin correlations, expressed by the correlation coefficient ρ, of individual uncertainty sources, as shown in Fig. 4.22. It is observed that, even for quite conservative

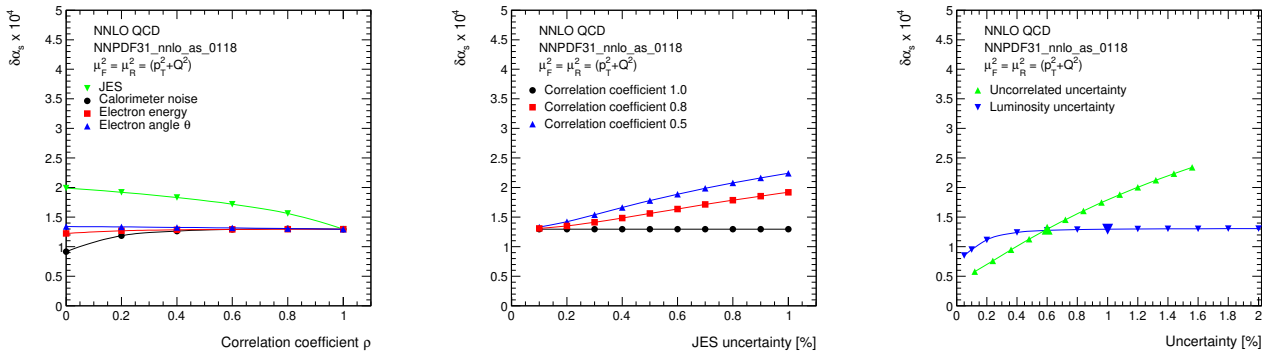

Figure 4.22: Studies of the size and correlations of experimental uncertainties impacting the uncertainty of $\alpha_s(M_Z)$. Left: Study of the value of the correlation coefficient ρ for different systematic uncertainties. Common systematic uncertainties are considered as fully correlated, $\rho = 1$. Middle: Size of the JES uncertainty for three different values of ρ_{JES}. Right: Impact of the uncorrelated and normalisation uncertainties on $\Delta\alpha_{\mathrm{s}}(M_{\mathrm{Z}})$.

scenarios, $\alpha_s(M_Z)$ will be determined with an uncertainty smaller than 2 ‰. For this, it is important to keep the size of the uncorrelated uncertainty or the uncorrelated components of other systematic uncertainties under good control.

In the present formalism theoretical uncertainties from scale variations of the NNLO predictions amount to about $\Delta\alpha_{\mathrm{s}}(M_{\mathrm{Z}}) = 0.0035$ (NNLO). These can be reduced with suitable cuts in P_{T} or Q^2 to about $\Delta\alpha_{\mathrm{s}}(M_{\mathrm{Z}}) \approx 0.0010$. However, it is expected that improved predictions, e.g. with resummed contributions or N^{3}LO predictions will significantly reduce these uncertainties in the future. Uncertainties on non-perturbative hadronisation effects will have to be considered as well, but these will be under good control due to the measurements of charged particle spectra at the LHeC and improved phenomenological models.

The running of the strong coupling: The dependence of the coupling strength as a function of the renormalisation scale μ_{R} is predicted by QCD, which is often called the 'running' of the strong coupling. Its study with experimental data represents an important consistency and validity test of QCD. Using inclusive jet cross sections the running of the strong coupling can be tested by determining the value of α_{s} at different values of μ_{R} by grouping data points with similar values of μ_{R} and determining the value of $\alpha_{\mathrm{s}}(\mu_{\mathrm{R}})$ from these subsets of data points. The assumptions on the running of $\alpha_{\mathrm{s}}(\mu_{\mathrm{R}})$ are then imposed only for the limited range of the chosen interval, and not to the full measured interval as in the previous study. Here we set $\mu_{\mathrm{R}}^2 = Q^2 + P_{\mathrm{T}}^2$. The experimental uncertainties from the fits to subsets of the inclusive jet pseudo-data are displayed in Fig. 4.23. These results demonstrate a high sensitivity to α_s over two orders of magnitude in renormalisation scale up to values of about $\mu_{\mathrm{R}} \approx 500\,\mathrm{GeV}$. In the range $6 < \mu_{\mathrm{R}} \lesssim 200\,\mathrm{GeV}$ the experimental uncertainty is found to be smaller than the expectation from the world average value. This region is of particular interest since it connects the precision determinations from lattice calculations or τ decay measurements, which are at low scales $\mathcal{O}(\mathrm{GeV})$, to the measurements at the Z pole and to the applications to scales which are relevant for the LHC, e.g. for Higgs or top physics or high-mass searches. This kinematic region of scales $\mathcal{O}(10\,\mathrm{GeV})$ cannot be accessed by (HL-)LHC experiments because of limitations due to pile-up and underlying event [30].

Strong coupling from inclusive DIS cross sections: Inclusive DIS cross sections are sensitive to $\alpha_{\mathrm{s}}(M_{\mathrm{Z}})$ through higher-order QCD corrections, contributions from the F_L structure function and the scale dependence of the cross section at high x ('scaling violations'). The value of $\alpha_{\mathrm{s}}(M_{\mathrm{Z}})$ can then be determined

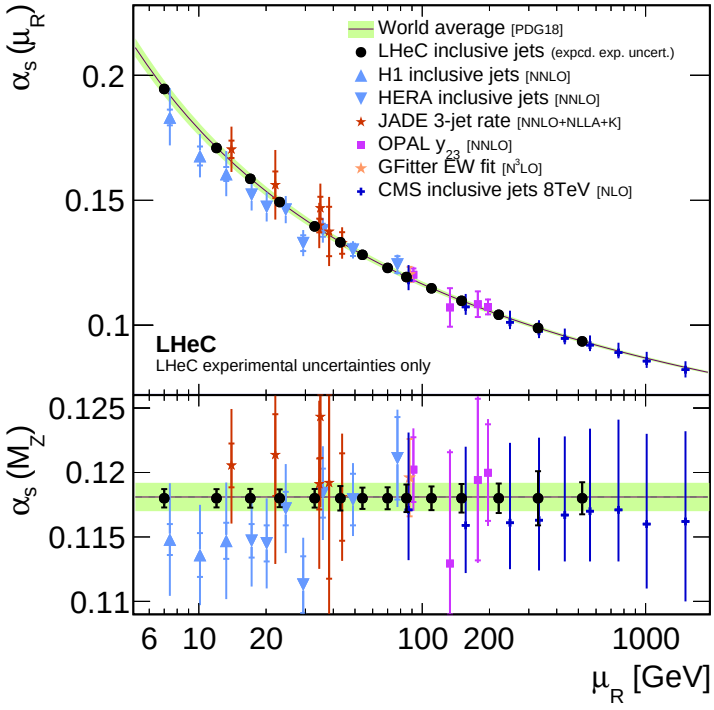

Figure 4.23: Uncertainties of $\alpha_s(M_Z)$ and corresponding $\alpha_s(\mu_R)$ in a determination of α_s using LHeC inclusive jet cross sections at different values of $\mu_R^2 = Q^2 + p_T^2$. Only experimental uncertainties are shown for LHeC and are compared with a number of presently available measurements and the world average value.

in a combined fit of the PDFs and $\alpha_s(M_Z)$. While a simultaneous determination of $\alpha_s(M_Z)$ and PDFs is not possible with HERA inclusive DIS data alone due to its limited precision and kinematic coverage [29, 27], the large kinematic coverage, high precision and the integrated luminosity of the LHeC data will allow for the first time such analysis.

For the purpose of the determination of $\alpha_s(M_Z)$ from inclusive NC/CC DIS data, a combined PDF+α_s fit to the simulated data is performed, similar to the studies in Sec. 4.1. Other technical details are outlined in Ref. [27]. In this fit, however, the numbers of free parameters of the gluon parameterisation is increased, since the gluon PDF and $\alpha_s(M_Z)$ are highly correlated and LHeC data are sensitive to values down to $x < 10^{-5}$, which requires additional freedom for the gluon parameterisation. The inclusive data are restricted to $Q^2 > 3.5\,\mathrm{GeV}^2$ in order to avoid a region where effects beyond fixed-order perturbation theory may become sizeable.

Exploiting the full LHeC inclusive NC/CC DIS data with $E_e = 50\,\mathrm{GeV}$, the value of $\alpha_s(M_Z)$ can be determined with an uncertainty $\Delta\alpha_s(M_Z) = \pm 0.00038$. With a more optimistic assumption on the dominant uncorrelated uncertainty of $\delta\sigma_{(\mathrm{uncor.})} = 0.25\,\%$, an uncertainty as small as

$$\Delta\alpha_s(M_Z)(\text{incl. DIS}) = \pm 0.00022_{(\mathrm{exp+PDF})} \tag{4.1}$$

is achieved. This would represent a considerable improvement over the present world average value. Given these small uncertainties, theoretical uncertainties from missing higher orders or heavy quark effects have to be considered in addition. In a dedicated study, the fit is repeated with a reduced data set which can be accumulated already during a single year of operation[1], corresponding to about $\mathcal{L} \sim 50\,\mathrm{fb}^{-1}$. Already these data will be able to improve the world average value. These studies are displayed in Fig. 4.24.

[1] Two different assumptions are made. One fit is performed with only electron data corresponding to $\mathcal{L} \sim 50\,\mathrm{fb}^{-1}$, and an alternative scenario considers further positron data corresponding to $\mathcal{L} \sim 1\,\mathrm{fb}^{-1}$.

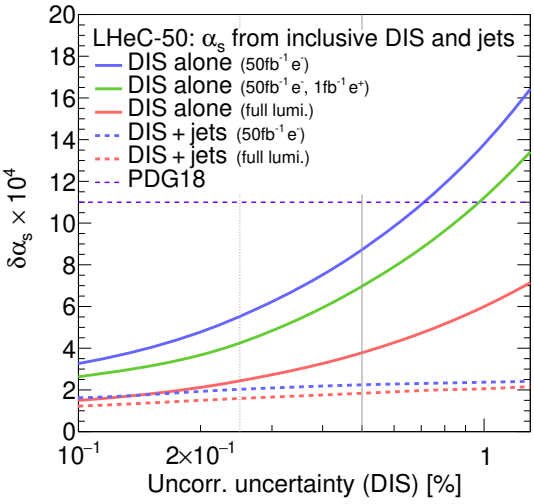

Figure 4.24: Uncertainties of $\alpha_s(M_Z)$ from simultaneous fits of $\alpha_s(M_Z)$ and PDFs to inclusive NC/CC DIS data as a function of the size of the uncorrelated uncertainty of the NC/CC DIS data. The full lines indicate the uncertainties obtained with different assumptions on the data taking scenario and integrated luminosity. The dashed lines indicate results where, additionally to the inclusive NC/CC DIS data, inclusive jet cross section data are considered.

Inclusive DIS and inclusive jet data: The highest sensitivity to $\alpha_s(M_Z)$ and an optimal treatment of the PDFs is obtained by using inclusive jet data together with inclusive NC/CC DIS data in a combined determination of $\alpha_s(M_Z)$ and the PDFs. Jet data will provide an enhanced sensitivity to $\alpha_s(M_Z)$, while inclusive DIS data has the highest sensitivity to the determination of the PDFs. Furthermore, a consistent theoretical QCD framework can be employed.

For this study, the double-differential inclusive jet data as described above, and additionally the inclusive NC/CC DIS data with $E_e = 50\,\text{GeV}$ as introduced in Sec. 4.1.4, are employed. Besides the normalisation uncertainty, all sources of systematic uncertainties are considered as uncorrelated between the two processes. A fit of NNLO QCD predictions to these data sets is then performed, and $\alpha_s(M_Z)$ and the parameters of the PDFs are determined. The methodology follows closely the methodology sketched in the previous study. Using inclusive jet and inclusive DIS data in a single analysis, the value of $\alpha_s(M_Z)$ is determined with an uncertainty of

$$\Delta\alpha_s(M_Z)(\text{incl. DIS \& jets}) = \pm 0.00018_{(\text{exp+PDF})}\,. \tag{4.2}$$

This result will improve the world average value considerably. However, theoretical uncertainties are not included and new mathematical tools and an improved understanding of QCD will be needed in order to achieve small values similar to the experimental ones. The dominant sensitivity in this study arises from the jet data. This can be seen from Fig. 4.24, where $\Delta\alpha_s(M_Z)$ changes only moderately with different assumptions imposed on the inclusive NC/CC DIS data. Assumptions made for the uncertainties of the inclusive jet data have been studied above, and these results can be translated easily to this PDF+α_s fit.

Discussion of $\alpha_s(M_Z)$ determinations at LHeC: The expected values for $\alpha_s(M_Z)$ obtained from inclusive jets or from inclusive NC/CC DIS data are compared in Fig. 4.25 with present determinations from global fits based on DIS data (called 'PDF fits') and the world average value [31]. It is observed that LHeC will have the potential to improve considerably the world average value. Already after one year of data taking, the experimental uncertainties of the NC/CC DIS data are competitive with the world average value. The measurement of jet cross sections will further improve that value.

Furthermore, LHeC will be able to address a long standing puzzle. All α_s determinations from global fits

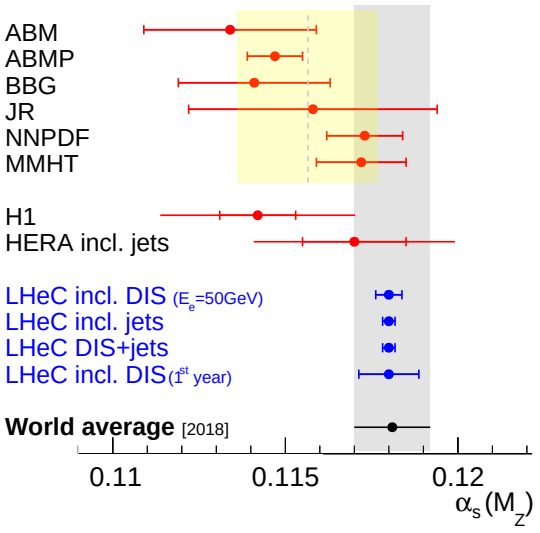

Figure 4.25: Summary of $\alpha_s(M_Z)$ values in comparison with present values. The figure is just a place-holder for the final plot.

based on NC/CC DIS data find a lower value of $\alpha_s(M_Z)$ than determinations in the lattice QCD framework, from τ decays or in a global electroweak fit. With the expected precision from LHeC this discrepancy will be resolved.

Strong coupling from other processes: A detailed study for the determination of $\alpha_s(M_Z)$ from NC/CC DIS and from inclusive jet data was presented in the previous paragraphs. However, a large number of additional processes and observables that are measured at the LHeC can also be considered for a determination of $\alpha_s(M_Z)$. Suitable observables or processes are di-jet and multi-jet production, heavy flavour production, jets in photoproduction or event shape observables. These processes all exploit the α_s dependence of the hard interaction. Using suitable predictions, also 'softer' processes can be exploited for an α_s determination. Examples could be jet shapes or other substructure observables, or charged particle multiplicities.

Since $\alpha_s(M_Z)$ is a parameter of a phenomenological model, the total uncertainty of $\alpha_s(M_Z)$ is always a sum of experimental and theoretical uncertainties which are related to the definition of the observable and to the applied model, e.g. hadronisation uncertainties, diagram removal/subtraction uncertainties or uncertainties from missing higher orders. Therefore, credible prospects for the total uncertainty of $\alpha_s(M_Z)$ from other observables or processes are altogether difficult to predict, even more since LHeC will explore a new kinematic regime that was previously unmeasured.

In a first approximation, the sensitivity to $\alpha_s(M_Z)$ for any process scales with the order n of α_s in the leading-order diagram of the process, α_s^n. Consequently, the experimental uncertainties reduce with increasing power n due to the increased sensitivity, and for instance the multi-jet production cross section represents an attractive observable for precise determinations of $\alpha_s(M_Z)$. Already at HERA three-jet cross section were proven to have a high sensitivity to $\alpha_s(M_Z)$, but the limited luminosity and centre-of-mass energy were limiting factors, since the size of the cross sections reduces with increasing n. At the LHeC, due to the higher $\sqrt{s}$ and integrated luminosity, three-, four- or five-jet cross sections represent attractive observables for a precise determinations of $\alpha_s(M_Z)$. Fixed order pQCD predictions may become limiting factors, since they are more complicated for large n and, therefore, theoretical uncertainties may dominate.

Di-jet observables are expected to yield a fairly similar experimental uncertainty than inclusive jet cross

sections as studied in the previous paragraphs, since both have $n = 1$ at LO. However, their theoretical uncertainties may be smaller, since di-jet observables are less sensitive to additional higher-order radiation, in particular at lower scales where $\alpha_s(\mu_R)$ is larger.

Event shape observables exploit additional radiation in DIS events and, consequently, the experimental uncertainties of $\alpha_s(M_Z)$ from these observables are expected to become very similar to that in Eq. (4.2), since both the event sample and the process is similar to the inclusive jet cross sections [2]. However, different reconstruction techniques of the observables may yield reduced experimental uncertainties, and the calculation of event shape observables allow for the resummation of large logarithms. Therefore, theoretical uncertainties are reduced in comparison to fixed order predictions.

Jet production cross sections in photoproduction represents a unique opportunity for another precision determination of $\alpha_s(M_Z)$. Similar measurements have been performed at HERA [**?**]. The sizeable photoproduction cross section provides a huge event sample, which is statistically independent from NC DIS events, and already the leading-order predictions are sensitive to $\alpha_s(M_Z)$. Also its running can be largely measured since the scale of the process is well estimated by the transverse momentum of the jets $\mu_R \sim P_T^{\text{jet}}$. Limiting theoretical aspects are due to the presence of a quasi-real photon and the poorly known photon PDF.

A different class of observables represent heavy flavour (HF) cross sections, which are discussed in Sec. 4.1.6. Due to flavour conservation, these are commonly proportional to $\mathcal{O}(\alpha_s^1)$ at leading-order. However, when considering inclusive HF cross sections above the heavy quark mass threshold heavy quarks can be factorised into the PDFs, and the leading structure functions $F_2^{c,b}$ are sensitive to α_s only beyond the LO approximation. The presence of the heavy quark mass as an additional scale stabilises perturbative calculations, and reduced theoretical uncertainties are expected.

At the LHeC the structure of jets and the formation of hadrons can be studied with unprecedented precision. This is so because of the presence of a single hadron in the initial state. Theefore, limiting effects like the underlying event or pile-up are absent or greatly diminished. Precise measurements of jet shape observables, or the study of jet substructure observables, are highly sensitive to the value of $\alpha_s(M_Z)$, because parton shower and hadronisation take place at lower scales where the strong coupling becomes large and an increased sensitivity to $\alpha_s(M_Z)$ is attained.

Finally, also the determination of $\alpha_s(M_Z)$ from inclusive NC DIS cross sections can be improved. For NC DIS the dominant sensitivity to α_s arises from the F_L structure function and from scaling violations of F_2 at lower values of Q^2 but at very high values of x. Dedicated measurements of these kinematic regions will further improve the experimental uncertainties from the estimated values in Eq. (4.1).

4.2.2 High Precision Tests of QCD at the LHeC and the Elimination of Renormalisation Scheme Dependence

TODO. SJB. integrate or shorten, by DB. QCD calculations are typically based on "conventional" scale setting; i.e., one simply guesses the value of the renormalization scale μ_r as a characteristic energy or momentum transfer; the theory uncertainties for this guess are the estimated by varying the renormalization scale over an arbitrary range; e.g., $\mu_r \in [\sqrt{s}/2, 2\sqrt{s}]$. Conventional scale setting introduces an inherent scheme-and-scale dependence for pQCD predictions, and it violates a fundamental principle of Renormalization Group Invariance (RGI): theoretical predictions cannot depend on an arbitrary convention such as the renormalization scheme. One often argues that the inclusion of higher-order terms will suppress the scale uncertainty; however, estimating unknown higher-order terms by simply varying the renormalization scale within an arbitrary range is unreliable since it is only sensitive to the β terms. In fact, the resulting pQCD series diverges strongly as $\alpha_s^n \beta_0^n n!$, the "renormalon" divergence [32]. Moreover, the conventional

[2] It shall be noted, that event shape observables in NC DIS can be defined in the laboratory rest frame or the Breit frame.

procedure of guessing the renormalization scale is inconsistent with the Gell-Mann-Low procedure [33] which determines the scale unambiguously in QED. pQCD predictions must analytically match Abelian theory in the $N_C \to 0$ limit [34].

The Principle of Maximum Conformality (PMC) [35, 36, 37, 38, 39] provides a systematic way to eliminate the renormalization scheme-and-scale ambiguities. The PMC scales are fixed by absorbing the β terms –e.g. the vacuum polarization contributions in QED – which govern the behavior of the running coupling via the Renormalization Group Equation (RGE). The resulting PMC predictions do not depend on the choice of the renormalization scheme so that PMC scale-setting satisfies the principles of renormalization group invariance [40, 41, 42]. Since the β terms do not appear in the pQCD series after the PMC, there is no renormalon divergence. The PMC method extends the Brodsky-Lepage-Mackenzie (BLM) scale-setting method [43] to all orders, and it reduces in the Abelian limit to the Gell-Mann-Low method [33].

In a recent paper [44], we have applied the PMC to make comprehensive analyses for two classic event shapes in $e^+e^- \to Z^0 \to$ hadrons: the thrust (T) [45, 46] and the C-parameter (C) [47, 48]. As shown by Gehrmann, N. Häfliger, and Monni [49], the resulting PMC renormalization scale depends dynamically on the virtuality of the underlying quark and gluon subprocess and thus the specific kinematics of each event. One can then determine $\alpha_s(Q^2)$ over a large range of Q^2 by comparing the PMC scale-set predictions with the experimental data. The PMC provides a remarkable way to verify the running of $\alpha_s(Q^2)$ from the event shape differential measurement at a single energy of $\sqrt{s}$. These new results [44] for $\alpha_s(M_Z^2)$ are consistent with the world average and are more precise than the values conventionally obtained from the analysis of event shapes currently used in the world average.

The thrust (T) variable [45, 46] is one of the most frequently studied event shape observables, which is defined as

$$T = \max_{\vec{n}} \left(\frac{\sum_i |\vec{p}_i \cdot \vec{n}|}{\sum_i |\vec{p}_i|} \right), \tag{4.3}$$

where the sum runs over all particles in the final state, and the $\vec{p}_i$ denotes the three-momentum of particle i. The unit vector $\vec{n}$ is varied to define the thrust direction $\vec{n}_T$ by maximizing the sum on the right-hand side. In general, the range of values is $0 \leq (1-T) \leq 1/2$, where $(1-T) \to 0$ corresponds to the two back-to-back jets and $(1-T) \to 1/2$ is the spherically symmetric events. For the three-particle events, we have $0 \leq (1-T) \leq 1/3$ [50].

Since a high degree of consistency between the PMC predictions and the measurements are obtained, we can extract $\alpha_s(Q^2)$ with high precision; the results in the $\overline{\rm MS}$ scheme are presented in Fig.(4.28). The values obtained for $\alpha_s(Q^2)$ are mutually compatible and are in excellent agreement with the world average in the range 1 GeV $< Q <$ 15 GeV. The results are not plagued by the renormalization scale μ_r uncertainty. In addition, unlike the α_s extracted from the differential distributions, the α_s extracted from the mean values are not afflicted with large logarithmic contributions nor non-perturbative effects.

4.2.3 Grand Unification [Claire Gwenlan]

4.2.4 New QCD Dynamics at Small x [Anna Stasto]

The LHeC machine will offer access to a completely novel kinematic regime of DIS characterized by very small values of x. From the kinematical plane in (x, Q^2) depicted in Fig. 4.3, it is clear that the LHeC will be able to probe Bjorken-x values as low as 10^{-6} for perturbative values of Q^2. At low values of x various phenomena may occur which go beyond the standard collinear perturbative description based on DGLAP evolution. Since the seminal works of Balitsky, Fadin, Kuraev and Lipatov [61, 62, 63] it has been known that, at large values of centre-of-mass energy $\sqrt{s}$ or, to be more precise, in the Regge limit, there are

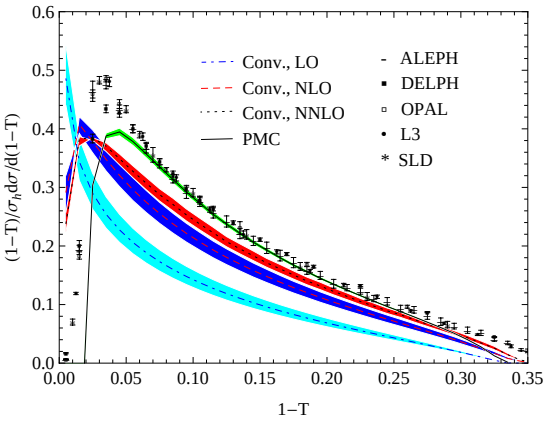

Figure 4.26: The thrust differential distributions using the conventional (Conv.) and PMC scale settings. The dotdashed, dashed and dotted lines are the conventional results at LO, NLO and NNLO [51, 52], respectively. The solid line is the PMC result. The bands for the theoretical predictions are obtained by varying $\mu_r \in [M_Z/2, 2M_Z]$. The PMC prediction eliminates the scale μ_r uncertainty and its error band is obtained by using $\alpha_s(M_Z) = 0.1181 \pm 0.0011$ [31]. The experimental data are taken from the ALEPH [53], DELPH [54], OPAL [55], L3 [56] and SLD [57] experiments.

large logarithms of energy which need to be resummed. Thus, even at low values of the strong coupling α_s, logarithms of energy $\ln s$ may be sufficiently large, such that terms like $(\alpha_s \ln s)^n$ will start to dominate the cross section.

The calculation of scattering amplitudes in the high-energy limit and the resummation of $(\alpha_s \ln s)^n$ series in the leading logarithmic order was performed in [61, 62, 63] and it resulted in the famous BFKL evolution equation. This small x evolution equation, written for the so-called gluon Green's function or the unintegrated gluon density, is a differential equation in $\ln 1/x$. An important property of this equation is that it keeps the transverse momenta unordered along the gluon cascade. This has to be contrasted with DGLAP evolution which is differential in the hard scale Q^2 and relies on the strong ordering in the transverse momenta of the exchanged partons in the parton cascade. The solution to the BFKL equation is a gluon density which grows sharply with decreasing x, as a power i.e. $\sim x^{-\omega_{IP}}$, where ω_{IP} is the hard Pomeron intercept, and in the leading logarithmic approximation equals $\frac{N_c \alpha_s}{\pi} 4 \ln 2$, which gives a value of about 0.5 for typical values of the strong coupling. The leading logarithmic (LLx) result yielded a growth of the gluon density which was too steep for the experimental data at HERA. The next-to-leading logarithmic (NLLx) calculation performed in the late 90s [64, 65] resulted in large negative corrections to the LLx value of the hard Pomeron intercept and yielded some instabilities in the cross section [66, 67, 68, 69, 70].

The appearance of the large negative corrections at NLLx motivated the search for the appropriate resummation which would stabilize the result. It was understood very early that the large corrections which appear in BFKL at NLLx are mostly due to the kinematics [71, 72, 73] as well as DGLAP terms and the running of the strong coupling. First attempts at combining the BFKL and DGLAP dynamics together with the proper kinematics [74] yielded encouraging results, and allowed a description of HERA data on structure functions with good accuracy. The complete resummation program was developed in a series of works [75, 76, 77, 78, 79, 80, 81, 82, 83, 84, 85, 86, 87, 88]. In these works the resummation for the gluon Green's function and the splitting functions was developed.

The low-x resummation was recently applied to the description of structure function data at HERA using the methodology of NNPDF [89]. It was demonstrated that the resummed fits provide a better description of the structure function data than the pure DGLAP based fits at fixed NNL order. In particular, it was shown that the χ^2 of the fits does not vary appreciably when more small x data are included in the case of the fits which include the effects of the small x resummation. On the other hand, the fits based on NNLO

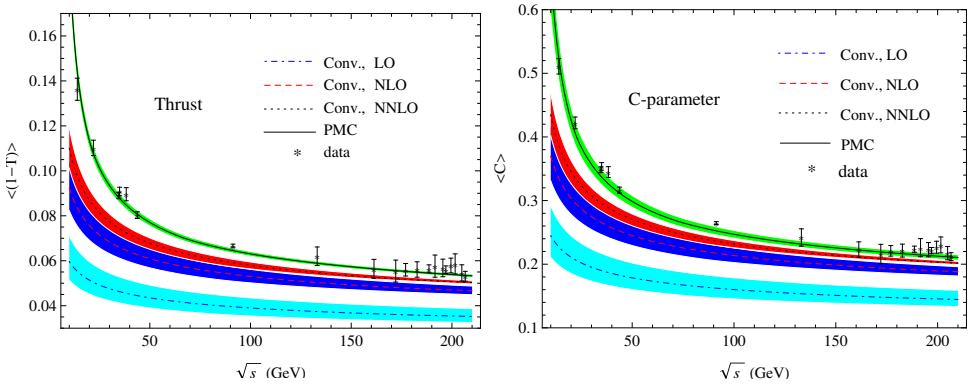

Figure 4.27: The mean values for the thrust (up) and C-parameter (down) versus the center-of-mass energy $\sqrt{s}$ using conventional (Conv.) and PMC scale settings. The dot-dashed, dashed and dotted lines are the conventional results at LO, NLO and NNLO [58, 59], respectively, and the corresponding error bands are obtained by varying $\mu_r \in [M_Z/2, 2M_Z]$. The solid line is the PMC result, and its error band is obtained by the squared averages of the errors for $\alpha_s(M_Z) = 0.1181 \pm 0.0011$ [31] and the estimated unknown higher-order contributions $\pm 0.2\ C_n$. The data are from the JADE and OPAL experiments. From ref. [44].

DGLAP evolution exhibit a worsening of their quality in the region of low x and low to moderate values of Q^2. This indicates that there is some tension in the fixed order fits based on DGLAP, and that resummation alleviates it. In addition, it was shown that the description of the longitudinal structure function F_L from HERA data is improved in the fits with the small x resummation. This analysis suggests that the small x resummation effects are indeed visible in the HERA kinematic region. Such effects will be strongly magnified at the LHeC, which probes values of x more than one order of magnitude lower than HERA. The NNPDF group also performed simulation of the structure functions F_2 and F_L with and without resummation in the LHeC range as well as for the next generation electron-hadron collider FCC-eh [89]. The predictions for the structure functions as a function of x for fixed values of Q^2 are shown in Figs. 4.29.

The simulations were done using APFEL [90] together with the HELL package [91] which implements the small x resummation. From Fig. 4.29 it is clear that LHeC will have much higher sensitivity to discriminate between fixed order and resummed scenarios than the HERA collider, with even better discrimination at the FCC-eh. The differences between the central values for the two predictions are of the order of 15% for the case of F_2 and this is much larger than the projected error bar on the reduced cross section or structure function F_2 which could be measured at LHeC. For comparison, the simulated pseudodata for F_2 are shown together with the expected experimental uncertainties. The total uncertainties of the simulated pseudo-data are at the few percent level at most, and are therefore much smaller than the uncertainties coming from the PDFs in most of the kinematic range.

It is evident that fits to the LHeC data will have power to discriminate between the different frameworks. In the right plot in Fig. 4.29, the predictions for the longitudinal structure function are shown. We see that in the case of the F_L structure function, the differences between the fixed order and resummed predictions are even larger, consistently over the entire range of x. This indicates the importance of the measurement of the longitudinal structure function F_L which can provide further vital constraints on the QCD dynamics in the low x region due to its sensitivity to the gluon density in the proton.

To further illustrate the power of a high energy DIS collider like the LHeC in exploring the dynamics at low x, fits which include the simulated data were performed. The NNLO+NLLx resummed calculation was used to obtain the simulated pseudodata, both for the LHeC, in a scenario of a 60 GeV electron beam on a 7 TeV proton beam as well as in the case of the FCC-eh scenario with a 50 TeV proton beam. All the experimental uncertainties for the pseudodata have been added in quadrature. Next, fits were performed to the DIS HERA as well as LHeC and FCC-eh pseudodata using the theory with and without the resummation at

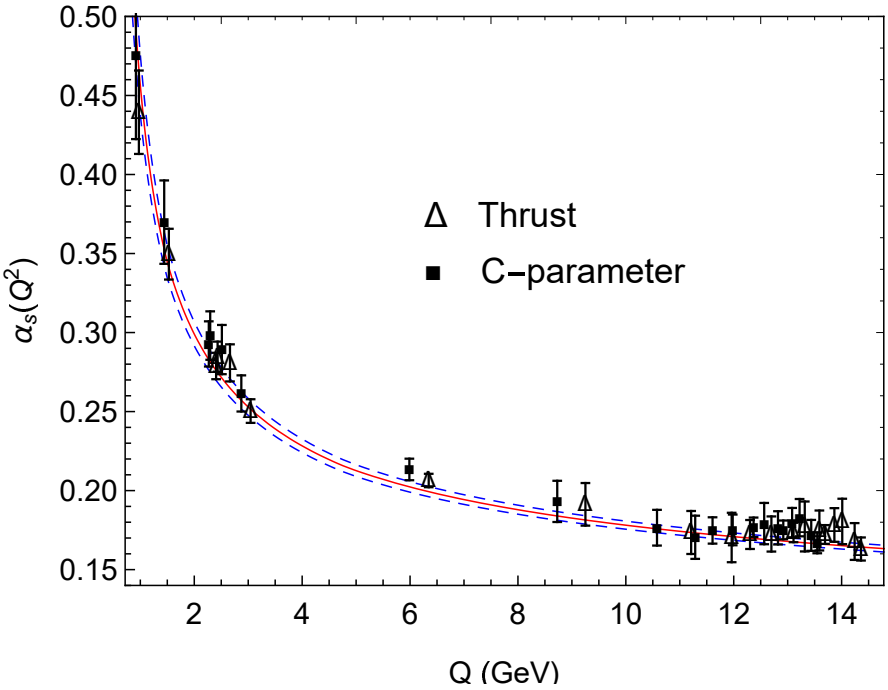

Figure 4.28: The running coupling $\alpha_s(Q^2)$ extracted from the thrust and C-parameter mean values by comparing PMC predictions with the JADE and OPAL data [55, 60] in the $\overline{\rm MS}$ scheme. The error bars are the squared averages of the experimental and theoretical errors. The three lines are the world average evaluated from $\alpha_s(M_Z^2) = 0.1181 \pm 0.0011$ [31]. From ref. [44].

low x. Hadronic data like jet, DY, top,... were not included for this analysis but, as demonstrated in [89], these data do not have much of the constraining power at low x, and therefore the results of the analysis at low x are independent of the additional non-DIS data sets. The quality of the fits characterized by the χ^2 was markedly worse when the NNLO DGLAP framework was used to fit the HERA data and the pseudodata from LHeC and/or FCC-eh than was the case with resummation. To be precise, the χ^2 per degree of freedom for the HERA data set was equal to 1.22 for the NNLO fit, and 1.07 for the resummed fit. For the case of the LHeC/FCC-eh the χ^2 per degree of freedom was equal to 1.71/2.72 and 1.22/1.34 for NNLO and NNLO+resummation fits, respectively. These results demonstrate the huge discriminatory power of the new DIS machines between the DGLAP and resummed frameworks, and the large sensitivity to the low x region while simultaneously probing low to moderate Q^2 values.

In Fig. 4.30 the comparison of the gluon and quark distributions from the NNLO + NLLx fits is shown at $Q = 100$ GeV as a function of x, with and without including the simulated pseudodata from LHeC as well as FCC-eh. The large differences at large x are due to the fact that only DIS data were included in the fits, and not the hadronic data. The central values of the extracted PDFs using only HERA or using HERA and the simulated pseudodata coincide with each other, but a large reduction in uncertainty is visible when the new data are included. The uncertainties from the fits based on the HERA data only increase sharply already at $x \sim 10^{-4}$. On the other hand, including the pseudodata from LHeC and/or FCC-eh can extend this regime by order(s) of magnitude down in x. Furthermore, fits without resummation, based only on NNLO DGLAP, were performed to the HERA data and the pseudodata. We see that in this case the extracted gluon and singlet quark densities differ significantly from the fits using the NNLO+NLLx. Already at $x = 10^{-4}$ the central values of the gluon differ by 10% and at $x = 10^{-5}$, which is the LHeC regime, the central values for the gluon differ by 15%. This difference is much larger than the precision with which the gluon can be extracted from the DIS data, which is of the order of $\sim 1\%$.

The presented analysis demonstrates that the fixed order prediction based on the DGLAP evolution would

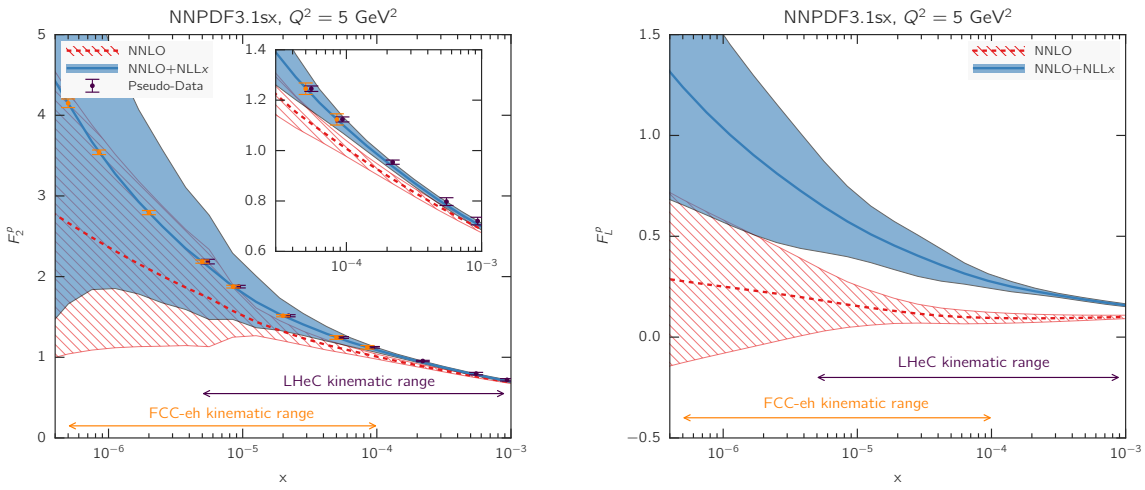

Figure 4.29: Predictions for the F_2 and F_L structure functions using the NNPDF3.1sx NNLO and NNLO+NLLx fits at $Q^2 = 5\,\text{GeV}^2$ for the kinematics of the LHeC and FCC-eh. In the case of F_2, we also show the expected total experimental uncertainties based on the simulated pseudo-data, assuming the NNLO+NLLx values as the central prediction. A small offset has been applied to the LHeC pseudo-data as some of the values of x overlap with the FCC-eh pseudo-data points. The inset in the left plot shows a magnified view in the kinematic region $x > 3 \times 10^{-5}$, corresponding to the reach of HERA data. Figure taken from Ref. [89].

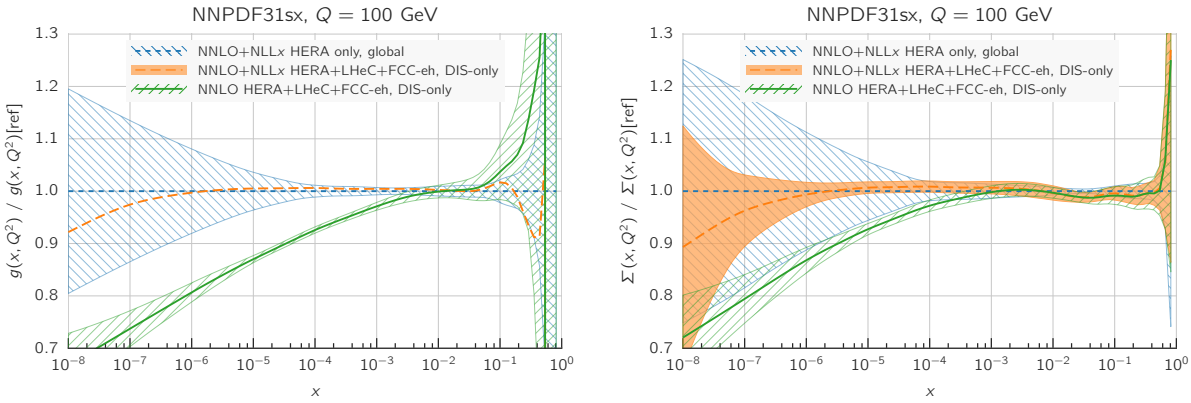

Figure 4.30: Comparison between the gluon (left plot) and the quark singlet (right plot) PDFs in the NNPDF3.1sx NNLO+NNLx fits without (blue hatched band) and with the LHeC+FCC-eh pseudo-data (orange band) on inclusive structure functions. For completeness, we also show the results of the corresponding NNPDF3.1sx NNLO fit with LHeC+FCC-eh pseudo-data (green hatched band). Figure from Ref. [89].

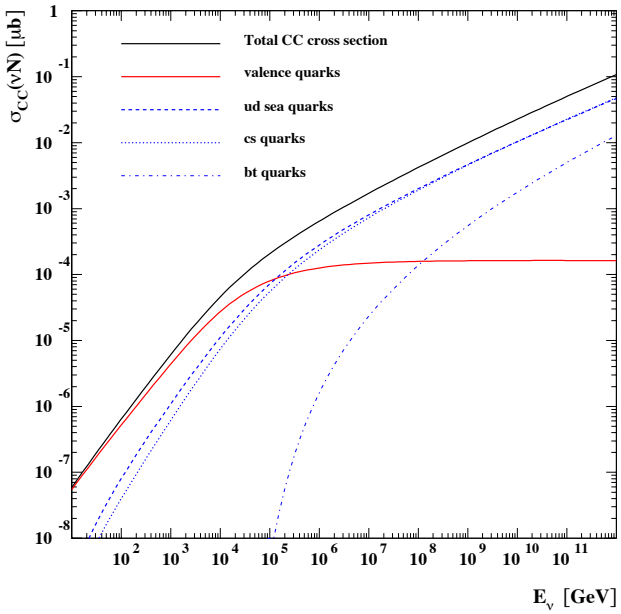

Figure 4.31: Charged current cross section for the neutrino - nucleon interaction on a isoscalar target as a function of neutrino energy. The total CC cross section is broken down into several contributions due to valence, up-down,strange-charm and bottom-top quarks. The calculation was based on Ref. [94].

likely fail to describe accurately the structure function data in the new DIS machines and that in that regime new dynamics including resummation are mandatory for quantitative predictions. Therefore, the LHeC machine has an unprecedented potential to pin down the details of the QCD dynamics at low values of Bjorken x.

Synergies with ultrahigh energy neutrino and astroparticle physics

The small-x region probed by the LHeC is also very important in the context of ultra-high energy neutrino physics and astroparticle physics. Highly energetic neutrinos provide a unique window into the Universe, due to their weak interaction with matter, for a review see for example [92]. They can travel long distances from distant sources, undeflected by the magnetic fields inside and in between galaxies, and thus provide complementary information to cosmic rays, gamma rays and gravitational wave signals. The IceCube observatory on Antarctica [93] is sensitive to neutrinos with energies from 100 GeV up (above 10 GeV with the use of their Deep Core detector). Knowledge about low-x physics becomes indispensable in two contexts: neutrino interactions and neutrino production. At energies beyond the TeV scale the dominant part of the cross section is due to the neutrino DIS CC and NC interaction with the hadronic targets [92].

In Fig. 4.31 we show the charged current neutrino cross section as a function of the neutrino energy for an isoscalar target (in the laboratory frame where the target is at rest), using a calculation [94] based on the resummed model in [74]. We see that at energies below ~ 50 TeV the cross section grows roughly linearly with energy, and in this region it is dominated by contributions from the large-x valence region. Beyond

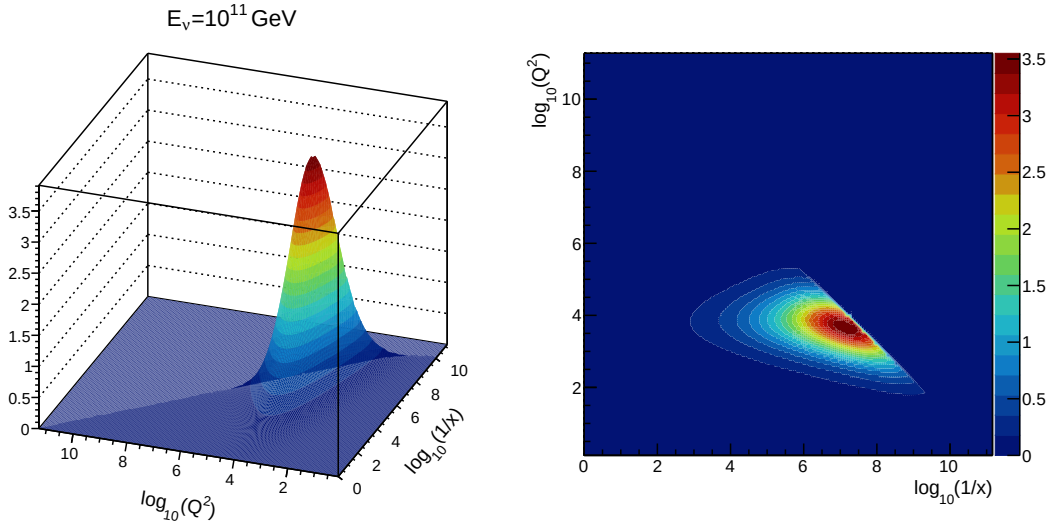

Figure 4.32: Differential charged current neutrino cross section $10^5 \cdot xQ^2 d\sigma^{CC}/dxdQ^2$ [nb] as a function of Q^2 and x for fixed neutrino energy $E_\nu = 10^{11}$ GeV. Left: surface plot; right: contour plot.

that energy the neutrino cross section grows slower, roughly as a power $\sim E_\nu^\lambda$ with $\lambda \simeq 0.3$. This high energy behaviour is totally controlled by the small-x behavior of the parton distributions. The dominance of the sea contributions to the cross section is clearly seen in Fig. 4.31. To illustrate more precisely the contributing values of x and Q^2, in Fig. 4.32 we show the differential cross section for the CC interaction $xQ^2 d\sigma^{CC}/dxdQ^2$ for a neutrino energy $E_\nu = 10^{11}$ GeV (in the frame where the hadronic target is at rest). We see a clear peak of the cross section at roughly a value of $Q^2 = M_W^2$ and an x value

$$x \simeq \frac{M_W^2}{2ME_\nu} \,,$$

which in this case is about 3×10^{-8}. We note that IceCube extracted the DIS cross section from neutrino observations [95] in the region of neutrino energies $10 - 1000$ TeV. The extraction is consistent, within the large error bands, with the predictions based on the QCD, like those illustrated in Fig. 4.31. It is important to note that the IceCube extraction is limited to these energies by the statistics due to the steeply falling flux of neutrinos at high energy. We thus see that the neutrino interaction cross section at high energies is sensitive to a region which is currently completely unconstrained by existing precision DIS data.

Another instance where dynamics at low x are crucial for neutrino physics is in understanding the mechanisms of ultra-high energy neutrino production. The neutrinos are produced in interactions which involve hadrons, either in γp or in pp interactions. They emerge as decay products of pions, kaons and charmed mesons, and possibly beauty mesons if energy is high enough [96]. For example, in the atmosphere neutrinos are produced in the interactions of the highly energetic cosmic rays with nitrogen and oxygen nuclei. The lower energy part of the atmospheric neutrino spectrum, up to about 100 TeV or so, is dominated by the decay of pions and kaons. This is called the conventional atmospheric neutrino flux. Above that energy the neutrino flux is dominated by the decay of the shorter-lived charmed mesons, thus this part of the neutrino flux is called the prompt-neutrino flux. The reason why the prompt-neutrino flux dominates at high energies is precisely related to the life-time of the intermediate mesons (and also baryons like Λ_c). The longer lived pions and kaons have high probability of the interaction before they decay, thus degrading their energy and leading to a steeply falling neutrino flux. The cross section for the production of charmed mesons is smaller than that for pions and kaons, but the charmed mesons $D^\pm, D^0, D_s$ and baryon Λ_c live shorter than pions and kaons, and thus they will decay prior to the interaction. Thus, at energies about 100 TeV the prompt neutrino flux will dominate over the conventional atmospheric neutrino flux. Therefore, the knowledge of this part of the spectrum is essential as it provides a background for the sought-after astrophysical neutrinos

[97]. Charmed mesons in high energy hadron-hadron interactions are produced through gluon-gluon fusion into $c\bar{c}$ pairs, where one gluon carries rather large x and the other one carries very small x. Since the scales are very small, of the order of the charm masses, the values of the longitudinal momentum fractions involved are also very small and thus the knowledge of the parton distributions in this region is essential [98]. The predictions for the prompt neutrino fluxed become extremely sensitive to the behaviour of the gluon distribution at low x (and low Q^2), where novel QCD phenomena like resummation as well as gluon saturation are likely to occur [99].

Finally, the low-x dynamics will become even more important at the HL-LHC and FCC colliders. With increasing centre-of-mass energy, hadron colliders will probe values of x previously unconstrained by HERA data. It is evident that all the predictions in pp interactions at high energy will heavily rely on the PDF extrapolations to the small x region which carry large uncertainties. As discussed in detail in this section, resummation will play an increasingly important role in the low x region of PDFs. A precision DIS machine is thus an indispensable tool for constraining the QCD dynamics at low x with great precision as well as for providing complementary information and independent measurements to hadronic colliders.

4.2.5 Pinning Down the Low x Gluon with F_2 and F_L Measurements [Max Klein]

4.2.6 The 3D Structure of the Proton [Anna Stasto]

As evident from the discussion in the previous sections, the LHeC machine will be able to measure the collinear parton distribution functions with unprecedented accuracy in its extended range of x and Q^2. Thus, it will allow to gain q new insight into the details of the one-dimensional structure of the proton and nuclei, including novel phenomena at low x. In addition to collinear dynamics, the LHeC opens a new window into the proton and nuclear structure by allowing to precisely investigate the partonic structure in more than just one dimension of the longitudinal momentum. Precision DIS thus gives access to multidimensional aspects of the hadron structure. This can be achieved by accurately measuring processes with more exclusive final states like production of jets, semi-inclusive production of hadrons and exclusive processes, in particular the elastic diffractive production of vector mesons and deeply virtual Compton (DVCS) scattering. These processes have the potential to provide the information not only on the longitudinal distribution of partons in the proton or nucleus but also on the dependence of the parton distribution on transverse momenta and momentum transfer. Therefore, future, high precision DIS machines like the LHeC or the Electron Ion Collider (EIC) in the US [100], open a unique window into the details of the 3D structure of hadrons.

The most general quantity that can be defined in QCD, that would contain very detailed information about the partonic content of the hadron, is the Wigner distribution [101]. This function $W(x, \mathbf{k}, \mathbf{b})$ is a 1+4 dimensional function. One can think of that quantity as the mother or master parton distribution, from which lower-dimensional distributions can be obtained. In the definition of the Wigner function, $\mathbf{k}$ is the transverse momentum of the parton and $\mathbf{b}$ is the 2-dimensional impact parameter, which can be defined as a Fourier conjugate to the momentum transfer of the process. The other, lower dimensional parton distributions can be obtained by integrating out different variables. Thus, transverse momentum dependent parton (TMD) distributions (or unintegrated parton distribution functions) $f_{\rm TMD}(x, \mathbf{k})$ can be obtained by integrating out the impact parameter $\mathbf{b}$ in the Wigner function, while the generalized parton densities (GPD), $f_{\rm GPD}(x, \mathbf{b})$, can be obtained from the Wigner function through the integration over the transverse momentum $\mathbf{k}$. In the regime of small x, or high energy, a suitable formalism is that of the dipole picture [102, 103, 104, 105, 106, 107], where the fundamental quantity which contains the details of the partonic distribution is the dipole amplitude $N(x, \mathbf{r}, \mathbf{b})$. This object contains the dependence on the impact parameter $\mathbf{b}$ as well as another transverse size $\mathbf{r}$, the dipole size, which can be related to the transverse momentum of the parton $\mathbf{k}$ through a Fourier transform. The important feature of the dipole amplitude is that it should obey the unitarity limit $N \leq 1$. The dipole amplitude N within this formalism can be roughly interpreted

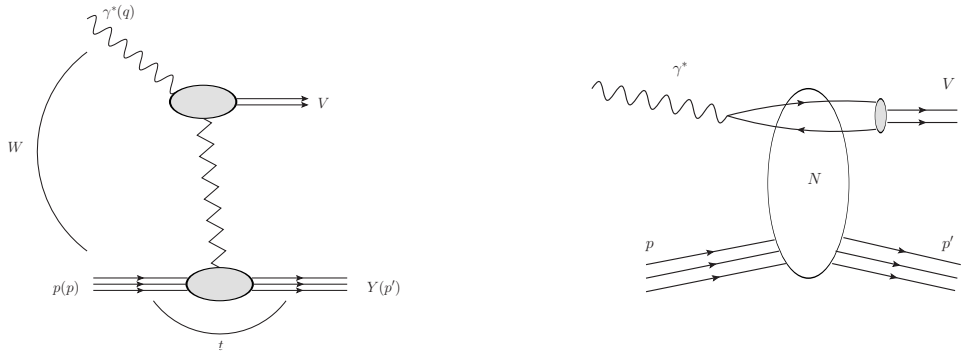

Figure 4.33: Left: diagram for the elastic diffractive production of the vector meson. Right: schematic illustration of the same process, elastic diffractive vector meson production, within the framework of the dipole picture. The initial virtual photon, fluctuates into a quark-antiquark pair which then scatters off the hadronic target and forms the vector meson. The details of the hadronic interaction of the dipole with the target are encoded in the dipole amplitude N.

as a Wigner function in the high energy limit, as it contains the information about the spatial distribution of the partons in addition to the dependence on the longitudinal momentum fraction x.

Detailed simulations of the elastic diffractive J/ψ vector meson production were performed for the LHeC kinematics and beyond [1], using the formalism of the dipole picture. This particular process is shown in Fig. 4.33, left plot. The proton is scattered elastically with momentum transfer t, and the vector meson is produced, which is separated from the final state proton by a rapidity gap. Of particular importance is the measurement of the t slope of this process, since it can be related directly to the impact parameter distribution of the partonic density in the target. The first type of analysis like this, in the context of the elastic scattering, was performed by Amaldi and Schubert [108], where it was demonstrated that the Fourier transform of the elastic cross section yields access to the impact parameter profile of the scattering amplitude. This method can be used in the context of the vector meson scattering in DIS, where the transverse distribution of partons, in the perturbative regime, can be extracted through the appropriate Fourier transform [109]. The additional advantage of studying diffractive vector meson production is the fact that the partonic distributions can be studied as a function of the hard scale in this process given by the mass of the vector meson M_V^2 in the photoproduction case or the Q^2 (or more precisely a combination of Q^2 and M_V^2) in the case of the diffractive DIS production of vector mesons, as well as the energy W of the photon-proton system available in the process.

The differential cross section for the elastic vector meson production can be expressed in the following form:

$$\frac{d\sigma^{\gamma^* p \to J/\psi p}}{dt} = \frac{1}{16\pi} |\mathcal{A}(x, Q, \Delta)|^2 \,, \tag{4.4}$$

where the amplitude for the process of elastic diffractive vector meson production in the high energy limit, in the dipole picture, is given by

$$\mathcal{A}(x, Q, \Delta) \;=\; \sum_{h\bar{h}} \int d^2\mathbf{r} \int dz \Psi^*_{h\bar{h}}(z, \mathbf{r}, Q)\, \mathcal{N}(x, \mathbf{r}, \Delta)\, \Psi^V_{h\bar{h}}(z, \mathbf{r}) \,. \tag{4.5}$$

In the above formula, $\Psi^*_{h\bar{h}}(z, \mathbf{r}, Q)$ is the photon wave function which describes the splitting of the virtual photon γ^* into a $q\bar{q}$ pair. This wave funtion can be calculated in perturbative QCD. The function $\Psi^V_{h\bar{h}}(z, \mathbf{r})$ is the wave function of the vector meson. Finally, $\mathcal{N}(x, \mathbf{r}, \Delta)$ is the dipole amplitude which contains all the information about the interaction of the quark-antiquark dipole with the target. The formula (4.5) can be interpreted as the process of fluctuation of the virtual photon into a $q\bar{q}$ pair, which subsequently interacts with the target through the dipole amplitude $\mathcal{N}$ and then forms the vector meson, given by the amplitude Ψ^V, see Fig.4.33, right plot. The two integrals in the definition (4.5) are performed over the dipole size which is denoted by $\mathbf{r}$, and z which is the longitudinal momentum fraction of the photon carried by the quark. The scattering amplitude depends on the value of the momentum transfer Δ, which is related to the Mandelstam variable $t = -\Delta^2$. The sum is performed over the helicity states of quark and antiquark.

The dipole amplitude $\mathcal{N}(x, \mathbf{r}, \Delta)$ can be related to the dipole amplitude in the coordinate space through the appropriate Fourier transform

$$N(x, \mathbf{r}, \mathbf{b}) = \int d^2\Delta \, e^{i\Delta\cdot\mathbf{b}} \mathcal{N}(x, \mathbf{r}, \Delta) \, . \tag{4.6}$$

We stress that $\mathbf{r}$ and $\mathbf{b}$ are two different transverse sizes here. The dipole size $\mathbf{r}$ is conjugated to the transverse momentum of the partons $\mathbf{k}$, whereas the impact parameter is roughly the distance between the center of the scattering target to the center-of-mass quark-antiquark dipole and is related to the Fourier conjugate variable, the momentum transfer Δ.

The dipole amplitude $N(x, \mathbf{r}, \mathbf{b})$ contains rich information about the dynamics of the hadronic interaction. It is a 5-dimensional function and it depends on the longitudinal momentum fraction, and two two-dimensional coordinates. The dependence on the longitudinal momentum fraction is obviously related to the evolution with the centre-of-mass energy of the process, while the dependence on $\mathbf{b}$ provides information about the spatial distribution of the partons in the target. The dipole amplitude is related to the distribution of gluons in impact parameter space. The dipole amplitude has a nice property that its value should be bounded from above by the unitarity requirement $N \leq 1$. The complicated dependence on energy, dipole size and impact parameter of this amplitude can provide a unique insight into the dynamics of QCD, and on the approach to the dense partonic regime. Besides, from Eqs. (4.4),(4.5) and (4.6) it is evident that the information about the spatial distribution in impact parameter $\mathbf{b}$ is related through the Fourier transform to the dependence of the cross section on the momentum transfer $t = -\Delta^2$.

To see how the details of the distribution, and in particular the approach to the unitarity can be studied through the VM elastic production, calculations based on the dipole model were performed [110], and extended to energies which can be reached at the LHeC as well as the FCC-eh. The parametrisations used in the calculation were the so-called IP-Sat [111, 112] and b-CGC [113] models. In both cases the impact parameter dependence has to be modelled phenomenologically. In the IP-Sat model the dipole amplitude has the following form

$$N(x, \mathbf{r}, \mathbf{b}) \; = \; 1 - \exp[-\frac{\pi^2 r^2}{2N_c} \alpha_s(\mu^2) x g(x, \mu^2) T_G(b)] \, , \tag{4.7}$$

with the impact parameter profile for the gluon

$$T_G(b) \; = \; \frac{1}{2\pi B_G} \exp(-b^2/2B_G) \, .$$

The function $xg(x, \mu^2)$ is the collinear gluon density, evolved using LO DGLAP (without quarks), from initial scale μ_0^2 up to scale μ^2 set by the dipole size $\mu^2 = \frac{4}{r^2} + \mu_0^2$. $\alpha_s(\mu^2)$ is the strong coupling. The parametrisation of the gluon density at the initial scale μ_0^2 is given by

$$xg(x, \mu_0^2) = A_g x^{-\lambda_g} (1 - x)^{5.6} \, .$$

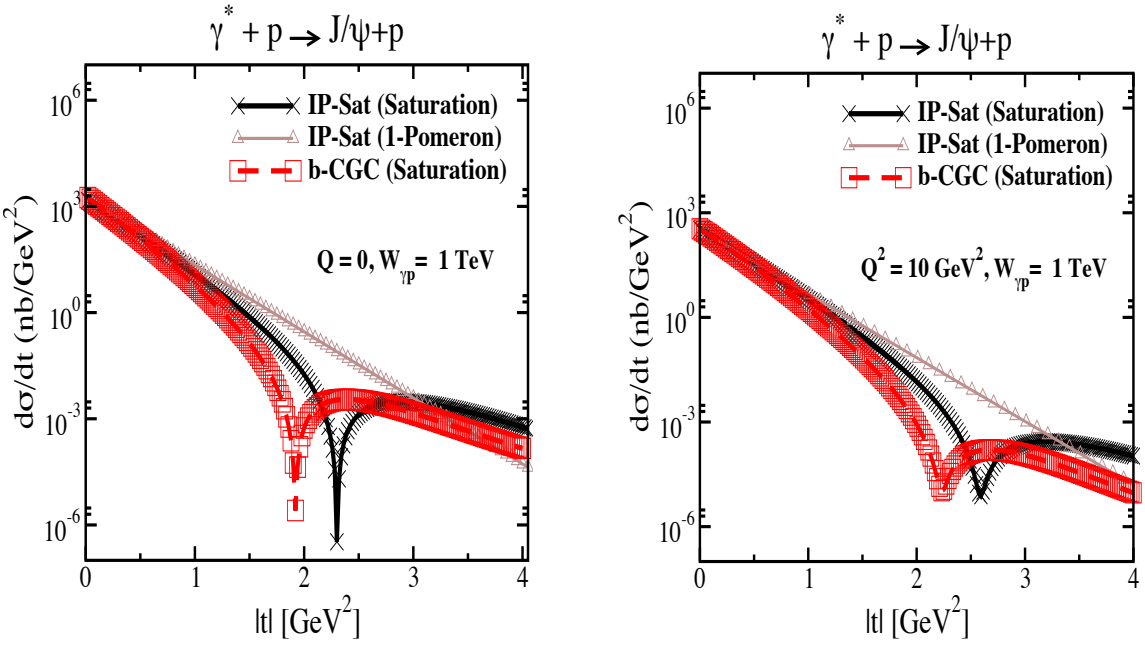

Figure 4.34: Differential cross section for the elastic J/ψ production as a function of $|t|$ within the IP-Sat (saturation), b-CGC and 1-Pomeron models at a fixed $W\gamma p = 1\,\text{TeV}$, which corresponds to the LHeC kinematics, and for two different values of photon virtuality $Q = 0$ and $Q^2 = 10\ \text{GeV}^2$. The thickness of points includes the uncertainties associated with the freedom to choose different values for the charm quark mass within the range $m_c = 1.2 - 1.4$ GeV.

The alternative parametrisation is given by the b-CGC model [113] which has the form

$$N(x,\mathbf{r},\mathbf{b}) \;=\; \begin{cases} N_0 \left(\frac{rQ_s}{2}\right)^{2\gamma_{\text{eff}}} & \text{for} \quad rQ_s \leq 2\,, \\ 1 - \exp(-\mathcal{A}\ln^2(\mathcal{B}rQ_s)) & \text{for} \quad rQ_s > 2\,. \end{cases} \tag{4.8}$$

Here the effective anomalous dimension γ_{eff} and the saturation scale Q_s of the proton explicitly depend on the impact parameter and are defined as

$$\begin{aligned} \gamma_{]\text{eff}} &= \gamma_s + \frac{1}{\kappa\lambda \ln 1/x} \ln\left(\frac{2}{rQ_s}\right)\,, \\ Q_s(x,b) &= \left(\frac{x_0}{x}\right)^{\lambda/2} \exp\left[-\frac{b^2}{4\gamma_s B_{\text{CGC}}}\right] \quad \text{GeV}\,, \end{aligned} \tag{4.9}$$

where $\kappa = \chi''(\gamma_s)/\chi'(\gamma_s)$, with $\chi(\gamma)$ being the leading-logarithmic BFKL kernel eigenvalue function [63]. The parameters $\mathcal{A}$ and $\mathcal{B}$ in Eq.(4.8) are determined uniquely from the matching of the dipole amplitude and its logarithmic derivatives at the limiting value of $rq_s = 2$. The b-CGC model is constructed by smoothly interpolating between two analytically known limiting cases [113], namely the solution of the BFKL equation in the vicinity of the saturation line for small dipole sizes $r < 2/Q_s$, and the solution of the BK equation deep inside the saturation region for large dipole sizes $r > 2/Q_s$.

Parameters μ_0, A_g, λ_g of the IP-Sat model and $N_0, \gamma_s, x_0\lambda$ of the b-CGC model were fitted to obtain the best description of the inclusive data for the structure function F_2 at HERA. The slope parameters B_g and B_{CGC}, which control the b -dependence in both models, were fitted to obtain the best description of elastic diffractive J/ψ production, in particular its t-dependence, at small values of t.

In Fig. 4.34 we show the differential cross section $d\sigma/dt$ as a function of $|t|$ and study its variation with energy and virtuality, and its model dependence. First, we show the differential cross section as a function

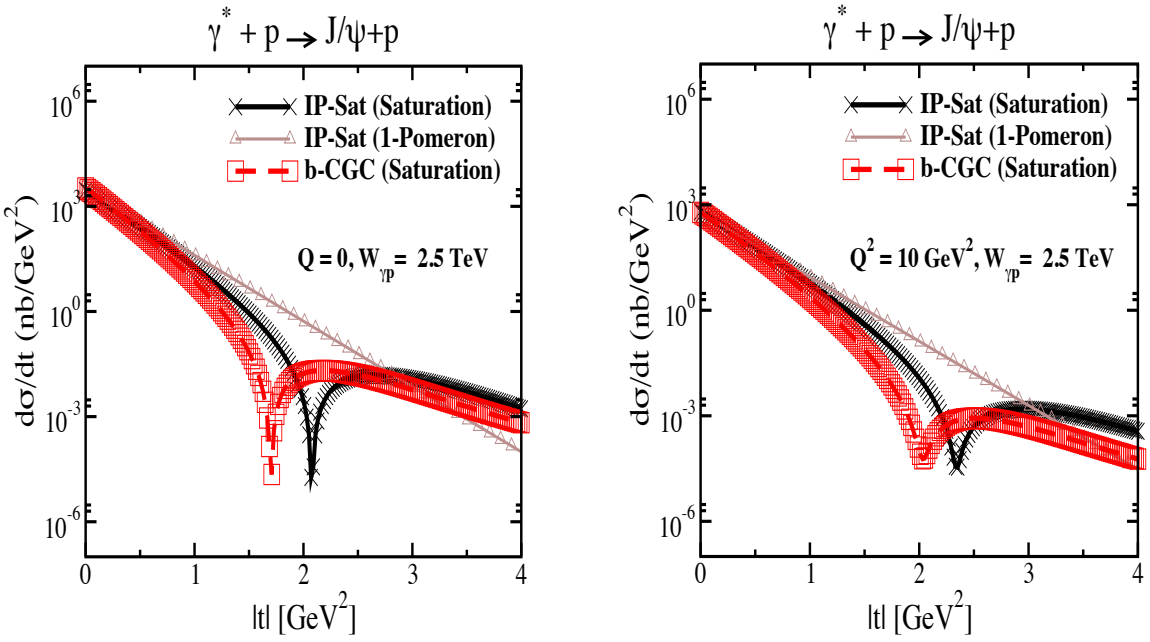

Figure 4.35: Differential cross section for elastic J/ψ production as a function of $|t|$ within the IP-Sat (saturation), b-CGC and 1-Pomeron models at a fixed $W\gamma p = 2.5\,\text{TeV}$, which corresponds to the region that can be explored by FCC-eh, and for two different values of photon virtuality $Q = 0$ (left plot) and $Q^2 = 10\,\text{GeV}^2$ (right plot). The thickness of points includes the uncertainties associated with the freedom to choose different values for the charm quark mass within the range $m_c = 1.2 - 1.4$ GeV .

of t for fixed energy $W = 1\,\text{TeV}$, in the case of the photoproduction of J/ψ (left plot) and for the case of DIS with $Q^2 = 10\,\text{GeV}^2$. The energy W corresponds to the LHeC kinematics. There are three different calculations in each plot, using IP-sat model, b-CGC model and the 1-Pomeron approximation. The last one is obtained by keeping just the first nontrivial term in the expansion of the eikonalized formula of the IP-Sat amplitude (4.7). First, let us observe that all three models coincide for very low values of t, where the dependence on t is exponential. This is because for low $|t|$, relatively large values of impact parameter are probed in Eq. (4.5) where the amplitude is small, and therefore the tail in impact parameter is Gaussian in all three cases. Since the Fourier transform of the Gaussian in b is an exponential in t, the result at low t follows. On the other hand, the three scenarios differ significantly for large values of $|t|$. In the case of the 1-Pomeron approximation the dependence is still exponential, without any dips, which is easily understood since the impact parameter profile is Gaussian in this case. For the two other scenarios, dips in $d\sigma dt$ as a function in t emerge. They signal the departure from the Gaussian profile in b for small values of b where the system is dense. A similar pattern can be observed when performing the Fourier transform of the Wood-Saxon distribution, which is the typical distribution used for the description of the matter density in nuclei. When Q^2 is increased the pattern of dips also changes. This is illustrated in Fig. 4.34. It is seen that dips move to higher values of $|t|$ for DIS than for photoproduction. This can be understood from the dipole formula Eq. 4.5 which contains the integral over the dipole size. Larger values of Q^2 select smaller values of dipole size r, where the amplitude is smaller and thus in the dilute regime, where the profile in b is again Gaussian. On the other hand, small scales select large dipole sizes for which the dipole amplitude is larger and thus the saturation effects more prominent, leading to the distortion of the impact parameter profile and therefore to the emergence of dips in the differential cross section $d\sigma/dt$ when studied as a function of t.

In the next figure Fig. 4.35 we show the same calculation but for higher energy $W = 2.5\,\text{TeV}$, which could be explored in the FCC-eh. In this case we see that the dips move to lower values of $|t|$. This can be easily understood, as with the increasing energy the dipole scattering amplitude increases, and thus the dilute-

dense boundary shifts to larger values of b, meaning that the $t$dependence deviation from the exponential fall off occurs for smaller values of $|t|$. Similar studies [110] show also the change of the position of the dips with the mass of the vector meson: for lighter vector mesons like ρ, ω, ϕ the dips occur at smaller t than for the heavier vector mesons J/ψ or Υ. We note that, of course, the details of the position of the dips depend crucially on the details of the models, which are currently not constrained by the existing HERA data. We also note the sizeable uncertainties due to the charm quark mass (the fits to inclusive HERA data from which parameters of the models have been extracted, are performed at each fixed value of the charm mass that is then used to compute exclusive J/ψ production).

We thus see that the precise measurement of the t-slope in the elastic diffractive production of vector mesons at the LHeC, and its variation with x and scales, provide a unique opportunity to explore the transition between the dilute and dense partonic regimes. As mentioned earlier, elastic diffractive production is one among several different measurements which can be performed to explore the 3D structure of the hadron. Another one is Deeply Virtual Compton Scattering which is a process sensitive to the spatial distribution of quarks inside the hadron. Previous preliminary analyses [1] indicate a huge potential of LHeC for the measurements of DVCS. Another example of a process that could be studied at the LHeC, is diffractive dijet production. It has been suggested [114] that this process is sensitive to the Wigner function, and that both the transverse momentum and spatial distribution of partons can be extracted by measuring this process. The transverse momentum of jets would be sensitive to the transverse momentum of the participating partons, whereas the momentum transfer of the elastically scattered proton would give a handle on the impact parameter distribution of the partons in the target [115, 116, 117], thus giving a possibility to extract information about the Wigner distribution.

So far we have referred to coherent diffraction, i.e., the proton remains intact after the collision. There also exists incoherent diffraction, where the proton gets excited into some state with the quantum numbers of the proton and separated from the rest of the event by a large rapidity gap. In order to apply the dipole formalism to the incoherent case, see Sec. 5.3.1 where the formulae applicable for both protons and nuclei are shown, one must consider a more involved structure of the proton (e.g. as composed by a fixed [118, 119, 120, 121] or a growing number with $1/x$ [122, 123, 124] of hot spots). As discussed in Sec. 5.3.1, coherent diffraction is sensitive to the gluon distribution in transverse space, while incoherent diffraction is particularly sensitive to fluctuations of the gluon distribution. A prediction of the model with a growing number of hot spots, both in models where this increasing number is implemented by hand [122, 123, 124] or in those where it is dynamically generated [121] from a fixed number at larger x, is that the ratio of incoherent to coherent diffraction will decrease with W, and that this decrease is sensitive to the details of the distribution of hot spots - thus, to the fluctuations of the gluon distribution in transverse space. In order to check these ideas, both the experimental capability to separate coherent form incoherent diffraction, a large lever arm in W as available at the LHeC, are required.

4.2.7 Inclusive diffraction [Paul Newman]

An important discovery of HERA was the observation of a large ($\sim 10\%$) fraction of diffractive events in DIS [125, 126]. In these events the proton stays intact or dissociates into a state with the proton quantum numbers, despite undergoing a violent, highly energetic collision, and is separated from the rest of the produced particles by a large rapidity gap. In a series of ground-breaking papers, the HERA experiments determined the deep inelastic structure of the t-channel exchange in these events in the form of diffractive parton densities.

The precise measurement of diffraction in DIS is of great importance for our understanding of the strong interaction. First, the mechanism through which a composite strongly interacting object interacts perturbatively while keeping colour neutrality offers information about the confinement mechanism. Second, diffraction is known to be highly sensitive to the low-x partonic content of the proton and its evolution

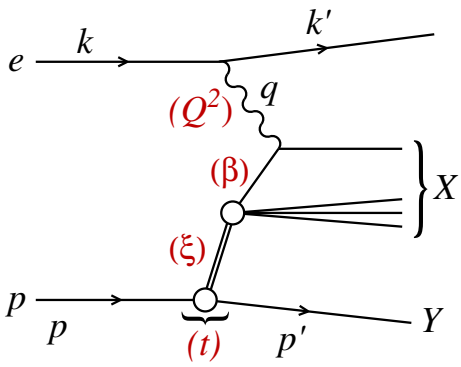

Figure 4.36: A diagram of a diffractive NC event in DIS together with the corresponding variables, in the one-photon exchange approximation. The large rapidity gap is between the system X and the scattered proton Y (or its low mass excitation).

with energy and it therefore has considerable promise to reveal deviations from standard linear evolution through higher twist effects or, eventually, non-linear dynamics. Third, it allows checks of basic theory predictions such as the relation between diffraction in ep scattering and nuclear shadowing [127]. Finally, the accurate extraction of diffractive parton distribution functions facilitates tests of the range of validity of the perturbative factorisation [128, 129, 130]. Therefore, it is of great importance the study of diffraction at the LHeC, that we present here, see [131] for details.

In Fig. 4.36 we show a diagram depicting a neutral current diffractive deep inelastic event. Charged currents could also be considered and they were measured at HERA [132] but with large statistical uncertainties and in a very restricted region of phase space. Although they could be measured at both the LHeC and the FCC-eh with larger statistics and more extended kinematics, in this first study we limit ourselves to neutral currents. The incoming electron or positron, with four momentum k, scatters off the proton, with incoming momentum p, and the interaction proceeds through the exchange of a virtual photon with four-momentum q. The kinematic variables for such an event include the standard deep inelastic variables

$$Q^2 = -q^2\,, \qquad x = \frac{-q^2}{2p\cdot q}\,, \qquad y = \frac{p\cdot q}{p\cdot k}\,,$$

where Q^2 describes the photon virtuality, x is the Bjorken variable and y the inelasticity of the process. In addition, the variables

$$s = (k+p)^2\,, \qquad W^2 = (q+p)^2\,,$$

are the electron-proton centre-of-mass energy squared and the photon-proton centre-of-mass energy squared, respectively. The distinguishing feature of the diffractive event $ep \to eXY$ is the presence of the large rapidity gap between the diffractive system, characterized by the invariant mass M_X and the final proton (or its low-mass excitation) Y with four momentum p'. In addition to the standard DIS variables listed above, diffractive events are also characterized by an additional set of variables defined as

$$t = (p-p')^2\,, \qquad \xi = \frac{Q^2+M_X^2-t}{Q^2+W^2}\,, \qquad \beta = \frac{Q^2}{Q^2+M_X^2-t}\,.$$

In the above t is the squared four-momentum transfer at the proton vertex, ξ (alternatively denoted by x_{IP}) can be interpreted as the momentum fraction of the 'diffractive exchange' with respect to the hadron, and β is the momentum fraction of the parton with respect to the diffractive exchange. The two momentum fractions combine to give Bjorken-x, $x = \beta\xi$.

The kinematic range in (β, Q^2, ξ) that we consider at the LHeC is restricted by the following cuts:

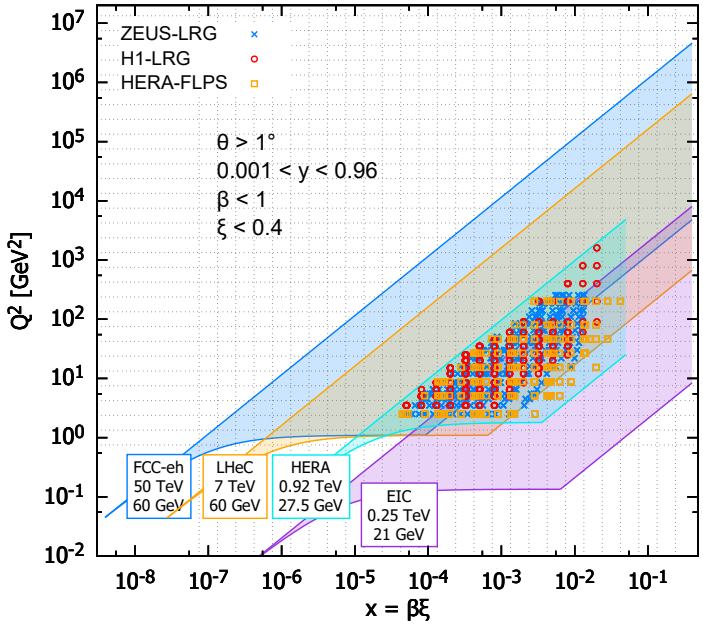

Figure 4.37: Kinematic phase space for inclusive diffraction in (x, Q^2) for the EIC (magenta region), the LHeC (orange region) and the FCC-eh (dark blue region) as compared with the HERA data (light blue region, ZEUS-LRG [133], H1-LRG [134], HERA-FLPS [135]). The acceptance limit for the electron in the detector design has been assumed to be 1°, and we take $\xi < 0.4$.

- $Q^2 \geq 1.8\,\mathrm{GeV}^2$: due to the fact that the initial distribution for the DGLAP evolution is parametrized at $\mu_0^2 = 1.8\,\mathrm{GeV}^2$. The renormalization and factorisation scales are taken to be equal to Q^2.
- $\xi < 0.4$: by physical and experimental limitations. This rather high ξ value is an experimental challenge and physically enters the phase-space region where the Pomeron contribution should become negligible. Within the two-component model, see Eq. (4.11) below, at high ξ the cross-section is dominated by the secondary Reggeon contribution, which is poorly fixed by the HERA data. We present this high ξ (> 0.1) region for illustrative purpose and for the sake of discussion of the fit results below.

In Fig. 4.37 the accessible kinematic range in (x, Q^2) is shown for three machines: HERA, LHeC and FCC-eh. For the LHeC design the range in x is increased by a factor ~ 20 over HERA and the maximum available Q^2 by a factor ~ 100. The FCC-eh machine would further increase this range with respect to LHeC by roughly one order of magnitude in both x and Q^2. We also show the EIC kinematic region for comparison.

In Fig. 4.38 the phase space in (β, Q^2) is shown for fixed ξ for the LHeC. The LHeC machine probes very small values of ξ, reaching 10^{-4} with a wide range of β. Of course, the range in β and ξ is correlated since $x = \beta\xi$. Therefore, for small values of ξ only large values of β are accessible while for large ξ the range in β extends to very small values. Above the solid, horizontal line labelled m_t^2 the top quark DPDF comes into play, and above the dashed line the $t\bar{t}$ production channel opens.

Diffractive cross sections in the neutral current case can be presented in the form of the reduced cross sections integrated over t [132]:

$$\frac{d^3\sigma^{\mathrm{D}}}{d\xi d\beta dQ^2} = \frac{2\pi\alpha_{\mathrm{em}}^2}{\beta Q^4} Y_+ \sigma_{\mathrm{red}}^{\mathrm{D}(3)},$$

where $Y_+ = 1 + (1-y)^2$ and the reduced cross sections can be expressed in terms of two diffractive structure

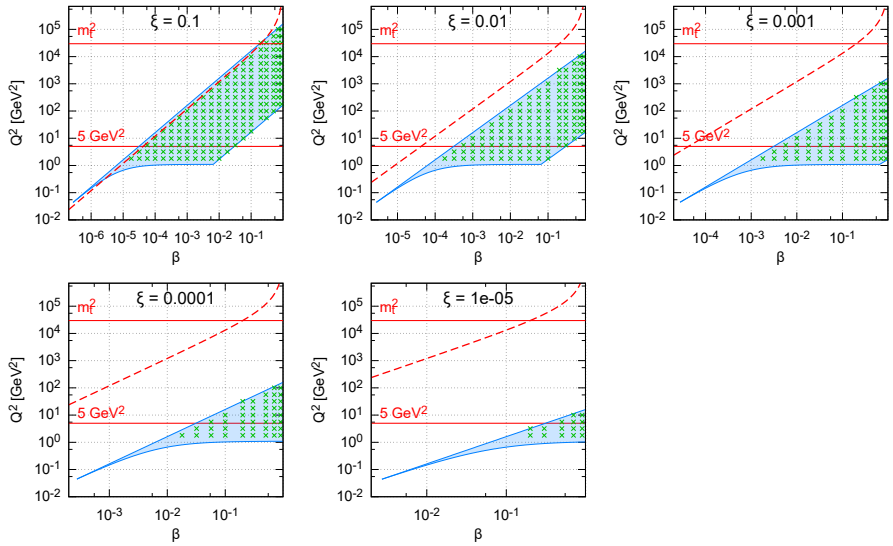

Figure 4.38: Kinematic phase space for inclusive diffraction in (β, Q^2) for fixed values of ξ for the LHeC design. The horizontal lines indicate correspondingly, $Q^2 = 5$ GeV^2, the lowest data value for the DGLAP fit performed in this study and m_t^2 the 6-flavour threshold. The dashed line marks the kinematic limit for $t\bar{t}$ production.

functions F_2^{D} and $F_{\mathrm{L}}^{\mathrm{D}}$. In the one-photon approximation, the relations are

$$\sigma_{red}^{\mathrm{D}(3)} = F_2^{\mathrm{D}(3)}(\beta, \xi, Q^2) - \frac{y^2}{Y_+} F_{\mathrm{L}}^{\mathrm{D}(3)}(\beta, \xi, Q^2) \; .$$

In this analysis we neglect Z^0 exchange, though it should be included in future studies.

Both $\sigma_{red}^{\mathrm{D}(3)}$ and $\sigma_{red}^{\mathrm{D}(4)}$ have been measured at the HERA collider [125, 126, 136, 137, 132, 133, 138, 139, 134] and used to obtain QCD-inspired parametrisations.

The standard perturbative QCD approach to diffractive cross sections is based on collinear factorisation [128, 129, 130]. It was demonstrated that, similarly to the inclusive DIS cross section, the diffractive cross section can be written, up to terms of order $\mathcal{O}(1/Q^2)$, in a factorized form

$$d\sigma^{ep\to eXY}(\beta, \xi, Q^2, t) \; = \; \sum_i \int_\beta^1 dz \; d\hat{\sigma}^{ei}\left(\frac{\beta}{z}, Q^2\right) \; f_i^{\mathrm{D}}(z, \xi, Q^2, t) \; , \tag{4.10}$$

where the sum is performed over all parton flavours (gluon, d-quark, u-quark, etc.). The hard scattering partonic cross section $d\hat{\sigma}^{ei}$ can be computed perturbatively in QCD and is the same as in the inclusive deep inelastic scattering case. The long distance part f_i^{D} corresponds to the diffractive parton distribution functions, which can be interpreted as conditional probabilities for partons in the proton, provided the proton is scattered into the final state system Y with specified 4-momentum p'. They are evolved using the DGLAP evolution equations [140, 141, 142, 143] similarly to the inclusive case. The analogous formula for the t-integrated structure functions reads

$$F_{2/\mathrm{L}}^{\mathrm{D}(3)}(\beta, \xi, Q^2) = \sum_i \int_\beta^1 \frac{dz}{z} \, C_{2/\mathrm{L},i}\left(\frac{\beta}{z}\right) f_i^{\mathrm{D}(3)}(z, \xi, Q^2) \; ,$$

where the coefficient functions $C_{2/rmL,i}$ are the same as in inclusive DIS.

Fits to the diffractive structure functions usually [132, 138] parametrise the diffractive PDFs in a two component model, which is a sum of two exchange contributions, $I\!P$ and $I\!R$:

$$f_i^{\mathrm{D}(4)}(z, \xi, Q^2, t) = f_{I\!P}^p(\xi, t) \, f_i^{I\!P}(z, Q^2) + f_{I\!R}^p(\xi, t) \, f_i^{I\!R}(z, Q^2) \; . \tag{4.11}$$

For both of these terms proton vertex factorisation is assumed, meaning that the diffractive exchange can be interpreted as colourless objects called a 'Pomeron' or a 'Reggeon' with parton distributions $f_i^{I\!P,I\!R}(\beta, Q^2)$. The flux factors $f^p_{I\!P,I\!R}(\xi, t)$ represent the probability that a Pomeron/Reggeon with given values ξ, t couples to the proton. They are parametrised using the form motivated by Regge theory,

$$f^p_{I\!P,I\!R}(\xi, t) = A_{I\!P,I\!R} \frac{e^{B_{I\!P,I\!R} t}}{\xi^{2\alpha_{I\!P,I\!R}(t)-1}} ,$$

with a linear trajectory $\alpha_{I\!P,I\!R}(t) = \alpha_{I\!P,I\!R}(0) + \alpha'_{I\!P,I\!R}\, t$. The diffractive PDFs relevant to the t-integrated cross-sections read

$$f_i^{\mathrm{D}(3)}(z, \xi, Q^2) = \phi^{\,p}_{I\!P}(\xi)\, f_i^{I\!P}(z, Q^2) + \phi^{\,p}_{I\!R}(\xi)\, f_i^{I\!R}(z, Q^2) ,$$

with

$$\phi^{\,p}_{I\!P,I\!R}(\xi) = \int dt\; f^p_{I\!P,I\!R}(\xi, t) .$$

Note that, the notions of 'Pomeron' and 'Reggeon' used here to model hard diffraction in DIS are, in principle, different from those describing the soft hadron-hadron interactions; in particular, the parameters of the fluxes may be different.

The diffractive parton distributions of the Pomeron at the initial scale $\mu_0^2 = 1.8\,\mathrm{GeV}^2$ are parametrized as

$$z f_i^{I\!P}(z, \mu_0^2) = A_i z^{B_i} (1 - z)^{C_i} ,$$

where i is a gluon or a light quark. In the diffractive parametrisations all the light quarks (anti-quarks) are assumed to be equal. For the treatment of heavy flavours, a variable flavour number scheme (VFNS) is adopted, where the charm and bottom quark DPDFs are generated radiatively via DGLAP evolution, and no intrinsic heavy quark distributions are assumed. The structure functions are calculated in a General-Mass Variable Flavour Number scheme (GM-VFNS) [144, 145] which ensures a smooth transition of $F_{2,\mathrm{L}}$ across the flavour thresholds by including $\mathcal{O}(m_h^2/Q^2)$ corrections. The parton distributions for the Reggeon component are taken from a parametrisation which was obtained from fits to the pion structure function [146, 147].

In Eq. (4.11) the normalization factors of fluxes, $A_{I\!P,I\!R}$ and of DPDFs, A_i enter in the product. To resolve the ambiguity we fix[3] $A_{I\!P}$ and use $f_i^{I\!R}(z, Q^2)$ normalized to the pion structure function, which results in A_i and $A_{I\!R}$ being well defined free fit parameters. For full details, please see [131].

Pseudodata for diffractive structure functions

The reduced cross sections are extrapolated using ZEUS-SJ DPDFs. Following the scenario of the ZEUS fit [138] we work within the VFNS scheme at NLO accuracy. The transition scales for DGLAP evolution are fixed by the heavy quark masses, $\mu^2 = m_h^2$ and the structure functions are calculated in the Thorne–Roberts GM-VFNS [148]. The Reggeon PDFs are taken from the GRV pion set [147], the numerical parameters are taken from Tables 1 and 3 of Ref. [138] and heavy quark masses are $m_c = 1.35\,\mathrm{GeV}, m_b = 4.3\,\mathrm{GeV}$, and $\alpha_{\mathrm{s}}(M_Z^2) = 0.118$.

The pseudodata were generated using the extrapolation of the fit to HERA data, which provides the central values, amended with a random Gaussian smearing with standard deviation corresponding to the relative error δ. An uncorrelated 5% systematic error was assumed giving a total error

$$\delta = \sqrt{\delta^2_{\mathrm{sys}} + \delta^2_{\mathrm{stat}}} . \tag{4.12}$$

[3] Here, as in the HERA fits, $A_{I\!P}$ is fixed by normalizing $\phi^{\,p}_{I\!P}(0.003) = 1$.

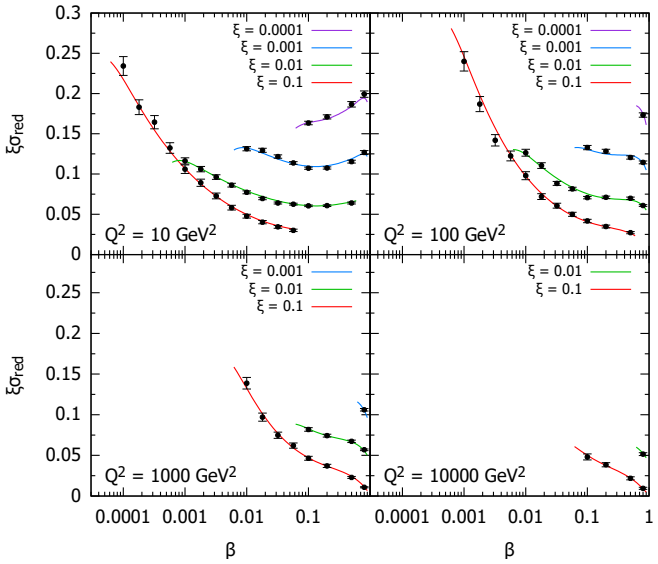

Figure 4.39: Selected subset of the simulated data for the diffractive reduced cross section as a function of β in bins of ξ and Q^2 for ep collisions at the LHeC. The curves for $\xi = 0.01, 0.001, 0.0001$ are shifted up by 0.04, 0.08, 0.12, respectively.

The statistical error was computed assuming a very modest integrated luminosity of $2\,\text{fb}^{-1}$, see [6, 149]. For the binning adopted in this study, the statistical uncertainties have a very small effect on the uncertainties in the extracted DPDFs. Obviously, a much larger luminosity would allow a denser binning that would result in smaller DPDF uncertainties.

In Fig. 4.39 we show a subset of the simulated data for the diffractive reduced cross section $\xi\sigma_{\text{red}}$ as a function of β in selected bins of ξ and Q^2 for the LHeC. For the most part the errors are very small, and are dominated by the systematics. The breaking of Regge factorisation evident at large ξ comes from the large Reggeon contribution in that region, whose validity could be further investigated at the LHeC.

Potential for constraining diffractive PDFs at the LHeC and FCC-eh

With the aim of establishing the experimental precision with which DPDFs could be extracted when LHeC data become available, we generate the central values of the pseudodata using the central set of the ZEUS-SJ fit that are distributed according to a Gaussian with experimental width, Eq. (4.12), that also provides the uncertainty in the pseudodata. We then include the pseudodata in a fit using the same functional form and, as expected, obtain a $\chi^2/\text{ndf} \sim 1$, which demonstrates the consistency of the approach.

To evaluate the precision with which the DPDFs can be determined, several pseudodata sets, corresponding to independent random error samples, were generated. Each pseudodata set was fitted to the reduced cross-sections .

The minimal value of Q^2 for the data considered in the fits was set to $Q^2\text{min} = 5\,\text{GeV}^2$. The reason for this cut-off is to show the feasibility of the fits including just the range in which standard twist-2 DGLAP evolution is expected to be trustable. At HERA, the Q^2_{min} values giving acceptable DGLAP (twist-2) fits were $8\,\text{GeV}^2$ [132] and $5\,\text{GeV}^2$ [133] for H1 and ZEUS, respectively. The maximum value of ξ was set by default to $\xi_{\text{max}} = 0.1$, above which the cross-section starts to be dominated by the Reggeon exchange.

The binning adopted in this study corresponds roughly to 4 bins per order of magnitude in each of ξ, β, Q^2. For $Q^2_{\text{min}} = 5\,\text{GeV}^2$, $\xi_{\text{max}} = 0.1$ and below the top threshold this results in 1229 and 1735 pseudodata points for the LHeC and FCC-eh, respectively. The top-quark region adds 17 points for the LHeC and 255 for

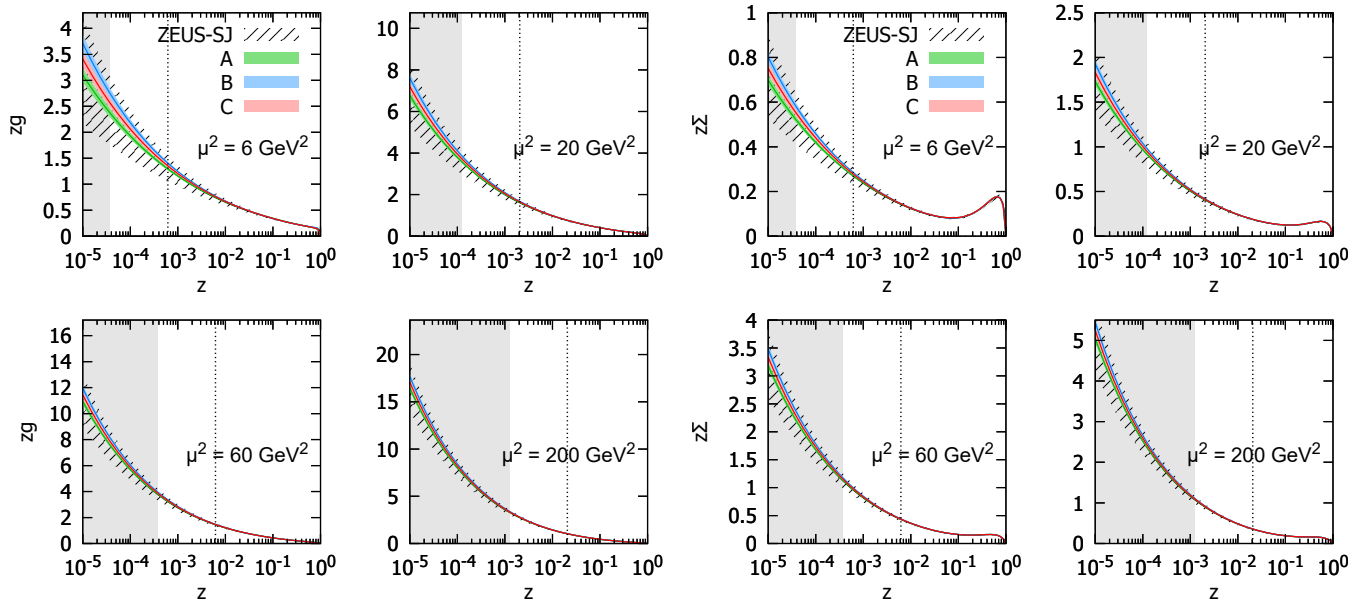

Figure 4.40: Diffractive PDFs for gluon and quark in the LHeC kinematics as a function of momentum fraction z for fixed values of scale μ^2. Results of fits to three (A,B,C) pseudodata replicas are shown together with the experimental error bands. For comparison, the extrapolated ZEUS-SJ fit is also shown (black) with error bands marked with the hatched pattern. The vertical dotted lines indicate the HERA kinematic limit. The bands indicate only the experimental uncertainties, see the text.

FCC-eh. Lowering $Q^2_{\min}$ down to $1.8\,\mathrm{GeV}^2$ we get 1589 and 2171 pseudodata points, while increasing ξ up to 0.32 adds ca. 180 points for both machines.

The potential for determination of the gluon DPDF was investigated by fitting the inclusive diffractive DIS pseudodata with two models with different number of parameters, named S and C (see [131]) with $\alpha_{IP,IR}(0)$ fixed, in order to focus on the shape of the Pomeron's PDFs. At HERA, both S and C fits provide equally good descriptions of the data with $\chi^2/\mathrm{ndf} = 1.19$ and 1.18, respectively, despite different gluon DPDF shapes. The LHeC pseudodata are much more sensitive to gluons, resulting in χ^2/ndf values of 1.05 and 1.4 for the S and C fits, respectively. This motivates the use of the larger number of parameters in the fit-S model, which we employ in the further studies. It also shows clearly the potential of the LHeC and the FCC-eh to better constrain the low-x gluon and, therefore, unravel eventual departures from standard linear evolution.

In Fig. 4.40 the diffractive gluon and quark distributions are shown for the LHeC and FCC-eh, respectively, as a function of z for fixed scales $\mu^2 = 6, 20, 60, 200\,\mathrm{GeV}^2$. The bands labelled A, B, C denote fits to three statistically independent pseudodata replicas, obtained from the same central values and statistic and systematic uncertainties. Hereafter the bands shown correspond to $\Delta\chi^2 = 2.7$ uncertainty (90 % CL). Also the extrapolated ZEUS-SJ DPDFs are shown with error bands marked by the '/' hatched area. Note that the depicted uncertainty bands come solely from experimental errors, neglecting theoretical sources, such as fixed input parameters and parametrisation biases. The extrapolation beyond the reach of LHeC/FCC-eh is marked in grey and the HERA kinematic limit is marked with the vertical dotted line. The stability of the results with respect to the replica used for the analysis is evident, so in the following only one will be employed. The DPDFs determination accuracy improves with respect to HERA by a factor of 5–7 for the LHeC and 10–15 for the FCC-eh.

For a better illustration of the precision, in Fig. 4.41 the relative uncertainties are shown for parton distributions at different scales. The different bands show the variation with the upper cut on the available

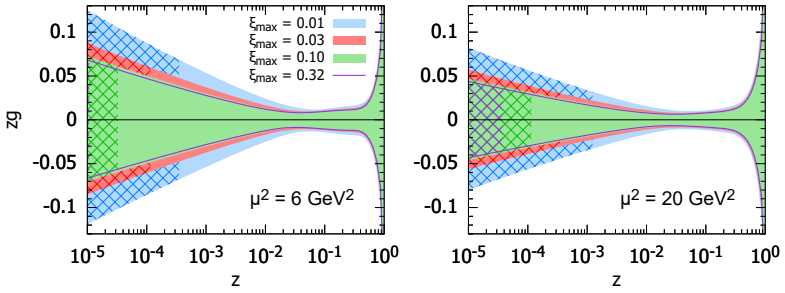

Figure 4.41: Relative uncertainties on the diffractive gluon PDFs for the LHeC kinematics. Two different choices of scales are considered $\mu^2 = 6$ and $\mu^2 = 20$ GeV^2. The blue, red, green bands and magenta line correspond to different maximal values of $\xi = 0.01, 0.03, 0.1, 0.32$, respectively. The cross-hatched areas show kinematically excluded regions. The bands indicate only the experimental uncertainties, see the text.

ξ range, from 0.01 to 0.32. We observe only a modest improvement in the achievable accuracy of the extracted DPDFs with the change of ξ by an order of magnitude from 0.01 to 0.1. An almost negligible effect is observed when further extending the ξ range up to 0.32. This is encouraging, since the measurement for the very large values of ξ is challenging. It reflects the dominance of the secondary Reggeon in this region.

We would like to stress again that only experimental errors are included in our uncertainty bands. Neither theoretical uncertainties nor the parametrisation biases are considered. For a detailed discussion of this and other aspects of the fits, please see see [131].

4.2.8 Diffractive Deep Inelastic Scattering at the LHeC (DDIS)

@Todo. SJB. To be merged into diffraction by AS.

The LHeC also will measure diffractive deep-inelastic reactions (DDIS) such as $ep \to e'p'X$ where the final proton stays intact and is isolated in phase space. It is a surprising fact that approximately 15% of the events in deep inelastic scattering $ep \to e'X$ are diffractive; i.e., leave the proton intact $ep \to e'p'X$ with approximately 90% of the proton beam LF momentum. These events are due to pomeron exchange: i.e., soft gluon exchange in the final state which returns the incoming proton to a color singlet. Since the DDIS process is leading twist; i.e., Bjorken scaling, one expects similar rates, modulo logarithmic evolution over the full range of LHeC kinematics. Since the magnitude of the DDIS cross section involves soft gluon exchange in the final state, it probes the QCD running coupling $\alpha_s(Q^2)$ at small Q^2. The data for DDIS from the H1 experiment is illustrated in Fig. .

In addition to Pomeron exchange $ep \to e'p'X$, one expects Reggeon exchange from $q\bar{q}$ exchange in the t-channel; i.e. flavor changing diffractive reactions at the LHeC such as $ep \to e'n'X$,

Its is important to note that the extraction of the gluon momentum fraction from deep inelastic lepton-proton scattering at the LHeC using the momentum sum rule can be misleading since the measured inclusive DIS cross section includes the DDIS events $ep \to eN'X$ where the final state proton or neutron carries off a significant LF momentum fraction $< x'_p >$ of the proton beam.

The DDIS amplitude has a complex phase since it arises –like the Sivers effect – from leading-twist, final-state interactions. It is this not included in the underlying light-front wavefunction of the proton. It is this not constrained by momentum and spin sum rules. The DDIS amplitude underlies the two-step Gribov-Glauber amplitude whose interference with one-step amplitudes causes shadowing and antishadowing of nuclear structure functions.

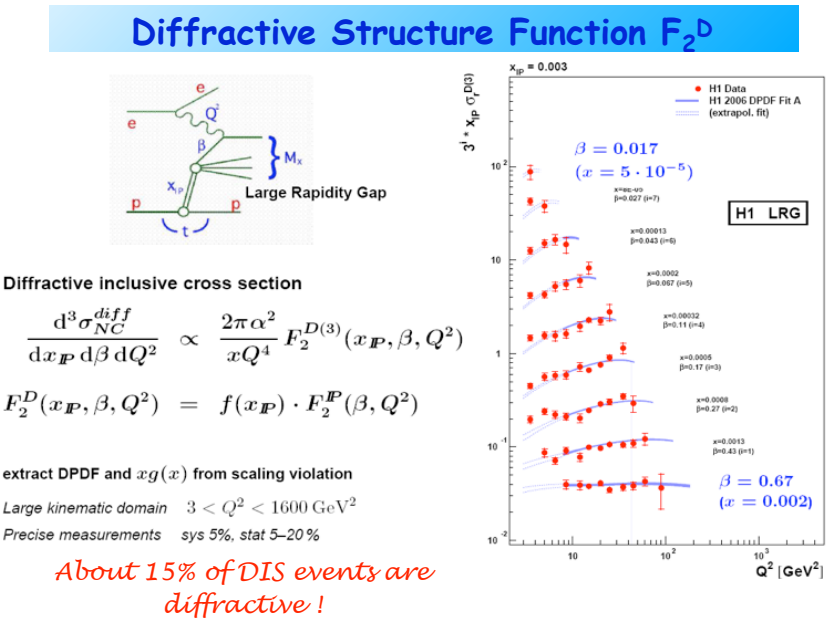

Figure 4.42: The diffractive deep inelastic structure function measured by H1 in $ep \to e'p'X$ events.

4.2.9 Light-Front Holography and Superconformal Algebra

The LHeC has the potential of probing the high mass spectrum of QCD, such as the spectroscopy and structure of hadrons consisting of heavy quarks. Insights into this new domain of hadron physics can now be derived by new non-perturbative color-confining methods based on light-front (LF) holography. A remarkable feature is universal Regge trajectories with universal slopes in both the principal quantum number n and internal orbital angular momentum L. A key feature is di-quark clustering and supersymmetric relations between the masses of meson, baryons, and tetraquarks. In addition the running coupling is determined at all scales, including the soft domain relevant to rescattering corrections to LHeC processes. The combination of lightfront holography with superconformal algebra leads to the novel prediction that hadron physics has supersymmetric properties in both spectroscopy and dynamics.

Light-front holography and recent theoretical advances: Five-dimensional AdS_5 space provides a geometrical representation of the conformal group. Remarkably, AdS_5 is holographically dual to $3+1$ spacetime at fixed LF time τ [150]. A color-confining LF equation for mesons of arbitrary spin J can be derived from the holographic mapping of the "soft-wall model" modification of AdS_5 space for the specific dilaton profile $e^{+\kappa^2 z^2}$, where z is the fifth dimension variable of the five-dimensional AdS_5 space. A holographic dictionary maps the fifth dimension z to the LF radial variable ζ, with $\zeta^2 = b_\perp^2(1-x)$. The same physics transformation maps the AdS_5 and $(3+1)$ LF expressions for electromagnetic and gravitational form factors to each other [151].

A key tool is the remarkable dAFF principle [152] which shows how a mass scale can appear in a Hamiltonian and its equations of motion while retaining the conformal symmetry of the action. When applying it to LF holography, a mass scale κ appears which determines universal Regge slopes, and the hadron masses. The resulting "LF Schrödinger Equation" incorporates color confinement and other essential spectroscopic and dynamical features of hadron physics, including Regge theory [**?**], the Veneziano formula [153], a massless pion for zero quark mass and linear Regge trajectories with the universal slope in the radial quantum number n and the internal orbital angular momentum L. The combination of LF dynamics, its holographic mapping

to AdS_5 space, and the dAFF procedure provides new insight into the physics underlying color confinement, the nonperturbative QCD coupling, and the QCD mass scale. The $q\bar{q}$ mesons and their valence LFWFs are the eigensolutions of the frame-independent a relativistic bound-state LF Schrödinger equation.

The mesonic $q\bar{q}$ bound-state eigenvalues for massless quarks are $M^2(n, L, S) = 4\kappa^2(n + L + S/2)$. This equation predicts that the pion eigenstate $n = L = S = 0$ is massless for zero quark mass. When quark masses are included in the LF kinetic energy $\sum_i \frac{k_{\perp i}^2 + m^2}{x_i}$, the spectroscopy of mesons are predicted correctly, with equal slope in the principal quantum number n and the internal orbital angular momentum L. A comprehensive review is given in Ref. [150].

The QCD Running Coupling at all Scales from Light-Front Holography: The QCD running coupling $\alpha_s(Q^2)$ sets the strength of the interactions of quarks and gluons as a function of the momentum transfer Q (see section 4.2.1). The dependence of the coupling Q^2 is needed to describe hadronic interactions at both long and short distances [154]. It can be defined [155] at all momentum scales from a perturbatively calculable observable, such as the coupling $\alpha_s^{g_1}(Q^2)$, which is defined using the Bjorken sum rule [156], and determined from the sum rule prediction at high Q^2 and, below, from its measurements [157, 158, 159]. At high Q^2, such "effective charges" satisfy asymptotic freedom, obey the usual pQCD renormalisation group equations, and can be related to each other without scale ambiguity by commensurate scale relations [160].

The high Q^2 dependence of $\alpha_s^{g_1}(Q^2)$ is predicted by pQCD. In the small Q^2 domain its functional behavior can be predicted by the dilaton $e^{+\kappa^2 z^2}$ soft-wall modification of the AdS_5 metric, together with LF holography [161], as $\alpha_s^{g_1}(Q^2) = \pi e^{-Q^2/4\kappa^2}$. The parameter κ determines the mass scale of hadrons and Regge slopes in the zero quark mass limit, and it was shown that it can be connected to the mass scale Λ_s, which controls the evolution of the pQCD coupling [161, 162, 163]. Measurements of $\alpha_s^{g_1}(Q^2)$ [164, 165] are remarkably consistent with this predicted Gaussian form, and a fit gives $\kappa = 0.513 \pm 0.007$ GeV, see Fig. 4.43.

The matching of the high and low Q^2 regimes of $\alpha_s^{g_1}(Q^2)$ determines a scale Q_0, which sets the interface between perturbative and non-perturbative hadron dynamics. This connection can be done for any choice of renormalisation scheme and one obtains an effective QCD coupling at all momenta. In the $\overline{\rm MS}$ scheme one gets $Q_0 = 0.87 \pm 0.08\,{\rm GeV}$ [166]. The corresponding value of $\Lambda_{\overline{\rm MS}}$ agrees well with the measured world average value and its value allows to compute hadron masses using the AdS/QCD superconformal predictions for hadron spectroscopy. The value of Q_0 can further be used to set the factorization scale for DGLAP evolution [141, 142, 143] or the ERBL evolution of distribution amplitudes [167, 168]. The use of the scale Q_0 to resolve the factorization scale uncertainty in structure functions and fragmentation functions, in combination with the scheme-independent *principle of maximum conformality* (PMC) [38] for setting renormalization scales, can greatly improve the precision of pQCD predictions for collider phenomenology at LHeC and HL-LHC.

Superconformal Algebra and Hadron Physics with LHeC data: If one generalises LF holography using *superconformal algebra* the resulting LF eigensolutions yield a unified Regge spectroscopy of mesons, baryons and tetraquarks, including remarkable supersymmetric relations between the masses of mesons and baryons of the same parity [4] [169, 170]. This generalisation further predicts hadron dynamics, including vector meson electroproduction, hadronic LFWFs, distribution amplitudes, form factors, and valence structure functions [171, 172]. Applications to the deuteron elastic form factors and structure functions are given in Refs. [173, 174]

The eigensolutions of superconformal algebra predict the Regge spectroscopy of mesons, baryons, and tetraquarks of the same parity and twist as equal-mass members of the same 4-plet representation with

[4] QCD is not supersymmetrical in the usual sense, since the QCD Lagrangian is based on quark and gluonic fields, not squarks or gluinos. However, its hadronic eigensolutions conform to a representation of superconformal algebra, reflecting the underlying conformal symmetry of chiral QCD and its Pauli matrix representation.

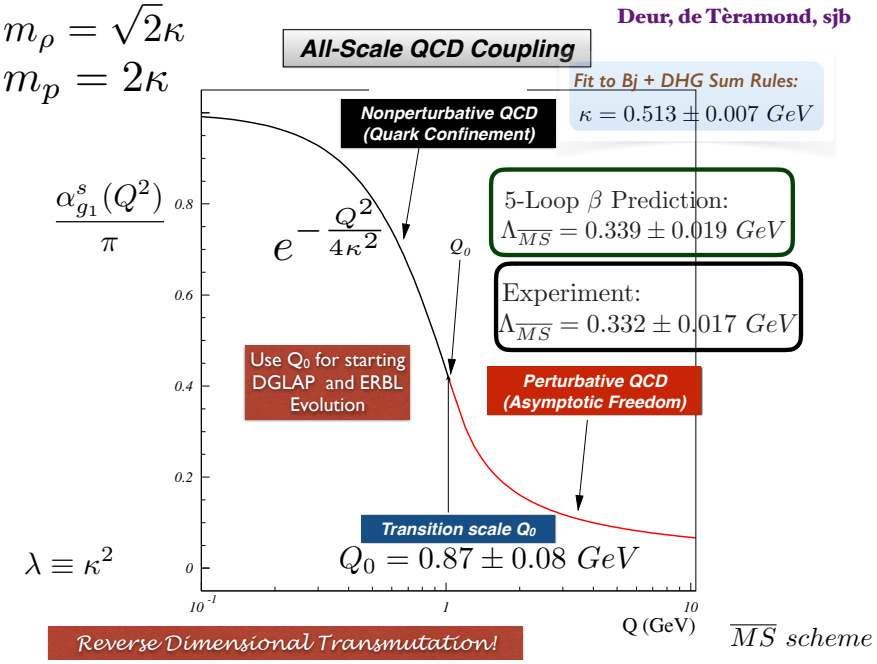

Figure 4.43: Prediction for the running coupling $\alpha_s^{g_1}(Q^2)$ at all scales. At lower Q^2 predictions are obtained from LF Holography and at higher Q^2 from perturbative QCD. The magnitude and derivative of the perturbative and non-perturbative coupling are matched at the scale Q_0. This matching connects the perturbative scale $\Lambda_{\overline{MS}}$ to the non-perturbative scale κ which underlies the hadron mass scale.

a universal Regge slope. [175, 176, 177]. A comparison with experiment is shown in Fig. 4.44. The $q\bar{q}$ mesons with orbital angular momentum $L_M = L_B + 1$ have the same mass as their baryonic partners with orbital angular momentum L_B [178, 175].

The predictions from LF holography and superconformal algebra can also be extended to mesons, baryons, and tetraquarks with strange, charm and bottom quarks. Although conformal symmetry is strongly broken by the heavy quark masses, the basic underlying supersymmetric mechanism, which transforms mesons to baryons (and baryons to tetraquarks), still holds and gives remarkable mass degeneracy across the entire spectrum of light, heavy-light and double-heavy hadrons.

The 4-plet symmetry of quark-antiquark mesons, quark-diquark baryons, and diquark-antidiquark tetraquarks are important predictions by superconformal algebra [169, 166]. Recently the AnDY experiment at RHIC has reported the observation of a state at 18 GeV which can be identified with the $[bb][\bar{b}\bar{b}]$ tetraquark [179]. The states with heavy quarks such as the $[bb][\bar{b}\bar{b}]$ tetraquark can be produced at the LHeC, especially at high x_F along the proton beam direction. New measurements at the LHeC are therefore inevitable to manifest the superconformal nature of hadronic bound states.

4.2.10 Disentangling non-linear QCD dynamics at the LHeC [Juan Rojo, et al.]

Introduction. The LHeC will extend the kinematic reach of HERA at small-x by one order of magnitude in the perturbative regime $Q \gtrsim 1$ GeV [1]. This extension will allow unprecedented tests of the strong interaction in this extreme region, where deviations from the linear DGLAP evolution are expected to appear. In particular, it has been argued that the strong growth of the gluon PDF at small-x should eventually lead to gluon recombination [180] to avoid violating the unitary bounds. The onset of such non-linear dynamics, also known as saturation, has been extensively searched but so far there is no conclusive evidence of its presence, at least within the HERA inclusive structure function measurements. In this

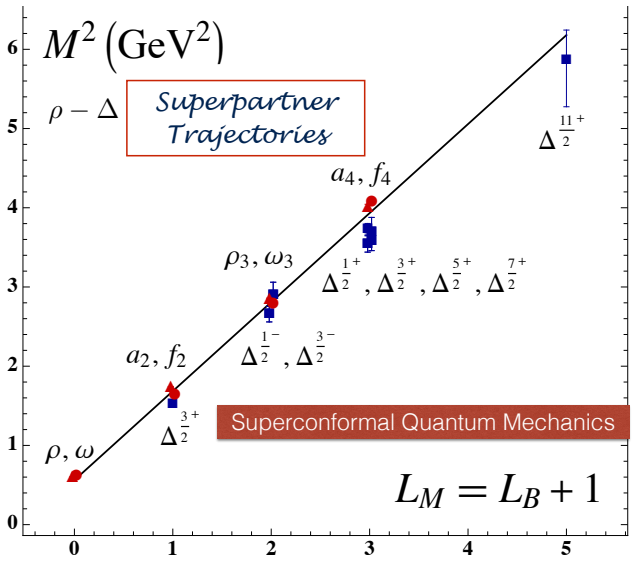

Figure 4.44: Comparison of the ρ/ω meson Regge trajectory with the $J = 3/2$ Δ baryon trajectory. Superconformal algebra predicts the mass degeneracy of the meson and baryon trajectories if one identifies a meson with internal orbital angular momentum L_M with its superpartner baryon with $L_M = L_B + 1$. See Refs. [178, 175].

context, the extended kinematic range of the LHeC provides unique avenues to explore the possible onset of non-linear QCD dynamics at small-x. The discovery of saturation, a radically new regime of QCD, would then represent an important milestone in our understanding of the strong interactions.

The main challenge in disentangling saturation lies in the fact that non-linear corrections are expected to be moderate even at the LHeC, since they are small (if present at all) in the region covered by HERA. Therefore, great care needs to be employed in order to separate such effects from those of standard DGLAP linear evolution. Indeed, it is well known that HERA data at small-x in the perturbative region can be equally well described, at least at the qualitative level, both by PDF fits based on the DGLAP framework as well as by saturation-inspired models. However, rapid progress both in theory calculations and methodological developments have pushed QCD fits to a new level of sophistication, and recently it has been shown that subtle but clear evidence of BFKL resummation at small-x is present in HERA data, both for inclusive and for heavy quark structure functions [12, 13]. Such studies highlight how it should be possible to tell apart non-linear from linear dynamics using state-of-the-art fitting methods even if these are moderate, provided that they are within the LHeC reach.

Here we want to assess the sensitivity of the LHeC to detect the possible onset of non-linear saturation dynamics. This study will be carried out by generalizing a recent analysis [9] that quantified the impact of LHeC inclusive and semi-inclusive measurements on the PDF4LHC15 PDFs [7, 181] by means of Hessian profiling [182]. There, the LHeC pseudo-data was generated assuming that linear DGLAP evolution was valid in the entire LHeC kinematic range using the PDF4LHC15 set as input. To ascertain the possibility of pinning down saturation at the LHeC, here we have revisited this study but now generating the LHeC pseudo-data by means of a saturation-inspired calculation. By monitoring the statistical significance of the tension that will be introduced (by construction) between the saturation pseudo-data and the DGLAP theory assumed in the PDF fit, we aim to determine the likelihood of disentangling non-linear from linear evolution effects at the LHeC. See also [183] for previous related studies along the same direction.

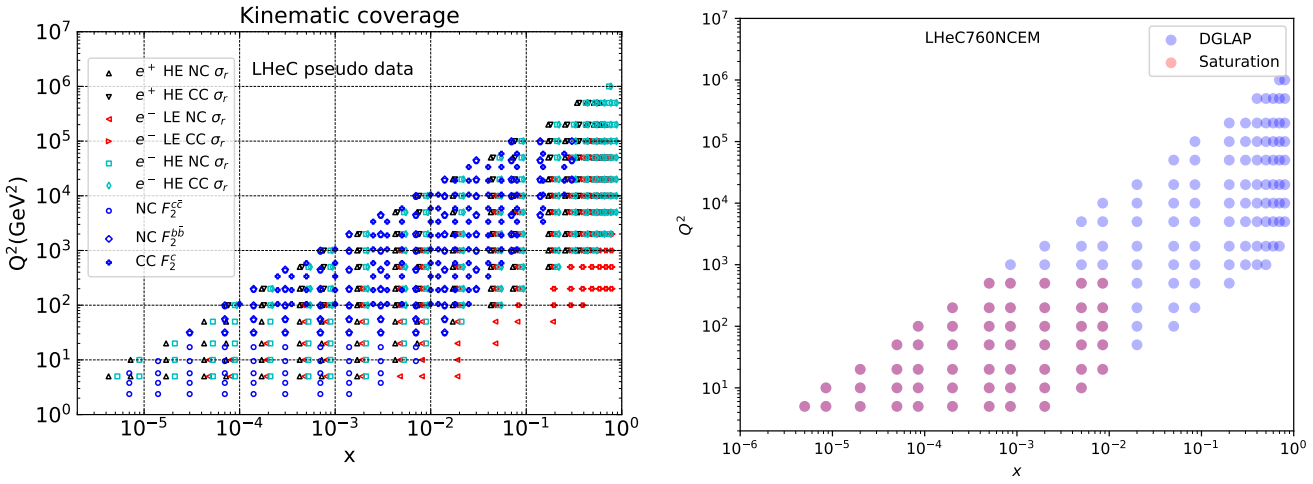

Figure 4.45: Left plot: the kinematic range in the (x, Q^2) plane of the LHeC pseudo-data on inclusive and semi-inclusive DIS structure functions used in the PDF projections of [9]. Right plot: the kinematic coverage of the NC e^-p scattering pseudo-data at the LHeC, where the blue (red) points indicate those bins for which DGLAP (saturation) predictions are available.

Analysis settings. In this study we adopt the settings of [184, 9], to which we refer the interested reader for further details. In [9] the impact on the proton PDFs of inclusive and semi-inclusive neutral-current (NC) and charged current (CC) DIS structure functions from the LHeC was quantified. These results were then compared with the corresponding projections for the PDF sensitivity of the High-Luminosity upgrade of the LHC (HL-LHC). In the left panel of Fig. 4.45 we display the kinematic range in the (x, Q^2) plane of the LHeC pseudo-data employed in that analysis, which illustrated how the LHeC can provide unique constraints on the behaviour of the quark and gluon PDFs in the very small-x region.

Since non-linear dynamics are known to become sizable only at small-x, for the present analysis it is sufficient to consider the NC e^-p inclusive scattering cross-sections from proton beam energies of $E_p = 7$ TeV and $E_p = 1$ TeV. In the right panel in Fig. 4.45 we show the bins in (x, Q^2) for which LHeC pseudo-data for inclusive structure functions has been generated according to a saturation-based calculation. Specifically, we have adopted here the DGLAP-improved saturation model of Ref. [185], in which the scattering matrix is modeled through eikonal iteration of two gluon exchanges. This model was further extended to include heavy flavour in [186]. The specific parameters that we use were taken from Fit 2 in [187], where parametrisations are provided that can be used for $x < 0.01$ and $Q^2 < 700$ GeV^2. These parameters were extracted from a fit to the HERA legacy inclusive structure function measurements [29] restricted to $x < 0.01$ and $0.045 < Q^2 < 650$ GeV^2. In contrast to other saturation models, the one we assume here [187] provides a reasonable description for large Q^2 in the small x region, where it ensure a smooth transition to standard fixed-order perturbative results.

Note that the above discussion refers only to the generated LHeC pseudo-data: all other aspects of the QCD analysis of [9] are left unchanged. In particular, the PDF profiling will be carried out using theory calculations obtained by means of DGLAP evolution with the NNLO PDF4LHC15 set (see also [188]), with heavy quark structure functions evaluated by means of the FONLL-B general-mass variable flavour number scheme [189]. In order to ensure consistency with the PDF4LHC15 prior, here we will replace the DGLAP pseudo-data by the saturation calculation only in the kinematic region for $x \lesssim 10^{-4}$, rather than for all the bins indicated in red in Fig. 4.45. The reason for this choice is that PDF4LHC15 already includes HERA data down to $x \simeq 10^{-4}$ which is successfully described via the DGLAP framework, and therefore if we assume departures from DGLAP in the LHeC pseudo-data this should only be done for smaller values of x.

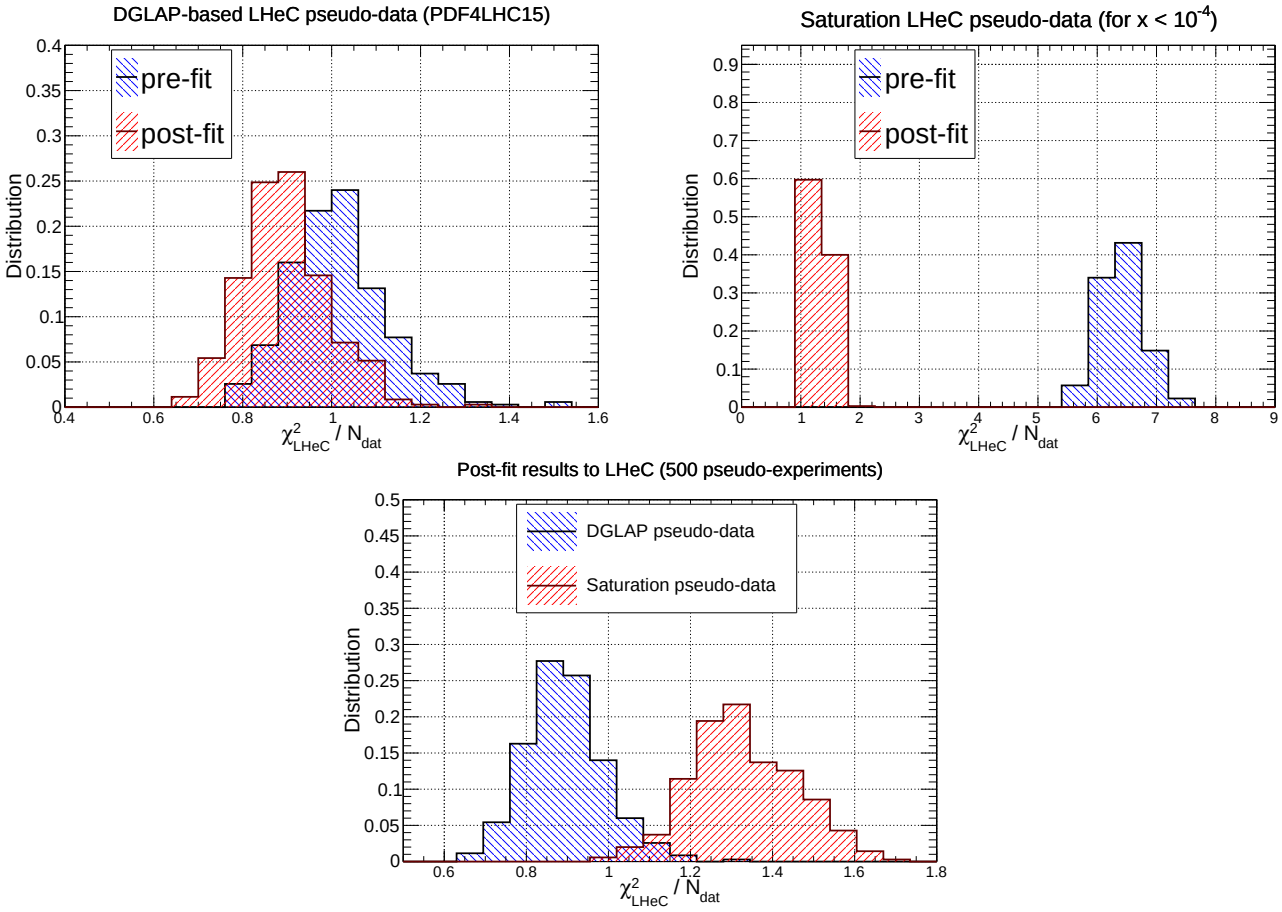

Figure 4.46: Upper plots: the distribution of pre-fit and post-fit values of $\chi^2/n_{\rm dat}$ for the $N_{\rm exp} = 500$ sets of generated LHeC pseudo-data. We compare the results of the profiling of the LHeC pseudo-data based on DGLAP calculations in the entire range of x (left) with those where the pseudo-data is based on the saturation model in the region $x < 10^{-4}$ (right plot). Bottom plot: comparison of the post-fit $\chi^2/n_{\rm dat}$ distributions between these two scenarios for the pseudo-data generation.

Results and discussion. Using the analysis settings described above, we have carried out the profiling of PDF4LHC15 with the LHeC inclusive structure function pseudo-data, which for $x \leq 10^{-4}$ ($x > 10^{-4}$) has been generated using the GBW saturation (DGLAP) calculations, and compare them with the results of the profiling where the pseudo-data follows the DGLAP prediction. We have generated $N_{\rm exp} = 500$ independent sets LHeC pseudo-data, each one characterised by different random fluctuations (determined by the experimental uncertainties) around the underlying central value.

To begin with, it is instructive to compare the data versus theory agreement, $\chi^2/n_{\rm dat}$, between the pre-fit and post-fit calculations, in order to assess the differences between the DGLAP and saturation cases. In the upper plots of Fig. 4.46 we show the distributions of pre-fit and post-fit values of $\chi^2/n_{\rm dat}$ for the $N_{\rm exp} = 500$ sets of generated LHeC pseudo-data. We compare the results of the profiling of the LHeC pseudo-data based on DGLAP calculations in the entire range of x with those where the pseudo-data is based on the saturation model in the region $x < 10^{-4}$. Then in the bottom plot we compare of the post-fit χ^2 distributions between the two scenarios. Note that in these three plots the ranges in the x axes are different.

From this comparison we can observe that for the case where the pseudo-data is generated using a consistent DGLAP framework (PDF4LHC15) as the one adopted for the theory calculations used in the fit, as expected the agreement is already good at the pre-fit level, and it is further improved at the post-fit level. However the situation is rather different in the case where a subset of the LHeC pseudo-data is generated using a saturation

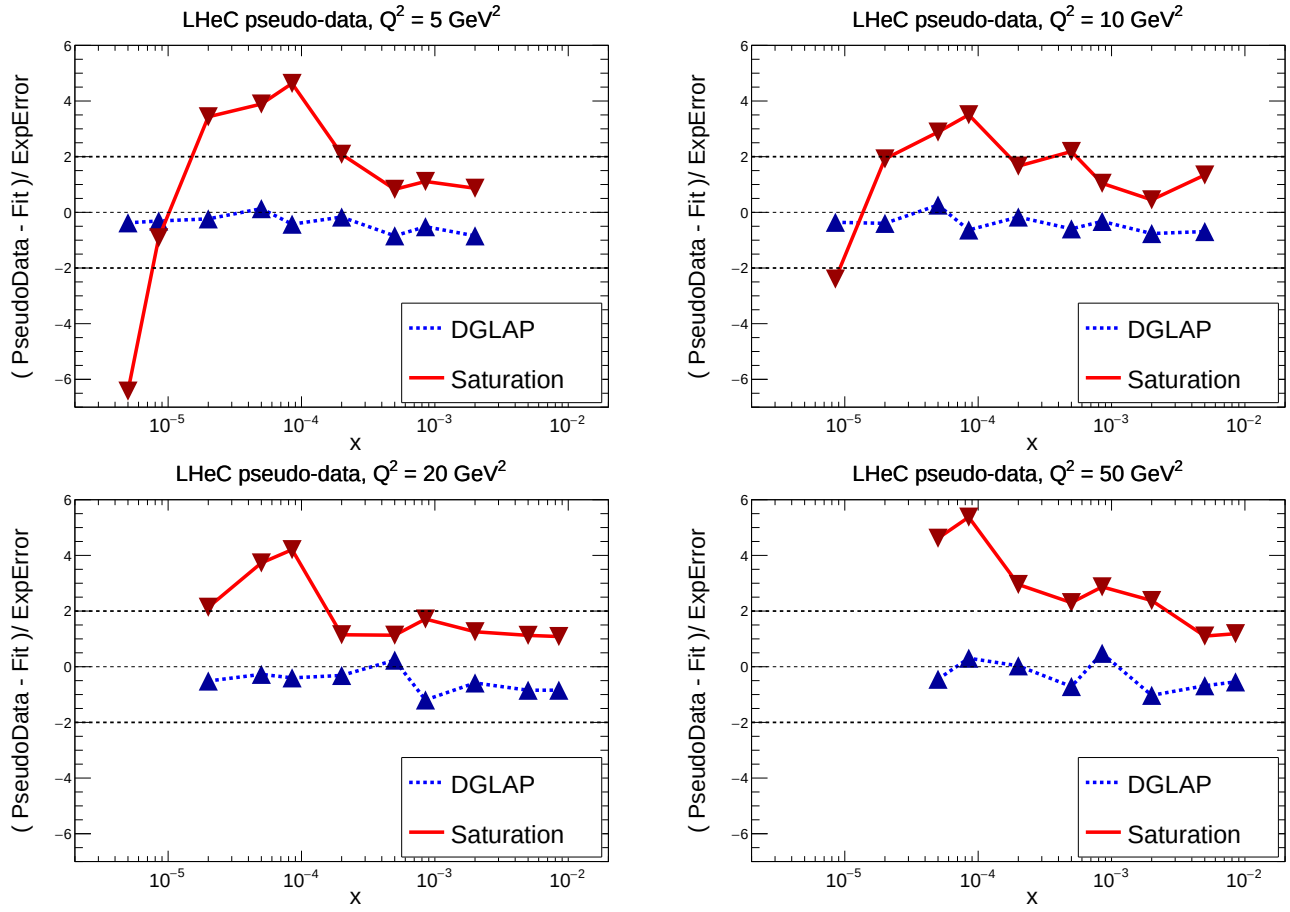

Figure 4.47: The pulls between the post-fit prediction and the central value of the LHeC pseudo-data, Eq. (4.13), for four different bins in Q^2. We compare the results of the profiling where the LHeC pseudo-data has been generated using a consistent DGLAP theory with that partially based on the saturation calculations.

model: at the pre-fit level the agreement between theory and pseudo-data is poor, with $\chi^2/n_{\rm dat} \simeq 7$. The situation markedly improves at the post-fit level, where now the $\chi^2/n_{\rm dat}$ distributions peaks around 1.3. This result implies that the DGLAP fit manages to absorb most of the differences in theory present in the saturation pseudo-data. This said, the DGLAP fit cannot entirely "fit away" the non-linear corrections: as shown in the lower plot of Fig. 4.46, even at the post-fit level one can still tell apart the $\chi^2/n_{\rm dat}$ distributions between the two cases, with the DGLAP (saturation) pseudo-data peaking at around 0.9 (1.3). This comparison highlights that it is not possible for the DGLAP fit to completely absorb the saturation effects into a PDF redefinition.

In order to identify the origin of the worse agreement between theory predictions and LHeC pseudo-data in the saturation case, it is illustrative to take a closer look at the pulls defined as

$$P(x,Q^2) = \frac{\mathcal{F}_{\rm fit}(x,Q^2) - \mathcal{F}_{\rm dat}(x,Q^2)}{\delta_{\rm exp}\mathcal{F}(x,Q^2)}\,, \tag{4.13}$$

where $\mathcal{F}_{\rm fit}$ is the central value of the profiled results for the observable $\mathcal{F}$ (in this case the reduced neutral current DIS cross-section), $\mathcal{F}_{\rm dat}$ is the corresponding central value of the pseudo-data, and $\delta_{\rm exp}\mathcal{F}$ represents the associated total experimental uncertainty. In Fig. 4.47 we display the pulls between the post-fit prediction and the central value of the LHeC pseudo-data for different bins in Q^2. We compare the cases where the pseudo-data has been generated using a consistent theory calculation (DGLAP) with that based on the GBW saturation model.

The comparisons in Fig. 4.47 show first of all that in the DGLAP case the pulls are $\mathcal{O}(1)$ in the entire kinematical range. This is of course expected, given that the LHeC pseudo-data is generated using the same theory as the one subsequently used for the fit. In the case where the pseudo-data has been partially generated with the saturation calculation, on the other hand, one finds a systematic tension between the theory used for the fit (DGLAP) and the one used to generate the pseudo-data (saturation). Indeed, we find that at the smallest values of x the theory prediction undershoots the data by a significant amount, while at higher x the opposite behaviour takes place. One can also see that in the region $10^{-4} \lesssim x \lesssim 10^{-3}$ the fit overshoots the pseudo-data by a large amount.

These comparisons highlight how a QCD fit to the saturation pseudo-data is obtained as a compromise between opposite trends: the theory wants to overshoot the data at very small x and overshoot it at larger values of x. These tensions result in a distorted fit, explaining the larger $\chi^2/n_{\rm dat}$ values as compared to the DGLAP case. Such a behaviour can be partially traced back by the different scaling in Q^2 between DGLAP and GBW shown in Fig. **??**: while a difference x dependence could eventually be absorbed into a change of the PDFs at the parametrisation scale Q_0, this is not possible with a Q^2 dependence.

The pull analysis of Fig. 4.47 highlights how in order to tell apart linear from non-linear QCD evolution effects at small-x it would be crucial to ensure a lever arm in Q^2 as large as possible in the perturbative region. This way it becomes possible to disentangle the different scaling in Q^2 for the two cases. The lack of a sufficiently large lever arm in Q^2 at HERA at small x could explain in part why both frameworks are able to describe the same structure function measurements at the qualitative level. Furthermore, we find that amplifying the significance of these subtle effects can be achieved by monitoring the χ^2 behaviour in the Q^2 bins more affected by the saturation corrections. The reason is that the total χ^2, such as that reported in Fig. 4.46, is somewhat less informative since the deviations at small-Q are washed out by the good agreement between theory and pseudo-data in the rest of the kinematical range of the LHeC summarised in Fig. 4.45.

To conclude this analysis, in Fig. 4.48 we display the comparison between the PDF4LHC15 baseline with the results of the PDF profiling of the LHeC pseudo-data for the gluon (left) and quark singlet (right) for $Q = 10$ GeV. We show the cases where the pseudo-data is generated using DGLAP calculations and where it is partially based on the GBW saturation model (for $x \lesssim 10^{-4}$). We find that the distortion induced by the mismatch between theory and pseudo-data in the saturation case is typically larger than the PDF uncertainties expected once the LHeC constraints are taken into account. While of course in a realistic situation such a comparison would not be possible, the results of Fig. 4.48 show that saturation-induced effects are expected to be larger than the typical PDF errors in the LHeC era, and thus that it should be possible to tell them apart using for example tools such as the pull analysis of Fig. 4.47 or other statistical methods.

Summary. Here we have assessed the feasibility of disentangling DGLAP evolution from non-linear effects at the LHeC. By means of a QCD analysis where LHeC pseudo-data is generated using a saturation model, we have demonstrated that the LHeC should be possible to identify non-linear effects with large statistical significance, provided their size is the one predicted by current calculations such as the that of [187] that have been tuned to HERA data. A more refined analysis would require to study whether or not small-x BFKL resummation effects can partially mask the impact of non-linear dynamics, though this is unlikely since the main difference arises in their Q^2 scaling. The discovery of non-linear dynamics would represent an important milestone for the physics program of the LHeC, demonstrating the onset of a new gluon-dominated regime of the strong interactions and paving the way for detailed studies of the properties of this new state of matter. Such discovery would have also implications outside nuclear and particle physics, for instance it would affect the theory predictions for the scattering of ultra-high energy neutrinos with matter [190].

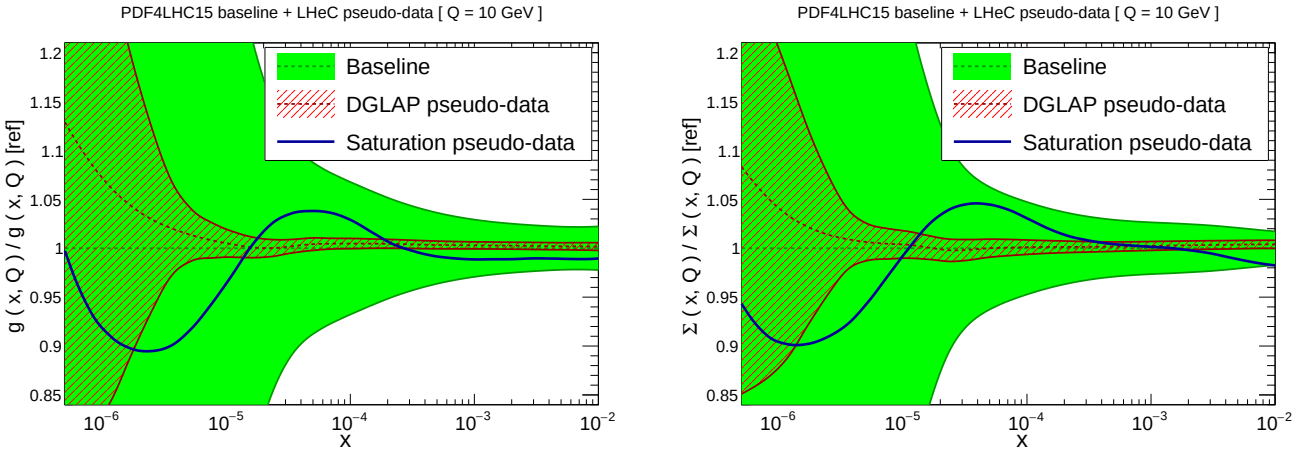

Figure 4.48: Comparison between the PDF4LHC15 baseline (green band) with the results of the profiling of the LHeC pseudo-data for the gluon (left) and quark singlet (right) for $Q = 10$ GeV. We show the cases where the pseudo-data is generated using DGLAP calculations (red hatched band) and where it is partially based on the GBW saturation model (blue curve).

4.3 Electroweak Physics [D. Britzger, H. Spiesberger]

With the discovery of the Standard Model (SM) Higgs boson at the CERN LHC experiments and subsequent measurement of its properties, all fundamental parameters of the SM have now been measured directly and with remarkable precision. To further establish the validity of the theory of electroweak interactions [191, 192, 193, 194, 195], validate the mechanism of electroweak symmetry breaking and the nature of the Higgs sector [196, 197, 198], new electroweak measurements have to be performed at highest precision. Such high-precision measurements can be considered as a portal to new physics, since non-SM contributions, as for instance loop-insertions, may cause significant deviations for some precisely measurable and calculable observables. At the LHeC, the greatly enlarged kinematic reach to higher mass scales in comparison to HERA [199, 200, 201] and the large targeted luminosity will enable electroweak measurements in ep scattering with higher precision than ever before.

4.3.1 Electroweak effects in inclusive NC and CC DIS cross sections

Electroweak NC interactions in inclusive $e^{\pm}p$ DIS are mediated by exchange of a virtual photon (γ) or a Z boson in the t-channel, while CC DIS is mediated exclusively by W-boson exchange as a purely *weak* process. Inclusive NC DIS cross sections are expressed in terms of generalised structure functions $\tilde{F}_2^{\pm}$, $x\tilde{F}_3^{\pm}$ and $\tilde{F}_{\mathrm{L}}^{\pm}$ at EW leading order (LO) as

$$\frac{d^2\sigma^{\mathrm{NC}}(e^{\pm}p)}{dxdQ^2} = \frac{2\pi\alpha^2}{xQ^4}\left[Y_+\tilde{F}_2^{\pm}(x,Q^2) \mp Y_- x\tilde{F}_3^{\pm}(x,Q^2) - y^2\tilde{F}_{\mathrm{L}}^{\pm}(x,Q^2)\right] ,$$

where α denotes the fine structure constant. The terms $Y_{\pm} = 1 \pm (1-y)^2$, with $y = Q^2/sx$, describe the helicity dependence of the process. The generalised structure functions are separated into contributions from pure γ- and Z-exchange and their interference [31, 202]:

$$\begin{aligned}
\tilde{F}_2^{\pm} &= F_2 - (g_V^e \pm P_e g_A^e)\varkappa_Z F_2^{\gamma Z} + [(g_V^e g_V^e + g_A^e g_A^e) \pm 2P_e g_V^e g_A^e]\,\varkappa_Z^2 F_2^Z ,\\
\tilde{F}_3^{\pm} &= \ -(g_A^e \pm P_e g_V^e)\varkappa_Z F_3^{\gamma Z} + [2g_V^e g_A^e \pm P_e(g_V^e g_V^e + g_A^e g_A^e)]\,\varkappa_Z^2 F_3^Z .
\end{aligned} \tag{4.14}$$

Similar expressions hold for $\tilde{F}_L$. In the naive quark-parton model, which corresponds to the LO QCD approximation, the structure functions are calculated as

$$\begin{aligned}
\left[F_2, F_2^{\gamma Z}, F_2^Z\right] &= x\sum_q \left[Q_q^2, 2Q_q g_V^q, g_V^q g_V^q + g_A^q g_A^q\right]\{q+\bar{q}\} ,\\
x\left[F_3^{\gamma Z}, F_3^Z\right] &= x\sum_q \left[2Q_q g_A^q, 2g_V^q g_A^q\right]\{q-\bar{q}\} ,
\end{aligned}$$

representing two independent combinations of the quark and anti-quark momentum distributions, xq and $x\bar{q}$. In Eq. (4.14), the quantities g_V^f and g_A^f stand for the vector and axial-vector couplings of a fermion ($f = e$ or $f = q$ for electron or quark) to the Z boson, and the coefficient $\varkappa_Z$ accounts for the Z-boson propagator including the normalisation of the weak couplings. Both parameters are fully calculable from the electroweak theory. The (effective) coupling parameters depend on the electric charge, Q_f and the third component of the weak-isospin, $I_{\mathrm{L},f}^3$. Using $\sin^2\theta_{\mathrm{W}} = 1 - \frac{M_{\mathrm{W}}^2}{M_{\mathrm{Z}}^2}$, one can write

$$\begin{aligned}
g_V^f &= \sqrt{\rho_{\mathrm{NC},f}}\left(I_{\mathrm{L},f}^3 - 2Q_f\kappa_{\mathrm{NC},f}\,\sin^2\theta_{\mathrm{W}}\right) , \ \text{and}\\
g_A^f &= \sqrt{\rho_{\mathrm{NC},f}}\, I_{\mathrm{L},f}^3 \qquad\qquad\qquad\qquad \text{with } f = (e,u,d) .
\end{aligned} \tag{4.15}$$

The parameters $\rho_{\mathrm{NC},f}$ and $\kappa_{\mathrm{NC},f}$ are calculated as real parts of complex form factors which include the higher-order loop corrections [203, 204, 205]. They contain non-leading flavour-specific components.

Predictions for CC DIS are written in terms of the CC structure functions W_2, xW_3 and W_L and higher-order electroweak effects are collected in two form factors $\rho_{\mathrm{CC},eq}$ and $\rho_{\mathrm{CC},e\bar{q}}$ [206, 207].

In this study, the on-shell scheme is adopted for the calculation of higher-order corrections. This means that the independent parameters are chosen as the fine structure constant α and the masses of the weak bosons, the Higgs boson and the fermions. The weak mixing angle is then fixed and G_{F} is a prediction, whose higher-order corrections are included in the well-known correction factor Δr [208, 209, 210] (see discussion of further contributions in Ref. [31]).

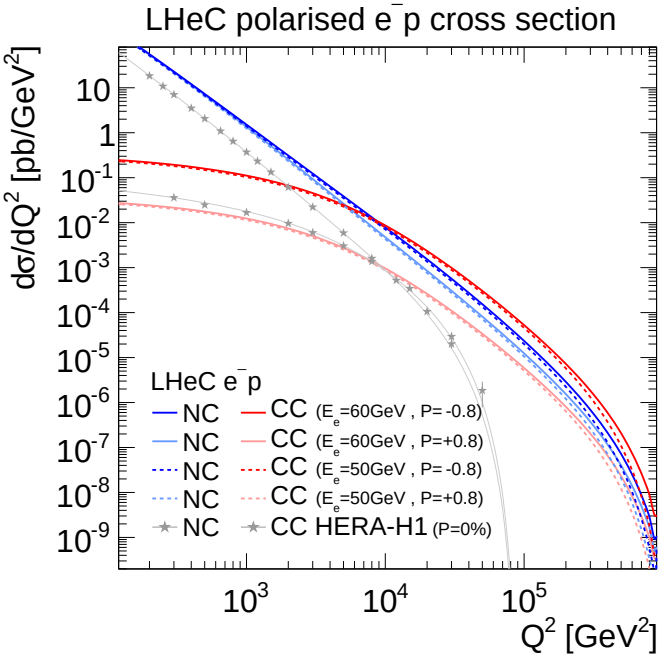

Figure 4.49: Single differential cross sections for polarised e^-p NC and CC DIS at LHeC for two different electron beam energies (E_e). Cross sections for longitudinal electron beam polarisations of $P_e = -0.8$ and $+0.8$ are displayed. For comparison also measurements at center-of-mass energies of $\sqrt{s} = 920\,\mathrm{GeV}$ by H1 at HERA for unpolarised ($P = 0\,\%$) electron beams are displayed [211].

The predicted single-differential inclusive NC and CC DIS cross sections for polarised e^-p scattering as a function of Q^2 are displayed in Fig. 4.49. For NC DIS and at higher Q^2, electroweak effects are important through γZ interference and pure Z-exchange terms and the polarisation of the LHeC electron beam of $P_e = \pm 0.8$ will considerably alter the cross sections. For CC DIS, the cross section scales linearly with P_e. Two different electron beam energies are displayed in Fig. 4.49, and albeit the impact of a reduction from $E_e = 60$ to $E_e = 50\,\mathrm{GeV}$ appears to be small, a significantly increased electron beam energy would yield higher precision for the measurement of electroweak parameters, since these are predominantly sensitive to the cross sections at highest scales, as will be shown in the following.

4.3.2 Methodology of a combined EW and QCD fit

A complete electroweak analysis of DIS data has to consider PDFs together with electroweak parameters [212]. In this study, the uncertainties of electroweak parameters are obtained in a combined fit of electroweak parameters and the PDFs, and the inclusive NC and CC DIS pseudo-data (see sect. **??**) are explored as input data. The PDFs are parameterised with 13 parameters at a starting scale Q_0^2 and NNLO DGLAP evolution is applied [213, 214]. In this way, uncertainties from the PDFs are taken into account, which is very reasonable, since the PDFs will predominantly be determined from those LHeC data in the

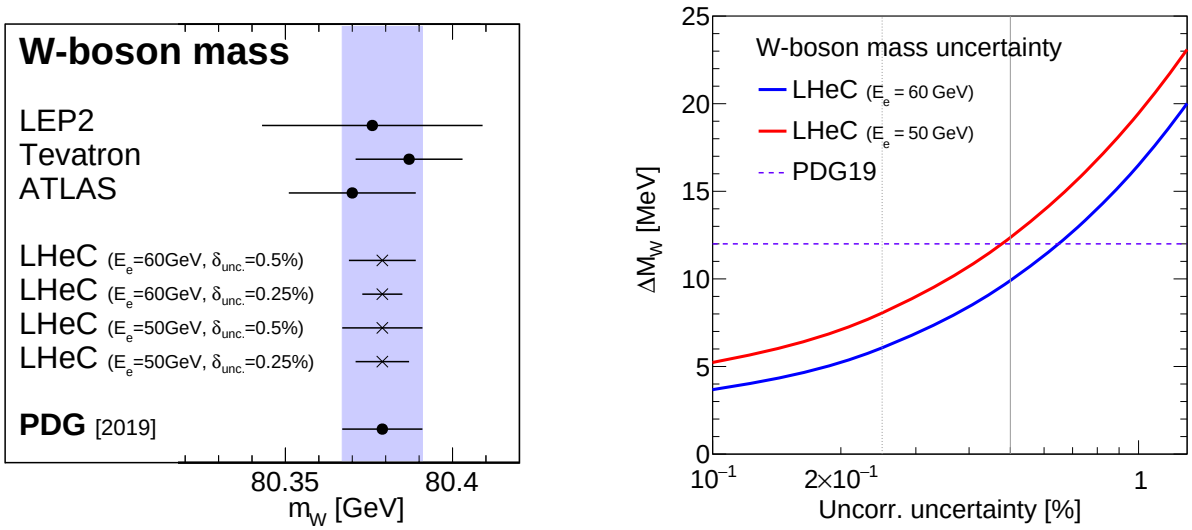

Figure 4.50: Left: Measurements of the W-boson mass assuming fixed values for the top-quark and Z-boson masses at the LHeC for different scenarios in comparison with today's measurements [218, 219, 220] and the world average value (PDG19) [221]. For LHeC, prospects for $E_e = 60\,\text{GeV}$ and $50\,\text{GeV}$ are displayed, as well as results for the two scenarios with 0.5 % or 0.25 % uncorrelated uncertainty (see text). Right: Comparison of the precision for M_W for different assumptions of the uncorrelated uncertainty of the pseudo-data. The uncertainty of the world average value is displayed as horizontal line. The nominal (and alternative) size of the uncorrelated uncertainty of the inclusive NC/CC DIS pseudo-data is indicated by the vertical line (see text),

future. The details of the PDF fit are altogether fairly similar to the PDF fits outlined in sect. **??**. Noteworthy differences are that additionally EW effects are included into the calculation by considering the full set of 1-loop electroweak corrections [215], and the χ^2 quantity [216], which is input to the minimisation and error propagation, is based on normal-distributed relative uncertainties. In this way, a dependence on the actual size of the simulated cross sections is avoided. The size of the pseudo-data are therefore set equivalent to the predictions [217].

4.3.3 Weak boson masses M_W and M_Z

The expected uncertainties for a determination of the weak boson masses, M_W and M_Z, are determined in the PDF+EW-fit, where one of the masses is determined together with the PDFs, while the other mass parameter is taken as external input. The expected uncertainties for M_W are

$$\Delta M_\text{W}(\text{LHeC-60}) = \pm 5_{(\text{exp})} \pm 8_{(\text{PDF})}\,\text{MeV} = 10_{(\text{tot})}\,\text{MeV} \quad \text{and}$$
$$\Delta M_\text{W}(\text{LHeC-50}) = \pm 8_{(\text{exp})} \pm 9_{(\text{PDF})}\,\text{MeV} = 12_{(\text{tot})}\,\text{MeV}$$

for LHeC with $E_e = 60\,\text{GeV}$ or $50\,\text{GeV}$, respectively. The breakdown into experimental and PDF uncertainties is obtained by repeating the fit with PDF parameters fixed. These uncertainties are displayed in Fig. 4.50 and compared to the values obtained by LEP2 [219], Tevatron [218], ATLAS [220] and the PDG value [221]. The LHeC measurement will become the most precise measurement from one single experiment and will greatly improve over the best measurement achieved by H1, which was $M_\text{W}(\text{H1}) = 80.520 \pm 0.115\,\text{GeV}$ [201]. If the dominating uncorrelated uncertainties can be reduced from the prospected 0.5 % to 0.25 %[5], a precision

[5]Due to performance reasons, the pseudo-data are generated for a rather coarse grid. With a binning which is closely related to the resolution of the LHeC detector, much finer grids in x and Q^2 are feasible. Already such a change would alter the uncertainties of the fit parameters. However, such an effect can be reflected by a changed uncorrelated uncertainty, and a value of 0.25 % appears like an optimistic, but achievable, alternative scenario.

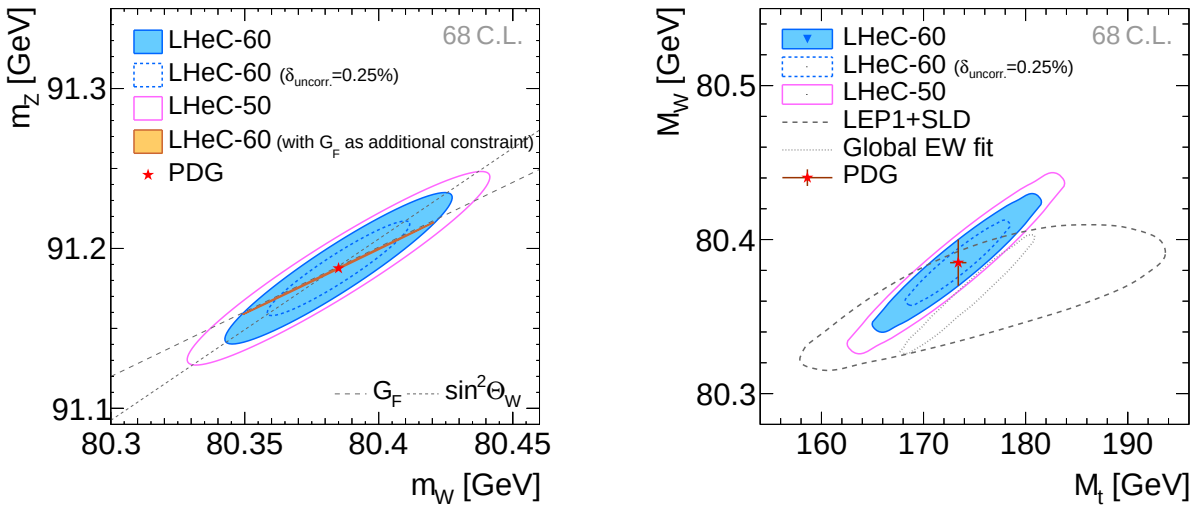

Figure 4.51: Simultaneous determination of the top-quark mass M_t and W-boson mass M_{W} from LHeC-60 or LHeC-50 data (left). Simultaneous determination of the W-boson and Z-boson masses from LHeC-60 or LHeC-50 data (right).

for M_{W} of up to

$$\Delta M_{\mathrm{W}}(\text{LHeC-60}) = \pm 3_{(\mathrm{exp})} \pm 5_{(\mathrm{PDF})}\,\mathrm{MeV} = 6_{(\mathrm{tot})}\,\mathrm{MeV} \quad \text{and}$$
$$\Delta M_{\mathrm{W}}(\text{LHeC-50}) = \pm 6_{(\mathrm{exp})} \pm 6_{(\mathrm{PDF})}\,\mathrm{MeV} = 8_{(\mathrm{tot})}\,\mathrm{MeV}$$

for LHeC-60 and LHeC-50 may be achieved, respectively. A complete dependence of the expected total experimental uncertainty ΔM_{W} on the size of the uncorrelated uncertainty component is displayed in Fig. 4.50, and with a more optimistic scenario an uncertainty of up to $\Delta M_{\mathrm{W}} \approx 5\,\mathrm{MeV}$ can be achieved. In view of such a high accuracy, it will be important to study carefully theoretical uncertainties. For instance the parametric uncertainty due to the dependence on the top-quark mass of 0.5 GeV will yield an additional error of $\Delta M_{\mathrm{W}} = 2.5\,\mathrm{MeV}$. Also higher-order corrections, at least the dominating 2-loop corrections will have to be studied and kept under control. Then, the prospected determination of the W-boson mass from LHeC data will be among the most precise determinations and significantly improve the world average value of M_{W}. It will also become competitive with its prediction from global EW fits with present uncertainties of about $\Delta M_{\mathrm{W}} = 7\,\mathrm{MeV}$ [221, 222, 223].

While the determination of M_{W} from LHeC data is competitive with other measurements, the experimental uncertainties of a demetermination of M_{Z} are estimated to ba about 11 MeV and 13 MeV for LHeC-60 and LHeC-50, respectively. Therefore, the precision of M_{Z} cannot compete with the precise measurements at the Z-pole by LEP+SLD and future e^+e^- colliders may even improve on that.

A simultaneous determination of M_{W} and M_{Z} is displayed in Fig. 4.51 (left). Although the precision of these two mass parameters is only moderate, a meaningful test of the high-energy behaviour of electroweak theory is obtained by using G_F as additional input: The high precision of the G_F measurement [224] yields a very shallow error ellipse and a precise test of the SM can be performed with only NC and CC DIS cross sections alone. Such a fit determines and simultaneously tests the high-energy behaviour of electroweak theory, while using only low-energy parameters α and G_F as input (plus values for masses like M_t and M_H needed for loop corrections).

4.3.4 Further mass determinations

Inclusive DIS data are sensitive to the top-quark mass M_t indirectly through radiative corrections. M_t-dependent terms are dominantly due to corrections from the gauge boson self-energy corrections. They are contained in the ρ and κ parameters and in the correction factor Δr. The leading contributions are proportional to M_t^2. This allows for an indirect determination of the top-quark mass using LHeC inclusive DIS data, and a determination of M_t will yield an uncertainty of $\Delta M_t = 1.8\,\text{GeV}$ to $2.2\,\text{GeV}$. Assuming an uncorrelated uncertainty of the DIS data of 0.25 % the uncertainty of M_t becomes as small as

$$\Delta M_t = 1.1 \;\text{ to }\; 1.4\,\text{GeV}$$

for 60 and 50 GeV electron beams, respectively. This would represent a very precise indirect determination of the top-quark mass from purely electroweak corrections and thus being fully complementary to measurements based on real t-quark production, which often suffer from sizeable QCD corrections. The precision achievable this way will be competitive with indirect determinations from global EW fits after the HL-LHC [225].

More generally, and to some extent depending on the choice of the renormalisation scheme, the leading self-energy corrections are proportional to $\frac{M_t^2}{M_\text{W}^2}$ and thus a simultaneous determination of M_t and M_W is desirable. The prospects for a simultaneous determination of M_t and M_W is displayed in Fig. 4.51 (right). It is remarkable that the precision of the LHeC is superior to that of the LEP+SLD combination [226]. In an optimistic scenario an uncertainty similar to the global electroweak fit [223] can be achieved. In a fit without PDF parameters similar uncertainties are found (not shown), which illustrates that the determination of EW parameters is to a large extent independent of the QCD phenomenology and the PDFs.

The subleading contributions to self-energy corrections have a Higgs-boson mass dependence and are proportional to $\log \frac{M_H^2}{M_\text{W}^2}$. When fixing all other EW parameters the Higgs boson mass could be constrained indirectly through these loop corrections with an experimental uncertainty of $\Delta m_H = ^{+29}_{-23}$ to $^{+24}_{-20}\,\text{GeV}$ for different LHeC scenarios, which is again similar to the indirect constraints from a global electroweak fit [223].

4.3.5 Weak Neutral Current Couplings

The vector and axial-vector couplings of up-type and down-type quarks to the Z, g_V^q and g_A^q, see Eq. (4.15), are determined in a fit of the four coupling parameters together with the PDFs.

Coupling parameter	PDG	Expected uncertainties		
		LHeC-60	LHeC-60 ($\delta_\text{uncor.} = 0.25\,\%$)	LHeC-50
g_A^u	$0.50\ ^{+0.04}_{-0.05}$	0.0022	0.0015	0.0035
g_A^d	$-0.514\ ^{+0.050}_{-0.029}$	0.0055	0.0034	0.0083
g_V^u	$0.18\ \pm 0.05$	0.0015	0.0010	0.0028
g_V^d	$-0.35\ ^{+0.05}_{-0.06}$	0.0046	0.0027	0.0067

Table 4.2: Light-quark weak NC couplings (g_A^u,g_A^d,g_V^u,g_V^d) and their currently most precise values from the PDG [221] compared with the prospected uncertainties for different LHeC scenarios. The LHeC prospects are obtained in a simultaneous fit of the PDF parameters and all four coupling parameters determined at a time.

The resulting uncertainties are collected in Table 4.2. The two-dimensional uncertainty contours at 68 % confidence level obtained from LHeC data with $E_e = 50\,\text{GeV}$ are displayed in Fig. 4.52 for the two quark families and compared with available measurements. While all the current determinations from e^+e^-, ep or $p\bar{p}$ data have a similar precision, the future LHeC data will greatly improve the precision of the weak

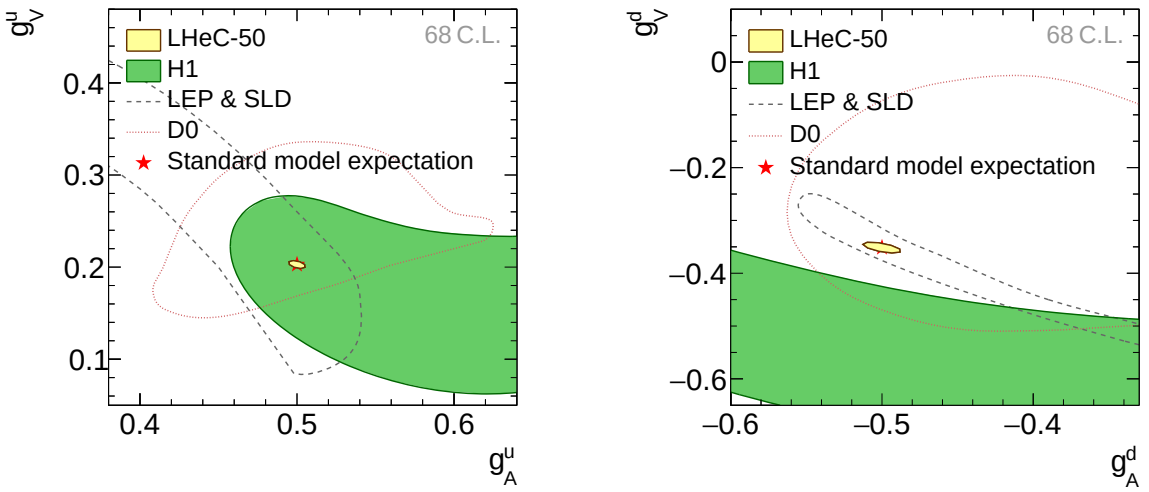

Figure 4.52: Weak NC vector and axial-vector couplings of u-type (left) and d-type quarks (right) at 68 % confidence level (C.L.) for simulated LHeC data with $E_e = 50\,\text{GeV}$. The LHeC expectation is compared with results from the combined LEP+SLD experiments [226], a single measurement from D0 [227] and one from H1 [201]. The standard model expectations are diplayed by a red star.

neutral-current couplings and expected uncertainties are an order of magnitude smaller than the currently most precise ones [221]. An increased electron beam energy of $E_e = 60\,\text{GeV}$ or improved experimental uncertainties would further improve this measurement.

The determination of the couplings of the electron to the Z boson, g_V^e and g_A^e, can be determined at the LHeC with uncertainties of up to $\Delta g_V^e = 0.0013$ and $\Delta g_A^e = \pm 0.0009$, which is similar to the results of a single LEP experiment and about a factor three larger than the LEP+SLD combination [226].

4.3.6 The neutral-current ρ_{NC} and κ_{NC} parameters

Beyond Born approximation, the weak couplings are subject to higher-order loop corrections. These corrections are commonly parameterised by quantities called ρ_{NC}, κ_{NC} and ρ_{CC}. They are sensitive to contributions beyond the SM and the structure of the Higgs sector. It is important to keep in mind that these effective coupling parameters depend on the momentum transfer and are, indeed, form factors, rather than constants. It is particularly interesting to investigate the so-called effective weak mixing angle defined as $\sin^2\theta_{\text{W}}^{\text{eff}} = \kappa_{\text{NC}}\sin^2\theta_{\text{W}}$. At the Z-pole it is well accessible through asymmetry measurements in e^+e^- collisions. In DIS at the LHeC, the scale dependence of the effective weak mixing angle is not negligible. It can be determined only together with the ρ parameter due to the Q^2 dependence and the presence of the photon exchange terms. Therefore, we introduce (multiplicative) anomalous contributions to these factors, denoted as $\rho'_{\text{NC,CC}}$ and κ'_{NC}, and test their agreement with unity (for more details see Ref. [201]), and uncertainties of these parameters are obtained in a fit together with the PDFs. The two-dimensional uncertainty contours of the anomalous form factors $\rho'_{\text{NC},f}$ and $\kappa'_{\text{NC},f}$ are displayed for three different LHeC scenarios in Fig. 4.53 (left), and compared with uncertainties from the LEP+SLD combination[6] [226]. It is found that these parameters can be determined with very high experimental precision.

Assuming the couplings of the electron are given by the SM, the anomalous form factors for the two quark families can be determined and results are displayed in Fig. 4.53 (right). Since these measurements represent

[6]Since in the LEP+SLD analysis the values of ρ_{NC} and $\kappa_{\text{NC}}\sin^2\theta_{\text{W}}$ are determined, we compare only the size of the uncertainties in these figures. Furthermore it shall be noted, that LEP is mainly sensitive to the parameters of leptons or heavy quarks, while LHeC data is more sensitive to light quarks (u,d,s), and thus the LHeC measurements are highly complementary.

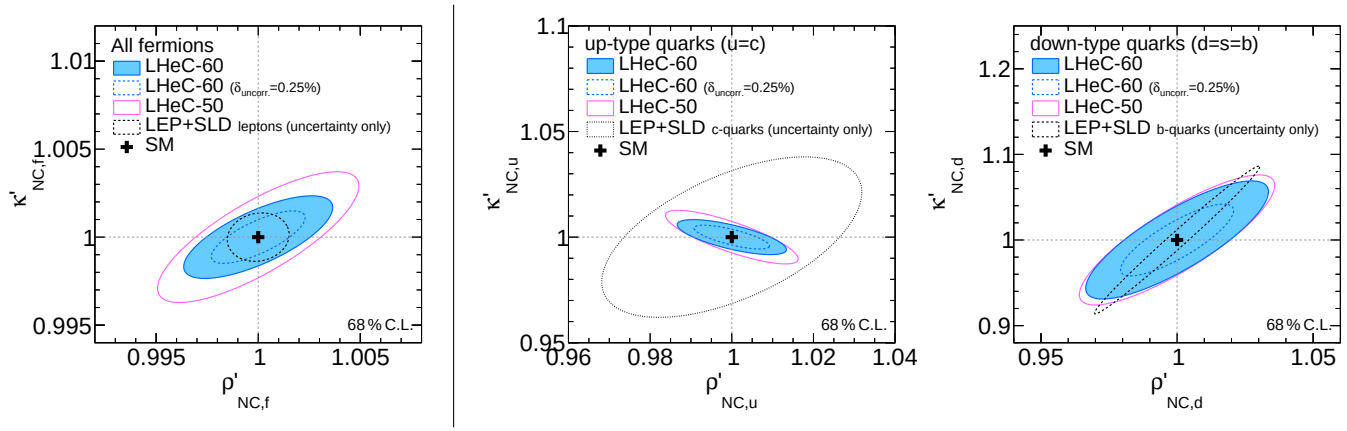

Figure 4.53: Expectations at 68 % confidence level for the determination of the $\rho'_{\rm NC}$ and $\kappa'_{\rm NC}$ parameters assuming a single anomalous factor equal for all fermions (left). The results for three different LHeC scenarios are compared with the achieved uncertainties from the LEP+SLD combination [226] for the determination the respective leptonic quantities. Right: uncertainties for the simultaneous determination of the anomalous form factors for u and d-type quarks, assuming known values for the electron parameters. The values are compared with uncertainties reported by LEP+SLD for the determination of the values $\rho_{{\rm NC},(c,b)}$ and $\sin\theta_{\rm W}^{{\rm eff},(c,b)}$ for charm or bottom quarks, respectively.

unique determinations of parameters sensitive to the light-quark couplings, we can compare only with nowadays measurements of the parameters for heavy-quarks of the same charge and it is found that the LHeC will provide high-precision determinations of the $\rho'_{\rm NC}$ and $\kappa'_{\rm NC}$ parameters.

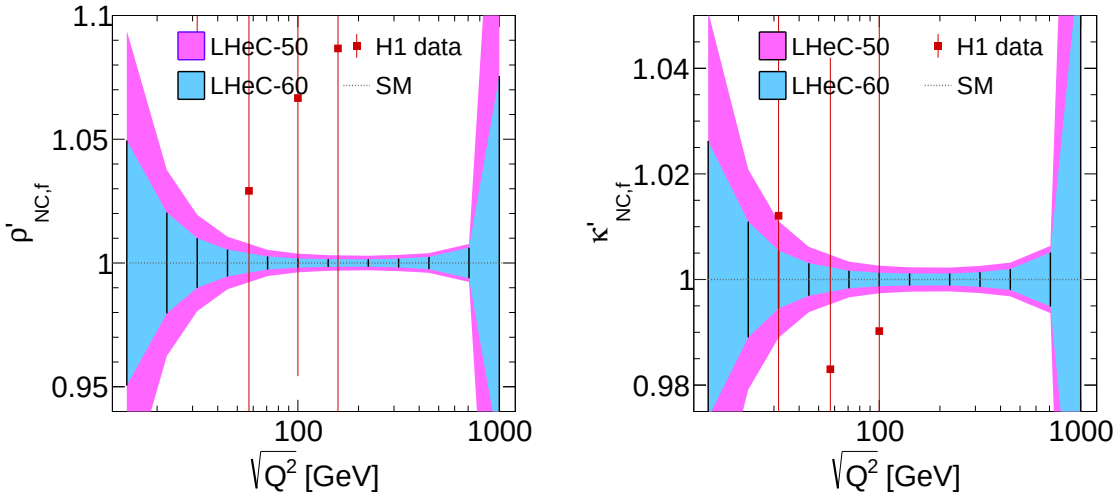

Figure 4.54: Test of the scale dependence of the anomalous ρ and κ parameters for two different LHeC scenarios. For the case of LHeC-60, i.e. $E_e = 60\,\text{GeV}$, we assume an uncorrelated uncertainty of 0.25 %. The uncertainties of the parameter $\kappa'_{\rm NC,f}$ can be interpreted as sensitivity to the scale-dependence of the weak mixing angle, $\sin\theta_{\rm W}^{\rm eff}(\mu)$.

A meaningful test of the SM can be performed by determining the effective coupling parameters as a function of the momentum transfer. In case of $\kappa'_{\rm NC}$, this is equivalent to measuring the running of the effective weak mixing angle, $\sin\theta_{\rm W}^{\rm eff}(\mu)$ (see also sect. 4.3.7). However, DIS is quite complementary to other measurements since the process is mediated by space-like momentum transfer, i.e. $q^2 = -Q^2 < 0$ with q being the boson four-momentum. Prospects for a determination of $\rho'_{\rm NC}$ or $\kappa'_{\rm NC}$ at different Q^2 values are displayed in Fig. 4.54 and compared to results obtaind by H1. The value of $\kappa'_{\rm NC}(\mu)$ can be easily translated to a measurement of

$\sin\theta_{\rm W}^{\rm eff}(\mu)$. From Fig. 4.54 one can conclude that this quantity can be determind with a precision of up to 0.1 % and better than 1 % over a wide kinematic range of about $25 < \sqrt{Q^2} < 700\,\text{GeV}$.

4.3.7 The effective weak mixing angle $\sin^2\theta_{\rm W}^{\rm eff,\ell}$

The leptonic effective weak mixing angle is defined as $\sin^2\theta_{\rm W}^{\rm eff,\ell}(\mu^2) = \kappa_{{\rm NC},\ell}(\mu^2)\sin^2\theta_{\rm W}$. Due to its high sensitivity to loop corrections it represents an ideal quantity for precision tests of the Standard Model. Its value is scheme dependent and it exhibits a scale dependence. Near the Z pole, $\mu^2 = M_{\rm Z}^2$, its value was precisely measured at LEP and at SLD. Those analyses were based on the measurement of asymmetries and their interpretation in terms of the leptonic weak mixing angle was simplified by the fact that many non-leptonic corrections and contributions from box graphs cancel or can be taken into account by subtracting their SM predictions. The highest sensitivity to $\sin^2\theta_{\rm W}^{\rm eff,\ell}(M_Z)$ to date arises from a measurement of $A_{\rm fb}^{0,b}$ [226], where the non-universal flavour-specific corrections to the quark couplings are taken from the SM and consequently these measurements are interpreted to be sensitive only to the universal, i.e. flavour-independent[7], non-SM contributions to $\kappa_{\rm NC}$. Applying this assumption also to the DIS cross sections, the determination of $\kappa'_{{\rm NC},f}$ can directly be interpreted as a sensitivity study of the leptonic effective weak mixing angle $\sin^2\theta_{\rm W}^{\rm eff,\ell}$.

Fit parameters	Parameter of interest	SM value	Expected uncertainties			
			LHeC-50	LHeC-60	LHeC-50	LHeC-60
			($\delta_{\rm uncor.} = 0.50\,\%$)		($\delta_{\rm uncor.} = 0.25\,\%$)	
$\kappa'_{{\rm NC},f}$, PDFs	$\sin^2\theta_{\rm W}^{\rm eff,\ell}(M_{\rm Z}^2)$	0.23154	0.00033	0.00025	0.00022	0.00015
$\kappa'_{{\rm NC},f}$, $\rho'_{{\rm NC},f}$, PDFs	$\sin^2\theta_{\rm W}^{\rm eff,\ell}(M_{\rm Z}^2)$	0.23154	0.00071	0.00036	0.00056	0.00023
$\kappa'_{{\rm NC},e}$, PDFs	$\sin^2\theta_{\rm W}^{\rm eff,e}(M_{\rm Z}^2)$	0.23154	0.00059	0.00047	0.00038	0.00028
$\kappa'_{{\rm NC},e}$, $\kappa'_{{\rm NC},u}$, $\kappa'_{{\rm NC},d}$, PDFs	$\sin^2\theta_{\rm W}^{\rm eff,e}(M_{\rm Z}^2)$	0.23154	0.00111	0.00095	0.00069	0.00056
$\kappa'_{{\rm NC},f}$	$\sin^2\theta_{\rm W}^{\rm eff,\ell}(M_{\rm Z}^2)$	0.23154	0.00028	0.00023	0.00017	0.00014

Table 4.3: Determination of $\sin^2\theta_{\rm W}^{\rm eff,\ell}(M_{\rm Z}^2)$ with inclusive DIS data at the LHeC for different scenarios. Since the value of the effective weak mixing angle at the Z pole cannot be determined directly in DIS, a fit of the $\kappa'_{{\rm NC},f}$ parameter is performed instead and its uncertainty is translated to $\sin^2\theta_{\rm W}^{\rm eff,\ell}(M_{\rm Z}^2)$. Different assumptions on the fit parameters are studied, and results include uncertainties from the PDFs. Only the last line shows results where the PDF parameters are kept fixed. See text for more details.

The prospects for a determination of $\sin^2\theta_{\rm W}^{\rm eff,\ell}$ are listed in Table 4.3. Two fits have been studied: one with a fixed parameter $\rho'_{\rm NC}$ and one where $\sin^2\theta_{\rm W}^{\rm eff,\ell}$ is determined together with $\rho'_{\rm NC}$ (see Fig. 4.53 (left)). At the LHeC, it will be possible to determine the value of $\sin^2\theta_{\rm W}^{\rm eff,\ell}(M_{\rm Z}^2)$ with an experimental uncertainty of up to

$$\Delta\sin^2\theta_{\rm W}^{\rm eff,\ell} = \pm 0.00015\,,$$

where PDF uncertainties are already included. If the PDF parameters are artificially kept fixed, the uncertainties are of very similar size, which demonstrates that these measurements are fairly insensitive to the QCD effects and the PDFs. The uncertainties are compared[8] to recent average values in Fig. 4.55. One can see that the LHeC measurement has the potential to become the most precise single measurement in the future with a significant impact to the world average value. It is obvious that a conclusive interpretation of

[7] Flavour-specific tests have been discussed to some extent in the previous section.

[8] It shall be noted, that in order to compare the LHeC measurements with the Z-pole measurements at $\mu^2 = M_{\rm Z}^2$ in a conclusive way, one has to assume the validity of the SM framework. In particular the scale-dependence of $\kappa_{{\rm NC},\ell}$ must be known in addition to the flavour-specific corrections. On the other hand, the scale dependence can be tested itself with the LHeC data which cover a large range of space-like Q^2. In this aspect, DIS provides a unique opportunity for precision measurements in the space-like regime ($\mu^2 < 0$) as has been discussed in the previous section, see Fig. 4.54 (right).

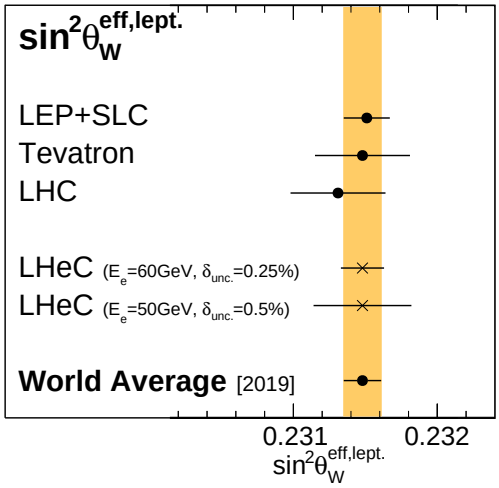

Figure 4.55: Comparison of the determination of $\sin^2\theta_{\mathrm{W}}^{\mathrm{eff},\ell}(M_Z^2)$ from LHeC inclusive DIS data with recent averaged values. Results from LEP+SLC [226], Tevatron [228], LHC [229, 230, 231, 232] and the world average value [232] are all obtained from a combination of various separate measurements (not shown individually) (see also Ref. [233] for additional discussion). For LHeC, the experimental and PDF uncertainties are displayed.

experimental results with such a high precision will require correspondingly precise theoretical predictions, and the investigation of two-loop corrections for DIS will become important.

This LHeC measurement will become competitive with measurements at the HL-LHC [30]. Since in pp collisions one of the dominant uncertainty is from the PDFs, future improvements can (only) be achieved with a common analysis of LHeC and HL-LHC data. Such a study will yield highest experimental precision and the challenging theoretical and experimental aspects for a complete understanding of such an analysis will deepen our understanding of the electroweak sector.

It may be further of interest, to determine the value of the effective weak mixing angle of the electron separately in order to compare with measurements in pp and test furthermore lepton-specific contributions to $\kappa_{\mathrm{NC,lept.}}$. Such fits are summarised in Table 4.3 and a reasonable precision is achieved with LHeC.

4.3.8 Electroweak effects in charged-current scattering

The charged-current sector of the SM can be uniquely measured at high scales over many orders of magnitude in Q^2 at the LHeC, due to the excellent tracking detectors, calorimetry, and high-bandwidth triggers. Similarly as in the NC case, the form factors of the effective couplings of the fermions to the W boson can be measured. In the SM formalism, only two of these form factors are present, $\rho_{\mathrm{CC},eq}$ and $\rho_{\mathrm{CC},e\bar{q}}$. We thus introduce two anomalous modifications to them, $\rho_{\mathrm{CC},(eq/e\bar{q})} \rightarrow \rho'_{\mathrm{CC},(eq/e\bar{q})}\rho_{\mathrm{CC},(eq/e\bar{q})}$ (see Ref. [201]). The prospects for the determination of these parameters are displayed in Fig. 4.56, and it is found, that with the LHeC these parameters can be determined with a precision up to 0.2–0.3 %. Also their Q^2 dependence can be uniquely studied with high precision up to $\sqrt{Q^2}$ values of about 400 GeV.

4.3.9 Direct W and Z production and Anomalous Triple Gauge Couplings [Ruibo Li, Tao Xu]

The triple gauge boson vertex can be precisely measured in gauge boson production processes through Vector Boson Fusion (VBF) at the LHeC. The measurement is sensitive to new physics contributions in anomalous

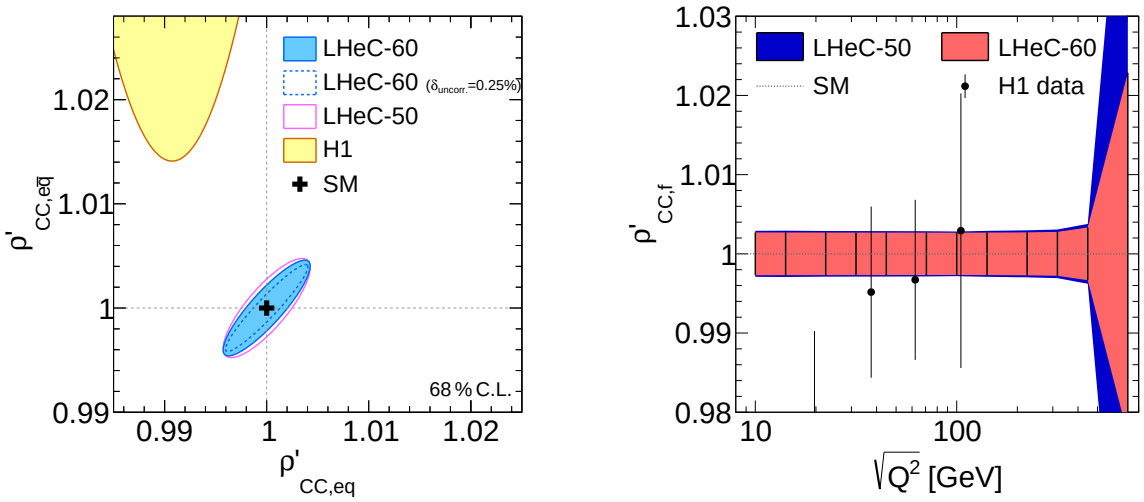

Figure 4.56: Left: anomalous modifications of the charged current form factors $\rho'_{\mathrm{CC},eq}$ and $\rho'_{\mathrm{CC},e\bar{q}}$ for different LHeC scenarios in comparison with the H1 measurement [201]. Right: scale dependent measurement of the anomalous modification of the charged current form factor $\rho'_{\mathrm{CC}}(Q^2)$, assuming $\rho'_{\mathrm{CC},eq} = \rho'_{\mathrm{CC},e\bar{q}} = \rho'_{\mathrm{CC}}$.

Tripe Gauge Couplings (aTGC). The LHeC has advantages of a higher center of mass energy and easier kinematic analysis in the measurement of aTGCs.

In the effective field theory language, aTGCs in the Lagrangian are generally parametrized as

$$\begin{aligned}\mathcal{L}_{TGC}/g_{WWV} &= ig_{1,V}(W^+_{\mu\nu}W^-_{\mu}V_{\nu} - W^-_{\mu\nu}W^+_{\mu}V_{\nu}) + i\kappa_V W^+_{\mu}W^-_{\nu}V_{\mu\nu} + \frac{i\lambda_V}{M_W^2}W^+_{\mu\nu}W^-_{\nu\rho}V_{\rho\mu} \\ &+ g_5^V\epsilon_{\mu\nu\rho\sigma}(W^+_{\mu}\overleftrightarrow{\partial}_{\rho}W^-_{\nu})V_{\sigma} - g_4^V W^+_{\mu}W^-_{\nu}(\partial_{\mu}V_{\nu} + \partial_{\nu}V_{\mu}) \\ &+ i\tilde{\kappa}_V W^+_{\mu}W^-_{\nu}\tilde{V}_{\mu\nu} + \frac{i\tilde{\lambda}_V}{M_W^2}W^+_{\lambda\mu}W^-_{\mu\nu}\tilde{V}_{\nu\lambda}, \end{aligned} \tag{4.16}$$

where $V = \gamma, Z$. The gauge couplings $g_{WW\gamma} = -e$, $g_{WWZ} = -e\cot\theta_W$ and the weak mixing angle θ_W are from the SM. $\tilde{V}_{\mu\nu}$ and $A\overleftrightarrow{\partial}_{\mu}B$ are defined as $\tilde{V}_{\mu\nu} = \frac{1}{2}\epsilon_{\mu\nu\rho\sigma}V_{\rho\sigma}$, $A\overleftrightarrow{\partial}_{\mu}B = A(\partial_{\mu}B) - (\partial_{\mu}A)B$, respectively. There are five aTGCs ($g_{1,Z}$, κ_V, and λ_V) conserving the C and CP condition with electromagnetic gauge symmetry requires $g_{1,\gamma} = 1$. Only three of them are independent because $\lambda_Z = \lambda_\gamma$ and $\Delta\kappa_Z = \Delta g_{1,Z} - \tan^2\theta_W\Delta\kappa_\gamma$ [234, 235, 236]. The LHeC can set future constrains on $\Delta\kappa_\gamma$ and λ_γ.

In the direct Z/γ production process, the anomalous WWZ and $WW\gamma$ couplings can be separately measured without being influenced by their interference [237, 238]. In the direct W production process, both the deviation in signal cross section and the kinematic distributions can effectively constrain the $WW\gamma$ aTGC, while anomalous WWZ contribution in this channel is insensitive as a result of the suppression from Z boson mass [239, 240, 241, 242, 243, 244].

The W decay into muon channel is the expected optimal measurement for the anomalous $WW\gamma$ coupling because of the discrimination of final states and mistagging efficiencies [242]. Fig. 4.57 shows the cross section of single W^+ production process followed by $W^+ \to \mu^+\nu_\mu$ decay, with different λ_γ and $\Delta\kappa_\gamma$ values. Large anomalous coupling leads to measurable deviation to the SM prediction. The cross section increases monotonically with $\Delta\kappa_\gamma$ and the absolute value of λ_γ within the region of $-1.0 \leq \lambda_\gamma/\Delta\kappa_\gamma \leq 1.0$.

Kinematic analysis is necessary for the precise aTGC measurement. At LHeC, the $e^-p \to e^-W^\pm j$ process with leptonic W boson decay can be fully reconstructed because the undetected neutrino information is reconstructed either with energy-momentum conservation or the recoil mass method. This allows angular

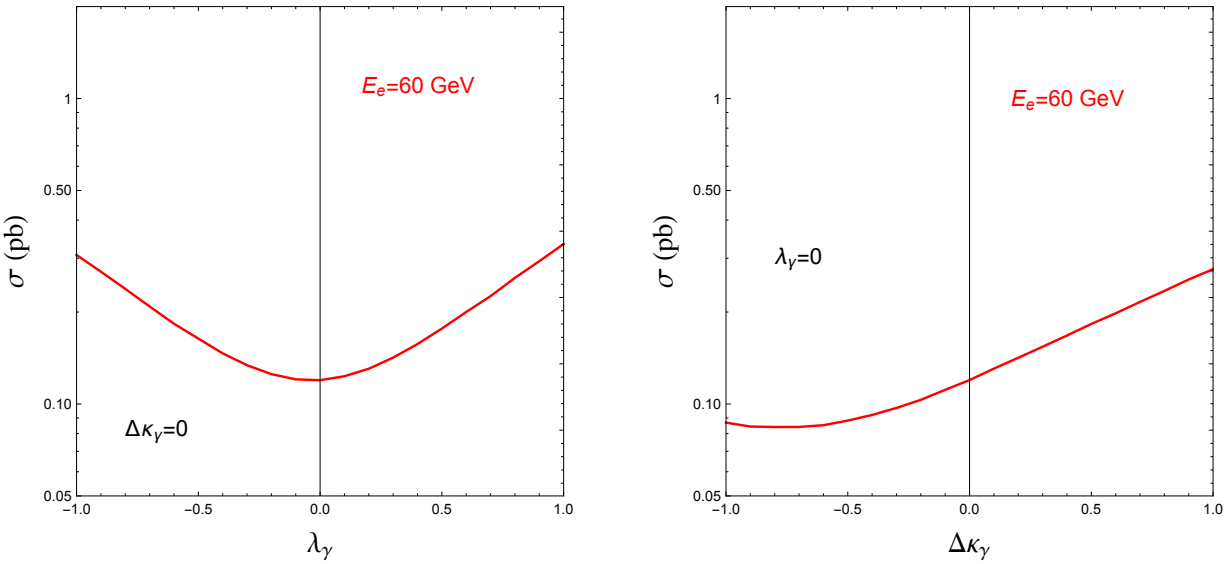

Figure 4.57: Total cross sections of the $e^-p \to e^-\mu^+\nu_\mu j$ process with varying λ_γ (left plot) and $\Delta\kappa_\gamma$ (right plot).

correlation observables sensitive to the W boson polarization to be used. Helicity amplitude calculation indicates λ_γ leads to a significant enhancement in the transverse polarization fraction of the W boson in the $e^-p \to e^-W^+j$ process, while $\Delta\kappa_\gamma$ leads to enhancement in the longitudinal component fraction [239]. The $\theta_{\ell W}$ angle is defined as the angle between the decay product lepton ℓ in the W rest frame and W moving direction in the collision rest frame. Making use of the energetic final states in the forward direction, a second useful angle $\Delta\phi_{ej}$ is defined as the separation of final state jet and electron on the azimuthal plane. In the optimized analysis with 1 ab^{-1} integrated luminosity, the $\Delta\phi_{ej}$ observable can impose stringent constraints on both λ_γ and $\Delta\kappa_\gamma$ to be within [-0.007, 0.0056] and [-0.0043, 0.0054] respectively. The $\cos\theta_{\mu W}$ observable is also sensitive to $\Delta\kappa_\gamma$ at the same order, but fails to constrain λ_γ. The analysis is detailed in [242].

Fig.4.58 shows the two-parameter aTGC constraint on the λ_γ–$\Delta\kappa_\gamma$ plane based on a χ^2 analysis of $\Delta\phi_{ej}$ with default $E_e = 60$ GeV at parton-level. Compare with the current LHC (blue and green) and LEP (red) bounds, the LHeC has significant improvement in constraining the $\Delta\kappa_\gamma$ parameter. The polarized electron beam is found to improve the aTGC measurement [238, 244]. In consideration of the "realistic" analysis at detector-level, one expects 2-3 ab^{-1} integrated luminosity to achieve same results. One uncertainty in the aTGC measurement comes from the PDF uncertainty. Future LHeC PDF measurement will improve the precision of aTGC measurement in the $x \simeq \mathcal{O}(10^{-2})$ region.

4.3.10 Conclusion

With LHeC inclusive NC and CC DIS data, unique measurements of electroweak parameters can be performed with highest precision. Since inclusive DIS is mediated through space-like momentum transfer (t-channel exchange) the results are often complementary to other experiments, such as pp or e^+e^- collider experiments, where measurements are performed in the time-like regime and most often at the Z peak. Among many other quantities, measurements of the weak couplings of the light quarks, u and d, or their anomalous form factors $\rho'_{\mathrm{NC},u/d}$ and $\kappa'_{\mathrm{NC},u/d}$, can be performed uniquely due to the important contributions of valence quarks in the initial state. Also scale dependent measurements of weak interactions can be performed over a large range in $\sqrt{Q^2}$, which provides an interesting portal to BSM physics. The W boson mass can be determined with very small experimental uncertainties, such that theoretical uncertainties are expected to become more important than experimental uncertainties. While the parameters of the PDFs are determined together with the EW parameters in the present study, it is found that the PDFs do not induce

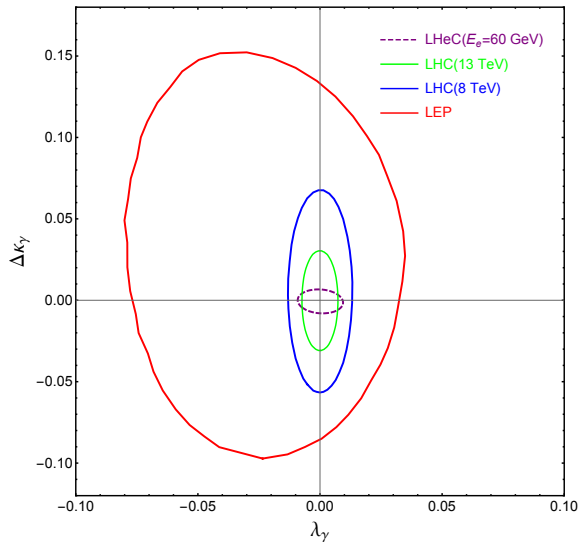

Figure 4.58: The 95% C.L. exclusion limit on the $\Delta\kappa_\gamma$-λ_γ plane. The purple dashed contour is the projected LHeC exclusion limit with 1 ab^{-1} integrated luminosity [242]. The blue, green and red contours are current bounds from LHC [245, 246] and LEP [247].

a limitation of the uncertainties. Considering the dominating top-quark mass dependence of higher-order electroweak effects, one can realize that the LHeC will be competitive with the global electroweak fit after the HL-LHC era [30, 225].

Besides proving its own remarkable prospect on high-precision electroweak physics, the LHeC will further significantly improve the electroweak measurements in pp collisions at the LHC by reducing the presently sizeable influence of PDF and α_s uncertainties. This is discussed in Sect. **??**.

4.4 Top Quark Physics [Christian Schwanenberger]

SM top quark production at a future ep collider is dominated by single top quark production, mainly via CC DIS production. An example graph is shown in Fig. 4.59 (left). The total cross section is 1.89 pb at the LHeC [248] and with an electron beam energy of 60 GeV, and an LHC proton beam of 7 TeV, leading to a center-of-mass energy of 1.3 TeV, respectively. The other important top quark production mode is $t\bar{t}$ photoproduction with a total cross section of 0.05 pb at the LHeC [249]. An example graph is shown in Fig. 4.59 (right). This makes a future LHeC a top quark factory and an ideal tool to study top quarks with a high precision, and to analyze in particular their electroweak interaction. Selected highlights in top quark physics are summarized here.

4.4.1 Wtq Couplings

One flagship measurement is the direct measurement of the CKM matrix element $|V_{tb}|$, i.e. without making any model assumptions such as on the unitarity of the CKM matrix or the number of quark generations. An elaborate analysis of the single top quark CC DIS process at the LHeC including a detailed detector simulation using the DELPHES package [250] shows that already at 100 fb^{-1} of integrated luminosity an uncertainty of 1% can be expected. This compares to a total uncertainty of 4.1% of the currently most accurate result at the LHC Run-I performed by the CMS experiment [251].

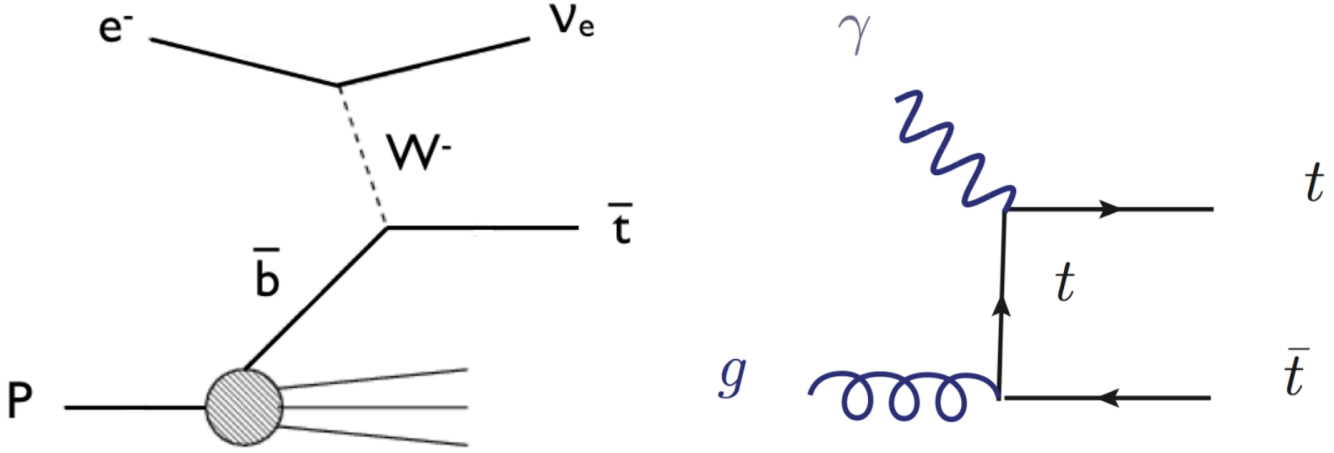

Figure 4.59: Example graphs for CC DIS top quark production (left) and top quark photoproduction (right).

The same analysis [248] can also be used to search for anomalous left- and right-handed Wtb vector and tensor couplings analyzing the following effective Lagrangian:

$$L = -\frac{g}{\sqrt{2}}\bar{b}\gamma^{\mu}V_{tb}(f_1^L P_L - f_1^R P_R)tW_{\mu}^{-} - \frac{g}{\sqrt{2}}\bar{b}\frac{i\sigma^{\mu\nu}q_{\nu}}{M_W}(f_2^L P_L - f_2^R P_R)tW_{\mu}^{-} + h.c.$$

In the SM $f_1^L = 1$ and $f_1^R = f_2^L = f_2^R = 0$. The effect of anomalous Wtb couplings is consistently evaluated in the production and the decay of the antitop quark, cf. Fig. 4.59 (left). Using hadronic top quark decays only, the expected accuracies in a measurement of these couplings as a function of the integrated luminosity are presented in Fig. 4.60 (upper left), derived from expected 95% C.L. limits on the cross section yields. The couplings can be measured with accuracies of 1% for the SM f_1^L coupling determining $|V_{tb}|$ (as discussed above) and of 4% for f_2^L, 9% for f_2^R, and 14% for f_1^R at 1 ab^{-1}.

Similarly, the CKM matrix elements $|V_{tx}|$ ($x = d, s$) can be extracted using a parameterization of deviations from their SM values with very high precision through W boson and bottom (light) quark associated production channels, where the W boson and b-jet (light jet $j = d, s$) final states can be produced via s-channel single top quark decay or t-channel top quark exchange as outlined in [252]. As an example, analyzing the processes

Signal 1: $pe^- \to \nu_e\bar{t} \to \nu_e W^-\bar{b} \to \nu_e\ell^-\nu_\ell\bar{b}$

Signal 2: $pe^- \to \nu_e W^- b \to \nu_e\ell^-\nu_\ell b$

Signal 3: $pe^- \to \nu_e\bar{t} \to \nu_e W^- j \to \nu_e\ell^-\nu_\ell j$

in an elaborate analysis including a detailed detector simulation using the DELPHES package [250], the expected accuracies on $|V_{td}|$ and $|V_{ts}|$ at the 2σ confidence level (C.L.) are shown as a function of the integrated luminosity in Fig. 4.60 (upper right, middle left). At 1 ab^{-1} of integrated luminosity and an electron polarization of 80%, the 2σ limits improve on existing limits from the LHC [253] (interpreted by [254]) by a factor of ≈ 3.5. Analyzing Signal 3 alone, and even more when combining Signals 1, 2 and 3, will allow for the first time to achieve an accuracy of the order of the actual SM value of $|V_{ts}^{SM}| = 0.04108^{+0.0030}_{-0.0057}$ as derived from an indirect global CKM matrix fit [255], and will therefore represent a direct high precision measurement of this important top quark property. In these studies, upper limits at the 2σ level down to $|V_{ts}| < 0.06$, and $|V_{td}| < 0.06$ can be achieved.

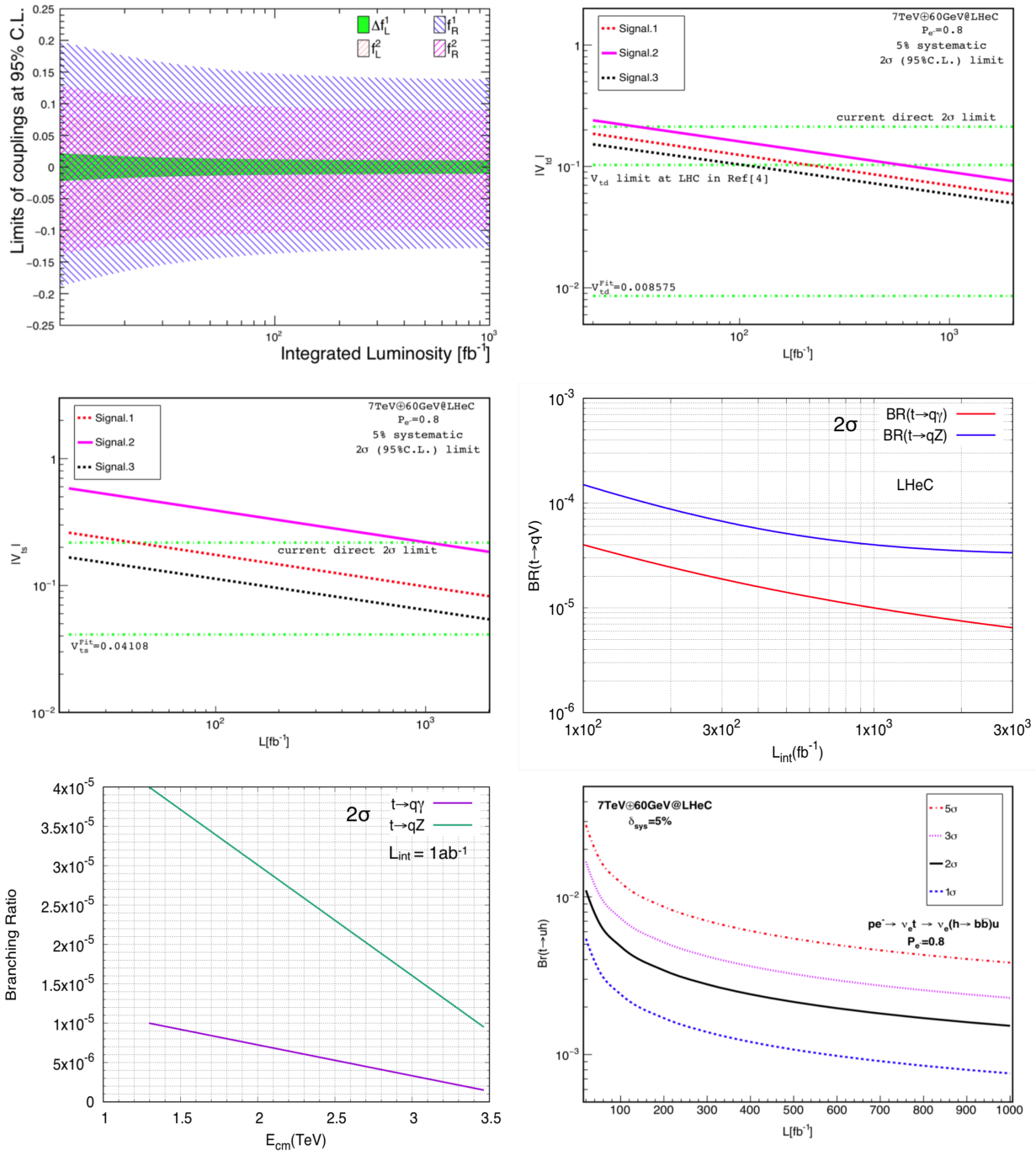

Figure 4.60: Expected sensitivities as a function of the integrated luminosity on the SM and anomalous Wtb couplings [248] (upper left), on $|V_{td}|$ (upper right) and $|V_{ts}|$ (middle left) [252], on FCNC $t \to qV$ branching ratios (middle right) [256, 257], and on FCNC $t \to uH$ branching ratios [258] (lower left). The expected upper limits on FCNC $t \to qV$ branching ratios are also shown as a function of the center-of-mass-energy (lower right).

4.4.2 FCNC Top Quark Couplings

Single top quark NC DIS production can be used to search for Flavor Changing Neutral Current (FCNC) $tu\gamma$, $tc\gamma$, tuZ, and tcZ couplings [256, 257] as represented by the Lagrangian

$$L = \sum_{q=u,c} \left(\frac{g_e}{2m_t} \bar{t}\sigma^{\mu\nu}(\lambda_q^L P_L + \lambda_q^R P_R) q A_{\mu\nu} + \frac{g_W}{4c_W m_Z} \bar{t}\sigma^{\mu\nu}(\kappa_q^L P_L + \kappa_q^R P_R) q Z_{\mu\nu} \right) + h.c. \ ,$$

where g_e (g_W) is the electromagnetic (weak) coupling constant, c_W is the cosine of the weak mixing angle, $\lambda_q^{L,R}$ and $\kappa_q^{L,R}$ are the strengths of the anomalous top FCNC couplings (the values of these couplings vanish at the lowest order in the SM), and P_L (P_R) denotes the left (right) handed projection operators. In an elaborate analysis of final states including at least one electron and three jets (hadronic top quark decay) with high transverse momentum and within the pseudorapidity acceptance range of the detector are selected. The distributions of the invariant mass of two jets (reconstructed W boson mass) and an additional jet tagged as b-jet (reconstructed top quark mass) are used to further enhance signal over background events, mainly given by W+jets production. Signal and background interference effects are included. A detector simulation with DELPHES [250] is applied.

The expected limits on the branching ratios BR($t \to q\gamma$) and BR($t \to qZ$) as a function of the integrated luminosity at the 2σ C.L. are presented in Fig. 4.60 (middle right). Assuming an integrated luminosity of $1\,\text{ab}^{-1}$, limits of BR($t \to q\gamma$) $< 1 \cdot 10^{-5}$ and BR($t \to qZ$) $< 4 \cdot 10^{-5}$ are expected. This level of precision is close to actual predictions of concrete new phenomena models, such as SUSY, little Higgs, and technicolor, that have the potential to produce FCNC top quark couplings. This will improve on existing limits from the LHC by one order of magnitude [259]. Figure 4.60 (lower left) shows how this sensitivity on BR($t \to q\gamma$) and BR($t \to qZ$) changes as a function of center-of-mass energy. At a future FCC-ep [259] with, for example, an electron beam energy of 60 GeV, and a proton beam energy of 50 TeV, leading to a center-of-mass energy of 3.5 TeV, the sensitivity on FCNC $tq\gamma$ couplings even exceed expected sensitivities from the High Luminosity-LHC (HL-LHC) with $300\,\text{fb}^{-1}$ at $\sqrt{s} = 14\,\text{TeV}$, and from the International Linear Collider (ILC) with $500\,\text{fb}^{-1}$ at $\sqrt{s} = 250\,\text{GeV}$ [260, 261].

Another example for a sensitive search for anomalous top quark couplings is the one for FCNC tHq couplings as defined in

$$L = \kappa_{tuH}\, \bar{t}uH + \kappa_{tcH}\, \bar{t}cH + h.c.$$

This can be studied in CC DIS production, where singly produced top anti-quarks could decay via such couplings into a light anti-quark and a Higgs boson decaying into a bottom quark-antiquark pair, $e^- p \to \nu_e \bar{t} \to \nu_e H \bar{q} \to \nu_e b\bar{b}\bar{q}$ [258]. Another signal involves the FCNC tHq coupling in the production vertex, i.e. a light quark from the proton interacts via t-channel top quark exchange with a W boson radiated from the initial electron producing a b quark and a Higgs boson decaying into a bottom quark-antiquark pair, $e^- p \to \nu_e H b \to \nu_e b\bar{b}b$ [258]. This channel is superior in sensitivity to the previous one due to the clean experimental environment when requiring three identified b-jets. Largest backgrounds are given by $Z \to b\bar{b}$, SM $H \to b\bar{b}$, and single top quark production with hadronic top quark decays. A 5% systematic uncertainty for the background yields is added. Furthermore, the analysis assumes parameterized resolutions for electrons, photons, muons, jets and unclustered energy using typical parameters taken from the ATLAS experiment. Furthermore, a b-tag rate of 60%, a c-jet fake rate of 10%, and a light-jet fake rate of 1% is assumed. The selection is optimized for the different signal contributions separately. Figure 4.60 (lower right), shows the expected upper limit on the branching ratio Br($t \to Hu$) with 1σ, 2σ, 3σ, and 5σ C.L. as a function of the integrated luminosity for the $e^- p \to \nu_e H b \to \nu_e b\bar{b}b$ signal process. For an integrated luminosity of $1\,\text{ab}^{-1}$, upper limits of Br($t \to Hu$) $< 0.15 \cdot 10^{-3}$ are expected at the 2σ C.L.

In Fig. 4.61 the different expected limits on various flavor-changing neutral current (FCNC) top quark couplings from the LHeC are summarized, and compared to results from the LHC and the HL-LHC. This

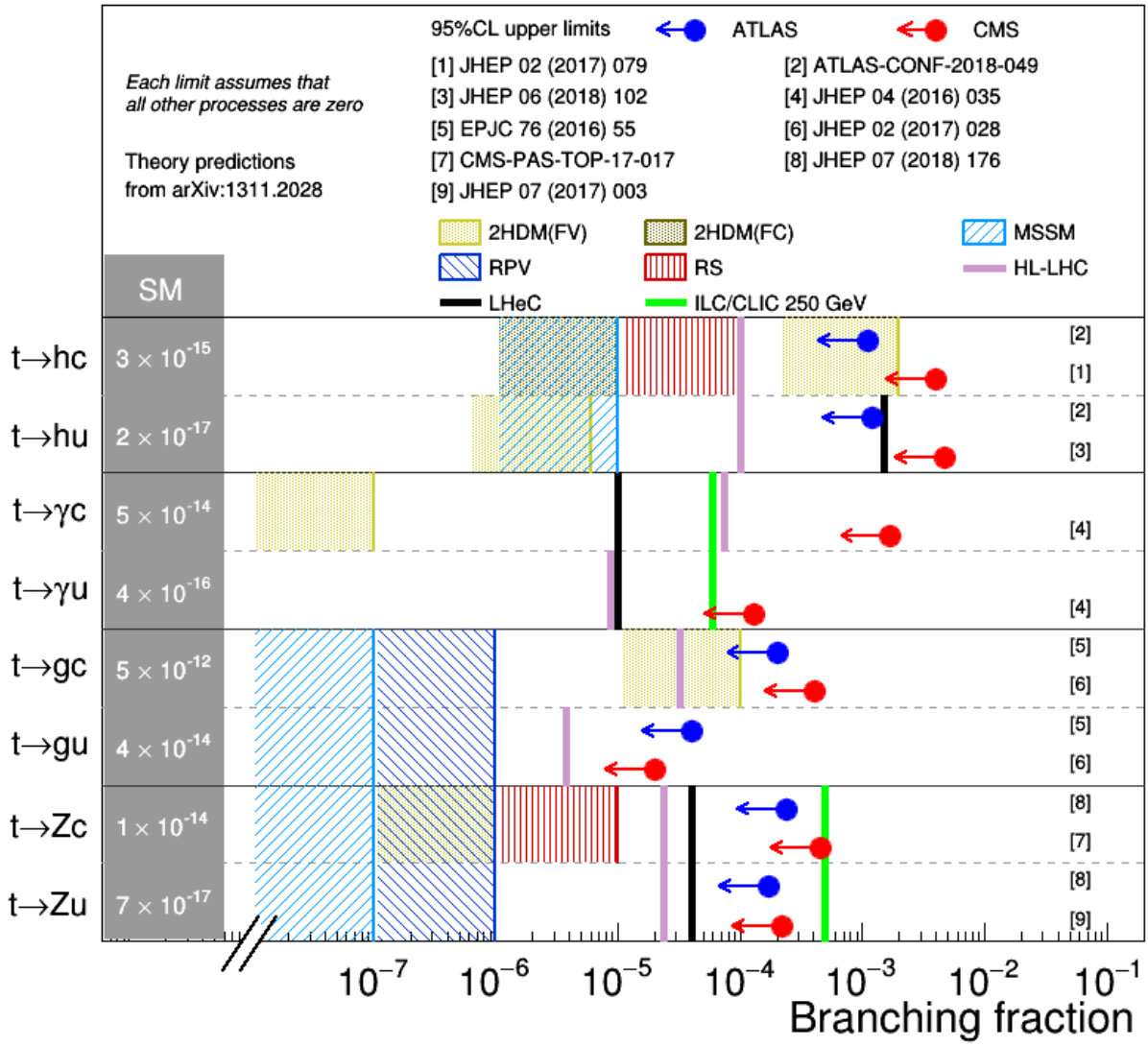

Figure 4.61: Comparison of top quark FCNC branching ratio limits at the LHC, HL-LHC, LHeC, and ILC/CLIC colliders.

clearly shows the competitiveness of the LHeC results, and documents the complementarity of the results gained at different colliders.

4.4.3 Other Top Quark Property Measurements and Searches for New Physics

Other exciting results not presented here involve, for example, the study of the CP-nature in $t\bar{t}H$ production [262], searches for anomalous $t\bar{t}\gamma$ and $t\bar{t}Z$ chromoelectric and chromomagnetic dipole moments in $t\bar{t}$ production [249], the study of top quark spin and polarization [263], and the investigation of the top quark structure function inside the proton [264, 1].

4.4.4 Summary Top Quark Physics

Top quark physics at the LHeC represents a very rich and diverse field of research involving high precision measurements of top quark properties, and senstive searches for new physics. Only a few highlights involving

Wtq and FCNC top quark couplings are presented here. One particular highlight is the expected direct measurement of the CKM matrix element $|V_{tb}|$ with a precision of less than 1%. Furthermore, FCNC top quark couplings can be studied with a precision high enough to explore those couplings in a regime that might be affected by actual new phenomena models, such as SUSY, little Higgs, and technicolor.

It has been shown [259], that results from future e^+e^--colliders, eh-colliders, and hh-colliders deliver complimentary information and will therefore give us a more complete understanding of the properties of the heaviest elementary particle known to date, and of the top quark sector in general.

4.5 Novel QCD phenomena at the LHeC [Stan J. Brodsky]

Section needs to be polished and parts to be integrated into other places.

Intrinsic Heavy Quark Phenomena One of the most interesting nonperturbative quantum field theoretic aspect of hadron light front wavefunctions in QCD are the intrinsic heavy-quark Fock states [265, 266, 267]. Consider a heavy-quark loop insertion to the proton's self-energy. The heavy-quark loop can be attached by gluons to just one valence quark. The cut of such diagrams yields the standard DGLAP gluon splitting contribution to the proton's heavy quark structure function. In this case, the heavy quarks are produced at very small x. However, the heavy quark loop can also be attached to two or more valence quarks in the proton self-energy. In the case of QED this is corresponds to the light-by light lepton loop insertion in an atomic wavefunction. In the case of QCD, the heavy quark loop can be attached by three gluons to two or three valence quarks in the proton self-energy. This is a non-Abelian insertion to the hadron's self-energy. The cut of such diagrams gives the "intrinsic" heavy-quark contribution to the proton's light-front wavefunction. in the case of QCD, the probability for an intrinsic heavy $Q\bar{Q}$ pair scales as $\frac{1}{M_Q^2}$; this is in contrast to heavy $\ell\bar{\ell}$ lepton pairs in QED where the probability for heavy lepton pairs in an atomic wavefunction scales as $\frac{1}{M_\ell^4}$. This difference in heavy-particle scaling in mass distinguishes Abelian from non-Abelian theories.

A basic property of hadronic light-front wavefunctions is that they have strong fall-off with the invariant mass of the Fock state. For example, the LFWFs of the color-confining AdS/QCD models [268] $\mathcal{M}^2 = [\sum_i k_i^\mu]^2$ of the Fock state constituents. This means that the probability is maximized when the constituents have equal true rapidity; i.e., $x_i \propto \sqrt{(\vec{k}_{\perp i}^2 + m_i^2)}$. Thus the heavy quarks carry most of the momentum in an intrinsic heavy quark Fock state. For example, the charm quark in the intrinsic charm Fock state $|uudc\bar{c}>$ of a proton carries about 40% of the proton's momentum: $x_c \sim 0.4$ After a high energy collision, the co-moving constituents can then recombine to form the final state hadrons. along the proton. Thus in a ep collision, the comoving udc quarks from the $|uudc\bar{c}>$ intrinsic 5-quark Fock state can recombine to a Λ_c, where $x_{\Lambda_c} = x_c + x_u + x_d \sim 0.5$. Similarly, the comoving dcc in the $|uudc\bar{c}c\bar{c}>$ intrinsic 7-quark Fock state can recombine to a $\Xi(ccd)^+$, with $x_{\Xi(ccd)} = x_c + x_c + x_d \sim 0.9$.

Thus, In the intrinsic heavy quark model, the wavefunction of a hadron in QCD can be represented as a superposition of Fock state fluctuations, *e.g.* $|n_V\rangle$, $|n_V g\rangle$, $|n_V Q\overline{Q}\rangle$, ... components where $n_V \equiv dds$ for Σ^-, uud for proton, $\overline{u}d$ for π^- and $u\overline{d}$ for π^+. Charm hadrons can be produced by coalescence in the wavefunctions of the moving hadron. Doubly-charmed hadrons require fluctuations such as $|n_V c\bar{c}c\bar{c}\rangle$. The probability for these Fock state fluctuations to come on mass shell is inversely proportional to the square of the quark mass, $\mathcal{O}(m_Q^{-2n})$ where n is the number of $Q\overline{Q}$ pairs in the hadron. Thus the natural domain for heavy hadrons produced from heavy quark Fock states is $\vec{k}_{\perp Q}^2 \sim m_Q^2$ and high light-front momentum fraction x_Q [265, 266, 266, 267]. For example, the rapidity regime for double-charm hadron production $y_{ccd} \sim 3$ at low energies is well within the kinematic experiment domain of a fixed target experiment such as SELEX at the Tevatron [269]. Note that the intrinsic heavy-quark mechanism can account for

many previous observations of forward heavy hadron production single and double J/ψ production by pions observed at high $x_F > 0.4$ in the low energy fixed target NA3 experiment, the high x_F production of $pp \to \Lambda_c, +X$ and $pp \to \Lambda_b + X$ observed at the ISR; single and double $\Upsilon(b\bar{b})$ production, as well as *quadra-bottom* tetraquark $[bb\bar{b}\bar{b}]$ production observed recently by the AnDY experiment at RHIC [179]. In addition the EMC collaboration observed that the charm quark distribution in the proton at $x_{bj} = 0.42$ and $Q^2 = 75\ GeV^2$ is 30 times larger that expected from DGLAP evolution. All of these experimental observations are naturally explained by the intrinsic heavy quark mechanism. The SELEX observation [269] of double charm baryons at high x_F reflects production from double intrinsic heavy quark Fock states of the baryon projectile. Similarly, the high x_F domain – which would be accessible in the forward high x_F domain – is the natural production domain for heavy hadron production at the LHeC.

The production of heavy hadrons based on intrinsic heavy quark Fock states is thus remarkable efficient and greatly extends the kinematic domain of the LHeC; e.g., for processes such as $\gamma^* b \to Z^0 b$. This is in contrast with the standard production cross sections based on gluon splitting, where only a small fraction of the incident momentum is effective in creating heavy hadrons.

Radiation Amplitude Zero @To be integrated elsewhere, e.g. merge with electroweak, or charm in CC, or BSM. The LHeC is ideal for testing a novel feature of the Standard Model: the "radiation amplitude zero" [270, 271, 272, 273] of the amplitude $\gamma W^- \to c\bar{b}$ and related amplitudes. See Fig. 4.62. The Born amplitude is predicted to vanish and change sign at $\cos\theta_{CM} = \frac{e_{\bar{b}}}{e_W} = -1/3$. This LHeC measurement tests W compositeness and its zero anomalous magnetic moment at leading order: $g_W = 2, \kappa_W = 1$, as well as $g_q = 2$ for quarks.. One can also test the radiation amplitude zero for the top quark from $\gamma b \to W^- t$.

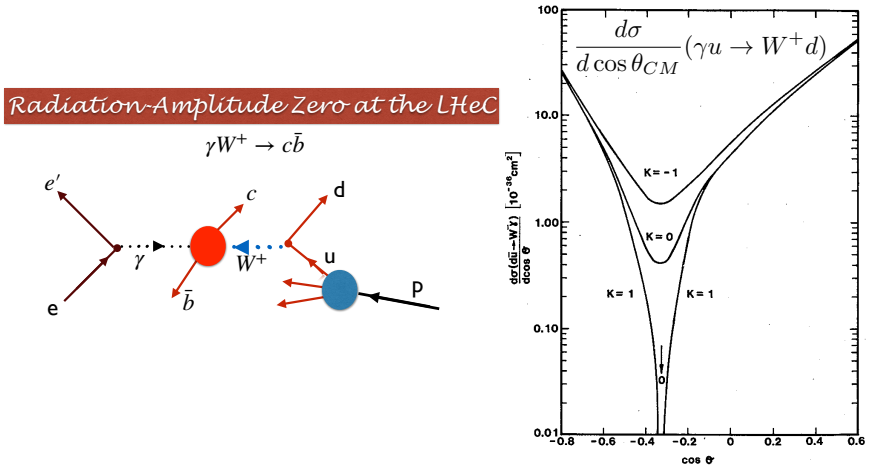

Figure 4.62: The radiation amplitude zero of the Standard Model in $\gamma W^+ \to c\bar{b}$ and $\gamma u \to W^+ d$. The prediction for the angular distribution $\frac{d\sigma}{dcos(\theta_{CM})}(\gamma u \to W^+ d)$ is from ref. [273].

Chapter 5

Nuclear Particle Physics with Electron-Ion Scattering at the LHeC [Nestor Armesto]

5.1 Introduction [Anna Stasto]

The LHeC accelerator, in addition to being a powerful machine for exploring the proton structure, will allow for the first time to study with great precision DIS off nuclei in a collider mode. The nuclear structure has been previously studied in fixed target experiments with charged lepton and neutrino beams, see [274, 275, 276, 277, 278, 279, 280, 281, 282, 283, 284, 285, 286] and references therein. Due to the energy limitations of the machines operating in this collision mode, the kinematic range covered by these experiments is rather narrow, mostly limited to relatively large values of $x \geq 0.01$ and low to moderate Q^2, in the range $Q^2 < 100\,\mathrm{GeV}^2$. The precise kinematic range covered by DIS experiments is shown in Fig. 5.1, where the DIS experiments overlap to a large degree with the data from hadronic collisions using the Drell-Yan process. These fixed target DIS and DY data dominate the data sets used in the fits for the nuclear parton distribution functions. In addition, in some analyses of nuclear PDFs, data for inclusive single hadron production dAu at RHIC and EW bosons and dijets in pPb at the LHC are employed.

As it is clear from Fig. 5.1 the LHeC will be able to cover a very large range in (x, Q^2) in eA, previously unexplored in experiment. It will extend the range in x down to $\sim 10^{-7}$ and have a huge lever arm in Q^2 from very low values up to $10^6\,\mathrm{GeV}^2$. It will also be complementary to the EIC [100] machine, by extending the range in x by two orders of magnitude and in Q^2 by about 2.5 orders of magnitude with respect to it.

Due to large statistics and modern, specialised detectors, it will be possible to study nuclear structure at the LHeC with unprecedented precision in a kinematical range far wider than previously possible and with the controlled systematics of one single experiment. There are a large number of important physics topics that can be addressed in eA collisions at the LHeC:

- A precise determination of nuclear parton densities for a single nucleus (lead, and eventually for lighter ions) in a wide kinematic range will be possible. In particular, the current huge uncertainties in gluon and sea quark densities at low x will be dramatically improved using the data from the LHeC. In analogy to the proton PDF extraction described in previous sections, full flavour decomposition in the nuclear case could be achieved using both NC and CC with heavy flavour identification.
- Precision measurement of semi-inclusive and exclusive processes will allow to explore more details of the nuclear structure. Similarly to the proton case, the DVCS and exclusive diffractive vector-meson production will provide unique insight into 3D nuclear structure.
- The LHeC will offer unprecedented opportunities to extract diffractive parton densities in nuclei for

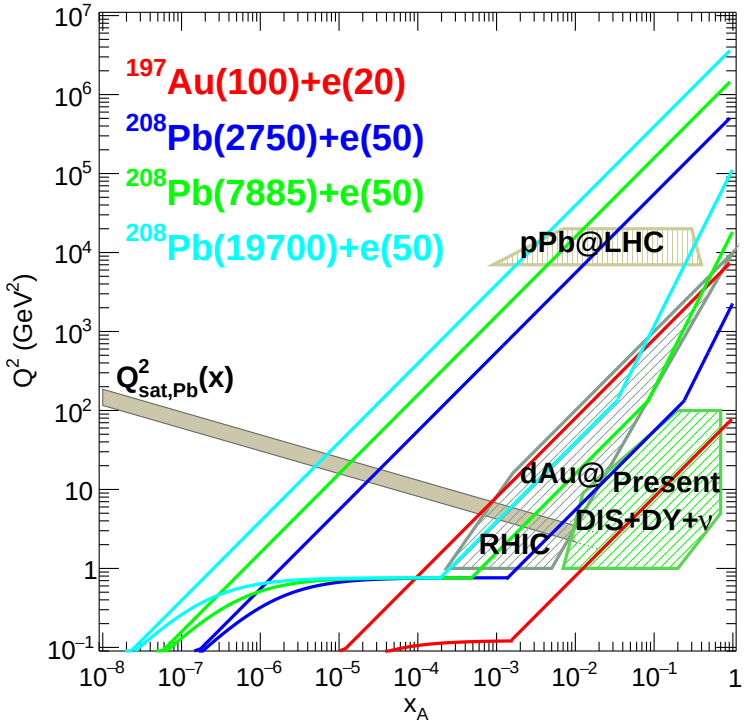

Figure 5.1: Kinematic regions in the $x - Q^2$ plane explored by different data sets (charged lepton and neutrino DIS, DY, dAu at RHIC and pPb at the LHC) used in present nPDF analyses [287], compared to the ones achievable at the EIC (red), the LHeC (ERL against the HL-LHC beams, dark blue) and two FCC-eh versions (with Pb beams corresponding to proton energies $E_p = 20\,\text{TeV}$ - green and $E_p = 50\,\text{TeV}$ - light blue). Acceptance of the detector for the electrons is taken to be $1^\circ < \theta < 179^\circ$, and $0.01(0.001) < y < 1$ for the EIC (all other colliders). The saturation scale Q_{sat} shown here for indicative purposes only, see also [288], has been drawn for a Pb nucleus considering an uncertainty ~ 2 and a behaviour with energy following the model in [289]. Note that it only indicates a region where saturation effects are expected to be important but there is no sharp transition between the linear and non-linear regimes.

the first time. A first detailed analysis [131] indicates that the achievable precision on diffractive PDFs in nuclei will be comparable to that possible in the proton case. The measurements of diffraction on protons and nuclei as well as the inclusive structure functions in the nuclear case, will allow to explore the very important relation between the nuclear shadowing and diffraction [290].

- The LHeC will be able to test and establish or exclude the phenomenon of parton saturation at low x in protons and nuclei. According to the Color Glass Condensate framework [291, 292], parton saturation is a density effect that can be achieved in two ways, either by decreasing the value of x or by increasing the size of the target by increasing A. The LHeC will be a unique machine to offer such two-pronged approach where the ideas of saturation could be precisely tested. It will be possible to search for parton saturation in a variety of ways which include, among others, the search for tensions in DGLAP fits, the study of the diffraction, in particular the ratios of diffractive to inclusive cross section, and the study of particle azimuthal correlations.

- Finally, the LHeC machine in eA mode will have a huge impact onto physics explored in pA and AA collisions, see Sec. 8.4, where it will provide vital input and constraints on the initial state in nuclear collisions, measurements of the impact of cold nuclear medium on hard probes and effects of hadronisation. It will also explore the initial state correlations on the final state observables relevant for understanding collectivity in small systems.

As commented below, these aims will require an experimental apparatus with large rapidity coverage and associated forward and backward electron, photons, hasdron and nuclear detectors, able to measure diffractive events in eA and to contribute to the separation of radiative events, most important for the case of DVCS and exclusive diffraction.

In this Chapter we do not address issues on the nuclear modification on jet yields and fragmentation that is expected to show dramatic effects and to be of fgreat importance for heavy- ion collisions. All these aspects were discussed in [1].

5.2 Nuclear Parton Densities [Nestor Armesto]

PDFs are essential ingredients in our understanding of the dynamics of the strong interaction. First, they encode important information about the structure of hadrons [293, 294]. Second, they are indispensable for the description of hadronic collisions within standard collinear factorisation [295]. Concerning nuclei, it has been known for more than 40 years that structure functions are affected by the nuclear environment [285, 286] so that they cannot be interpreted as a superposition of structure functions of free nucleons. In the standard approach, within collinear factorization, the nuclear modification is included in the parametrisation of the parton densities. This means that the parton densities in a bound nucleon are different from those in a free nucleon, and the difference is encoded in the non-perturbative initial conditions of the parton densities at some low, initial scale Q_0^2. The present status of nuclear parton densities (nPDFs), see for example [296, 297], can be summarised as follows:

- Modern analyses [298, 299, 300, 287] are performed at next-to-leading order (NLO) and next-to-next-to-leading order (NNLO) [301, 16]. Differences between them mainly arise from the different sets of data included in the analyses[1] and from the different functional forms employed for the initial conditions.
- Many sets of data are presented as ratios of cross section for a given nucleus over that in deuterium. Therefore, it has become customary to work in terms of ratios of nPDFs:

$$R_i(x,Q^2) = \frac{f_i^{\rm A}(x,Q^2)}{A f_i^{\rm p}(x,Q^2)} \ , \quad i = u,d,s,c,b,g,\ldots , \tag{5.1}$$

  with $f_i^{{\rm p}(A)}(x,Q^2)$ the corresponding parton density in a free proton p or in nucleus A. These nuclear modification factors are parametrised at some initial scale Q_0^2 (assuming isospin symmetry to hold). The nPDFs are then obtained multiplying the nuclear modification factors by some given set of free proton PDFs.
- Data come from a large variety of nuclei and the number of data points for any of them is very small compared to the proton analyses. The most up to date analyses include between 1000 and 2000 data points for 14 nuclei. In particular, for the Pb nucleus there are less than 50 points coming from the fixed target DIS and DY experiments and from particle production data in pPb collisions at the Large Hadron Collider (LHC). The fit for a single nucleus is therefore impossible and the modelling of the A-dependence of the parameters in the initial conditions becomes mandatory [287, 300].
- The kinematic coverage in Q^2 and x with existing data is very small compared to that of present hadronic colliders. The ultimate precision and large coverage of the kinematic plane for nPDFs can only be provided by a high energy electron-ion collider. Meanwhile, the only experimental collision system where nPDFs can be potentially be constrained are hadronic and ultraperipheral collisions

[1] The main difference lies on the use or not of neutrino-Pb cross sections (whose usage has been controversial [302, 303, 304], particularly the NuTeV data [275] from Fe nucleus) from CHORUS and $\pi^{0,\pm}$ transverse momentum spectra from dAu collisions at the Relativistic Heavy Ion Collider (RHIC).

(UPCs). It is important to stress though, that extracting PDFs from these collisions presents many theoretical challenges. These are related to the question of applicability of the collinear factorization for nuclear collisions, higher twist effects, scale choices and other theoretical uncertainties.

All in all, all parton species are very weakly constrained at small $x < 10^{-2}$ [305], gluons at large $x > 0.2$, and the flavour decomposition is largely unknown - a natural fact for u and d due to the approximate isospin symmetry in nuclei[2]. The impact of presently available LHC data, studied using reweighting [182, 306] in [307, 308] and included in the fit in [287], is quite modest with some constrains on the gluon and the strange quark in the region $0.01 < x < 0.3$. On the other hand, theoretical predictions for nuclear shadowing of quark and gluon PDFs based on s-channel unitarity and diffractive nucleon PDFs are available down to $x \sim 10^{-4} - 10^{-5}$ [290, 309, 310]. Predictions on the flavour dependence of nuclear effects in the antishadowing region [311] cannot be confirmed with present data.

Future runs at the LHC will offer several possibilities for improving our knowledge on nPDFs [312]. But the ideal place to determine parton densities is DIS, either at the Electron Ion Collider (EIC) [100] in the USA or, in a much larger kinematic domain (see Fig. 5.1), at the LHeC. DIS measurements in such configurations offer unprecedented possibilities to enlarge our knowledge on parton densities through a complete unfolding of all flavours.

In the following, we show the possibilities for constraining the PDFs for a Pb nucleus at the LHeC. In the next subsection, Subsec. 5.2.1, we discuss the corresponding pseudodata for the inclusive cross section in electron-nucleus scattering. Next, in Subsec. 5.2.2 we discuss how the pseudodata will be introduced in a global nPDF fit. Finally, in Subsec. 5.2.3 it is demonstrated how the PDFs of Pb can be extracted with a very good precision from the LHeC data only, without any resource to any other set of data.

5.2.1 Pseudodata [Max Klein]

The LHeC provides measurements of eA scattering cross sections in the deep inelastic scattering region $Q^2 > 1\,\mathrm{GeV}^2$ reaching values of Q^2 up to about $5 \cdot 10^5\,\mathrm{GeV}^2$ and corresponding x values between a few times 10^{-6} and near to $x = 1$. This enables the determination of a complete set of nPDFs in ePb scattering at the LHeC from the inclusive neutral and charged current cross sections with a clean separation of up and down valence and sea quark distributions. The very high Q^2 which reaches much beyond the W mass squared makes the CC measurements extremely valuable for the separation of different flavours when taken together with the NC, from photon and Z boson exchange. Charm tagging in CC determines the anti-strange quark distribution in a wide kinematic range to typically $10 - 20\,\%$ precision, while charm and beauty tagging in NC provide high precision determinations of xc and xb from nuclei. Using coherent data from just this one experiment the uncertainties of these nPDFs will follow from a straightforward $\Delta\chi^2 = 1$ criterion.

The QCD analyses illustrated subsequently of pseudo LHeC cross section data employ sets of simulated NC and CC measurements under assumptions which are summarised in Table 5.1, see [313]. The cross section simulation was done numerically employing derivative formulae from [314] and found to compare well to a detailed Monte Carlo simulation when tested for the conditions of the H1 experiment. The assumptions made are all reasonable when comparing with the H1 achievements, which shall probably be exceeded owing to new detector techniques and higher statistics. The control of radiative corrections in eA scattering is a special challenge as these grow $\propto Z^2$. The LHeC detector thus needs to be equipped with reliable photon detectors and the exploitation of the energy-momentum conservation, via the $E - p_z$ cut, should further reduce the effect of photon radiation to a few per cent level. It is also to be noted that the semi-inclusive measurements of the s, c and b quark distributions carry additional uncertainties for tagging, acceptance and background influences.

[2]The u-d difference is suppressed by a factor $2Z/A - 1$.

Table 5.1: Summary of assumed uncertainties for future inclusive cross section measurements at the LHeC.

Source of uncertainty	Error on the source or cross section
scattered electron energy scale	0.1 %
scattered electron polar angle	0.1 mrad
hadronic energy scale	0.5 %
calorimeter noise ($y < 0.01$)	1-3 %
radiative corrections	1-2 %
photoproduction background	1 %
global efficiency error	0.7 %

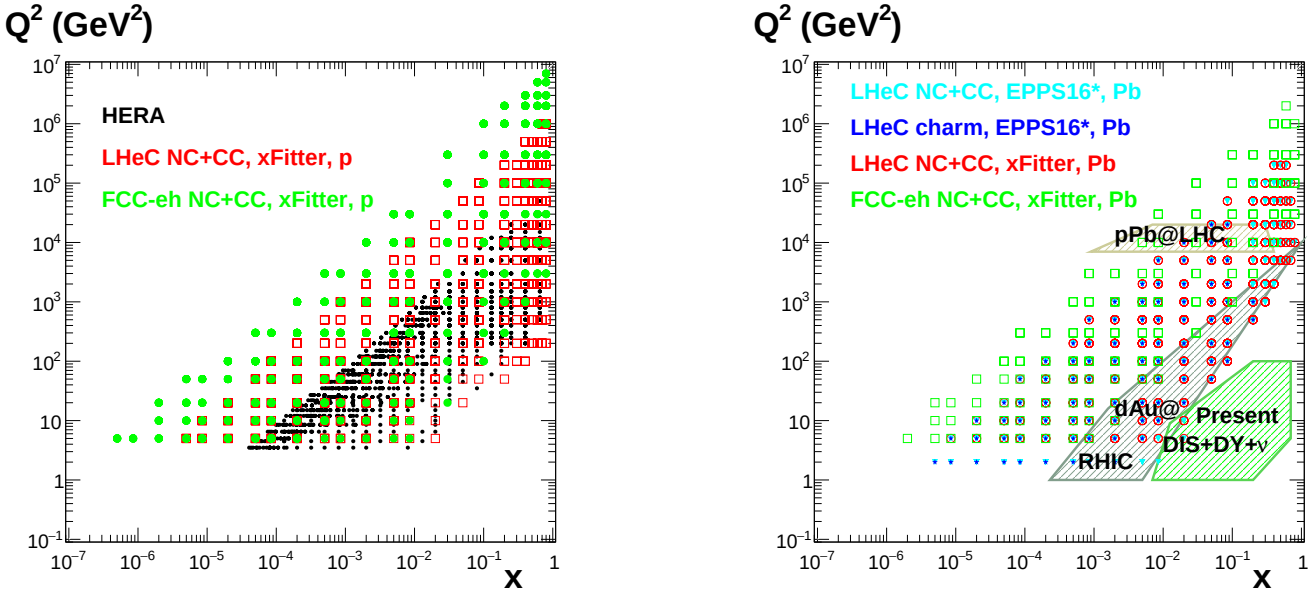

Figure 5.2: *Left*: kinematic $x - Q^2$ plot of the NC+CC pseudodata on a proton at the LHeC (red symbols) and the FCC-eh (green symbols) used in the xFitter analysis in Subsec. 5.2.3; data used in analysis at HERA (black symbols) are shown for comparison. *Right*: kinematic $x - Q^2$ plot of the pseudodata on Pb used in the EPPS16 analysis at the LHeC (NC+CC, light blue symbols, and charm, dark blue symbols) in Subsec. 5.2.2, and in the xFitter analysis in Subsec. 5.2.3 (at the LHeC, red symbols, and the FCC-eh, green symbols); the regions explored by currently available data sets (charged lepton and neutrino DIS, DY, dAu at RHIC and pPb at the LHC) used in present nPDF analyses [287] are shown for comparison.

Fig. 5.2 illustrates the kinematic reach of the NC+CC pseudodata at the LHeC and the FCC-eh, in ep and ePb collisions. Besides, the LHeC is the ideal environment to determine the strange, charm and beauty (also the top) PDFs. The principal technique is charm tagging (in CC for xs, in NC for xc) and beauty tagging (in NC for xb). The beam spot of the LHeC has the transverse extension of about $(7\,\mu\text{m})^2$. Modern Si detectors have a resolution of a few microns to be compared with typical decay lengths of charm and beauty particles of hundreds of μm. The experimental challenges then are the beam pipe radius, coping at the LHeC with strong synchrotron radiation effects, and the forward tagging acceptance, similar to the HL-LHC challenges.

A study was made of the possible measurements of the anti-strange density (Fig. 5.3 top) using impact parameter tagging in eA CC scattering, and of the charm and beauty structure functions in NC (Figs. 5.3 middle and 5.3 bottom respectively). Following experience on heavy flavour tagging at HERA and ATLAS, assumptions were made on the charm and beauty tagging efficiencies, to be 10 % and 60 %, respectively. The light quark background in the charm analysis is assumed to be controllable to per cent level, while the charm background in the beauty tagging sample is assumed to be 10 %. The tagging efficiencies and

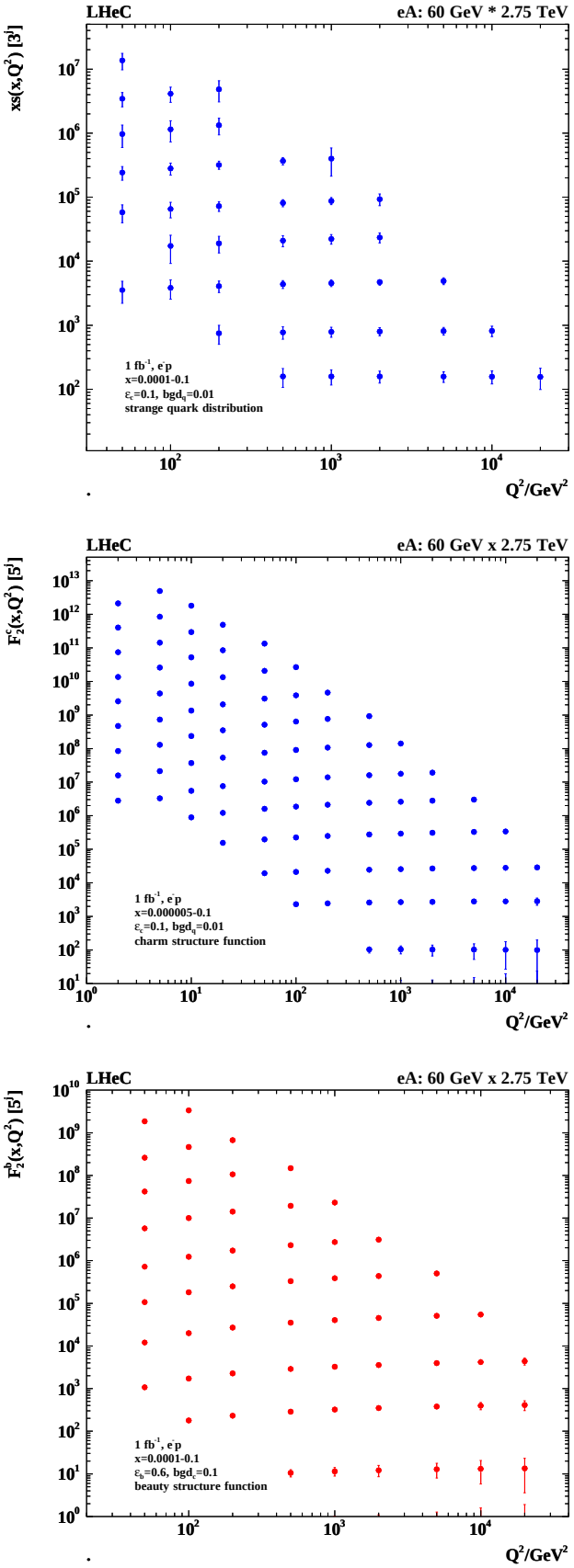

Figure 5.3: *Top*: Simulation of the measurement of the (anti)-strange quark distribution $x\bar{s}(x, Q^2)$ in charged current eA scattering through the t-channel reaction $W^- \bar{s} \to c$; *Middle*: Simulation of the measurement of the charm quark distribution expressed as $F_2^c = e_c^2 x(c+\bar{c})$ in neutral current eA scattering; *Bottom*: Simulation of the measurement of the bottom quark distribution expressed as $F_2^b = e_b^2 x(b+\bar{b})$ in neutral current eA scattering. The data are plotted with full systematic and statistical errors added in quadrature.

background contaminations affect the statistical error. Moreover, an additional systematic error is assumed in the simulated NC (CC) measurements of 3 (5) %. These result in very promising measurements of the heavier quark distributions: to about $10-20\,\%$ total uncertainty on the strange and $3-5\,\%$ on the charm and beauty measurements, for typically x between 10^{-4} and 0.1 and Q^2 extending from below threshold m_Q^2 up to a few times $10^4\,\mathrm{GeV}^2$. The knowledge of the heavy quark densities is of prime relevance for understanding nuclear structure and the development of QCD as has often been emphasised.

5.2.2 Nuclear gluon PDFs in a global-fit context [Hannu Paukkunen]

To illustrate the impact of the LHeC ePb pseudodata in the global context, they have been added [315] into the EPPS16 global analysis of nuclear PDFs [287]. The EPPS16 strategy is to parametrize the nuclear modification ratios $R_i(x,Q^2)$ between the bound-proton PDFs $f_i^{\mathrm{p/Pb}}$ and proton PDFs f_i^{p},

$$R_i(x,Q^2) \equiv \frac{f_i^{\mathrm{p/Pb}}(x,Q^2)}{f_i^{\mathrm{p}}(x,Q^2)}$$

at the charm mass threshold $Q^2 = m^2_{\mathrm{charm}} = (1.3\ \mathrm{GeV})^2$. At higher Q^2 the nuclear PDFs are obtained by solving the standard DGLAP evolution equations at next-to-leading order in QCD. As the LHeC pseudodata reach to significantly lower x than the data that were used in the EPPS16 analysis, an extended small-x parametrisation was used for gluons, see Figure 5.4. The framework is almost identical to that in Ref. [316]. The introduced functional form allows for rather wild – arguably unphysical – behaviour at small-x and e.g. significant enhancement is allowed. This is in contrary to the theoretical expectations from the saturation conjecture and looks also as an improbable scenario given the recent LHCb D- and B-meson measurements [317, 318] which impressively indicate [319] gluon shadowing down to $x \sim 10^{-5}$ at interaction scales as low as $Q^2 \sim m^2_{\mathrm{charm}}$. On the other hand, given that there are no prior DIS measurements at these kinematics for nuclei other than the proton, and that the D- and B-meson production in pPb collisions could be affected by strong final-state effects (which could eventually be resolved by e.g. measurements of forward prompt photons [320] in pPb), we hypothesize that any kind of behaviour is possible at this stage. Anyway, with the extended parametrisation – called here EPPS16* – the uncertainties in the small-x regime get significantly larger than what they are in the standard EPPS16 set. This is reflected as significantly larger PDF error bands in comparison to the projected LHeC pseudodata. This is shown in Figure 5.5 where EPPS16* predictions are compared with the LHeC pseudodata for inclusive NC and CC reactions, as well as charm production in neutral-current scattering. The uncertainties are estimated using the Hessian method [321] and the same overall tolerance $\Delta\chi^2 = 52$ as in the EPPS16 analysis has been used when defining the error bands. Because there are no small-x data constraints for gluons, the gluon uncertainty is enormous and the Hessian method used for estimating the uncertainties is not particularly accurate, i.e. the true $\Delta\chi^2 = 52$ error bands are likely to be even larger. At some point the downward uncertainty will be limited by positivity constraints e.g. for F_{L}, but will depend strongly on which Q^2 the positivity constraints are set (in the EPPS16 analysis F_{L} is required to remain positive at $Q^2 = m^2_{\mathrm{charm}}$).

Upon including the LHeC ePb pseudodata in the fit, the new nPDFs adapt to reproduce the pseudodata and their uncertainties are greatly reduced, as shown in Figure 5.6. The overall tolerance has been kept fixed to the default value $\Delta\chi^2 = 52$. The impact on the nuclear modification of the gluon PDF is illustrated in Figure 5.7 at two values of Q^2: $Q^2 = 1.69\,\mathrm{GeV}^2$ (the parametrisation scale) and $Q^2 = 10\,\mathrm{GeV}^2$. Already the inclusive pseudodata are able to reduce the small-x gluon uncertainty quite significantly, and the addition of the charm data promises an even more dramatic reduction in the errors. The analysis indicates that – unless very low Q^2 and very small x are considered – the LHeC will nail the nuclear gluon PDF to a high precision.

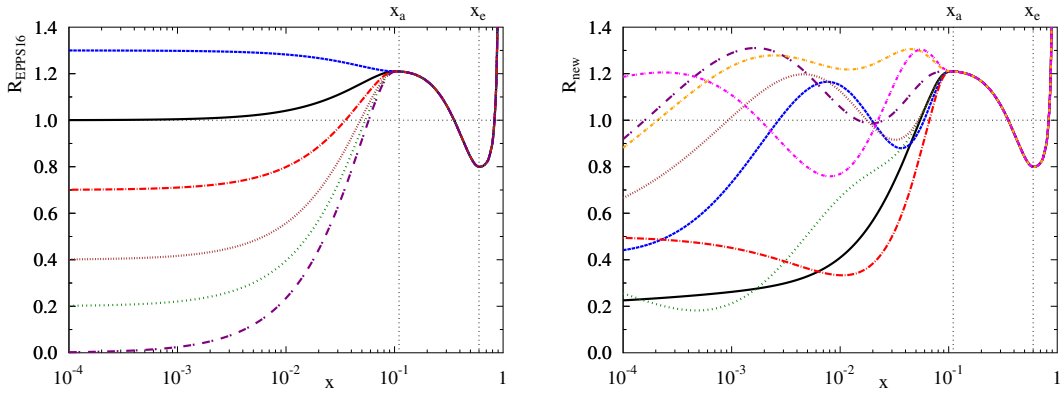

Figure 5.4: Left: Functional behaviour allowed at small x in the EPPS16 analysis. Right: Possible functional variation at small x in the extended parametrisation.

5.2.3 nPDFs from DIS on a single nucleus [Nestor Armesto]

Another approach that becomes possible with the large kinematic coverage and amount of data for a single nucleus, Pb, at the LHeC and FCC-eh, is to perform a fit to only Pb data in order to extract the Pb PDFs. Then the corresponding ratios or nuclear modification factors for each parton species can be obtained using either a proton PDF set from a global fit or, as we do here (see [322, 323, 259]), from a fit to proton LHeC and FCC-eh pseudodata. In this way, there will be no need of introducing a nuclear size dependence in the parameters for the initial condition for DGLAP evolution. Such nPDFs can then be used for comparing to those obtained from global fits and for precision tests of collinear factorisation in nuclear collisions.

The fits are performed using xFitter [324], where 484 (150) NC+CC Pb data points at the LHeC (FCC-eh) have been used in the fitted region $Q^2 > 3.5$ GeV^2, see Fig. 5.2. A HERAPDF2.0-type parametrisation [29] has been employed to provide both the central values for the reduced cross sections (therefore, the extracted nuclear modification factors are centered at 1) and the fit functional form; in this way, neither theory uncertainties (treatment of heavy flavours, value of α_s, order in the perturbative expansion) nor the uncertainty related to the functional form of the initial condition – parametrisation bias – are considered in our study, in agreement with our goal of estimating the *ultimate experimental achievable* precision in the extraction of nPDFs. We have worked at NNLO using the Roberts-Thorne improved heavy quark scheme, and $\alpha_s(m_Z^2) = 0.118$. The treatment of systematics and the tolerance $\Delta\chi^2 = 1$ are identical to that in the HERAPDF2.0 fits, as achievable in a single experiment.

The results for the relative uncertainties in the nuclear modification factors, are shown in Figs. 5.8, 5.9 and 5.10 for valence, sea and gluon respectively. The uncertainties in these plots reflect the assumed uncertainties in the pseudodata, both statistics (mainly at large x) and systematics from detector efficiencies, radiative corrections, etc., see Sec. 5.2.1. As expected, the uncertainty in the extraction of the valence at small x is sizeably larger than that for the sea and gluon. While a very high precision looks achievable at the LHeC and the FCC-eh, for the comparison with EPPS16 (or any other global fit) shown in the plots and with previous works in that setup [316, 315] some caution must be taken. First, the effective EPPS16 tolerance criterium $\Delta\chi^2 \simeq 52$ implies that naively the uncertainty bands should be compared after rescaling by a factor $\sqrt{52}$. Second, the treatment of systematics is rather different, considering correlations in the xFitter exercise and taking them as fully uncorrelated (and added quadratically to the statistical ones) in the EPPS16 one. Finally, EPPS16 uses parametrisations for the nuclear modification factors for different parton species while in xFitter just the (n)PDF combinations that enter the reduced cross sections are parametrised and employed for the fit. In this respect let us note that, in analogy to proton PDFs, full flavour decomposition can be achieved using both NC and CC with heavy flavour identification that will

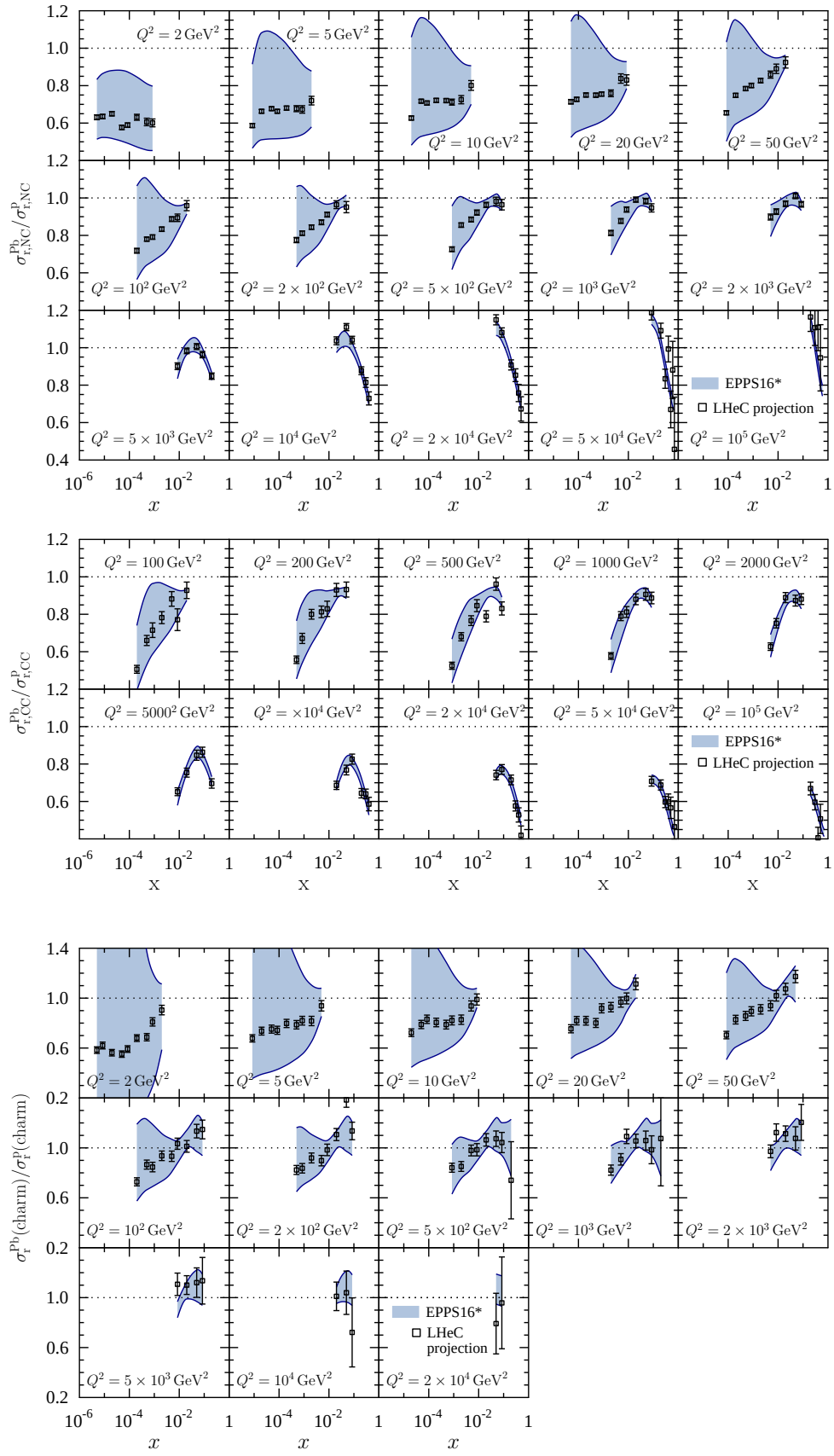

Figure 5.5: Top: Ratios of neutral-current reduced cross sections between ePb and ep collisions compared with the predictions from a EPPS16-type global fit of nuclear PDFs using an extended parametrisation for gluons. Middle: Charged-current cross sections. Bottom: Neutral-current charm-production cross-section ratios.

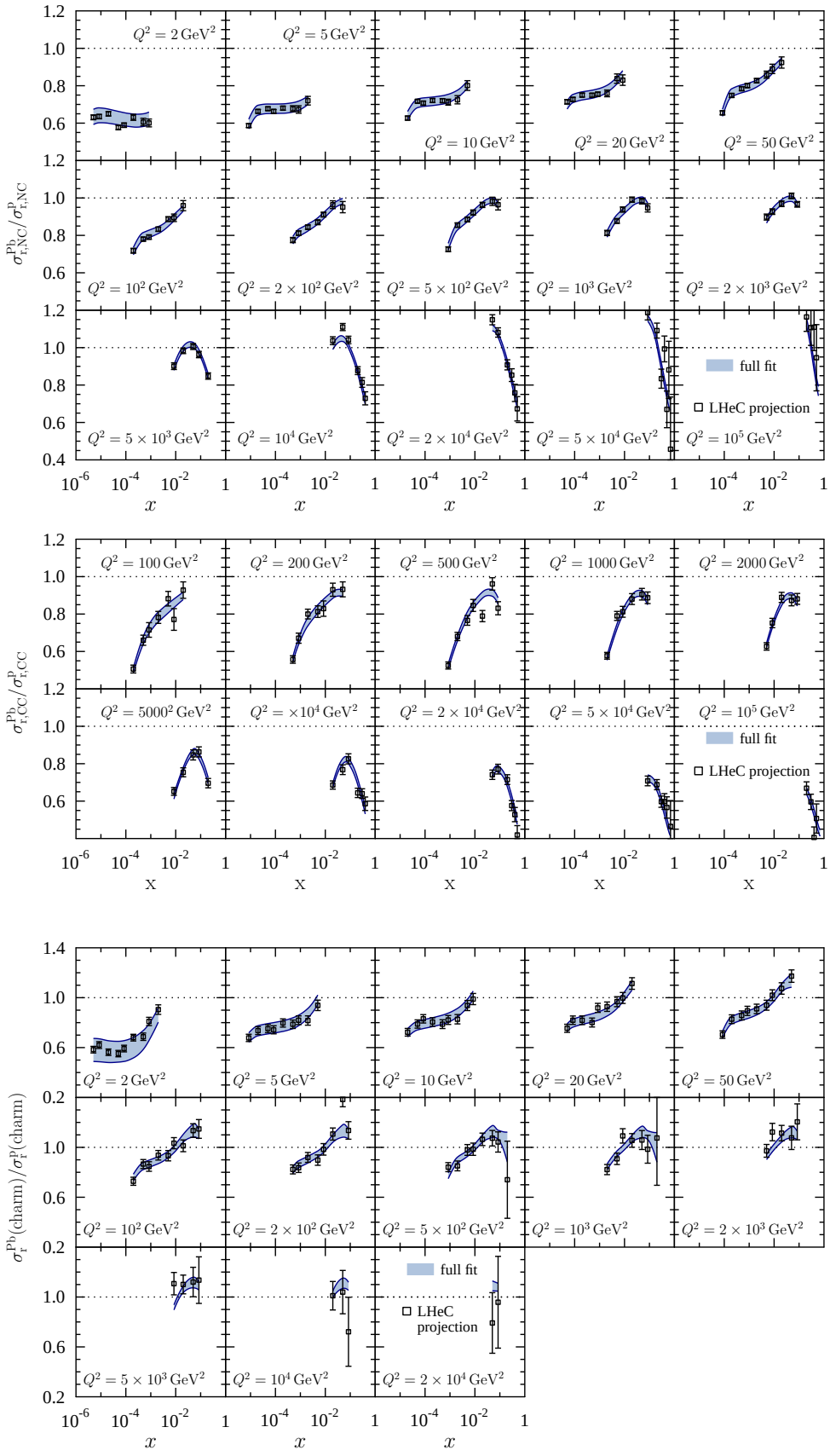

Figure 5.6: As Figure 5.5 but after including the LHeC pseudodata in the global analysis.

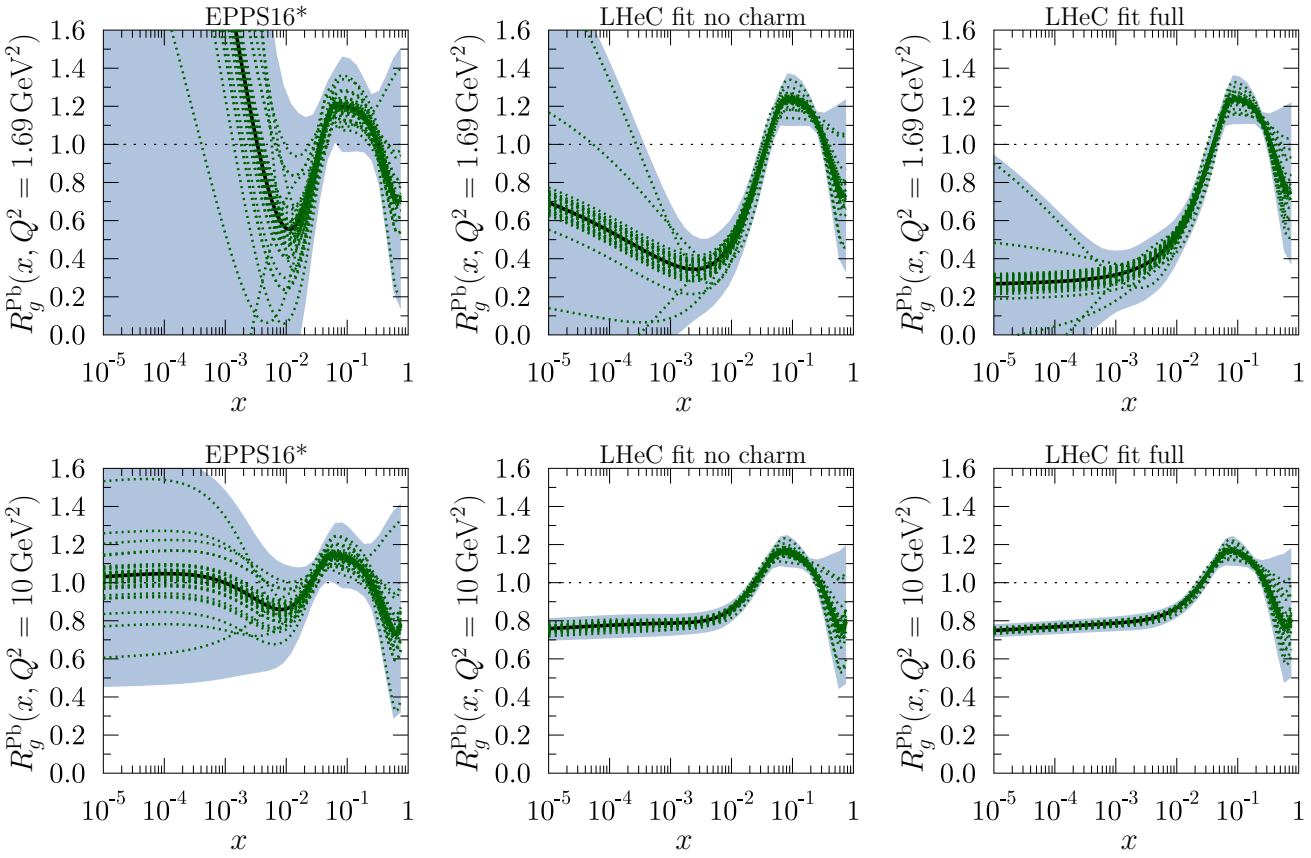

Figure 5.7: Upper panels: The gluon nuclear modification for Pb nucleus at $Q^2 = 1.69\,\mathrm{GeV}^2$ in EPPS16* (left), LHeC analysis without charm pseudodata (middle), and full LHeC analysis (right). The blue bands mark the total uncertainty and the green curves correspond to individual Hessian error sets. Lower panels: As the upper panels but at $Q^2 = 10\,\mathrm{GeV}^2$.

verify the existing ideas on flavour dependence of nuclear effects on parton densities [311].

5.3 Nuclear diffraction [Anna Stasto, Paul Newman]

In Sec. 4.2.6 we have discussed specific processes which will allow one to probe the details of the 3D structure of the proton. Inclusive diffraction on nuclei can provide important information about the nuclear diffractive parton distribution similarly to the diffraction on the proton, see Sec. 4.2.7. The same processes can be studied in the context of electron-ion scattering and used to learn about the partonic structure of nuclei. The diffractive vector meson production can be studied in the nuclear case as well, within the framework of the dipole model suitable for high energy and including non-linear effects in density. In the nuclear case though, one needs to make a distinction between the coherent and incoherent diffraction. In the coherent process, the nucleus scatters elastically and stays intact after the collision. In incoherent diffraction, the nucleus breaks up, and individual nucleons can be set free. Still, there will be a large rapidity gap between the produced diffractive system and the dissociated nucleus. It is expected that this process will dominate the diffractive cross section from medium to large values of momentum transfer. It is only in the region of small values of momentum transfer where the elastic diffraction is the dominant contribution. Dedicated instrumentation in the forward region must be constructed in order to clearly distinguish between the two scenarios. ***We need here some blurb on the ZDC***

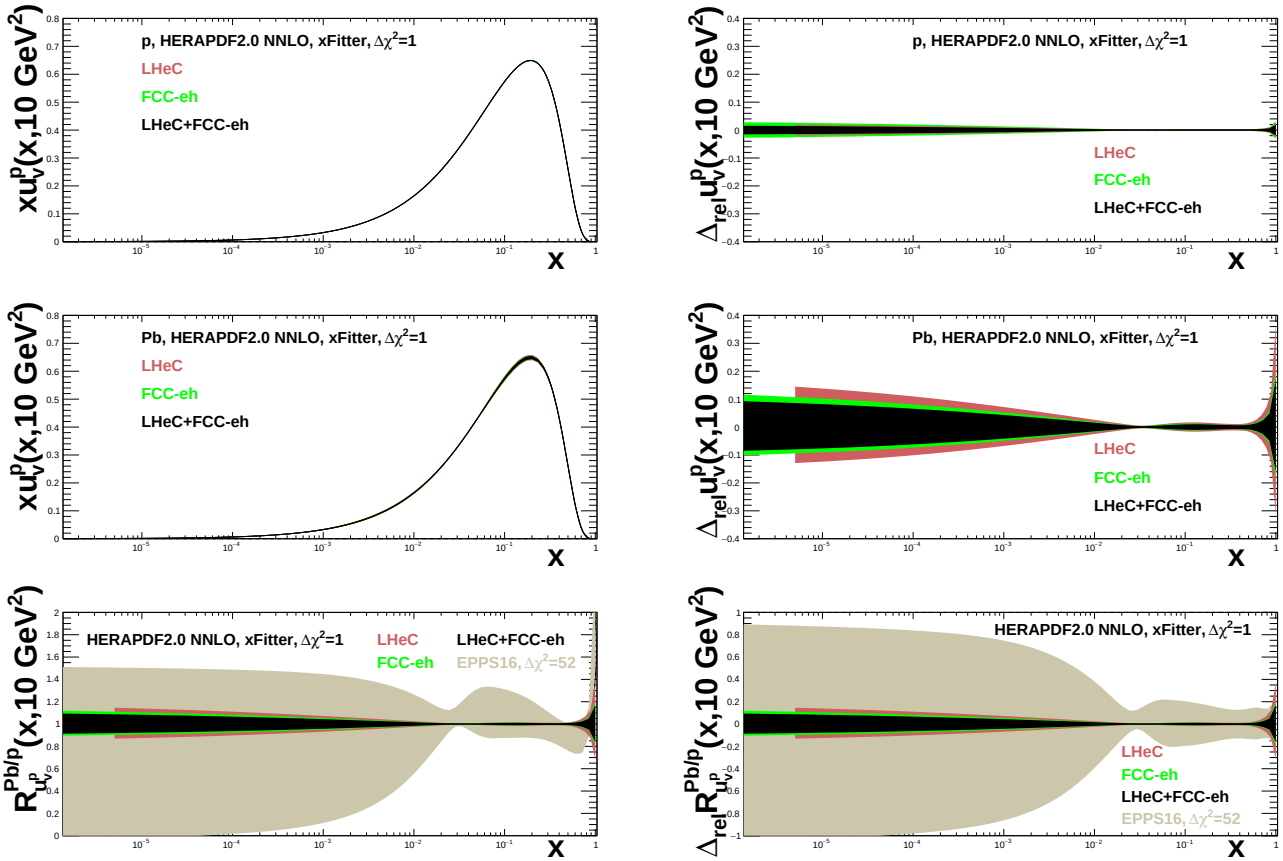

Figure 5.8: Distributions (left) and their relative uncertainties (right) of the valence u-quark density in proton (top), Pb (middle) and the corresponding nuclear modifications factor (bottom) in an analysis of ep and ePb LHeC and FCC-eh NC plus CC pseudodata using xFitter (both a single set of data and all combined), compared to the results of EPPS16 [287], see the text for details.

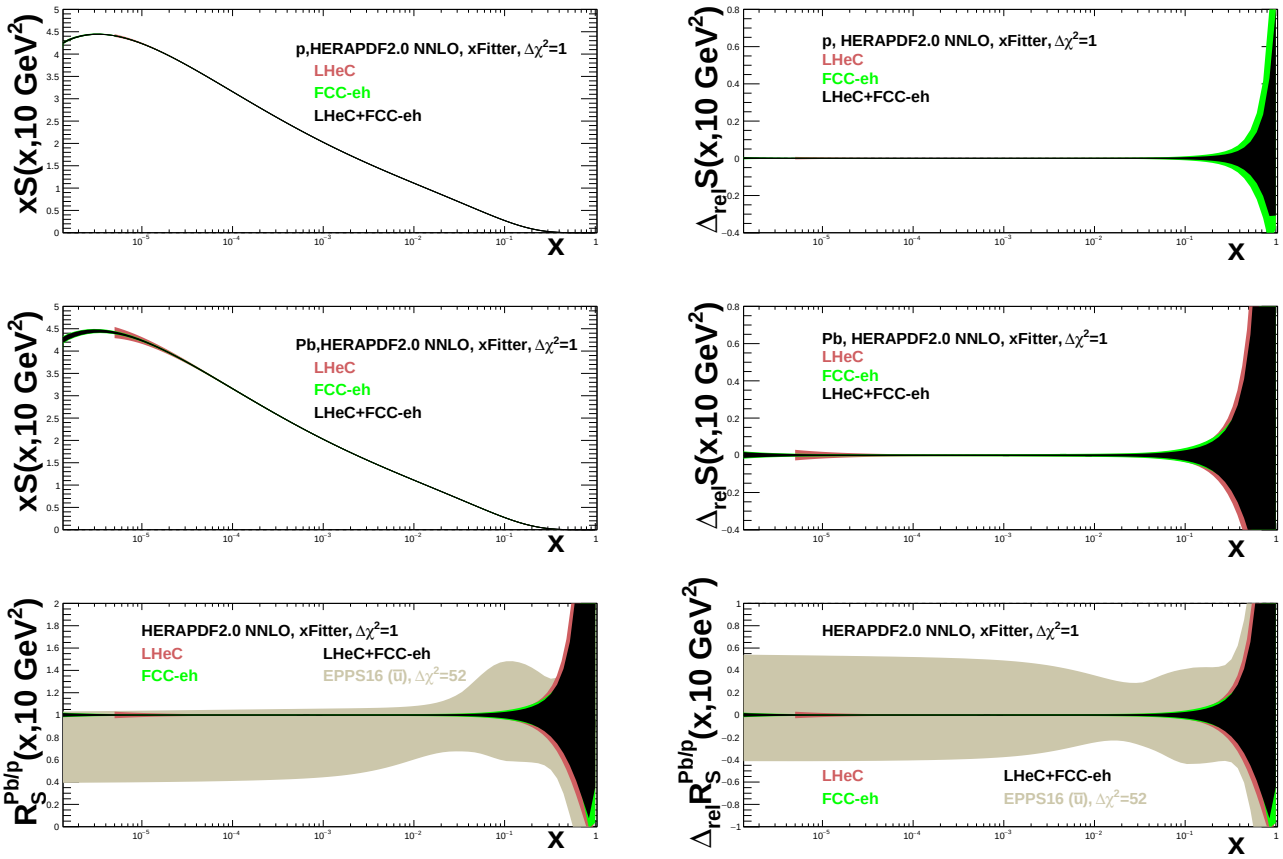

Figure 5.9: Distributions (left) and their relative uncertainties (right) of the sea quark density in proton (top), Pb (middle) and the corresponding nuclear modifications factor (bottom) in an analysis of ep and ePb LHeC and FCC-eh NC plus CC pseudodata using xFitter (both a single set of data and all combined), compared to the results of EPPS16 [287] for $\bar{u}$, see the text for details.

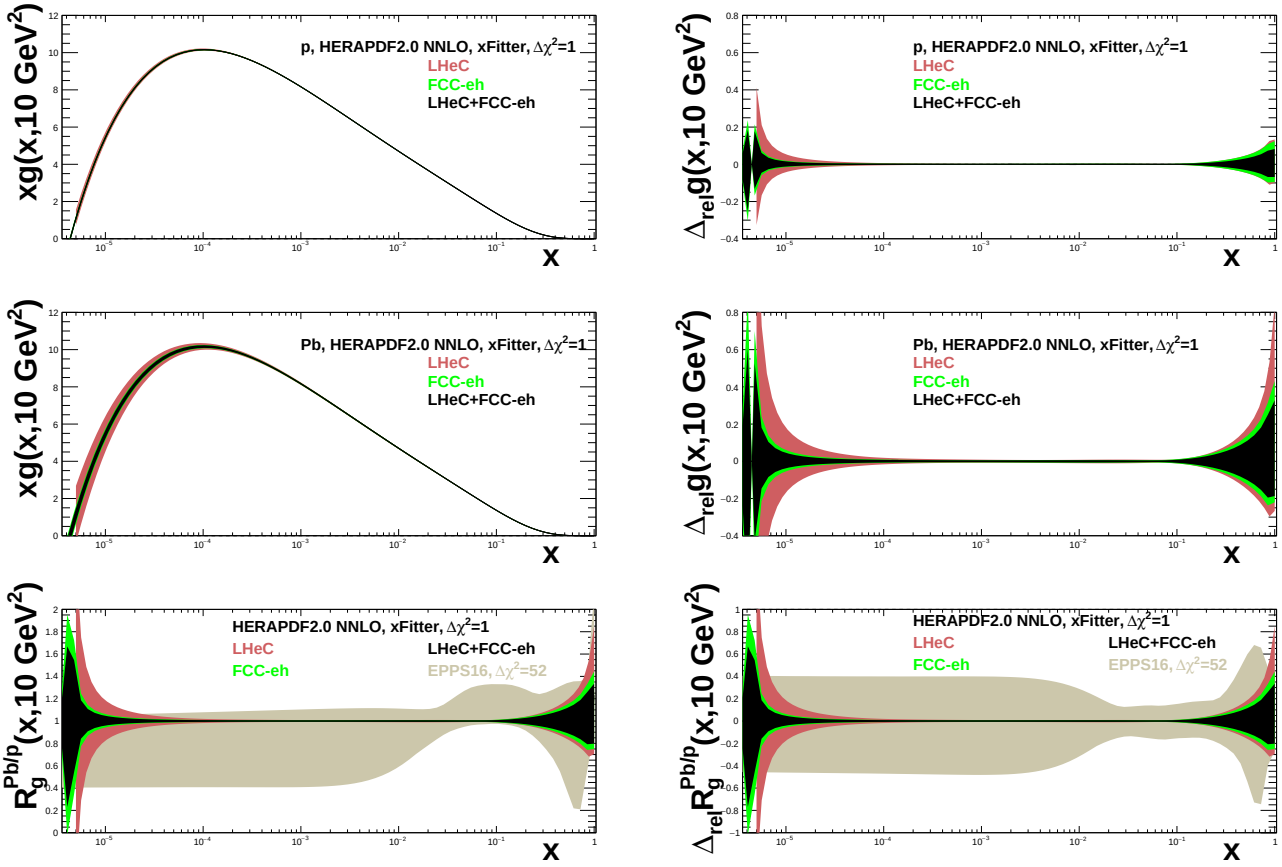

Figure 5.10: Distributions (left) and their relative uncertainties (right) of the gluon density in proton (top), Pb (middle) and the corresponding nuclear modifications factor (bottom) in an analysis of ep and ePb LHeC and FCC-eh NC plus CC pseudodata using xFitter (both a single set of data and all combined), compared to the results of EPPS16 [287], see the text for details.

5.3.1 Exclusive vector meson diffraction

Calculations in the case of Pb for the elastic diffractive J/ψ production were performed using the dipole model [120], see Sec. 4.2.6. In order to apply the dipole model calculation to the nuclear case, one takes the independent scattering approximation that is Glauber theory [325]. The dipole amplitude can then be represented in the form

$$N_A(x, \mathbf{r}, \mathbf{b}) \;=\; 1 - \prod_{i=1}^{A} \left[1 - N(x, \mathbf{r}, \mathbf{b} - \mathbf{b}_i)\right] . \tag{5.2}$$

Here $N(x, \mathbf{r}, \mathbf{b} - \mathbf{b}_i)$ is the dipole amplitude for the nucleon (see Sec. 4.2.6) and $\mathbf{b}_i$ denote the transverse positions of the nucleons in the nucleus. The interpretation of Eq. (5.2) is that $1 - N$ is the probability not to scatter off an individual nucleon, and thus $\prod_{i=1}^{A} [1 - N(\mathbf{r}, \mathbf{b} - \mathbf{b}_i, x)]$ is the probability not to scatter off the entire nucleus.

In addition, in the following simulation one includes the fluctuations of the density profile in the proton, following the prescription given in [118, 119, 120]. To include these proton structure fluctuations one assumes that the gluonic density of the proton in the transverse plane is distributed around three constituent quarks (hot spots). These hot spots are assumed to be Gaussian. In practical terms one replaces the proton profile $T_p(\mathbf{b})$

$$T_p(\mathbf{b}) = \frac{1}{2\pi B_p} e^{-b^2/(2B_p)}$$

by the function

$$T_p(\mathbf{b}) = \sum_{i=1}^{3} T_q(\mathbf{b} - \mathbf{b}_{q,i}) \; ,$$

where the 'quark' density profile is given by

$$T_q(\mathbf{b}) = \frac{1}{2\pi B_q} e^{-b^2/(2B_q)} \; .$$

Here $\mathbf{b}_{q,i}$ are the location of the hotspots that are sampled from a two dimensional Gaussian distribution whose width is given by parameter B_{qc}. The free parameters B_q and B_{qc} were obtained in [119] by comparing with HERA data on coherent and incoherent J/ψ production at photon-proton centre-of-mass energy $W =$ 75 GeV, corresponding to $x_{IP} = 10^{-3}$. The proton fluctuation parameters obtained are $B_{qc} = 3.3$ GeV^{-2}, $B_q = 0.7$ GeV^{-2}.

The results for the differential cross section at $t = 0$ for diffractive elastic production of J/ψ as a function of (virtual) photon-proton energy W for fixed values of Q^2 are shown in Figs. 5.11 and Figs. 5.12. The calculations for Pb are compared to those on the proton target. We see that the cross sections for the nuclear case increase with energy slower than for the proton case and are always smaller. Note that we have already rescaled the diffractive cross section by a factor A^2, as appropriate for comparison of the diffractive cross section on proton and nucleus. In the absence of nuclear corrections this ratio should be equal to 1. The differences between the scattering off a nucleus and a proton are also a function of Q^2. They are larger for smaller values of Q^2 and for photoproduction. This is understood from the dipole formulae, see Eqs. (4.4), (4.5), (4.6). As explained previously, larger values of scale Q^2 select smaller size dipoles, for which the density effects are smaller. Similarly, the differences between Pb and proton are larger for higher energies. This is because the dipole amplitude grows with decreasing values of x which are probed when the energy is increased, and thus the non-linear density effects are more prominent at low values of x and low values of Q^2.

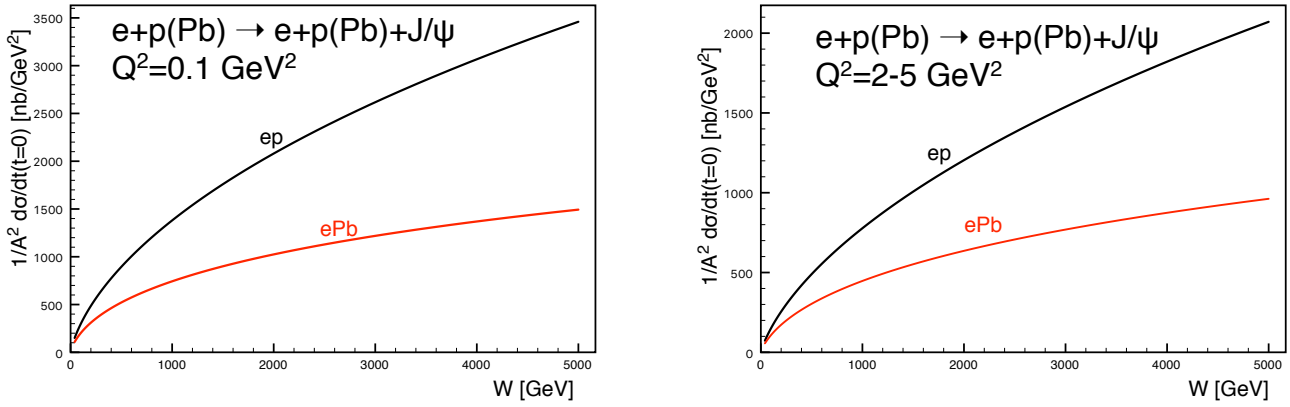

Figure 5.11: Cross section for the elastic diffractive production of the vector meson J/ψ in ePb (red solid curves) and ep (black solid curves) collisions, as a function of the energy W. Left plot: photoproduction case $Q^2 \simeq 0$, right plot $Q^2 = 2 - 5$ GeV^2

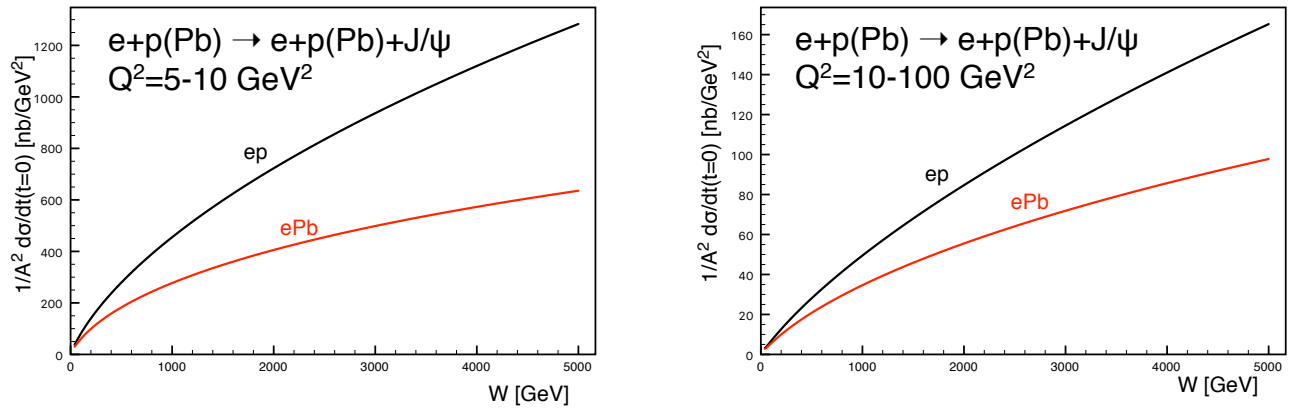

Figure 5.12: Cross section for the elastic diffractive production of the vector meson J/ψ in ePb (red solid curves) and ep (black solid curves) collisions, as a function of the energy W. Left plot: $Q^2 = 5 - 10$ GeV^2, right plot $Q^2 = 10 - 100$ GeV^2.

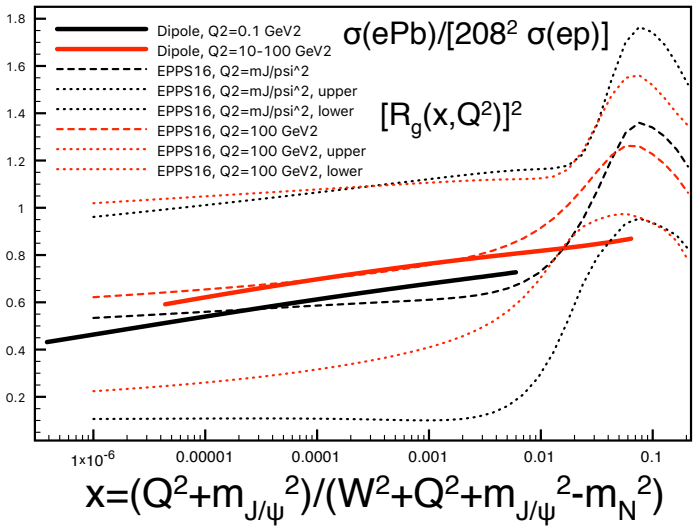

Figure 5.13: Ratio of coherent diffractive cross sections for Pb and proton as a function of variable x defined in Eq. (5.3). Solid lines: dipole model calculation, for $Q^2 = 0.1$ GeV^2 (black) and $Q^2 = 10 - 100$ GeV^2. Dotted and dashed lines correspond to the nuclear ratio for the gluon density squared using the EPPS16 parametrisation of the nuclear parton distribution functions. Black and red dashed lines are the central sets for $Q^2 = M^2_{J/\psi}$ and $Q^2 = 100$ GeV^2 respectively. The dotted lines correspond to the lowest and highest sets in EPPS16 parametrisation. The difference between the two dotted lines is indicative of the parametrisation uncertainty for the nuclear ratio. These ratios, that can also be measured in ultraperipheral collisions [326], are larger that the values $0.2-0.4$ at $x \simeq 10^{-5}$ predicted by the relation between diffraction and nuclear shadowing [290].

These findings case be summarised by inspecting the ratio of the cross sections, presented as a function of x defined as

$$x = \frac{Q^2 + m^2_{J/\psi}}{Q^2 + W^2 + m^2_{J/\psi} - m^2_N} \, . \tag{5.3}$$

which is shown in Fig. 5.13. We observe that the ratio is smaller for smaller values of Q^2, and it decreases for decreasing value of x. The results from the dipole model calculations are compared with the ratio of the gluon density squared obtained from the nuclear PDFs using the EPPS16 set. The reason why one can compare the diffractive cross section ratios with the ratios for the gluon density squared can be understood from Eqs. (4.4) and (4.5). The diffractive amplitude is proportional to the gluon density $xg(x, Q^2)$. On the other hand the diffractive cross section will be proportional to the amplitude squared, thus resulting sensitive to the square of the gluon density. The nuclear PDFs have large uncertainties, which is indicated by the region between the two sets of dotted lines. The EPPS16 parametrisation is practically unconstrained in the region below $x = 0.01$. Nevertheless, the estimate based on the dipole model calculation and the central value of the EPPS16 parametrisation are consistent with each other. This strongly suggests that nuclear effects alone will have difficulties in disentangling saturation effects and that only through an analysis of data on proton and nucleus firm conclusions will be established on the existence of a new non-linear regime of QCD.

In Fig. 5.14 we show the differential cross section $d\sigma/dt$ as a function of the negative momentum transfer $-t$ for the case of coherent and incoherent production. Coherent and incoherent diffraction cross sections are computed from the dipole model in the following way. The coherent diffractive cross section is obtained by averaging the diffractive scattering amplitude over the target configurations and taking the square

$$\frac{d\sigma}{dt} = \frac{1}{16\pi} |\langle \mathcal{A}(x, Q, \Delta) \rangle|^2 \, .$$

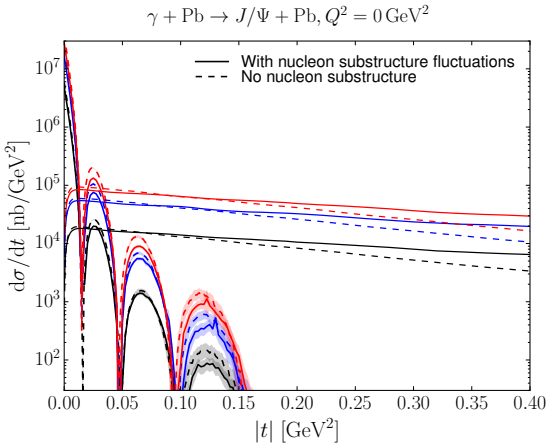

Figure 5.14: The differential cross section for the elastic diffractive production of J/ψ in ePb as a function of the negative momentum transfer $-t$, for photoproduction $Q^2 = 0$. Lines showing dips are for coherent production, and those extending to large $|t|$ for incoherent. Solid (dashed) lines are the results with (without) nucleon substructure fluctuations. Black, blue, red are for $W = 0.1, 0.813, 2.5$ TeV, respectively.

Here the brackets $\langle \dots \rangle$ refer to averages over different configurations of the target. The incoherent cross section is obtained by subtracting the coherent cross section from the total diffractive cross section. It is standardly assumed that it takes the form of a variance of the diffractive scattering amplitude

$$\frac{d\sigma}{dt} = \frac{1}{16\pi}\left(\langle|\mathcal{A}(x,Q,\Delta)|\rangle^2 - |\langle\mathcal{A}(x,Q,\Delta)\rangle|^2\right),$$

which should be valid for small $|t|$. The t dependence, and the relation between the impact parameter and t through the Fourier transform, makes diffractive scattering a sensitive probe of the internal geometric structure of hadrons and nuclei. In particular, because the incoherent cross section has the form of a variance of the amplitude, it is sensitive to the amount of fluctuations in impact parameter space.

The results in Fig. 5.14 (results for higher Q^2 are very similar) indicate that the incoherent production is dominant for most values of $-t$, except for the very small momentum transfers, about $|t| < 0.02$ GeV^2. Thus, dedicated instrumentation which will allow to distinguish between the two cases is essential if one wants to measure the coherent process in a reasonably wide range of $|t|$. As in the proton case, the coherent t distribution exhibits the characteristic dips. However, in the case of the nuclear targets the dips occur for much smaller values of momenta t. This is related to the much larger value of the dipole amplitude for a wide range of impact parameters in the case of nuclear targets compared to the proton case.

Another interesting aspect, see Sec. 4.2.6, is the effect of the transverse structure of the proton in nuclear coherent and incoherent diffraction. For example, in the formulation shown above [120] a fixed number of hot spots was considered, while in [124] (see also [121] for a realisation using small-x evolution) a growing number with $1/x$ is implemented. In both cases, the ratio of incoherent to coherent diffraction decreases with W, being smaller for larger nuclei. This decrease is sensitive to the details of the distribution of hot spots - thus, to the fluctuations of the gluon distribution in transverse space. It also shows interesting dependences on the mass of the produced vector meson and on Q^2, being the ratio smaller for lighter vector mesons and for lower Q^2. Besides, they have some effects on the distributions in momentum transfer, see Fig. 5.14. In order to check these ideas, both the experimental capability to separate coherent form incoherent diffraction, and a large lever arm in W and Q^2 as available at the LHeC, are required.

We thus conclude that by investigating coherent and incoherent diffractive scattering on nuclei, one gets unique insight into the spatial structure of matter in nuclei. On the one hand, the coherent cross section,

which is obtained by averaging the amplitude before squaring it, is sensitive to the average spatial density distribution of gluons in transverse space. On the other hand, the incoherent cross section, which is the variance of the amplitude with respect to the initial nucleon configurations of the nucleus, measures fluctuations of the gluon density inside the nucleus. In the case of a nucleus, diffractive production rate is controlled by two different scales related to the proton and nucleus size. At momentum scales corresponding to the nucleon size $|t| \sim 1/R_p^2$ the diffractive cross section is almost purely incoherent. The t-distribution in coherent diffractive production off nucleus gives rise to a dip-type structure for both saturation and non-saturation models, while in the case of incoherent production at small $|t|$, both saturation and non-saturation models do not lead to dips [120]. This is in drastic contrast to the diffractive production off the proton where only saturation models lead to a dip-type structure in the t-distribution at values of $|t|$ that can be experimentally accessible. Therefore, diffractive production offers a unique opportunity to measure spatial distribution of partons in the protons and nuclei. It is also excellent tool to investigate the approach to unitarity in the high energy limit of QCD.

While we have focused here on J/ψ production, lighter vector mesons like ρ, ω, ϕ could also be studied. They should show a different Q^2 dependence and their larger sizes would make them lie closer to the black disk regime. Also the dominance of two-jet events in photoproduction would provide sensitivity to the approach to the unitarity limit [290].

5.3.2 Inclusive diffraction on nuclei

In Sec. 4.2.7, a study of the prospects for extracting diffractive partons densities in the proton was presenting following [131]. Similar considerations apply to diffraction in eA as to ep collisions. The main difference is the larger contribution from incoherent diffraction[3] $e + A \to e + X + A^*$ than from coherent diffraction $e+A \to e+X+A$, the former dominating for $|t|$ larger than a few hundredths of a GeV^2. In the following we focus on coherent diffraction, which could be distinguished from the incoherent case using forward detectors [1].

Assuming the same framework (collinear factorization for hard diffraction, Eq. (4.10), and Regge factorization, Eq. (4.11) described for ep in Sec. 4.2.7 to hold for eA, nuclear diffractive PDFs (nDPDFs) can be extracted from the diffractive reduced cross sections. It should be noted that such nDPDFs have never been measured. With the same electron energy $E_e = 60$ GeV and nuclear beams with $E_N = 2.76$ TeV/nucleon for the LHeC, respectively, the kinematic coverage is very similar to that shown in Fig. 4.37. For details, please see [131].

The nuclear modification factors for $F_2^{D(3)}$ and $F_L^{D(3)}$ from the FGS models [290] are shown in Fig. 5.15, where, in analogy to Eq. (5.1), the diffractive nuclear modification factor reads

$$R_k^A(\beta, \xi, Q^2) = \frac{f_{k/A}^{D(3)}(\beta, \xi, Q^2)}{A\, f_{k/p}^{D(3)}(\beta, \xi, Q^2)} \,. \tag{5.4}$$

The pseudodata for the reduced cross sections are generated assuming 5% systematic error and statistic errors calculated for the luminosity of 2 fb^{-1}. A selected subset of the simulated data is shown in Fig. 5.16. The large kinematic coverage and small uncertainty (dominated by the assumed systematics) illustrated in this figure compared to Fig. 4.39 make it clear that an accurate extraction of nDPDFs in ^{208}Pb in an extended kinematic region, similar to that shown in Figs. 4.40 and 4.41, will be possible.

[3] A^* denotes a final state in which the nucleus has dissociated to a system of at least two hadrons, but the rapidity gap signature that defines the diffractive event is still present.

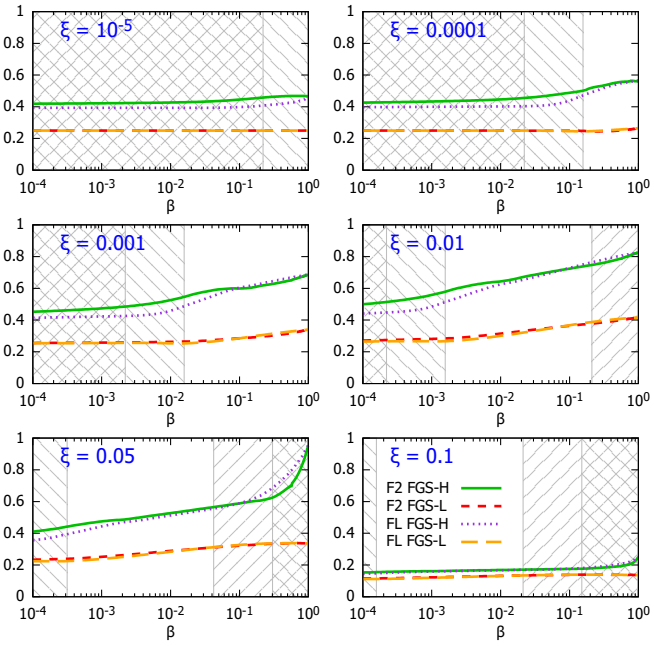

Figure 5.15: Nuclear modification factor, Eq. (5.4), for $F_2^{D(3)}$ and $F_L^{D(3)}$ in ^{208}Pb versus β, at $Q^2 = 10$ GeV^2 and for different ξ, for the models H and L in [290]. The '\' and '/' hatched areas show kinematically excluded regions for $E = 2.76$ and 19.7 TeV/nucleon, respectively.

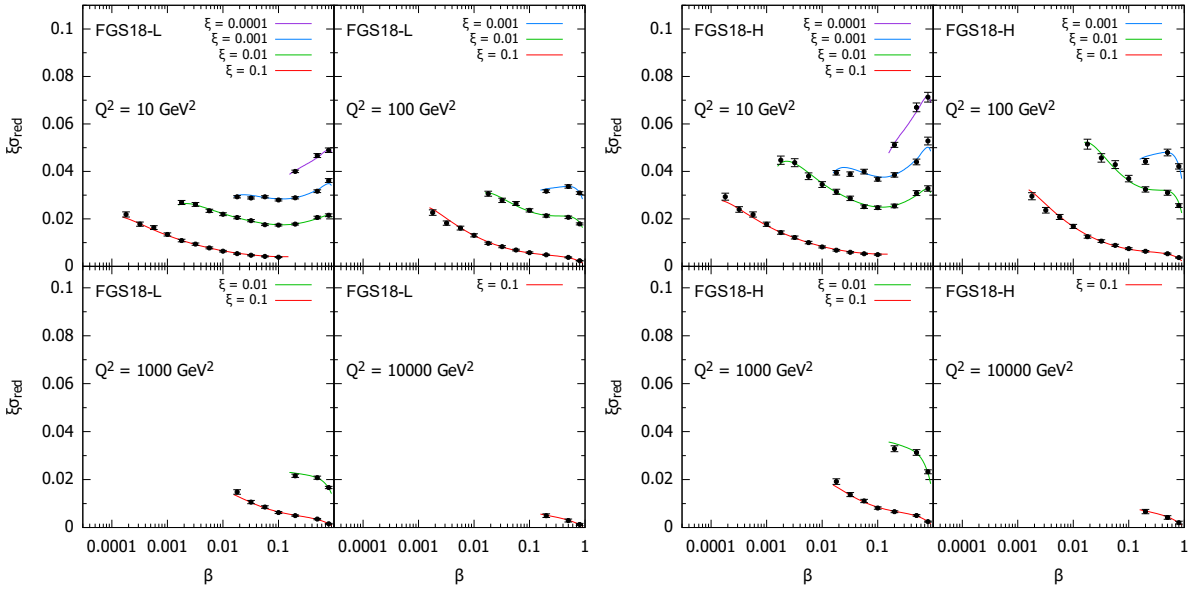

Figure 5.16: A selected subset of simulated data for the diffractive reduced cross section as a function of β in bins of ξ and Q^2 for $e\,^{208}$Pb collisions at the LHeC, in the models in [290]. The curves for $\xi = 0.01, 0.001, 0.0001$ are shifted up by 0.01, 0.02, 0.03, respectively.

5.4 New Dynamics at Small x with Nuclear Targets [Nestor Armesto]

As discussed in Sec. 4.2.4, theoretical expectations [292] indicate that fixed-order perturbation theory leading to the DGLAP evolution equations should eventually fail. When x decreases, $\alpha_s \ln x$ becomes large and these large logarithms must be resummed, leading to the BFKL equation. Furthermore, when parton density becomes large the linear approximation that underlies both DGLAP and BFKL breaks, and non-linear processes must be taken into account to compute parton evolution. The CGC [291] offers a non-perturbative but weak coupling effective theory to treat dense parton systems in a systematic and controlled way. One of the important predictions of the CGC is that in a dense parton system saturation occurs with emergence of a new dynamical scale – the saturation scale Q_s, which increases with the energy.

Parton density in a hadron becomes high both through evolution – when energy or $1/x$ becomes large, and/or when partons are accumulated by overlapping nucleons – when mass number A becomes large in a nucleus. In the nucleus rest frame, the virtual photon fluctuations at small $x < (2m_N R_A)^{-1}$, with m_N the nucleon mass and R_A the nuclear radius, acquire a lifetime larger than the nuclear size and, thus, all partons within a transverse area $\sim 1/Q^2$ are simultaneously probed. Actually, the parameter determining the transition between linear and non-linear dynamics is the parton density and, therefore, the onset of this new regime of QCD and its explanation must be tested, as commented in [1], exploring both decreasing values of x and increasing values of A in a kinematic $x - Q^2$ region where, in order to be sensitive to differences in evolution, enough lever arm in $Q^2 \gg \Lambda^2_{\rm QCD}$ at small x is available. The saturation scale Q_s that characterises the typical gluon momentum in a saturated hadron wave function increases with nuclear size, $Q_s^2 \propto A^{1/3}$. Therefore, in eA collisions the perturbatively saturated regime is achieved at parametrically larger x than in a proton – a prediction not only of the CGC but of all multiple scattering models that anticipate an approach to the black disk, unitarity limit.

The opportunities to establish the existence of saturation in lepton-nucleus collisions are numerous. They include inclusive observables, both total and diffractive cross sections, and less inclusive ones like correlations:

- Tension in DGLAP fits for inclusive observables: As discussed in [1, 183] and in Sec. 4.2.10, deviations from fixed-order perturbation theory can be tested by the tension that would appear in the description within a DGLAP fit of observables with different sensitivities to the sea and the glue, for example F_2 and F_L (or reduced cross sections at different energies) or $F_2^{\rm inclusive}$ and $F_2^{\rm heavy\ quarks}$. In [327], such exercise was performed considering F_2 and F_L pseudodata for eAu collisions at the EIC [100] using reweighting techniques. While the results for EIC energies are shown not to be conclusive due to the reduced lever arm in $Q^2 > Q_s^2 \gg \Lambda^2_{\rm QCD}$, the much larger centre-of-mass energies at the LHeC (and FCC-eh) should make possible a search for tensions between different observables.

- Saturation effects on diffraction: A longstanding prediction of saturation [105, 328, 329] is a modification of the diffractive cross section in nuclei with respect to protons, with a suppression (enhancement) at small (large) β due to the approach of the nucleus to the black disk limit, where elastic and diffractive scattering become maximal, and the behaviour of the different Fock components of the virtual photon wave function. Such effects can also be discussed in terms of a competition of nuclear shadowing with the probability that the event remains diffractive in the multiple scattering process [290]. This leads to the generic expectation of an enhancement of the ratio of the coherent diffractive cross section in nucleus over that in protons, in non-linear approaches with respect to linear ones [100].

- Correlations: Correlations have been considered since long ago as sensitive probes of the underlying production dynamics. For example, the cross section for the production of two jets with the same hardness and widely separated in rapidity, called Mueller-Navelet jets [330], was proposed as a test of BFKL versus DGLAP dynamics, but the effect of saturation has not been widely studied although it has the large potentiality of differentiating linear resummation from non-linear saturation where non-trivial nuclear effects could appear. They were analysed in [1] for the LHeC kinematics, both

in inclusive and diffractive events, see the formalism in [331]. On the other hand, the azimuthal decorrelation of particles and jets when saturation effects are at work – at small x, studied by the difference between collisions involving proton and nuclei, was proposed long ago at the Relativistic Hadron Collider [332, 333]. It was studied in [1] for the LHeC kinematics, see recent developments in [334] and the extension to forward dijet production in [335]. It could also be analysed in ultraperipheral collisions at the LHC, see Sec. 8.4.

5.5 Collective effects in dense environments – the 'ridge'

One of the most striking discoveries [336] at the LHC is that in all collision systems, from small (pp and pA) to large (AA), many of the features (see the reviews [337, 338, 339] and references therein) that in heavy ion collisions are taken as indicative of the production of a dense hot partonic medium appear. The most celebrated of such features is the long rapidity range particle correlations collimated in azimuth, named the ridge, shown in Fig. 5.17. The dynamics underlying this phenomena, either the formation of QGP and the existence of strong final state interactions, or some initial state dynamics that leaves imprint on the final observables, is under discussion [340]. While observed in photoproduction on Pb in UPCs at the LHC [341], its existence in smaller systems like e^+e^- [342] at LEP and ep at HERA [343] has been scrutinised but the results are not conclusive. In this respect, ep and eA collisions may offer crucial information. For example, the collision of the virtual photon with the proton at the LHeC can be considered as a high energy collision of two jets or "flux tubes". As discussed in Refs. [344, 345] and illustrated in Fig. 5.17, this can lead to the production of "ridges" and other novel configurations of gluons and quarks.

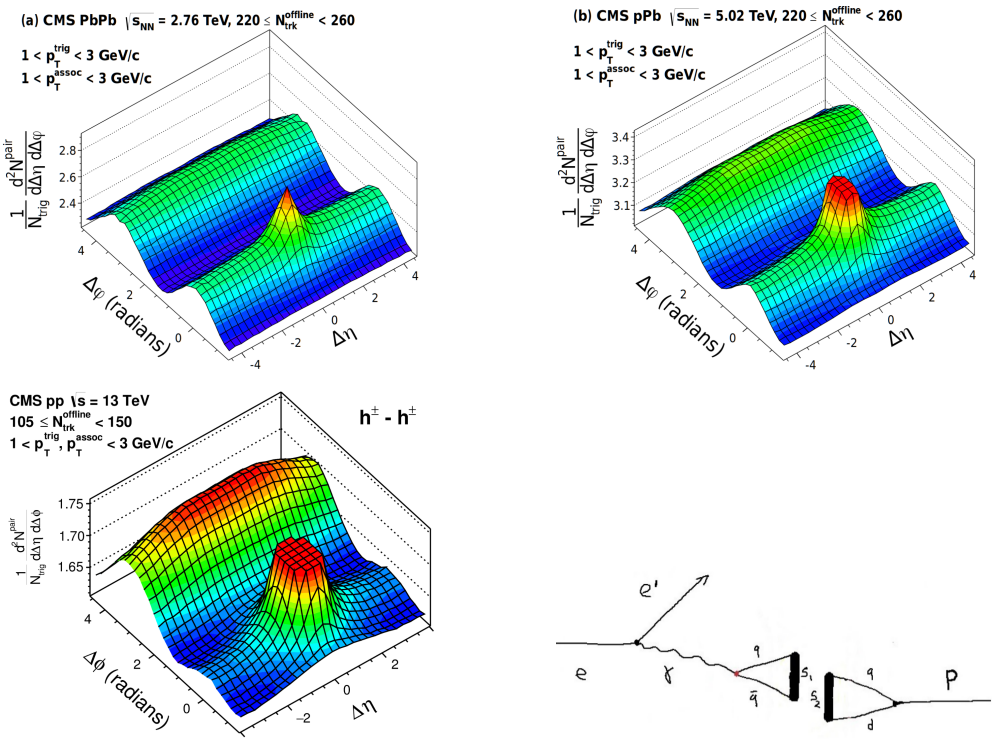

Figure 5.17: Top left to bottom right: Collective effects seen in high-multiplicity two-particle azimuthal correlation, as observed by CMS in PbPb, pPb [346], and pp [347] collisions. Schematic illustration for the production of "ridge"-like effects in ep or eA scattering at the LHeC [345].

5.6 Novel QCD Nuclear Phenomena at the LHeC

One of the most important theoretical tool in high energy physics is Dirac's light-front (LF) time: $\tau = x^+ = t + z/c$, the time along the light-front [348], a concept which allows all of the tools and insights of Schrödinger's quantum mechanics and the Hamiltonian formalism to be applied to relativistic physics [349]. When one takes a photograph, the object is observed at a fixed LF time. Similarly, Compton $\gamma p \to \gamma' p''$ and deep-inelastic lepton-proton scattering are measurements of proton structure at fixed LF time. Unlike ordinary "instant time" t, physics at fixed τ is Poincaré invariant; i.e., independent of the observer's Lorentz frame. Observations at fixed τ are made within the causal horizon. LF time τ reduces to ordinary time t in the nonrelativistic limit $c \to \infty$.

The LF wavefunctions (LFWF) of hadrons $\Psi_n^H(x_i, \vec{k}_{\perp i}, \lambda_i) =< \Psi_H | n >$, the Fock state projections of the eigensolution of the QCD LF Hamiltonian $H_{QCD}|\Psi_H >= M_H^2 \Psi_H >$. They encode the underlying structure of bound states in quantum field theory and underlie virtually every observable in hadron physics. Hadronic LFWFs can also be measured directly by the Ashery method [350], the coherent diffractive dissociation of high energy hadrons into jets [351, 352]. The diffractive dissociation of a high energy hadron into quark and gluon jets by two-gluon exchange, the cross-section measures the square of the second transverse derivative of the projectile LFWF. Similarly, the dissociation of a high energy atom such as positronium or "true muonium" ($[\mu^+\mu^-]$) can be used to measure the transverse derivative of its LFWFs.

Hadronic LFWFs are defined at fixed $\tau = -x^+ = t+z/c$; they are thus off-shell in the total $P^- = P^0 - P^z$, not energy P^0 [349]. Thus LFWFs are also off-shell in $\mathcal{M}^2 = P^+P^- - P_\perp^2 = [\sum_i k_i^\mu]^2 = \sum_i \frac{k_\perp^2 + m^2}{x}_i$, the invariant mass squared of the constituents in the n-particle Fock state. LFWFs are thus functions of the invariant mass squared of the constituents in the Fock state. For a two-particle Fock state: $\mathcal{M}^2 = \frac{k_\perp^2 + m^2}{x(1-x)}$. Thus the constituent transverse momenta $k_{\perp i}^2$ do appear alone as a separate factor in the LFWF; the transverse momenta are always always coupled to the longitudinal LF momentum fractions x_i. This is the light-front version of rotational invariance. Only positive $k_i^+ = k_i^0 + k_i^z \geq 0$ and $0 \leq x_i = \frac{k^+ -}{P^+} \leq 1$ appear, where $\sum_i x_i = 1$. In addition, $J^z = \sum_i L_i^z + S_i^z$, as well as $P^+ = \sum_i k_i^+$ and $\vec{P}_\perp = \sum_i \vec{k}_{\perp i}$ are conserved at every vertex, essential covariant kinematical constraints. A remarkable property: the anomalous gravitomagnetic moment of every LF Fock state vanishes at $Q^2 = 0$. The LFWFs of bound states are off-shell in $P^- = \sum k^- I$, but they tend to be maximal at minimal off-shellness; i.e. minimal invariant mass. In fact, in the holographic LFWFs where color is confined, the LFWFs of hadrons have fast Gaussian fall-off in invariant mass. This feature also underlie intrinsic heavy quark Fock states: the LFWFs have maximal support when all of the constituents have the same rapidity y_i; i.e., $x_i \propto \sqrt{m_i^2 + k_{\perp i}^2}$. Thus the heavy quarks have the highest momentum fractions x_i.

Conversely, light-front wavefunctions provide the boost-invariant transition amplitude which convert the free quark and gluons into the hadronic eigenstates of QCD. Thus knowing the LFWFs, allows one to compute "hadronization at the amplitude level" – how the colored quarks and gluons produced in a deep inelastic scattering event $ep \to e'X$ at the LHeC are confined and emerge as final-state hadrons.

The LF formalism leads to many novel nuclear phenomena, such as "hidden color" [353] "color transparency" [354], "nuclear-bound quarkonium" [355], "nuclear shadowing and antishadowing" of nuclear structure functions, etc. For example, there are five distinct color-singlet QCD Fock state representations of the six color-triplet quarks of the deuteron. These hidden-color Fock states become manifest when the deuteron fluctuates to a small transverse size, as in measurements of the deuteron form factor at large momentum transfer. One can also probe the hidden-color Fock states of the deuteron by studying the final state of the dissociation of the deuteron in deep inelastic lepton scattering at the LHeC $eD \to e'X$ where X can be $\Delta^{++} + \Delta^-$, six quark jets, or other novel color-singlet final states.

The LF wave functions provide the input for scattering experiments at the amplitude level, encoding the

structure of a projectile at a single light-front time τ [349]. For example, consider photon-ion collisions. The incoming photon probes the finite size structure of the incoming nucleus at fixed LF time, like a photograph – not at a fixed instant time, which is acausal. Since the nuclear state is an eigenstate of the LF Hamiltonian, its structure is independent of its momentum, as required by Poincaré invariance. One gets the same answer in the ion rest frame, the CM frame, or even if the incident particles move in the same direction, but collide transversely. There are no colliding "pancakes" using the LF formalism.

The resulting photon-ion cross-section is not point-like; it is shadowed: $\sigma(\gamma A \to X) = A^\alpha \sigma(\gamma N \to X)$, where A is the mass number of the ion, N stands for a nucleon, and the power $\alpha \approx 0.8$ reflects Glauber shadowing [356]. The shadowing stems from the destructive interference of two-step and one-step amplitudes, where the two-step processes involve diffractive reactions on a front-surface nucleon which shadows the interior nucleons. Thus the photon interacts primarily on the front surface. Similarly a high energy ion-ion collision $A_1 + A_2 \to X$ involves the overlap of the incident frame-independent LFWFs. The initial interaction on the front surface of the colliding ions can resemble a shock wave.

In the case of a deep inelastic lepton-nucleus collision $\gamma^* A \to X$, the two-step amplitude involves a leading-twist diffractive deep inelastic scattering (DDIS) $\gamma^* N_1 \to V^* N_1$ on a front surface nucleon N_1 and then the on-shell propagation of the vector system V^* to a downstream nucleon N_2 where it interacts inelastically: $V^* N_2 \to X$. If the DDIS involves Pomeron exchange, the two-step amplitude interferers destructively with the one-step amplitude $\gamma^* N_1 \to X$ thus producing shadowing of the nuclear parton distribution function at low $x_{bj} < 0.1$ where x_{bj} is the Bjorken scaling variable. On the other hand, if the DDIS process involves $I = 1$ Reggeon exchange, the interference is constructive, producing *flavor-dependent* leading-twist antishadowing [356] in the domain $0.1 < x_{bj} < 0.2$.

One can also show that the Gribov-Glauber processes, which arise from leading-twist diffractive deep inelastic scattering on nucleons and underly the shadowing and antishadowing of nuclear structure functions [356], prevent the application of the operator product expansion to the virtual Compton scattering amplitude $\gamma^* A \to \gamma^* A$ on nuclei and thus negate the validity of the momentum sum rule for deep inelastic nuclear structure functions [357].

Chapter 6

Higgs Physics with LHeC [Uta Klein, Bruce Mellado]

@From SJB. To be merged into Higgs chapter. Fig. 6.1 illustrates some key tests of electroweak theory at the LHeC, such as the Higgs coupling to Z^0 and $W^{\pm}$. The process $ep \to e'HX$ measures the fundamental $Z^0Z^0 \to H$ coupling underlying the $Z^0q \to Hq$ subprocess, Higgs emission in $ep \to \nu_e HX$ measures the Higgs coupling scattering to the W^- via the $W^-u \to H^0d$, and $W^-c \to Hb$ subprocesses. One can also measure the Higgs coupling to the b quark in $\gamma^*b \to Hb$ reactions. These processes are also sensitive to the heavy quark distributions in the proton $c(x,Q)$ and $b(x,Q)$, thus providing a test of the intrinsic non-perturbative heavy-quark Fock states in the proton at high x.

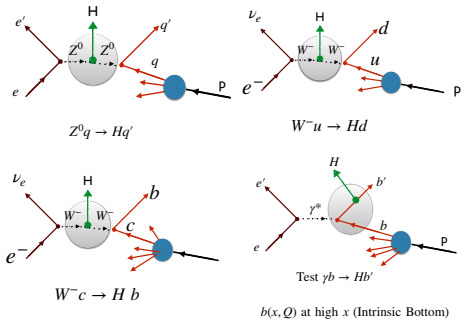

Figure 6.1: Representative Standard Model Higgs Production Processes at the LHeC

6.1 Signal Strength and Couplings [Max, Uta Klein]

6.2 Htt Coupling Measurement [Bruce Mellado]

6.3 Higgs Decay into Invisible Particles [Masahiro Kuze]

6.4 ep Measurement Potential in the EFT Framework [Jorge De Blas]

Chapter 7

Searches for Physics Beyond the Standard Model

[Georges Azuelos, Oliver Fischer, Monica D'Onofrio]

7.1 Introduction

The LHC was originally envisioned as the ultimate machine to search for physics beyond the Standard Model at the TeV scale. The absence of hints from New Physics (NP) in LHC data to date are presently changing this paradigm to two alternative scenarios: NP may actually reside at an even larger energy scale; NP may be at or below the TeV scale but more weakly coupled and thus hidden in the SM backgrounds [358].

The possibility for undiscovered NP below the TeV scale could be addressed by the LHeC, which is projected to operate when the LHC will be in its high luminosity phase. The electron-proton collider will endow the LHC searches with complementary search channels, which will allow to measure the same phenomenon in a different environment, add precision measurements, or lead to the discovery of a weak signal. A similar *pp*-*ep* synergy could be envisaged with higher proton beam energies at the FCC 100-km tunnel. With an electron beam of 60 GeV, the expected center of mass energies for *ep* could be 2.9 TeV for $E_p = 19$ TeV (Low-Energy FCC) and 3.5 TeV for $E_p = 50$ TeV (FCC).

It has been stated that in many cases the LHeC can provide detailed tests of features that are shared by leptons and quarks, see Ref. [1] and references therein. Below we list recent developments which discuss new physics opportunities at the LHeC and its potential future high-energy upgrades.

7.2 Extensions of the SM Higgs Sector

Presently it appears as if the discovered 125 GeV scalar is indeed the SM Higgs boson. It is not clear, however, if the scalar potential is truly that of the SM or if it is extended, possibly with additional degrees of freedom. Several extensions of the Higgs sector have been proposed and can be studied at the *ep* colliders with results often complementary to those of *pp* colliders and other future facilities.

7.2.1 Modifications of the Top-Higgs interaction

In electron-proton collisions the heavy top-quarks can be produced in association with a Higgs boson, which allows us to study the sensitivity of the LHeC or the FCC-he to the top-Higgs (tH) interaction. In Ref. [262] the sensitivity of the process $pe^- \to \bar{t}H\nu_e$ to the CP nature of the tH coupling is investigated, by considering a CP phase ζ_t at the ttH and bbH vertices. The authors conclude, based on several observables and with appropriate error fitting methodology, that better limits on ζ_t are obtained at LHeC than at HL-LHC. At

the design luminosity of 1 ab^{-1}, almost all values of ζ_t are excluded up to 4σ C.L. and the SM top-Higgs coupling could be measured relative to its SM value with a precision of $\kappa = 1.00 \pm 0.17$.

Flavour changing neutral currents (FCNC) are completely absent at tree-level in the SM and strongly constrained especially by low energy experiments. Anomalous flavor changing neutral current Yukawa interactions between the top quark, the Higgs boson, and either an up or charm quark are studied in Ref. [359], considering the Higgs decay modes $H \to \gamma\gamma, bb$ and $\tau\tau$ and considering $E_e = 150$ GeV. The results are updated in Ref. [258] for $E_e = 60$ GeV, including estimates for smaller electron beam energies, and the 2σ sensitivity on the branching ratio $\mathrm{Br}(t \to uh)$ is found to be 0.15×10^{-2}. Making use of the polarisation of the electron beam and multivariate techniques, Ref. [360] shows that limits on the branching ratio $\mathrm{Br}(t \to uh)$ of $\mathcal{O}(0.1)\%$ can be obtained, an improvement over present LHC limits of 0.19% [361, 362]. These results vary with E_e and E_p.

7.2.2 Charged scalars

The prospects to observe a light charged Higgs boson through the decay $H^+ \to c\bar{b}$ are investigated within the framework of the Two Higgs Doublet Model (2HDM) Type III, assuming a four-zero texture in the Yukawa matrices and a general Higgs potential [363]. The charged current production processes $e^-p \to \nu H^+ q$ are considered. The analyzed signature stems from the subsequent decay $H^+ \to c\bar{b}$. The parton level analysis includes irreducible SM backgrounds and limits from Higgs and flavor physics. The authors show that for $L = 100$ fb^{-1} a charged Higgs boson could be observed with about 3σ significance for masses between 100 and 200 GeV.

A similar study for the FCC-he (with $\sqrt{s} \approx 3.5$ TeV) is presented in Ref. [364], where a next-to-minimal supersymmetric model (NMSSM) was considered where $H^\pm \to sc + su$. Using dedicated optimisation techniques, the authors show that a light charged boson $H^\pm$ can be observed with maximal significance of 4.4 (2.2)σ provided its mass is at most $m_{H^\pm} = 114(121)$ GeV, for the total luminosity of 1 ab^{-1}.

An analysis for the prospects to discover the doubly charged Higgs bosons in the Georgi-Machacek model at the LHeC and the FCC-he is presented in Ref. [365]. Therein the production of a doubly-charged member of five-plet Higgs-bosons ($H_5^{\pm\pm}$), produced from vector boson fusion is studied. The authors find that 2 to 3 σ limits can be obtained for mixings $\sin(\theta_H)$ as low as 0.2, for $M(H_5) < 300$ GeV. The prospects can be improved at the FCC-he collider, where doubly charged Higgs bosons can be tested for masses $M_{H_5} < 400$ GeV, also for small scalar mixing angles.

The discovery prospects for the singly charged Higgs, $H_5^\pm$, in the Georgi-Machacek model are evaluated in Ref. [366]. The authors perform a multivariate analysis, including a fast detector simulation, and they consider the LHeC and the FCC-he for a mass range from 200 – 1000 GeV. They find that the LHeC can improve over current LHC limits on $H_5^\pm$ for masses up to about 400 GeV and scalar mixing angles $\sin\theta_H \sim 0.5$.

7.2.3 Neutral scalars

Neutral scalar bosons generally appear in many extensions of the scalar potential. They can be added directly, as $SU(1)$ singlets, or be part of higher representation $SU(2)$ multiplets. They generally mix with the Higgs boson, from which they inherit a Higgs-like phenomenology.

The potential of testing the heavier CP-even scalar that is contained in the 2HDM Type-I is presented in Ref. [367]. Therein, the lighter scalar particle is considered to be a SM-like Higgs boson and the properties of a heavy scalar, assumed to have the specific mass 270 GeV, is discussed. The authors state that the final state $H \to hh$ is of particular interest, as it connects to the findings in Ref. [358].

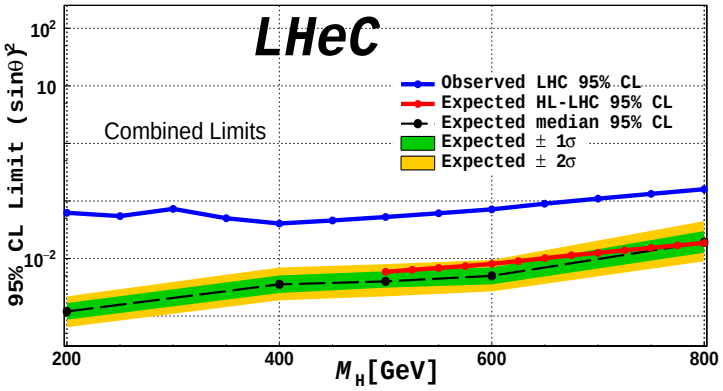

Figure 7.1: Expected exclusion limits (green and yellow bnds) for a heavy scalar search at the LHeC, assuming a systematic uncertainty on the SM background of 2% (from [368]). The blue line represents the current LHC limit at 95% CL as extracted from [369], the red line the forecast of the HL-LHC sensitivity via $h_2 \to ZZ$ searches from ref. [370]. The LHeC results correspond to an integrated luminosity of 1 ab^{-1}.

The prospects to search for a generic heavy neutral scalar particle are presented in detail Ref. [368]. The model is a minimal extension of the SM with one additional complex scalar singlet that mixes with the SM Higgs doublet, which governs its production and decay mode. The heavy scalar is produced via vector-boson fusion and decays into two vector bosons. A multivariate analysis is performed and detector simulation is taken into account. Masses between 200 and 800 GeV and scalar mixings as small as $\sin^2\alpha \sim 10^{-3}$ are considered. The resulting sensitivity for a total luminosity of 1 ab^{-1} is shown in Fig. 7.1, including existing bounds from the LHC and future HL-LHC projections. A significant improvement over existing LHC limits is found, with the LHeC probing scalar boson masses below ~ 500 GeV, a region which remains difficult at the HL-LHC.

The scalar bosons from the 2HDM Type-III framework may give rise to flavour violating signatures, which is discussed in Ref. [371]. The prospects to observe the light and heavy CP-even neutral Higgs bosons via their decays into flavor violating $b\bar{s}$ channels were studied with specific Yukawa textures and a general Higgs potential. The considered signature consists in one jet originating from b-hadron fragmentation (b-tagged jets) and one light-flavor jet in the central rapidity region, with a remaining jet in the forward region. Relevant SM backgrounds were considered and it is found that flavour violating decays of the SM-like Higgs boson would be accessible with $L = 100$ fb^{-1} at ep colliders, while for the heaviest scalar boson, with a mass of about 170 GeV, a total luminosity of about 1 ab^{-1} will give rise to $\mathcal{O}(1)$ events.

The prospects of observing the light CP-even neutral Higgs bosons via their decays into b-quarks, in the neutral and charged current production processes, considering the NMSSM framework, the MSSM with an additional singlet superfield, are studied in Ref. [372]. In this work the following constraints are incorporated into the spectrum: neutralino relic density corresponding to the observed dark matter relic density; direct and indirect mass bounds from searches for specific sparticles; the SM-like Higgs boson has a mass around 126 GeV and an invisible branching ratio below 0.25. The signal is given by three jets plus an electron or missing transverse momentum (E_T^{miss}) arising from the neutral (charged) current interaction, where two jets are required to be originating from a b-quark and the remaining jet is required to be in the forward region. For the cut-based analysis a number of reducible and irreducible SM backgrounds are considered and it includes a fast detector simulation with an adaption of the LHeC detector. It is found that the boson h_1 could be observable for some of the NMSSM benchmark points, at up to 2.5σ level in the $e + 3j$ channel up to masses of 75 GeV; in the $3j + E_T^{miss}$ channel h_1 could be discovered at 2.4σ level up to masses of 88 GeV with $L = 100$ fb^{-1}, and a 5σ observation is possible with $L = 1$ ab^{-1} for masses up to 90 GeV.

7.2.4 Modifications of Higgs self-couplings

As in the chapter on Higgs physics above, the e^-p collisions are a very convenient environment to study the property of the SM Higgs boson itself. The latter is produced through vector-boson fusion processes and the precise measurement of its properties provides a unique opportunity to probe the interaction HVV, $(V = W^{\pm}, Z)$. These interactions are in general sensitive to certain classes of beyond the SM physics, which can be parametrized, for instance, via higher dimensional operators and their coefficients, cf. Refs. [373, 374, 375, 376].

The prospects to infer the strengths of the two couplings HWW and HZZ were studied in Refs. [373, 374] in the context of electron-proton collisions. The authors find that the higher-dimensional operator coefficients can be tested for values around $\mathcal{O}(10^{-1})$ at the LHeC. This sensitivity is improved at the FCC-he due to larger center-of-mass energies, which in general enhances the vector-boson fusion cross sections.

The Higgs self-coupling itself HHH can be tested through the measurement of the di-Higgs production cross section as was shown in Ref. [375]. With appropriate error fitting methodology this study illustrates that the Higgs boson self-coupling could be measured with an accuracy of $g^{(1)}_{HHH} = 1.00^{+0.24(0.14)}_{-0.17(0.12)}$ of its expected SM value at $\sqrt{s} = 3.5(5.0)$ TeV, considering an ultimate 10 ab^{-1} of integrated luminosity.

An analysis presented in Ref. [376] studies the LHeC sensitivity to dimension-six operators. The authors employ jet substructure techniques to reconstruct the boosted Higgs boson in the final state. A shape analysis on the differential cross sections shows in some cases improvements with respect to the high-luminosity LHC forecasts.

7.2.5 Exotic Higgs boson decays

The LHeC sensitivity to an invisibly decaying Higgs boson was investigated in Ref. [377]. Therein the focus is on the neutral current production channel due to the enhanced number of observables compared to the charged current counterpart. The signal contains one electron, one jet and large missing energy. A cut-based parton level analysis yields the estimated sensitivity of Br($h \rightarrow$invisible) = 6% at 2σ level. Exotic decays of the Higgs boson into a pair of light spin-0 particles referred to as Φ was discussed in Ref. [378]. The studied signature is a final state with 4 b-quarks, which is well motivated in models where the scalars can mix with the Higgs doublet, and suffers from multiple backgrounds at the LHC. The analysis is carried out at the parton level, where simple selection requirements render the signature nearly free of SM background and makes Φ with masses in the range [20, 60] GeV testable for a hVV $(V = W, Z)$ coupling strength relative to the SM at a few per-mille level and at 95% confidence level.

The prospects of testing exotic Higgs decays into pairs of light long-lived particles at the LHeC were studied in Ref. [379] where it was shown that proper lifetimes as small as μm could be tested, which is significantly better compared to the LHC. This is shown in Fig. 7.2 (left). This information can be interpreted in a model where the long-lived particles are light scalars that mix with the Higgs doublet, where both, production and decay, are governed by this scalar mixing angle. The area in the mass-mixing parameter space that give rise to at least 3 observable events with a displaced vertex are shown in Fig. 7.1. It is apparent that mixings as small as $\sin^2\alpha \sim 10^{-7}$ can be tested at the LHeC for scalar masses between 5 and 15 GeV (Ref. [Fischer et al., input for ESPP]).

7.3 Searches for supersymmetry

Several SUSY scenarios might remain still elusive in searches performed at pp colliders. While the null results from current searches by the LHC experiments have produced impressive constraints on the SUSY

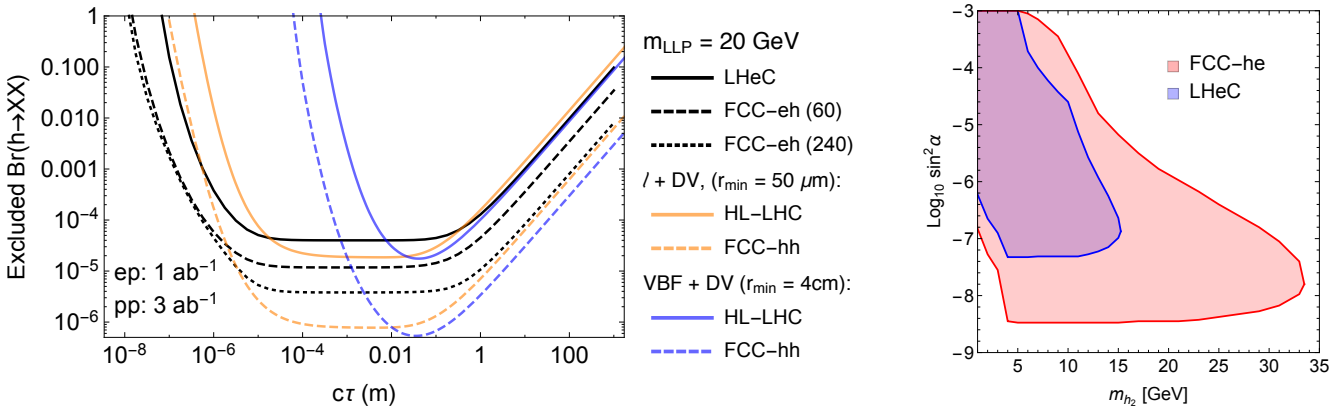

Figure 7.2: Sensitivity contours for displaced vertex searches for Higgs decays into long-lived scalar particles (LLP), which are pair produced from decays of the Higgs boson and decay themselves via scalar mixing into fully visible final states. *Left:* As a function of the LLP lifetime for a fixed mass from Ref. [379]. *Right:* For a specific model, where lifetime and production rate of the LLP are governed by the scalar mixing angle. The contours are for 3 events and consider displacements larger than 50μm to be free of background.

coloured sector (squarks and gluinos) because of their large production cross sections in strong interactions, less stringent constraints have been placed on weakly-produced SUSY particles, namely neutralinos $\tilde{\chi}^0$, charginos $\tilde{\chi}^{\pm}$, and sleptons $\tilde{\ell}^{\pm}$. Some of these scenarios where *ep* colliders might have discovery potential complementary to that of the HL-LHC are discussed below. These include R-parity conserving SUSY models, e.g. motivated by dark matter, or R-parity violating SUSY models, e.g. including single production of bottom and top squarks and low mass gluinos.

7.3.1 Search for the SUSY Electroweak Sector: prompt signatures

Electroweakino scenarios where charginos, neutralinos, and sleptons are close in mass can be characterised with the neutralino mass m and the mass splitting between charginos and neutralinos Δm. Scenarios with $\Delta m < 50$GeV are referred to as *compressed*. A subtlety arises for $\Delta m \leq 1$ GeV, when the $\tilde{\chi}_1^{\pm}/\tilde{\chi}_2^0$ becomes long lived and its decays are displaced. For $\Delta m > 1$ GeV the decays are prompt, the visible decay products from $\tilde{\ell}$ and $\tilde{\chi}_1^{\pm}/\tilde{\chi}_2^0$ have very soft transverse momenta (p_T) and the SM backgrounds are kinematically similar to the signal. The analyses therefore become challenging and sensitivities decrease substantially. Two SUSY scenarios are considered in Ref. [380] where the LSP $\tilde{\chi}_1^0$ is Bino-like, $\tilde{\chi}_1^{\pm}$ and $\tilde{\chi}_2^0$ are Wino-like with almost degenerate masses, and the mass difference between $\tilde{\chi}_1^0$ and $\tilde{\chi}_1^{\pm}$ is small. The signal is produced via the process "$p\,e^- \to j\,e^-\,\tilde{\chi}\tilde{\chi}$", where $\tilde{\chi} = \tilde{\chi}_1^0$, $\tilde{\chi}_1^{\pm}$ or $\tilde{\chi}_2^0$. Conservative leading order cross sections are considered for the SUSY signal models. The kinematic observables are input to the TMVA package to perform a multivariate analysis at the detector level.

In the compressed-slepton scenario, the case where the left-handed slepton $\tilde{\ell}_L$ and sneutrino $\tilde{\nu}$ are slightly heavier than $\tilde{\chi}_1^{\pm}$ or $\tilde{\chi}_2^0$ is considered. When fixing the mass difference $\Delta m = m_{\tilde{\ell}} - m_{\tilde{\chi}_1^{\pm},\tilde{\chi}_2^0} = 35$ GeV and ignoring the systematic uncertainty on the background, the analysis indicates that the 2 (5)-σ limits on the $\tilde{\chi}_1^{\pm}$, $\tilde{\chi}_2^0$ mass are 616 (517) GeV for 2.5 ab^{-1} luminosity at the FCC-eh, and 266 (227) GeV for 1 ab^{-1} luminosity at the LHeC, respectively. An illustration of the model assumptions in terms of sleptons and neutralino masses and the current constraints at the LHC is presented in Fig. 7.3 (left). Results are illustrated in Fig. 7.3 (right). The effects of varying Δm are investigated: fixing $m_{\tilde{\chi}_1^{\pm},\tilde{\chi}_2^0}$ to be 400 GeV, it is found that at the FCC-eh the significance is maximal when Δm is around 20 GeV.

In the decoupled-slepton scenarios where only $\tilde{\chi}_1^0$, $\tilde{\chi}_1^{\pm}$ and $\tilde{\chi}_2^0$ are light and other SUSY particles are heavy and decoupled, the 2-σ limits obtained on the $\tilde{\chi}_1^{\pm}$, $\tilde{\chi}_2^0$ mass are 230 GeV for 2.5 ab^{-1} luminosity at the

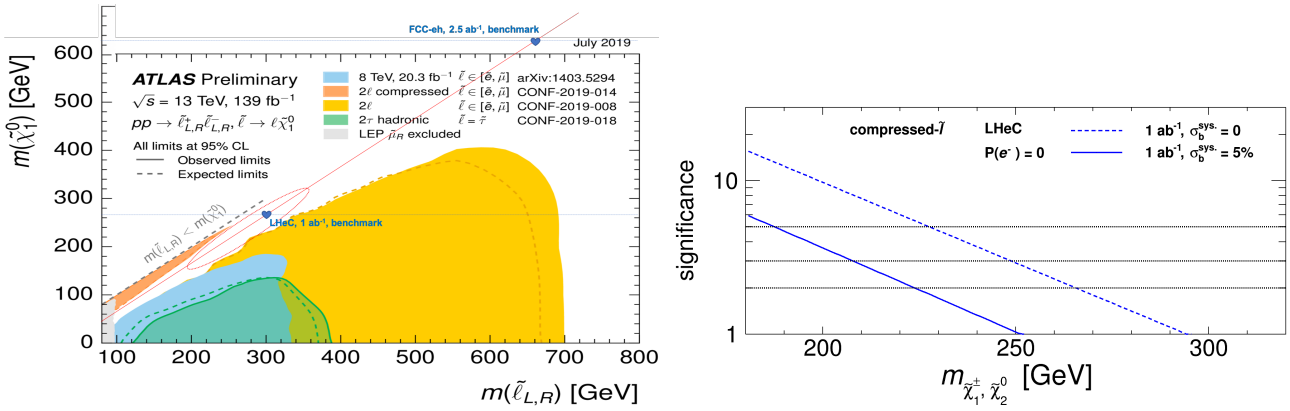

Figure 7.3: *Left:* Benchmark assumption on slepton masses and 2019 reach of current ATLAS searches for sleptons (Ref. ATLAS public twiki). *Right:* Significances as varying the masses of $\tilde{\chi}_1^{\pm}$ and $\tilde{\chi}_2^0$ for the compressed-slepton scenario at the LHeC with unpolarized beams and 1 ab^{-1} luminosity. For dashed (solid) curve, a systematic uncertainty of 0% (5%) on the background is considered. The figure is from Ref. [380].

FCC-eh when neglecting the systematic uncertainty on the background. Large systematic uncertainties on the SM background processes can substantially affect the sensitivity, hence good control of experimental and theoretical sources of uncertainties is very important.

Finally, it is also found that the possibility of having a negatively polarized electron beam ($Pe^- = 80\%$) could potentially extend the sensitivity to electroweakinos by up to 40%.

Overall, since the sensitivity to the electroweak SUSY sector depends on the mass hierarchy of $\tilde{\chi}_1^{\pm}$, $\tilde{\chi}_1^0$, $\tilde{\chi}_2^0$ and sleptons, and given the difficulty to probe efficiently small Δm regions at the current LHC and possibly at the HL-LHC, measurements at ep colliders may prove to offer complementary or additional reaches, in particular for the compressed scenarios.

7.3.2 Search for the SUSY Electroweak Sector: long-lived particles

Studies on Higgsinos (χ) with masses $\mathcal{O}(100)$ GeV are motivated by natural SUSY theories and help to avoid large fine-tuning on the Higgs boson mass. In these scenarios the low energy charginos (χ^+)/neutralinos(χ^0) are all Higgsino-like and their masses are nearly degenerate, only slightly above the neutralino.

As mentioned above, a compressed spectrum with nearly degenerate masses results in a kinematic suppression of the heavier χ^+ decays into $W^{\pm}\chi^0$, which has twofold consequences: it yields final states without hard leptons; it enhances the χ^+ lifetime up to $\mathcal{O}(1)$ mm. At the LHC the absence of hard leptons with sizable transverse momentum makes this signature difficult to investigate. One possibility is to search for the tracks from χ^+, which effectively disappear once it decays and are thus called "disappearing tracks".

The discovery prospects for prompt signatures of electroweakino decays in electron-proton collisions are presented in Ref. [381]. The light χ^+ (and χ^0) can be produced in pairs via in vector boson fusion of the charged or neutral currents. A cut-based analysis of these processes at the LHeC, assuming prompt χ^+ decays, yields 2σ discovery prospects for masses up to 120 GeV.

Taking into account the finite lifetime of the charginos, two comments are in order: first, the lifetimes and boosts of the χ^+ are in general too small to resolve a disappearing track; second, the soft final state is not a problem per se and can in principle be observed.

Instead of searching for a disappearing track, the long lifetimes of the χ^+ can be exploited via the measurement of the impact parameter of the soft hadronic final, as is discussed in Ref. [379]. The crucial machine

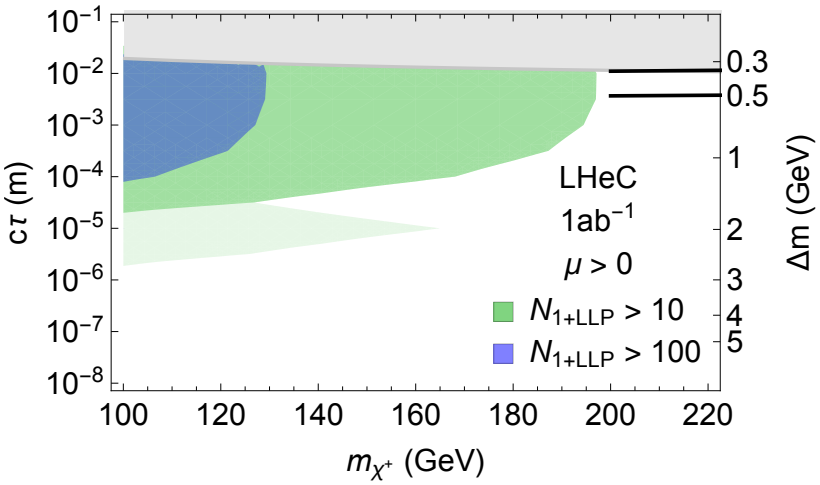

Figure 7.4: Exclusion limits on Higgsino masses as a function of their lifetime from Ref. [379]. Colored regions denote where 10 or 100 events with at least one LLP decay are observed. Light shading indicates the uncertainty in the predicted number of events due to different hadronization and LLP reconstruction assumptions. The black curves are the optimistic and pessimistic projected bounds from HL-LHC disappearing track searches.

performance parameters are the tracking resolution, which is as good as $\mathcal{O}(10)\,\mu$m, and the absence of pile up, which allows to identify and measure a single soft pion's impact parameter. In this way the LHeC can test χ with masses up to 200 GeV, the corresponding sensitivity is shown in Fig. 7.4, and the bounds on disappearing track searches at the HL-LHC are shown as black lines in the figure. Considering non-prompt decays of Higgsinos thus significantly improves the discovery prospects compared to the prompt analysis. Further means of improving the prospects is an increased center-of-mass energy, which enhances the production rate of the Higgsinos.

7.3.3 R-parity violating signatures

Supersymmetry typically evokes the so-called R-parity, which implies that each fundamental vertex contains an even number of sparticles and helps preventing rapid proton decays. In general, R-parity need not be an exact symmetry of the theory, such that interactions can be present that allow for sparticles to decay into SM particles and include the possibility to violate lepton and/or baryon number.

R-partiy violating interactions are particularly interesting in electron-proton collisions, where single super-partners might be produced resonantly, and detected via the corresponding $2 \to 2$ process. This is discussed in Refs. [382, 383] for the case of the *sbottom*, showing that a good level of precision could be achieved at LHeC compared with all the knowledge derived from indirect measurements.

Single (anti-)top quark production associated with a lightest neutralino in the MSSM with R-parity breaking coupling is investigated in Ref. [384] for the LHeC. The study includes calculations of the NLO QCD contributions and concluded that the available constraints would allow a notable production rate.

Certain SUSY scenarios might produce prompt signals of multiple soft jets, which generally resemble QCD backgrounds at the LHC and are thus notoriously difficult to test. The largely QCD-free environment of electron-proton collisions allows to test this class of signatures. One example of this signal can come from gluinos, which are tested at the LHC via signatures that involve large amounts of missing energy. If the gluino has an all-hadronic decay – as in R-parity violating scenarios or Stealth SUSY models – the current experimental searches have a gap in sensitivity for masses between about 50 to 70 GeV [385]. Gluinos within this gap can be tested at the LHeC [386], where a three sigma exclusion sensitivity was demonstrated with

simple signal selection cuts.

7.4 Feebly Interacting Particles

New physics may interact with the SM via the so-called portal operators, including the vector, scalar, pseudoscalar, or neutrino portal. In these scenarios, the SM is often extended by an entire sector of new physics, comprising new forces and several particle species, which may be connected to the big open questions of Dark Matter or the origin of neutrino mass.

These hypothetical new sectors derive their typically very feeble interaction strength with the known particles from mass mixing with a SM particle that shares their quantum numbers. Some examples are being discussed below.

7.4.1 Searches for heavy neutrinos

The observation of neutrino oscillations requires physics beyond the SM that gives rise to the light neutrino masses. One well-motivated class of models for this purpose is the so-called symmetry protected type I seesaw scenario, which features heavy neutrinos with signatures that are in principle observable at colliders, cf. Ref. [387] and references therein. A comprehensive overview over collider searches for the heavy and mostly sterile neutrinos can be found in Ref. [388], where the promising signatures for such searches at electron-proton colliders have been identified.

In electron-proton collisions heavy neutrinos can be produced via the charged current. The heavy neutrino production cross section is dependent on the active-sterile neutrino mixing with the electron flavor called $|\theta_e|^2$. The most promising searches at the LHeC are given by processes with lepton flavor violating final states and displaced vertices, the prospects of which are evaluated in Ref. [389] and are shown in Fig. 7.5. It is remarkable, that the prospects to detect heavy neutrinos with masses above about 100 GeV are much better in electron-proton collisions compared to proton-proton or electron-positron, due to the much smaller reducible backgrounds.

The prospects of heavy neutrino detection can be further enhanced with jet substructure techniques when the W boson in the decay $N \to eW,\ W \to jj$ is highly boosted. Ref. [390] shows that these techniques can help to distinguish the heavy neutrino signal from the few SM backgrounds. A considerable improvement in the bounds of $|V_{eN}|^2$ over present limits from LHC, $0v2\beta$ experiments and from electroweak precision data is obtained with 1 ab^{-1} of integrated luminosity at the LHeC.

An alternative approach is employed in Ref. [396] where the dominant sterile neutrino interactions with the SM are taken to be higher dimension effective operators (parameterizing a wide variety of UV-complete new physics models) while contributions from neutrino mixing is neglected. The study shows prospects of Majorana neutrino detection for masses lower than 700 and 1300 GeV can be discovered at the LHeC with $E_e = 50$ and 150 GeV, respectively, for $E_p = 7$ TeV. Recently the influence of vector and scalar operators on the angular distribution of the final anti-lepton was investigated. The forward-backward asymmetry is studied in Ref. [397], wherein, in particular, the feasibility of initial electron polarisation as a discriminator between different effective operators is studied.

Prospects of testing left-right symmetric models, featuring additional charged and neutral gauge bosons and heavy neutrinos, were studied in the context of electron-proton collisions in Refs. [398, 399]. The authors show that the production of heavy right-handed neutrinos of mass $\mathcal{O}(10^2\text{-}10^3)$ GeV at the LHeC, with a lepton number violating final state, can yield information on the parity breaking scale in left-right symmetric theories. Heavy neutrinos of sub-TeV mass in inverse see-saw model with Yukawa coupling of $\mathcal{O}(0.1)$ are investigated for the LHeC in Ref. [400].

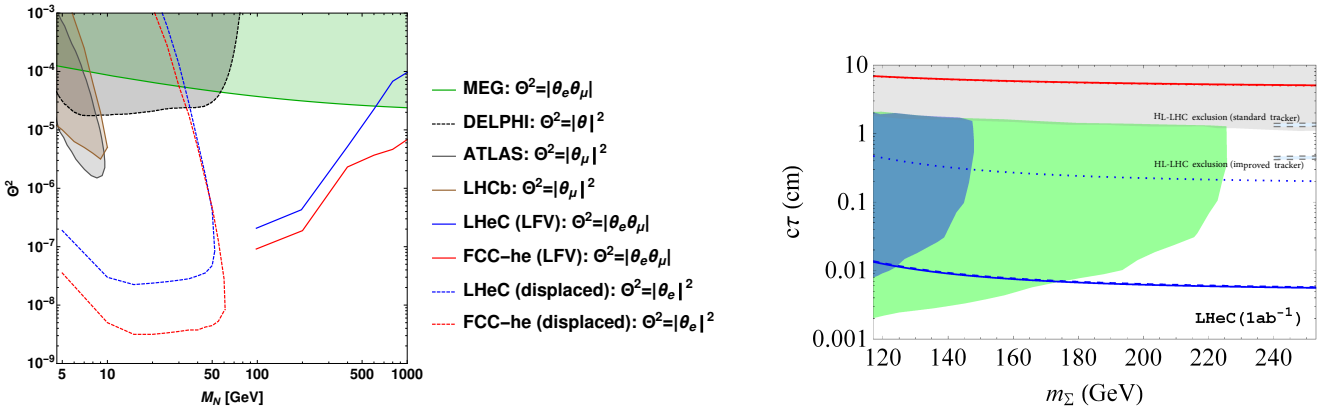

Figure 7.5: *Left:* Sensitivity of the LFV lepton-trijet searches (at 95% C.L.) and the displaced vertex searches (at 95% C.L.) from Ref. [389] compared to the current exclusion limits from ATLAS [391], LHCb [392], LEP [393], and MEG [394]. *Right:* Prospects of displaced vertex searches from charged fermion triplet $\Sigma^{\pm}$. The blue and green shaded regions denote the expected observability of 10 (100) events, dashed lines denote HL-LHC exclusion sensitivity, and the red line is connected to the light neutrino properties. For details, see text and Ref. [395].

7.4.2 Fermion triplets in type III seesaw

Another technically natural way of generating the light neutrino masses is the so-called Type III seesaw mechanism, which extends the SM with a fermion $SU(2)$ triplet. In minimal versions of these models the neutral and charged triplet fermions have almost degenerate masses around the TeV scale.

The prospects of studying this mechanism via searches for the new fermions are evaluated in Ref. [395], wherein signatures from long-lived particles at various experiments were considered. The triplet fermions, primarily produced through their gauge interactions, can be observed via displaced vertices and disappearing track searches for masses of a few hundred GeV.

The authors find that the LHeC can observe displaced vertices from the decays of the charged fermion triplet components via the soft pion impact parameters for triplet masses up to about 220 GeV and has a complementary sensitivity to the light neutrino mass scale, which governs the lifetime of the neutral fermion, compared the LHC and MATHUSLA. The final results from Ref. [395] for the LHeC are shown in the right panel of Fig. 7.5.

7.4.3 Dark photons

Minimal extensions of the SM often involve additional gauge factors. In particular the $U(1)_X$ extensions are interesting, because they are often connected to a dark charge that can be associated with the dark matter.

An SM-extending $U(1)_X$ predicts an additional gauge boson that naturally mixes with the $U(1)_Y$ factor of the SM kinetically [401]. This kinetic mixing lets the SM photon couple to fermions that carry the dark charge X, and the other gauge boson to the electric charge. Both interactions are suppressed by the mixing parameter ϵ. In most models the additional gauge boson also receives a mass, possibly from spontaneous breaking of the $U(1)_X$, and the corresponding mass eigenstate is called a dark photon. Dark photons typically have masses around the GeV scale and their interactions are QED-like, scaled with the small mixing parameter ϵ. It can decay to pairs of leptons, hadrons, or quarks, which can give rise to a displaced vertex signal due to its long lifetime.

The prospects for the dark photon searches via their displaced decays in ep collisions are presented in Ref. [402]. The most relevant performance characteristics of the LHeC are the very good tracking resolution

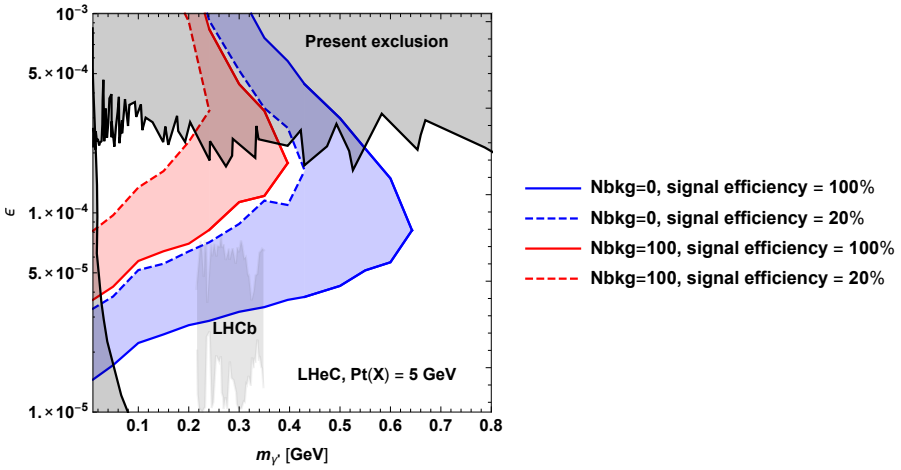

Figure 7.6: Projected sensitivity of dark photon searches at the LHeC via displaced dark photon decays from Ref. [402]. The sensitivity contour lines are at the 90% confidence level and consider a transverse momentum cut on the final state hadrons of 5 GeV. The blue and red areas denote the assumption of zero and 100 background events, respectively, the solid and dashed lines correspond to a reconstruction efficiency of 100% and 20%, respectively. See Ref. [402] for details.

and the very low level of background, which allow the detection of a secondary vertex with a displacement of $\mathcal{O}(0.1)$ mm.

The resulting sensitivity contours in the mass-mixing parameter space are shown in Fig. 7.6, where the different colors correspond to different assumptions on the irreducible background and the solid and dashed lines consider different signal reconstruction efficiencies. Also shown for comparison are existing exclusion limits from different experiments, and the region that is currently investigated by the LHCb collaboration [403].

The domain in parameter space tested in electron-proton collisions is complementary to other present and planned experiments. In particular for masses below the di-muon threshold, searches at the LHC are practically impossible. It is remarkable that dark photons in this mass range can be part of a dark sector that explains the observed Dark Matter in the Universe via a freeze-in mechanism, cf. e.g. Ref. [404].

7.4.4 Axion-like particles

The axion is the Goldstone boson related to a global $U(1)$ symmetry, which is spontaneously broken at the so-called Peccei-Quinn scale, assumed to be around the GUT scale. Its mass, being inversely proportional to the Peccei-Quinn scale, is therefore usually in the sub-eV regime and the axion provides a dynamical solution to the strong CP problem of the standard model. Axions are a very attractive candidate for "cold" dark matter, despite their tiny mass.

Axion-like particles (ALP) are motivated by the original idea of the QCD axion and similarly, they are good dark matter candidates. ALPs are pseudoscalar particles that are usually assumed to be relatively light (i.e. with masses around and below one GeV) and couple to the QCD field strength. In addition, they may have a number of further interactions, for instance they can interact with the other fields of the SM and also mix with the pion. Particularly interesting is the possibility to produce ALPs via vector boson fusion processes.

A recent study [405] has evaluated the prospects of detecting ALPs at the LHeC via the process $e^-\gamma \to e^- a$ in a model independent fashion. The investigated signature is the decay $a \to \gamma\gamma$, which allows to test the effective ALP-photon coupling for ALPs with masses in the range of 10 GeV $< m_a <$ 3 TeV. It was found that sensitivities can improve current LHC bounds considerably, especially for ALP masses below 100 GeV,

and the authors state that ALP searches at ep colliders might become an important handle on this class of new physics scenarios [405].

7.5 Anomalous Couplings

New physics beyond the SM can modify SM interactions, for instance at the loop level. Such contributions could either modify the interaction strength of SM particles or introduce additional interactions that are not present in the SM, such as flavor changing neutral couplings (FCNC).

7.5.1 Triple Gauge couplings

In the SM, the triple gauge boson couplings (TGC) W^+W^-V, $V = \gamma, Z$ are precisely defined and any significant deviation from the SM predicted values would indicate new physics. Present constraints on anomalous triple vector boson couplings are dominated by LEP (but they are not free of assumptions) and the WWZ and $WW\gamma$ vertices can be tested at LHeC in great detail.

The search for anomalous $WW\gamma$ and WWZ couplings with polarized electron beam were studied in ref. [238] via the processes $ep \to \nu q\gamma X$ and $ep \to \nu qZX$. It was found that the LHeC sensitivity with $E_e = 60$ GeV and $L = 100/\text{fb}$ is comparable with existing experimental limits from lepton and hadron colliders, and that anomalous Z couplings might be better, reaching $(\Delta\kappa_{\gamma,Z}, \lambda_{\gamma,Z})$ as small as $\mathcal{O}(10^{-1}, 10^{-2})$. In general, beam polarization and larger electron beam energies improve the sensitivity, and the LHeC was found to give complementary information on the anomalous couplings compared to the LHC.

The prospects of testing anomalous triple gauge couplings are also investigated in Ref. [237]. Therein the authors study the kinematics of an isolated hard photon and a single jet with a substantial amount of missing transverse momentum. They show that the LHeC is sensitive to anomalous triple gauge couplings via the azimuthal angle differences in the considered final state. It is pointed out that in such an analysis it is possible to probe the $WW\gamma$ vertex separately, with no contamination from possible BSM contributions to the WWZ coupling. The estimations consider $E_e = 100$, 140, 200 GeV and it is claimed that while higher energies yield better sensitivities, the differences are not very large. For $L = 200/\text{fb}$ and $E_e = 140$ GeV the exclusion power of the LHeC is superior to all existing bounds, including those from LEP.

The process $e^-p \to e^-\mu^+\nu j$ is investigated in Ref. [242]. The analysis is carried out at the parton level and includes the cross section measurement and a shape analysis of angular variables, in particular of the distribution of the azimuthal angle between the final state forward electron and jet. It is shown that the full reconstruction of leptonic W decay can be used for W polarization which is another probe of anomalous triple gauge couplings. The results show that the LHeC could reach a sensitivity to λ_γ and Δk_γ as small as $\mathcal{O}(10^{-3})$ for $L = 2 - 3/\text{ab}$.

7.5.2 Anomalous top-gauge-couplings

Like all the flavor changing neutral currents the top quark FCNC interactions are also extremely suppressed in the SM, which renders them a good test of new physics. The contributions from FCNC to top interactions can be parameterized via an effective theory and studied by analysing specific processes.

One promising candidate for an FCNC process is $\gamma p \to W^-t, W^+\bar{t}$, as studied in Ref. [406] via a model independent effective Lagrangian in the unitary gauge and including anomalous Wtb and $Wtb\gamma$ interactions. The four independent anomalous form factors are $\Delta F_{1L} = F_{1L} - 1, F_{2L}, F_{1R}$, and F_{2R}, and the LHeC's sensitivity to these is found to be $-0.0187 < \Delta f_{1L} < 0.0172$, $-0.1884 < f_{1R} < 0.1957$, $-0.1014 < f_{2L} <$

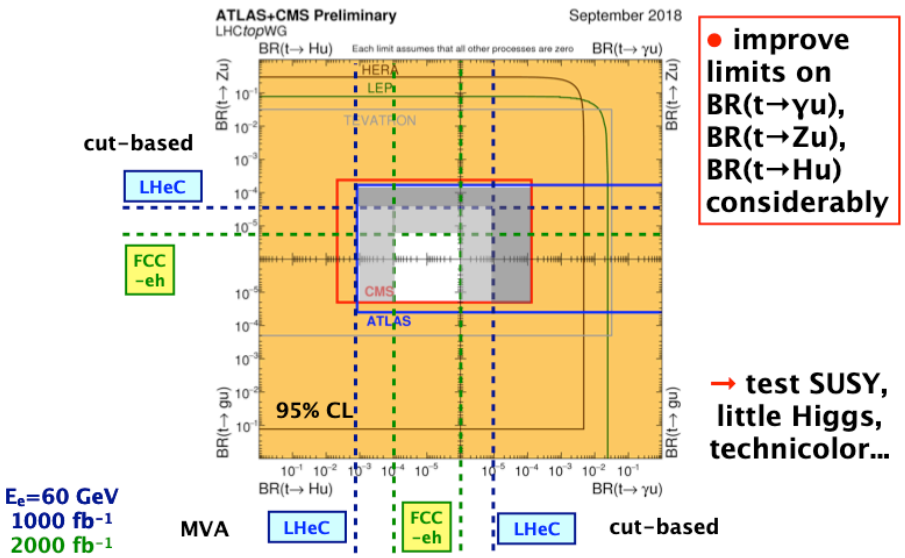

Figure 7.7: [CAPTION MISSING]

0.0939 and $-0.0871 < f_{2R} < 0.1058$ for an integrated luminosity of $L = 10$ ab^{-1} with $E_e = 140$ GeV. These numbers are incorrect: they correspond to 10 fb-1 for LHeC with electron beam of 140 GeV. We should take the values from Table I of the reference. Also, replace f by F. The sensitivity on $F_{iL/R}$ is considerably better at the LHeC than at the LHC, while the limits on the other form factors are comparable.

Another process to test anomalous Wtb coupling is $e^-p \to \nu_e \bar{t}$, which is investigated in Ref. [248]. The authors find that Δf_{1L} can be measured at an accuracy of $\sim 10^{-2} - 10^{-3}$ at 95% C.L., while the other form factors can be tested at the level of $10^{-1} - 10^{-2}$, including a systematic uncertainty varying between 10%-1% and considering $L = 100$ fb^{-1} for $E_e = 60$ GeV.

A more general framework is given by the full basis of $SU(2)_L \times U(1)$ operators, including the relevant four-fermion ones. This approach is employed in Ref. [407] to estimate the LHeC sensitivity to anomalous tbW couplings. This work indicates that the LHeC can significantly improve on the bounds as expected from the HL-LHC for f_{1L}, and lead to somewhat tighter bounds on f_{1R}. In agreement with Refs. [406, 248] the tests of tensor couplings f_{2L}, f_{2R} are found to improve the HL-LHC sensitivity only moderately.

The single top quark production via flavor changing neutral current interactions of type $tq\gamma$ are studied in Refs. [256, 408], investigating the signal processes $e^-p \to e^-W^\pm q + X$ and $e^-p \to e^-W^\pm bq + X$. The analysis uses $E_e = 50$ and 60 GeV and is based on a fast simulation including hadronisation and reconstruction. From the kinematic distributions of jets the top and W masses are reconstructed and signal enhancing selection cuts are employed. The resulting sensitivity limits for the anomalous $tq\gamma$ couplings are found to be $\mathcal{O}(0.01)$ for $L = 100$/fb, which was expressed in terms of the branching ratios $\mathrm{Br}(t \to u\gamma)$ and $\mathrm{Br}(t \to c\gamma)$, found to be as small as 4×10^{-6} and 4×10^{-5}, respectively.

The top quark FCNC with a Z-boson was studied in Ref. [409] for $E_e = 60$ GeV. An effective theory was employed where the anomalous FCNC couplings are of vector and tensor nature, which were shown to be distinguishable using kinematics and polarisation information. For $L = 2$ ab^{-1}, couplings of $\mathcal{O}(0.01)$ can be tested at the 95% confidence level.

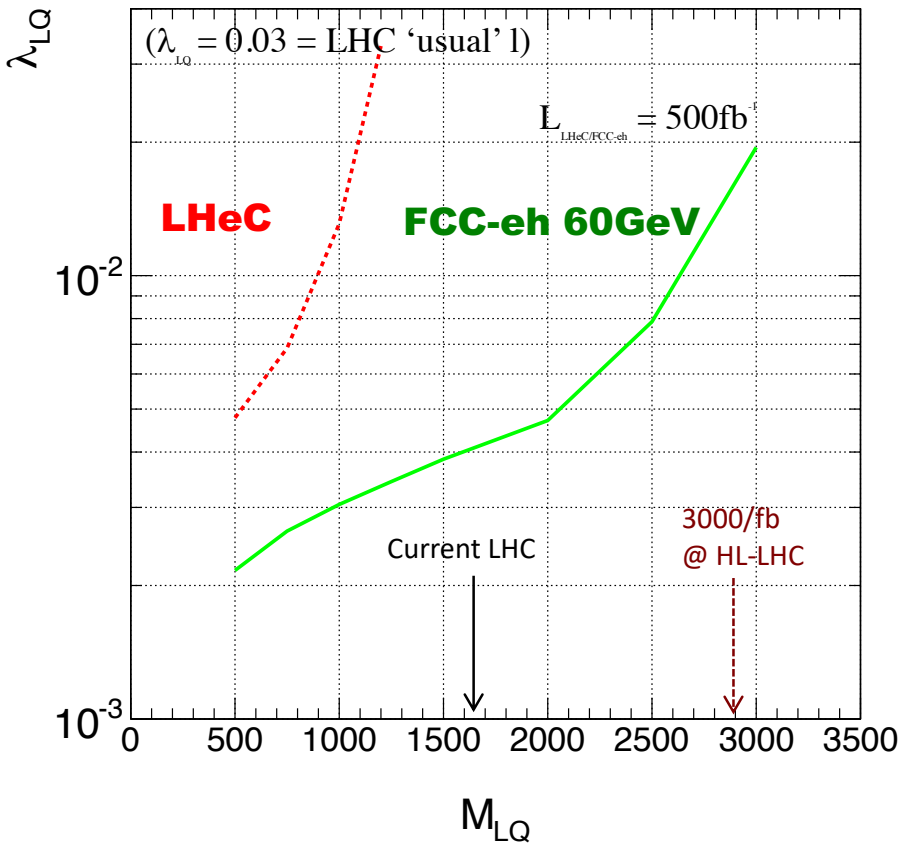

Figure 7.8: Exclusion contours for scalar lepto-quark as a function of their mass and coupling λ for LHeC and FCC-eh, assuming 500 fb^{-1} luminosity. The current (2019) LHC limits and projections for HL-LHC are displaced for comparison.

7.6 Theories with heavy resonances

Many other BSM scenarios exist which could manifest via the presence of new resonances. The high centre of mass energy of pp colliders allow a better in reach in most of these scenarios. Nonetheless, the LHeC and FCC-eh can contribute to searches for new physics in this area, relevant studies on various areas including scalar and vector-lepton quarks and excited leptons, are collected in this section.

7.6.1 Leptoquarks

In recent years the experiments that study heavy flavored mesons revealed intriguing hints for new physics: in semi-leptonic decays of B mesons a violation of lepton flavor universality is apparent in both, the charged current and neutral current mediated processes. The SM is disfavored presently at the level of 3 to 5σ, cf. Ref. [410]. In this context BSM theories involving leptoquarks (LQs) have been studied thoroughly, which can give rise to the lepton universality violating decays of heavy mesons at the tree level. Leptoquarks first appeared in Ref. [411] in Pati and Salam's $SU(4)$ model, where lepton number was considered to be the fourth colour.

In ep collisions the LQs can be produced in an s-channel resonance, the signature being a peak in the invariant mass of the outgoing ℓq system. This was suggested for instance with respect to HERA in Ref. [412]. In

general, the signal strength allows one to infer the coupling constant λ between the electron and the quark. This is barely possible at the LHC, where the dominant pair production process via the strong interaction is insensitive to λ.

For LQs with masses below the center-of-mass energy of the collider, suitable searches promise a sensitivity to λ as small as $\mathcal{O}(10^{-3})$. Contrary to the LHC environment, at the LHeC many properties of the LQs can be measured with good precision [1]. The sensitivity of the LHeC and the FCC-he as a function of the LQ mass and coupling is shown in Fig. 7.8, assuming 500 fb^{-1} luminosity. Searches into final state events characterised by the presence of lepton-jet resonances at the LHC led to stringent constraints overcoming the LHeC reach [ref] while possible hints of signal at the HL-LHC could be studied at the FCC-eh.

Signals of the first generation scalar leptoquarks at LHeC were also studied in Ref. [413]. The authors consider single production at the LHeC in the context of simplified models. The numerical results show that the production cross-sections are much larger than those at the LHC and that the possible signals can have prospects for discovery.

The connection of the specific LQ type called $\tilde{R}_2$ with right-handed neutrinos in the context of discovery prospects at the LHeC are presented in Ref. [414]. In this model the LQ can have a sizable branching ratio into (heavy) neutrinos, which softens existing LHC constraints and provides new interesting search channels. In the analysis the authors investigate the signatures $\ell^- + n$ jets and $\ell^+\tau^-\bar{b} + \not{E}_T + n$ jets at the LHeC with $E_e = 150$ GeV and $L = 100$/fb. They find that for this luminosity LQ with mass up to 1.4 TeV can be detected at the 5σ level via the signature $\ell^- + n$ jets.

7.6.2 Vector-like quarks

In composite Higgs models, new vector-like quarks are introduced, in particular the top-partner (T) with charge 2/3. The prospects of detecting T at the LHeC are discussed in Ref. [415]. For this search a simplified model is considered where T is produced from positron proton scattering via intergenerational mixing and decays as $T \to tZ$, with the final state $\nu_e\ell^+\ell^- bjj'$, considering $E_e = 140$ GeV. The authors find that for $L = 1$/ab masses for the top partner T around 800 GeV can be tested when the model-related coupling constants are $\mathcal{O}(0.1)$ and that mixing between T and the first generation quarks can significantly enhance the LHeC sensitivity.

Another search strategy for singly produced top partners is given by their decays $T \to Wb$ and $T \to th$, which is presented in Ref. [416]. The analysis is based on a simplified model where the top partner is an $SU_L(2)$ singlet and interacts only with the third generation of quarks. It considers collisions of positrons and protons with $E_e = 140$ GeV, the analysis is carried out at the parton level and investigates the kinematic distributions of the final states. Useful kinematic variables for the bW final state were found to be the transverse momentum of the lepton, b-jet missing energy, while for the th final state the most useful observable is the transverse hadronic energy. For masses of $\mathcal{O}(1)$ TeV the LHeC is found to be sensitive to the new interactions when they are $\mathcal{O}(0.1)$ for $L = 1$/ab, in agreement with [415]. A very similar analysis was performed for the $T \to Wb$ signal channel with comparable results [417].

7.6.3 Excited fermions (ν^*, e^*, u^*)

The potential of searches for excited spin-1/2 and spin-3/2 neutrinos are discussed in Ref. [418]. For the analysis the authors consider effective currents that describe the interactions between excited fermions, gauge bosons, and SM leptons. For the signature, the production of the excited electron neutrino ν^* and its subsequent decay $\nu^* \to We$ with $W \to jj$ was chosen. The analysis is carried out at the parton level, considers $E_e = 60$ GeV, and consists in a study of the kinematic distributions of the final states. It is

concluded that the signature can be well distinguished from backgrounds, and that other lepton-hadron colliders would be required to test the excited neutrinos of different flavors.

Analyses in similar models, considering electron-proton collisions at energies of the FCC-he and beyond, were carried out for excited electron neutrinos and are presented in Ref. [419]. An analysis for the prospects of testing excited electrons is discussed in Ref. [420], and testing excited quarks in a composite model framework is investigated in Ref. [421].

7.6.4 Color octet leptons

Unresolved issues of the SM, like family replication and quark-lepton symmetry, can be addressed by composite models, where quarks, leptons, and gauge bosons are composite particles made up of more basic constituents. One general class of particles, predicted in most composite models, are color octet leptons, which are bound states of a heavy fermion and a heavy scalar particle that is assumed to be color-charged. In this scenario each SM lepton is accompanied by a color octet lepton, which may have spin 1/2 or 3/2. Since they are unobserved, the compositeness scale is expected to be at least $\mathcal{O}(1)$ TeV.

At the LHeC, the color octet partner of the electron e_8 can be produced through the process $e^- p \to e_8 g + X$ and studied via its decays products. An analysis including the study of kinematic distributions that were obtained at the parton level is presented in Ref. [422]. It was shown that discovery prospects exist for masses of $\mathcal{O}$(TeV). A similar analysis is performed for the FCC-he at much higher energies in Ref. [423].

7.7 Summary and conclusion

The lack of new physics at the LHC to date forces the community to develop new theoretical ideas as well as to explore the complementarities of *pp* machines with other possible future facilities. In the context of *ep* colliders, several studies are being carried out to understand the potential to search for new physics, i.e. considering that many interactions can be tested at high precision that are otherwise not easily accessible.

At *ep* colliders, most BSM physics is accessed via vector-boson fusion, which suppresses the production cross section quickly with increasing mass. Nonetheless, scalar extensions of the SM as well as neutrino-mass related BSM physics can be well tested at *ep* due to the smallness and reducibility of the SM backgrounds. The absence of pile up and complicated triggering makes searches for soft-momenta final state particles feasible, so that results for BSM theories for example characterised by the presence of non-prompt, long-lived particles are complementary to those at the LHC. Additionally, the excellent angular acceptance and resolution of the detector also renders the LHeC a very suitable environment for displaced vertex searches. An increase in the centre of mass energy as high as the one foreseen at the FCC would naturally boost the reach in most scenarios considerably.

Finally, it is worth noting that the LHeC can offer different or indirect ways to search for new physics. It was shown recently that Lorentz invariance violation in the weak vector-boson sector can be studied in electron-proton scattering [424] via a a Fourier-analysis of the parity violating asymmetry in deep inelastic scattering. Moreover, New Physics could be related to nucleon, nuclear, and top structure functions as discussed in Refs. [425, 264, 426]. Investigating of the $B_c^{(*)}$ meson and doubly heavy baryon also was shown to have discovery potential for New Physics [427, 428, 429].

Chapter 8

The Influence of the LHeC on Physics at HL-LHC [Maarten Boonekamp]

Example reference: LHeC [1]

8.1 Precision Electroweak Measurements at the LHC [Maarten Boonekamp]

8.2 Higgs Physics

8.2.1 Resolving QCD Uncertainties in pp Higgs Physics using LHeC [Max Klein]

8.2.2 Combined ep and pp Higgs Coupling Determinations [Jorge De Blas]

8.3 High Mass Searches at the LHC [Uta Klein]

8.4 Heavy Ion Physics with eA Input [Nestor Armesto]

The study of hadronic collisions at RHIC and the LHC, proton-proton, proton-nucleus and nucleus-nucleus, has produced several observations of crucial importance for our understanding of QCD in complex systems where a large number of partons is involved [430, 431]. The different stages of a heavy ion collision, as we presently picture it, are schematically drawn in Fig 8.1.

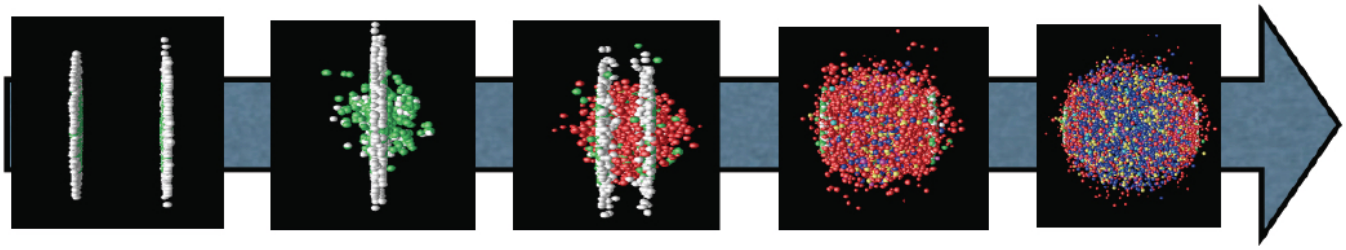

Figure 8.1: Sketch of a heavy ion collision with time running left to right, going from the approach of two ultrarelativistic Lorentz-contracted nuclei, the collision and parton creation in the central rapidity region, the beginning of expansion and formation of the QGP, the expansion of the QGP until hadronisation, and finally the expansion of the hadronic gas.

First, the hot and dense partonic medium created in heavy ion collisions, the quark-gluon plasma (QGP), experiences a collective behaviour of which azimuthal asymmetries and transverse spectra with a specific ordering in particle masses are the most prominent observables. This collectivity can be very well described by relativistic hydrodynamics [432]. For this description, the system has to undergo some dynamics leading to rough isotropisation in a short time, $\lesssim 1$ fm/c, for which both strong and weak coupling explanations have been proposed [340].

Second, collisions between smaller systems, pp and pA, show many of the features [338, 339] that in heavy ion collisions are taken as indicative of the production of a dense hot partonic medium. The most celebrated of such features, the long rapidity range particle correlations collimated in azimuth, named the ridge, has been found in all collisions systems. The dynamics underlying this phenomena, either the formation of QGP and the existence of strong final state interactions, or some initial state dynamics that leaves imprint on the final observables, is under discussion [340].

Finally, the QGP is extremely opaque to both highly energetic partons [433] and quarkonia [434] traversing it. These observables, whose production in pp can be addressed through perturbative methods, are called hard probes [435]. The quantification of the properties of the QGP extracted through hard probes is done by a comparison with predictions based on assuming a nuclear collision to be a superposition of collisions among free nucleons. Such predictions contain uncertainties coming both from nuclear effects other than those in QGP (named cold nuclear matter effects), and from uncertainties in the dynamics determining the interaction between the energetic parton or bound state and the medium. In the case of partons, this has motivated the development of sophisticated jet studies in heavy ion collisions [436].

eA collisions studied in the energy range relevant for the corresponding hadronic accelerator – the LHeC for the LHC – would substantially improve our knowledge on all these aspects and, indeed, on all stages of a heavy ion collisions depicted in Fig 8.1. Besides, they can reduce sizeably the uncertainties in the extracted QGP parameters, the central goal of the heavy program for the understanding of the different phases of QCD. Here we provide three examples of such synergies:

- Nuclear parton densities: The large lack of precision presently existing in the determination of parton densities induce large uncertainties in the understanding of several signatures of the QGP. For example, for J/ψ suppression, its magnitude at midrapidity at the LHC is compatible with the sole effect of nuclear shadowing on nPDFs [434], see Fig. 8.2. While from data at lower energies and at forward and backward rapidities it is clear that this is not the only effect at work, only a reduction on the nPDF uncertainty as feasible at the LHeC , see Sec. 5.2, will make possible a precise quantification of the different mechanisms producing either suppression (screening, gluon dissociation, energy loss) or enhancement (recombination or coalescence), that play a role in this observable.

- Initial conditions for the collective expansion and the small system problem: At present, the largest uncertainty in the determination of the transport coefficients of the partonic matter created in heavy ion collisions [438, 439] (see Fig. 8.3), required in hydrodynamic calculations, and in our understanding of the speed of the approach to isotropisation and of the dynamics prior to it [440], comes from our lack of knowledge of the nuclear wave function and of the mechanism of particle production at small to moderate scales – i.e. the soft and semihard regimes. Both aspects determine the initial conditions for the application of relativistic hydrodynamics. This is even more crucial in the discussion of small systems, where details of the transverse structure of protons are key [441] not only to provide such initial conditions but also to establish the relative role of initial versus final state dynamics. For example, the description of azimuthal asymmetries in pp and pPb collisions at the LHC demands that the proton is modelled as a collection of constituent quarks or hot spots [432, 441]. ep and eA collisions at the LHeC can constrain both aspects in the pertinent kinematic region, Secs. 4.2.6 and 5.3. Besides, they can clarify the mechanisms of particle production and the possible relevance of initial state correlations on the final state observables as suggested e.g. by CGC calculations, see Secs.

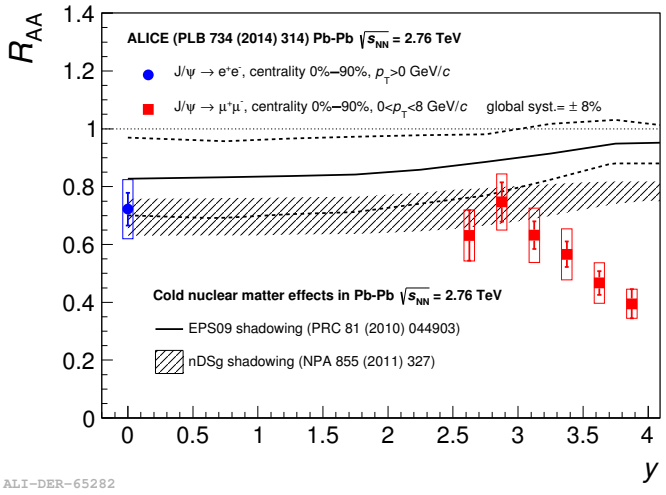

Figure 8.2: ALICE inclusive J/ψ nuclear modification factor versus rapidity [437], compared to nPDF calculations. Taken from [434].

4.2.4 and 5.4, whose importance for LHC energies can be established at the LHeC.

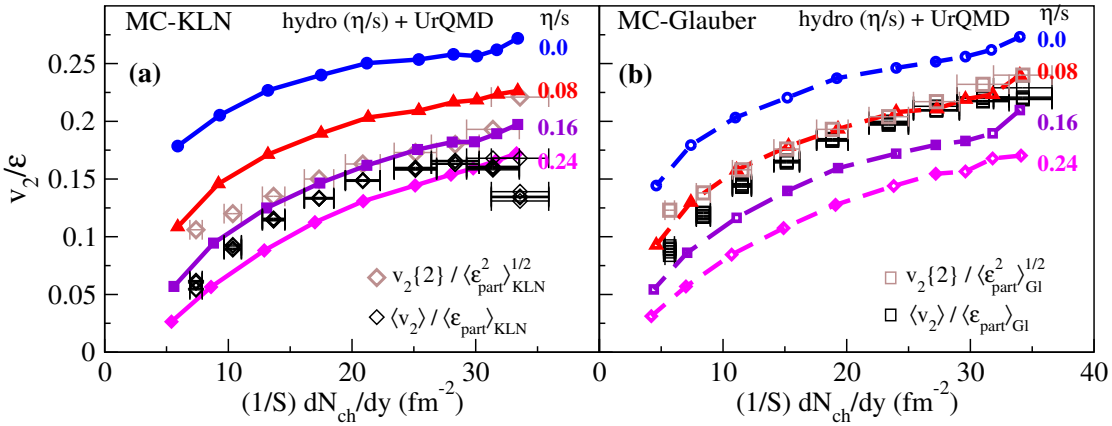

Figure 8.3: Comparison of the universal $v_2(\eta/s)/\varepsilon$ vs. $(1/S)(dN_{\rm ch}/dy)$ curves with experimental data for $\langle v_2\rangle$ [442], $v_2\{2\}$ [443], and $dN_{\rm ch}/dy$ [444] from the STAR Collaboration. The experimental data used in (a) and (b) are identical, but the normalisation factors $\langle\varepsilon_{\rm part}\rangle$ and S used on the vertical and horizontal axes, as well as the factor $\langle\varepsilon^2_{\rm part}\rangle^{1/2}$ used to normalize the $v_2\{2\}$ data, are taken from the MC-KLN model in (a) and from the MC-Glauber model in (b). Theoretical curves are from simulations with MC-KLN initial conditions in (a) and with MC-Glauber initial conditions in (b). Taken from [438].

- Impact on hard probes: Besides the improvement in the determination of nPDFs that affects the quantification of hard probes, commented above, eA collisions can help to understand the dynamics of the probes by analysing the effects of the nuclear medium on them. As two examples, the abundant yields of jets and large transverse momentum particles at the LHeC [1] will allow precise studies of the nuclear effects on jet observables and of hadronisation inside the nuclear medium. These two aspects are of capital importance not only in heavy ion collisions but also in small systems where the lack of jet modification is the only QGP-like characteristics not observed in pPb. On the other hand, measurements of exclusive quarkonium production at the LHeC [1] will provide a better understanding of the cold nuclear matter effects on this probe, on top of which the effects of the QGP will provide a a quantitative characterisation of this new form of QCD matter.

As discussed in Sec. 5.2, pPb and PbPb collisions at the LHC offer possibilities for constraning nPDFs, through the measurement of EW vector boson production [445], dijets [306], D mesons at forward rapidities [319] and exclusive charmonium and dijet photoproduction in ultraperipheral collisions [446, 447, 448]. Specifically, dijets in UPCs could constrain nPDFs in the region $10^{-3} \lesssim x \lesssim 0.7$ and $200 \lesssim Q^2 \lesssim 10^4$ GeV^2. eA collisions would provide more precise nPDFs, whose compatibility with these mentioned observables would clearly establish the validity of collinear factorisation and the mechanisms of particle production in collisions involving nuclei.

Furthermore, eA offers another system where photon-photon collisions, recently measured in UPCs at the LHC [449], can be studied. For example, the observed acoplanarity of the produced muon pairs can be analysed in eA in order to clarify its possible origin and constrain the parton densities in the photon.

Finally, the possible existence of a new non-linear regime of QCD - saturation - at small x is also under study at the LHC, for example using dijets in the forward rapidity region in pPb collisions [450]. As discussed in Sec. 5.5, the ridge phenomenon (two particle correlations peaked at zero and π azimuthal angles and stretched along the full rapidity of the detector) observed in all collision systems, pp, pPb and PbPb at the LHC, has been measured in photoproduction on Pb in UPCs at the LHC [341]. For the time being, its existence in smaller systems like e^+e^- [342] at LEP and ep at HERA [343] has been scrutinised but the results are not conclusive. These studies are fully complementary to those in ep and eA, where its search at the smallest possible values of x at the LHeC would be most interesting. For example, the collision of the virtual photon with the proton at the LHeC can be considered as a high energy collision of two jets or "flux tubes".

In conclusion, ep and eA collisions as studied at the LHeC will have a large impact on the heavy ion programme, as the comparison of the kinematic reach of DIS and hadronic machines shown in Fig. 8.4 makes evident. It should be noted that there exist proposals for extending such programme into Run 5 and 6 of the LHC [312], by running lighter ions and with detector upgrades in ATLAS and CMS (starting in Run 4) and LHCb (Upgrade II [451]).

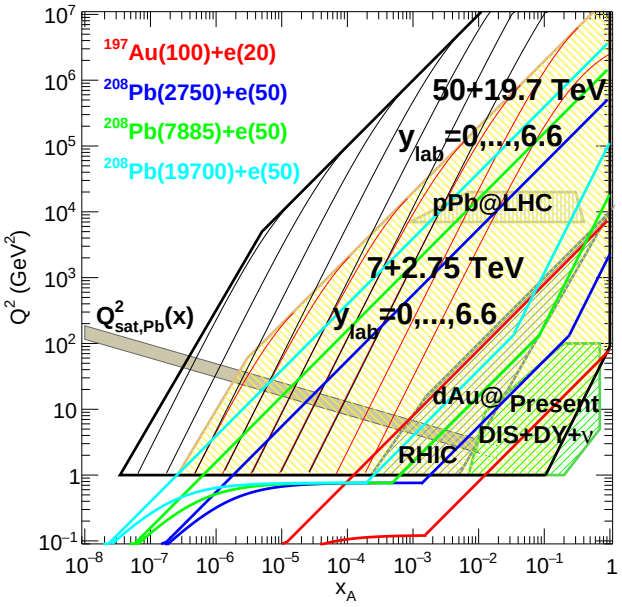

Figure 8.4: Kinematic regions in the $x-Q^2$ plane explored by data sets (charged lepton and neutrino DIS, DY, dAu at RHIC and pPb at the LHC) used in present nPDF analyses [287], compared to the ones achievable at the EIC (red), the LHeC (ERL against the HL-LHC beams, dark blue) and two FCC-eh versions (with Pb beams corresponding to proton energies of 20 TeV - green and 50 TeV - light blue). Acceptance is taken to be $1^\circ < \theta < 179^\circ$, and $0.01(0.001) < y < 1$ for the EIC (all other colliders). The areas delimitated by thick brown and black lines show the regions accessible in pPb collisions at the LHC and the FCC-hh (50 TeV) respectively, while the thin lines represent constant rapidities from 0 (right) to 6.6 (left) for each case. The saturation scale Q_{sat} shown here for indicative purposes only, see also [288], has been drawn for a Pb nucleus considering an uncertainty ~ 2 and a behaviour with energy following the model in [289]. Note that it only indicates a region where saturation effects are expected to be important but there is no sharp transition between the linear and non-linear regimes.

Chapter 9

The Electron Energy Recovery Linac [Erk Jensen, Gianluigi Arduini, Rogelio Tomas]

We studied different options for the electron accelerator for LHeC in [452], of which the Energy Recovery Linac (ERL) option is retained in this update of the CDR. This is due to the higher achievable luminosity of the Linac-Ring option, as compared to the Ring-Ring option, as well as the interference of the installation of an electron ring in the LHC tunnel with its operation [453].The clear advantage of the ERL compared to its contenders in 2012 is the possibility to keep the overall energy consumption at bay; its disadvantage is that operation at lepton energies above 70 GeV would lead to excessive synchrotron radiation losses and is thus practically excluded. Since there is no fundamental beam loading in an ERL by its principle, higher average currents and thus higher luminosities would not lead to larger power consumption.

9.1 Introduction - Design Goals [Gianluigi Arduini, Erk Jensen, Rogelio Tomas]

The main guidelines for the design of the Electron ERL and the Interaction Region (IR) with the LHC :

- electron-hadron operation in parallel with high luminosity hadron-hadron collisions in LHC/HL-LHC;
- centre-of-mass collision energy in the TeV scale;
- power consumption of the electron accelerator smaller than 100 MW;
- peak luminosity approaching 10^{34} $\mathrm{cm}^{-2}\mathrm{s}^{-1}$;
- integrated luminosity exceeding by at least two orders of magnitude that achieved by HERA at DESY.

The electron energy E_e chosen in the previous version of the CDR [452] was 60 GeV. This could be achieved with an ERL circumference of 1/3 of that of the LHC. Cost considerations and machine–detector performance aspects, in particular the amount of synchrotron radiation losses in the IR, have led to define a new reference configuration with $E_e = 49.19$ GeV and a circumference of ≈ 5.4 km, 1/5 of that of the LHC.

The ERL consists of two superconducting (SC) linacs operated in CW connected by three pairs of arcs to allow three accelerating and three decelerating passes (see Figure 9.1). The length of the high energy return arc following the interaction point should be such to provide a half RF period wavelength shift to allow the deceleration of the beam in the linac structures in three passes down to the injection energy and its safe disposal. SC Cavities with an unloaded quality factor Q_0 exceeding 10^{10} are required to minimize the requirements on the cryogenic cooling power and to allow an efficient ERL operation. The choice of having three accelerating and three decelerating passes implies that the circulating current in the linacs is six times the current colliding at the Interaction Point (IP) with the hadron beam.

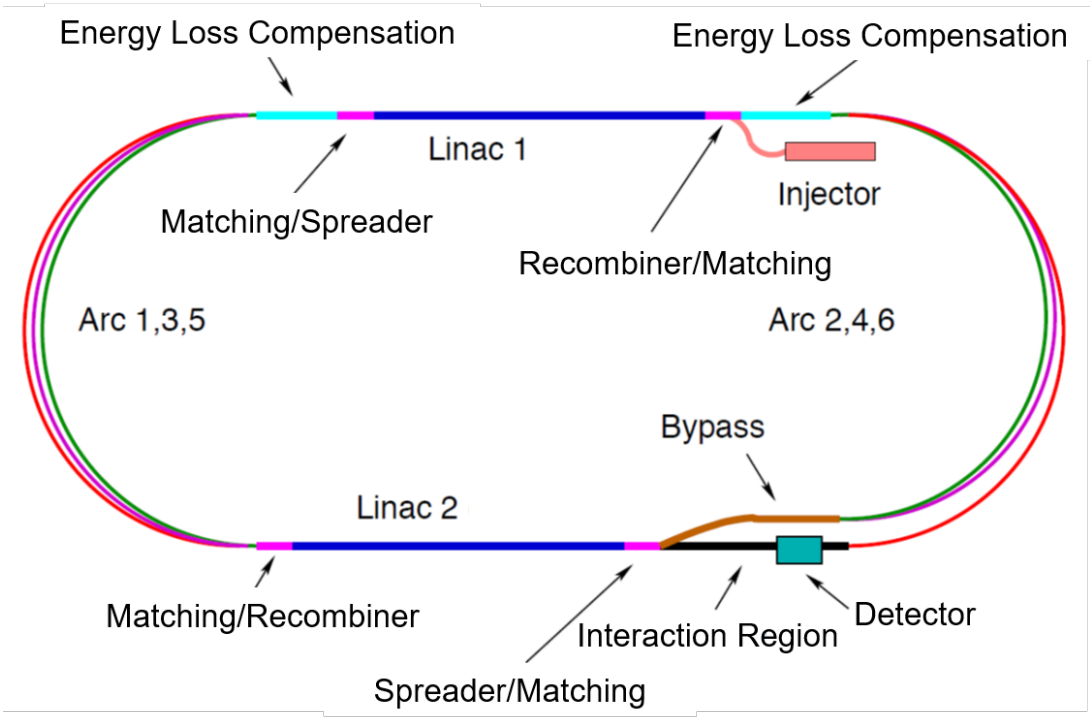

Figure 9.1: Schematic layout of the LHeC design based on an Energy Recovery Linac.

The choice of an Energy Recovery Linac offers the advantages of a high brightness beam and it avoids performance limitations due to the beam-beam effect seen by the electron beam, which was a major performance limitation in many circular lepton colliders (e.g. LEP) and for the LHeC Ring-Ring option. The current of the ERL is limited by its source and an operational goal of $I_e = 20\,\text{mA}$ has been set, corresponding to a bunch current of 500 pC at a bunch frequency of 40 MHz. This implies operating the SRF cavities with the very high current of 120 mA for a virtual beam power (product of the beam current at the IP times the maximum beam energy) of 1 GW. The validation of such performance in terms of source brightness and ERL 3-turn stable and efficient operation in the PERLE facility [454] is a key milestone for the LHeC design.

A small beam size at the IP is required to maximize luminosity and approach peak luminosities of $10^{34}\,\text{cm}^{-2}\text{s}^{-1}$ and integrated luminosities of $1\,\text{ab}^{-1}$ in the HL-LHC lifetime. in particular $\beta^* < 10\,\text{cm}$ needs to be achieved for the colliding proton beam compatibly with the optics constraints imposed by the operation in parallel to proton-proton physics in the other Interaction Points (IPs) during the HL-LHC era [455]. The peak luminosity values quoted above exceed those at HERA by 2-3 orders of magnitude. The operation of HERA in its first, extended running period 1992–2000, provided and integrated luminosity of about $0.1\,\text{fb}^{-1}$ for the H1 and ZEUS experiments, corresponding to the expected integrated luminosity collected over 1 day of LHeC operation!

9.2 The ERL Configuration of the LHeC [Alex Bogacz]

The main parameters of the LHeC ERL are listed in Table 9.1; their choices and optimization criteria will be discussed in the following sections.

Table 9.1: Parameters of LHeC ERL —for reference

Description	unit	parameters
Injector energy	GeV	0.5
Total number of linacs		2
Number of acceleration passes		3
Maximum electron energy	GeV	49.19
Bunch charge	pC	499
Bunch spacing	ns	24.95
Electron current	mA	20
Transverse normalized emittance	µm	20
Total energy gain per linac	GeV	8.114
Frequency	MHz	801.58
Acceleration gradient	MV/m	19.73
Cavity iris diameter	mm	130
Number of cells per cavity		5
Cavity length (active/real estate)	m	0.918/1.5
Cavities per cryomodule		4
Cryomodule length	m	7
Length of 4-CM unit	m	29.6
Acceleration per cryomodule (4-CM unit)	MeV	289.8
Total number of cryomodules (4-CM units) per linac		112 (28)
Total linac length (with with spr/rec matching)	m	828.8 (980.8)
Return arc radius (length)	m	536.4 (1685.1)
Total ERL length	km	5.332

9.2.1 Baseline Design - Lattice Architecture [Alex Bogacz]

The ERL, as sketched in Figure 9.1, is arranged in a racetrack configuration; hosting two superconducting linacs in the parallel straights and three recirculating arcs on each side. The linacs are 828.8 m long and the arcs have 536.4 m radius, additional space of 76 m is taken up by utilities like Spreader/Recombiner, matching and energy loss compensating sections adjacent to both ends of each linac (total of 4 sections) [456]. The total length of the racetrack is 5.332 km: 1/5 of the LHC circumference ($2 \times (828.8 + 2 \times 76 + \pi \times 536.4)$ m). Each of the two linacs provides 8.114 GV accelerating voltage, therefore a 49.19 GeV energy is achieved in three turns. After the collision with the protons in the LHC, the beam is decelerated in the three subsequent turns. The injection and dump energy has been chosen at 0.5 GeV.
Injection into the first linac is done through a fixed field injection chicane, with its last magnet (closing the chicane) being placed at the beginning of the linac. It closes the orbit 'bump' at the lowest energy, injection pass, but the magnet (physically located in the linac) will deflect the beam on all subsequent linac passes. In order to close the resulting higher pass 'bumps', the so-called re-injection chicane is instrumented, by placing two additional opposing bends in front of the last chicane magnet. This way, the re-injection chicane magnets are only 'visible' by the higher pass beams. The second linac in the racetrack is configured exactly as a mirror image of the first one, with a replica of the re-injection chicane at its end, which facilitates a fixed-field extraction of energy recovered beam to the dump.

Linac Configuration and Multi-pass Optics Appropriate choice of the linac optics is of paramount importance for the transverse beam dynamics in a multi-pass ERL. The focusing profile along the linac (quadrupole gradients) need to be set (and they stay constant), so that multiple pass beams within a vast

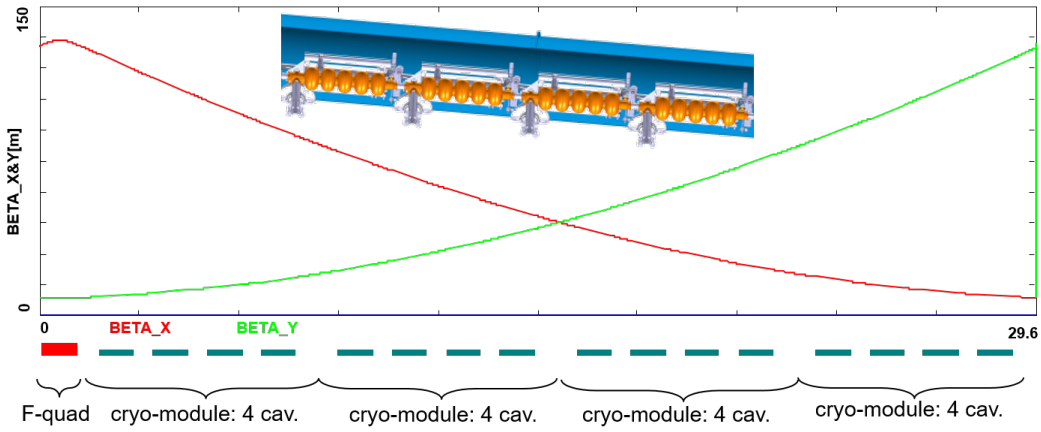

Figure 9.2: Layout of a half-cell composed out of four cryo-modules (each hosting four, 5-cell cavities: top insert) and a focusing quad. Beta functions reflect 130° FODO optics.

energy range may be transported efficiently (provide adequate transverse focusing for given linac aperture).The linac optics is configured as a strongly focusing, 130° FODO. In a basic FODO cell a quadrupole is placed every four cryomodules, so that the full cell contains two groups of 16 RF cavities and a pair of quads (F, D) as illustrated in Figure 9.2. The entire linac is built out of 14 such cells. Energy recovery in a racetrack topology explicitly requires that both the accelerating and decelerating beams share the individual return arcs [457]. This in turn, imposes specific requirements for TWISS function at the linacs ends: TWISS functions have to be identical for both the accelerating and decelerating linac passes converging to the same energy and therefore entering the same arc.

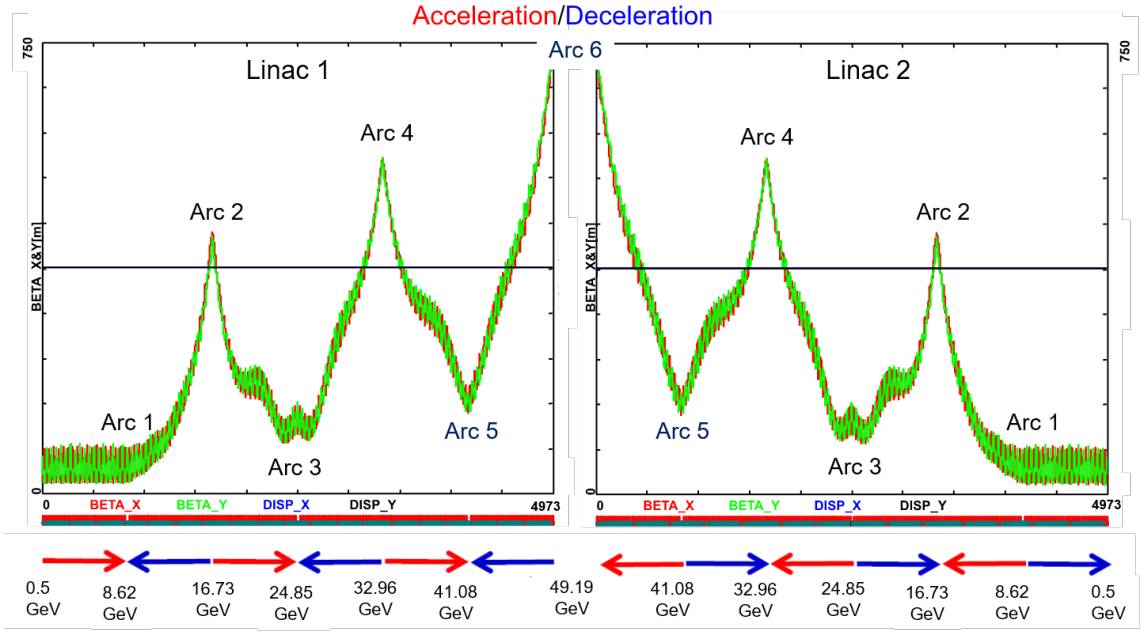

Figure 9.3: Beta function in the optimized multi-pass linacs (3 accelerating passes and 3 decelerating passes in each of two linacs. The matching conditions are automatically built into the resulting multi-pass linac beamline.

To visualize beta functions for multiple accelerating and decelerating passes through a given linac, it is convenient to reverse the linac direction for all decelerating passes and string them together with the interleaved

accelerating passes, as illustrated in Figure 9.3. This way, the corresponding accelerating and decelerating passes are joined together at the arc's entrance/exit. Therefore, the matching conditions are automatically built into the resulting multi-pass linac beamline. One can see that both linacs uniquely define the TWISS functions for the arcs: Linac 1 fixes input to all odd arcs and output to all even arcs, while Linac 2 fixes input to all even arcs and output to all odd arcs. The optics of the two linacs are mirror-symmetric; They were optimized so that, Linac 1 is periodic for the first accelerating pass and Linac 2 has this feature for last decelerating one. In order to maximize the BBU threshold current [458], the optics is tuned so that the integral of β/E along the linac is minimized. The resulting phase advance per cell is close to 130°. Non-linear strength profiles and more refined merit functions were tested, but they only brought negligible improvements.

Recirculating Arcs - Emittance Preserving Optics Synchrotron radiation effects on beam dynamics, such as the transverse emittance dilution induced by quantum excitations have a paramount impact on the collider luminosity. All six horizontal arcs are accommodated in a tunnel of 536.4 m radius. The transverse emittance dilution accrued through a given arc is proportional to the emittance dispersion function, H, averaged over all arc's bends, as expressed by Equation 9.1.

$$\Delta\epsilon = \frac{2\pi}{3} C_q r_0 < H > \frac{\gamma^5}{\rho^2}, \tag{9.1}$$

where

$$C_q = \frac{55}{32\sqrt{3}} \frac{\hbar}{mc}$$

and r_0 is the classical electron radius, γ is the Lorentz boost.
Here, $H = (1+\alpha^2)/\beta \times D^2 + 2\alpha \times DD' + \beta \times D'^2$ where D, D' are the bending plane dispersion and its derivative, with $< ... > = \frac{1}{\pi} \int_{bends} ... \, d\theta$.

Therefore, emittance dilution can be mitigated though appropriate choice of arc optics (values of α, β, D, D' at the bends). In the presented design, the arcs are configured with a FMC (Flexible Momentum Compaction) optics to ease individual adjustment of, $< H >$, in various energy arcs.

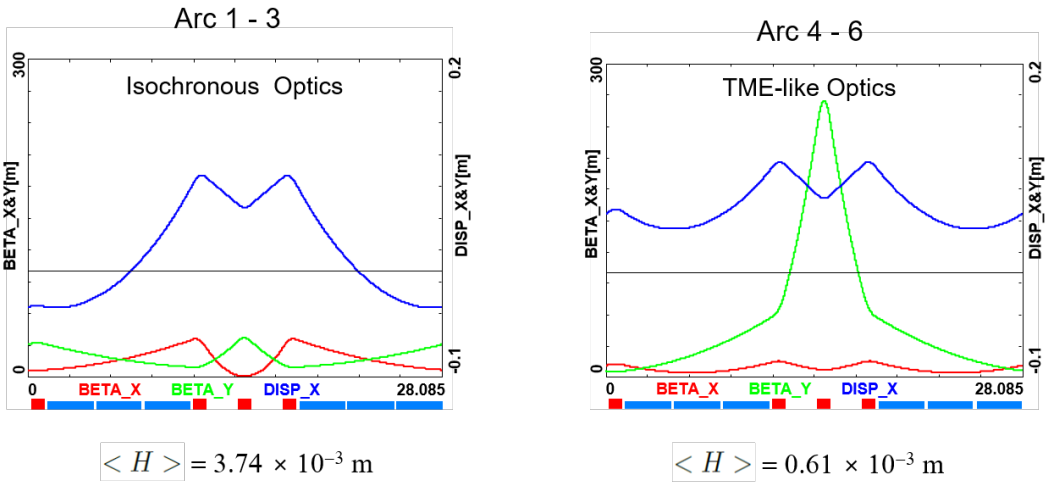

$< H >$ = 3.74 × 10^{-3} m

$< H >$ = 0.61 × 10^{-3} m

Figure 9.4: Two styles of FMC cells appropriate for different energy ranges. Left: lower energy arcs (Arc 1-3) configured with 'Isochronous' cells, Right: higher energy arcs configured with 'TME-like' cells. Corresponding values of the emittance dispersion averages, $< H >$, are listed for both style cells.

Optics design of each arc takes into account the impact of synchrotron radiation at different energies. At the highest energy, it is crucial to minimize the emittance dilution due to quantum excitations; therefore, the cells are tuned to minimize the emittance dispersion, H, in the bending sections, as in the TME (Theoretical Minimum Emittance) lattice. On the other hand, at the lowest energy, it is possible to compensate for the bunch elongation with isochronous optics which, additionally, contains the bunch-length. All styles of FMC lattice cells, as illustrated in Figure 9.4, share the same footprint for each arc. This allows us to stack magnets on top of each other or to combine them in a single design. Here, we use shorter, 28.1 m, FMC cell configured with six 3 m bends, in groups of flanked by a quadrupole singlet and a triplet, as illustrated in Figure 9.4. The dipole filling factor of each cell is 63 %; therefore, the effective bending radius, ρ, is 336.1 m. Each arc is followed by a matching section and a recombiner (mirror symmetric to spreader and matching section). Since the linacs are mirror-symmetric, the matching conditions described in the previous section, impose mirror-symmetric arc optics (identical betas and sign reversed alphas at the arc ends).

Path length adjusting chicanes were also foreseen to tune the beam time of flight in order to hit the proper phase at each linac injection. Later investigations proved them to be effective only with the lowest energy beam, as these chicanes triggers unbearable energy losses if applied to the higher energy beams. A possible solution may consist in distributing the perturbation along the whole arc with small orbit excitations.

Spreaders and Recombiners The spreaders are placed directly after each linac to separate beams of different energies and to route them to the corresponding arcs. The recombiners facilitate just the opposite: merging the beams of different energies into the same trajectory before entering the next linac. As illustrated in Figure 9.5, each spreader starts with a vertical bending magnet, common for all three beams, that initiates the separation. The highest energy, at the bottom, is brought back to the horizontal plane with a chicane. The lower energies are captured with a two-step vertical bending adapted from the CEBAF design [459].

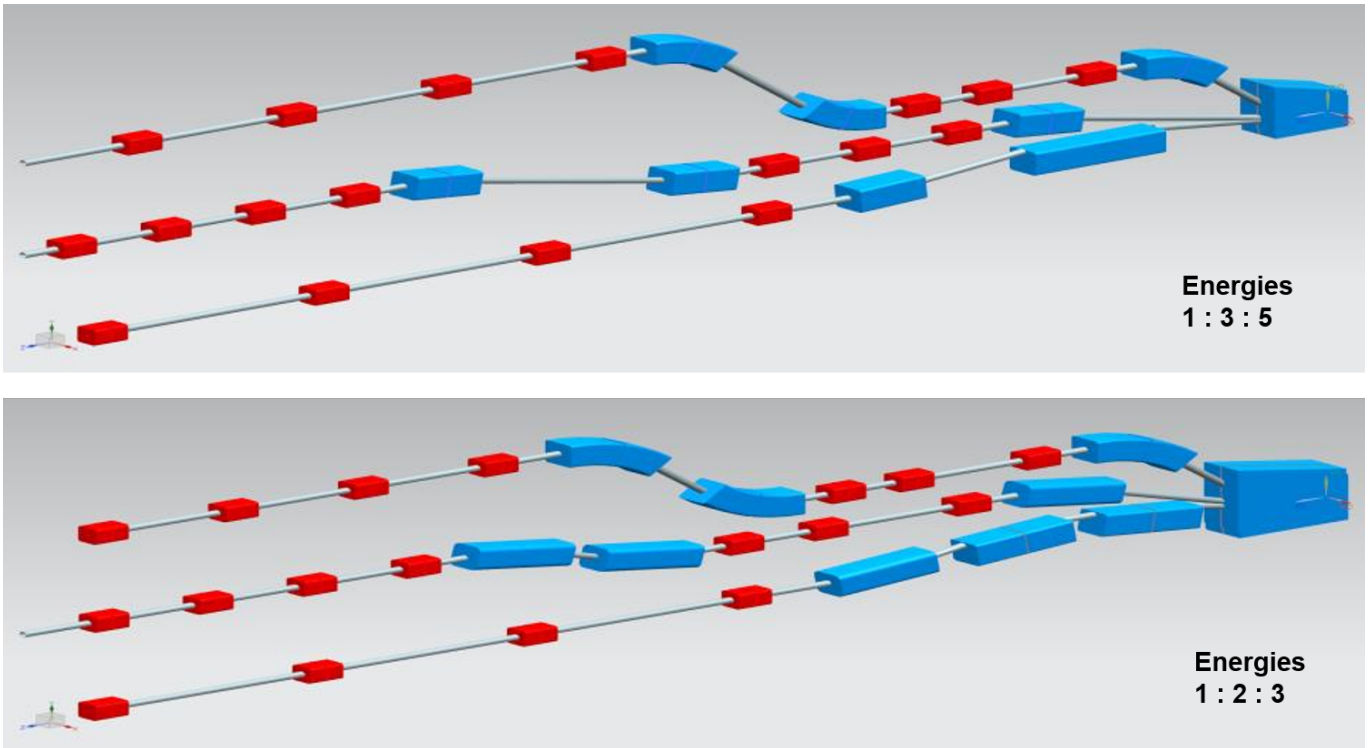

Figure 9.5: Layout of a three-beam switch-yard for different energy ratios: 1 : 3 : 5 and 1 : 2 : 3 corresponding to specific switch-yard geometries implemented on both sides of the racetrack

Functional modularity of the lattice requires spreaders and recombiners to be achromats (both in the horizontal and vertical plane). To facilitate that, the vertical dispersion is suppressed by a pair of quadrupoles located in-between vertical steps; they naturally introduce strong vertical focusing, which needs to by compensated by the middle horizontally focusing quad. The overall spreader optics is illustrated in Figure 9.6. Complete layout of two styles of switch-yard with different energy ratios is depicted in Figure 9.5. Following the spreader, there are four matching quads to 'bridge' the Twiss function between the spreader and the following 180° arc (two betas and two alphas).

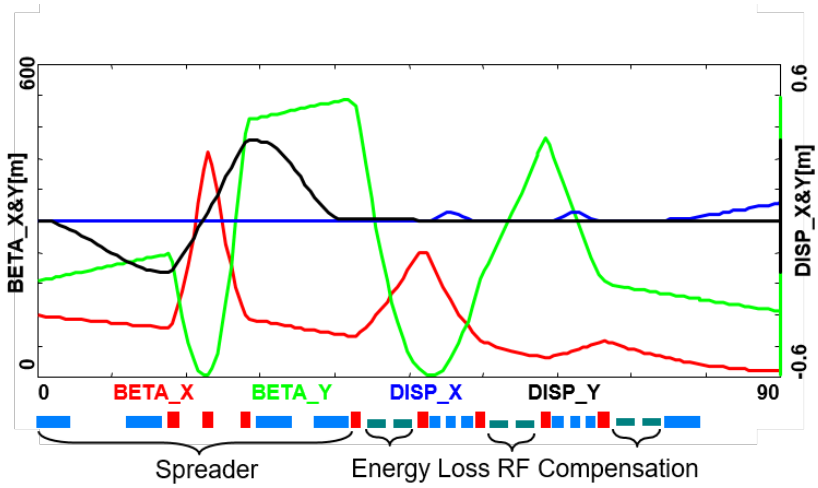

Figure 9.6: Spreader optics; featuring a vertical achromat, pathlength adjucting 'doglegs' and betatron matching quads, interleaved with enerfy loss compensation RF.

Combined spreader-arc-recombiner optics, features a high degree of modular functionality to facilitate momentum compaction management, as well as orthogonal tunability for both the beta functions and dispersion, as illustrated in Figure 9.7.

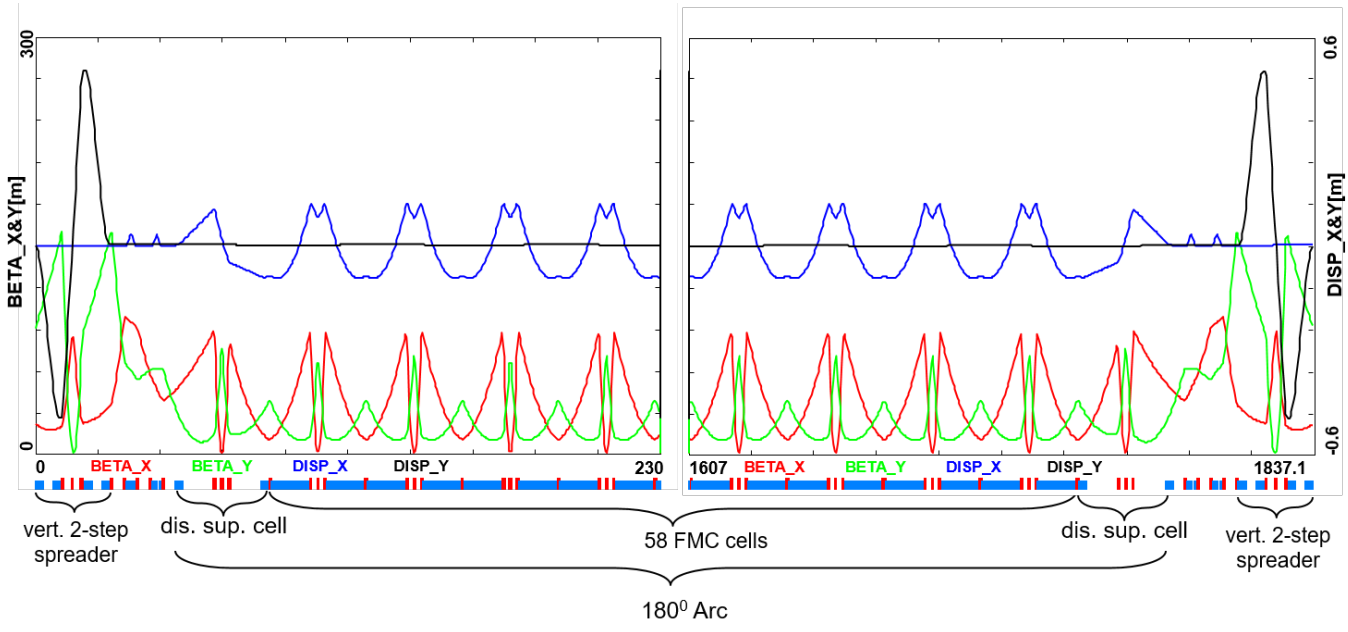

Figure 9.7: Complete Optics for Arc 3 (including switch-yard); featuring: low emittance 180° arc based on DBA-like cells (30 cells flanked by dispersion suppression cell with missing dipoles on each side), spreaders and recombiners with matching sections and doglegs symmetrically placed on each side of the arc proper.

IR Bypasses After the last spreader the 49.19 GeV beam goes straight to the interaction region. However the lower energy beams; at 16.7 and 33.0 GeV, need to be further separated horizontally in order to avoid interference with the detector. Different design options for the bypass section were explored [460] and the one that minimizes the extra bending has been chosen and implemented in the lattice.

Ten arc-like dipoles are placed very close to the spreader, to provide an initial bending, θ, which results in $X = 10$ m separation from the detector located 120 m downstream. The straight section of the bypass is approximately 240 m long. After the bypass, in order to reconnect to the footprint of Arc 6, 7 of 30 standard cells in Arc 2 and Arc 4 are replaced with 7 higher field, junction cells. The number of junction cells is a compromise between the field strength increase and the length of additional bypass tunnel, as can be inferred from the scheme summarized in Figure . The stronger bending in the junction cells creates a small mismatch, which is corrected by adjusting the strengths of the quadrupoles in the last junction cell and in the first regular cell.

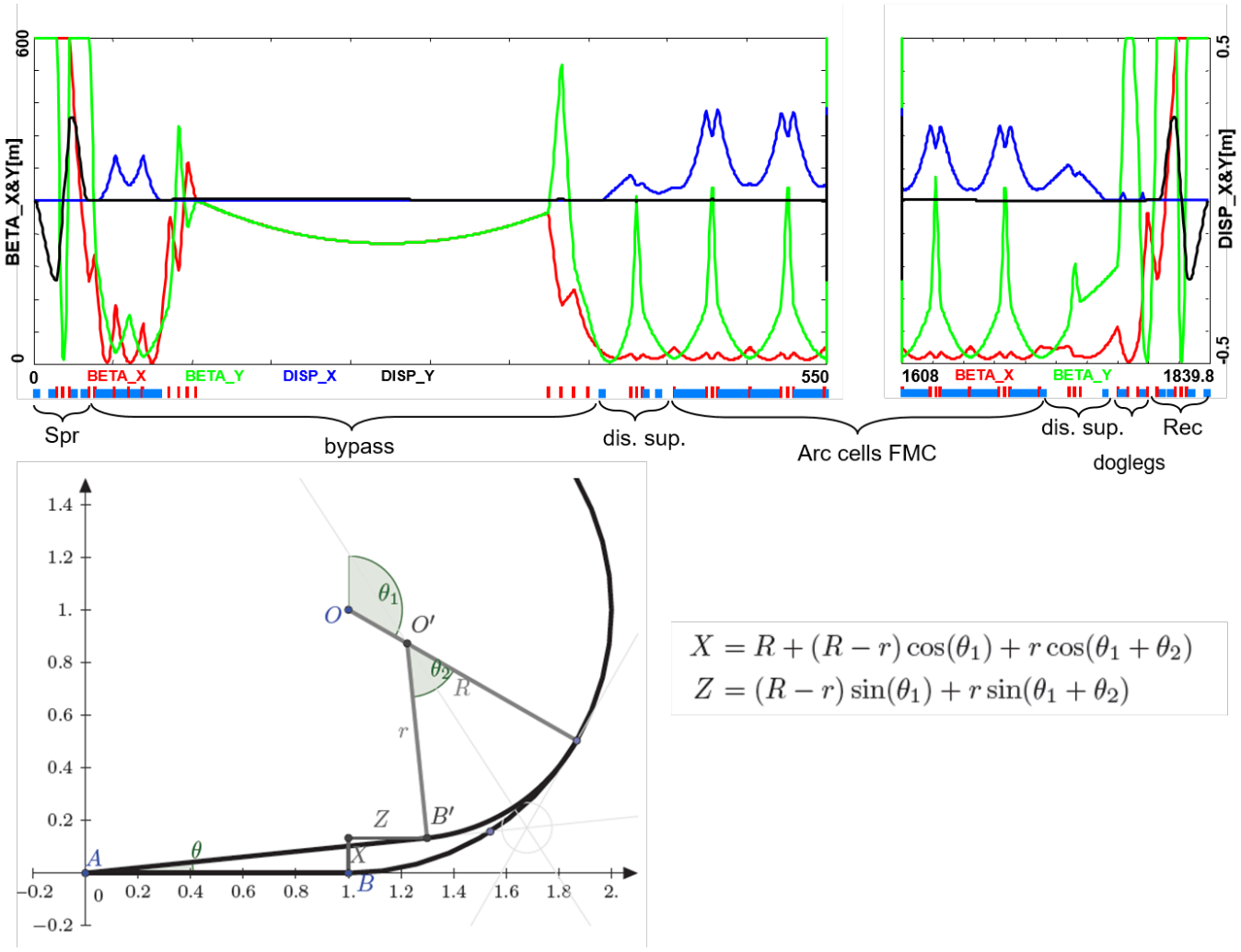

Figure 9.8: Optics and layout of Arc 4 including the detector bypass. The lattice (top insert) features a vertical spreader, an initial horizontal bending , a straight section, a modified dispersion suppressor, seven junction cells, and four regular cells. The bypass geometry (bottom insert), features a long IP line, AB, stretched to about 1/5 of the arc radius. All geometric dependencies of the bypass parameters are summarized in the inserted formulae as well.

Synchrotron Radiation Effects - Emittance Dilution ERL efficiency as a source of multi-GeV electrons for a high luminosity collider is limited by the incoherent synchrotron radiation effects on beam dynamics; namely the transverse emittance dilution and the longitudinal momentum spread (induced by quantum excitations). The fist effect, the transverse emittance increase, will have a paramount impact on the collider luminosity, due to stringent limits on the allowed emittance increase. The second one, accrued momentum spread, governs asymmetries of accelerated and decelerated beam profiles. These asymmetries substantially complicate multi-pass energy recovery and matching, and ultimately they limit the energy reach of the ERLs due to recirculating arc momentum acceptance.

Arc optics was designed to ease individual adjustment of momentum compaction (needed for the longitudinal phase-space control, essential for operation with energy recovery) and the horizontal emittance dispersion, H, in each arc. Table 9.2 lists arc-by-arc dilution of the transverse, $\Delta\epsilon$, and longitudinal, $\Delta\sigma_{\frac{\Delta E}{E}}$, emittance dilution due to quantum excitations calculated using analytic formulas, Equations 9.2, 9.3 and 9.4, introduced by M. Sands [461].

$$\Delta E = \frac{2\pi}{3} r_0 \; mc^2 \; \frac{\gamma^4}{\rho}, \tag{9.2}$$

$$\Delta\epsilon_N = \frac{2\pi}{3} C_q r_0 < H > \frac{\gamma^6}{\rho^2}, \tag{9.3}$$

$$\frac{\Delta\epsilon_E^2}{E^2} = \frac{2\pi}{3} C_q r_0 \; \frac{\gamma^5}{\rho^2}, \tag{9.4}$$

where

$$C_q = \frac{55}{32\sqrt{3}} \; \frac{\hbar}{mc}.$$

Here, r_0 is the classical electron radius, γ is the Lorentz boost and $C_q \approx 3.832 \times 10^{-13}\ m$ for electrons (or positrons).

Table 9.2: Energy loss and emittance dilution (horizontal and longitudinal) due to synchroton radiation generated by all six 180° arcs. Here, $\Delta\sigma_{\frac{\Delta E}{E}} = \sqrt{\frac{\Delta\epsilon_E^2}{E^2}}$

Beamline	Beam energy [GeV]	ΔE [MeV]	$\Delta\epsilon_N^x$ [mm mrad]	$\Delta\sigma_{\frac{\Delta E}{E}}$ [%]
arc 1	8.62	1	0.0017	0.00052
arc 2	16.73	10	0.092	0.0027
arc 3	24.85	50	0.99	0.0074
arc 4	32.96	155	0.88	0.015
arc 5	41.08	375	3.28	0.026
arc 6	49.19	770	9.68	0.041

Here, the LHeC luminosity requirement of total transverse emittance dilution (normalized) of 10 mm mrad is met by-design, employing low emittance optics arcs, as implemented in our scheme.
Finally, one can see from Equations 9.3 and 9.4 an underlying universal scaling of the transverse and longitudinal emittance dilution with energy and arc radius; they are both proportional to γ^5/ρ^2. This in

turn, has a profound impact on arc size scalability with energy; namely the arc radius should scale as $\gamma^{5/2}$ in order to preserve both the transverse and longitudinal emittance dilutions, which is a figure of merit for a synchrotron radiation dominated ER.

Apart from the horizontal 180° arcs, there are other sources of emittance dilution due to synchrotron radiation, namely vertical Spreaders and Recombiners, as well as horizontal 'Doglegs' used to compensate seasonal variation of path-length. To minimize contribution to the vertical emittance dilution, special optics with small vertical $< H >$ has been introduced in Spr/Rec sections. The effects on vertical emittance dilution coming from these beamlines (Spr/Rec) are summarized in Table 9.3.

Table 9.3: Energy loss and emittance dilution (vertical and longitudinal) due to synchroton radiation generated by a given beamline. Here, $\Delta\sigma_{\frac{\Delta E}{E}} = \sqrt{\frac{\Delta\epsilon_E^2}{E^2}}$

Beamline	Beam energy [GeV]	ΔE [MeV]	$\Delta\epsilon_N^y$ [mm mrad]	$\Delta\sigma_{\frac{\Delta E}{E}}$ [%]
Spr/Rec 1	8.62	0	0.035	0.0008
Spr/Rec 2	16.73	3	0.540	0.0044
Spr/Rec 3	24.85	6	0.883	0.0066
Spr/Rec 4	32.96	22	5.549	0.0143
Spr/Rec 5	41.08	7	0.402	0.0062
Spr/Rec 6	49.19	110	83.164	0.0446

Similarly, the horizontal emittabce dilution induced by Doglegs in various arcs is summarized in Table 9.4.

Table 9.4: Energy loss and emittance dilution (horizontal and longitudinal) due to synchroton radiation generated by a Dogleg. Here, $\Delta\sigma_{\frac{\Delta E}{E}} = \sqrt{\frac{\Delta\epsilon_E^2}{E^2}}$

Beamline	Beam energy [GeV]	ΔE [MeV]	$\Delta\epsilon_N^y$ [mm mrad]	$\Delta\sigma_{\frac{\Delta E}{E}}$ [%]
Doglegs 1	8.62	0	0.011	0.0002
Doglegs 2	16.73	1	0.124	0.0023
Doglegs 3	24.85	3	0.221	0.0043
Doglegs 4	32.96	11	1.521	0.0176
Doglegs 5	41.08	23	8.402	0.0266
Doglegs 6	49.19	39	11.164	0.0311

Combining all three contributions: (180° arc, Spr/Rec and Doglegs), the net commutative emittance dilution is summarized in Table 9.5.

Table 9.5: Energy loss and cumulative emittance dilution (transverse and longitudinal) due to synchroton radiation at the end of a given beamline (complete Arc including: 180° arc, Spr/Rec and Doglegs): Entire ER cycle (3 passes'up' + 3 passes 'down'). Here, $\Delta\sigma_{\frac{\Delta E}{E}} = \sqrt{\frac{\Delta\epsilon_E^2}{E^2}}$

Beamline	Beam energy [GeV]	ΔE [MeV]	$\Delta\epsilon_N^x$ [mm mrad]	$\Delta\sigma_{\frac{\Delta E}{E}}$ [%]
Arc 1	8.62	1	0.0017	0.00052
Arc 2	16.73	10	0.094	0.0033
Arc 3	24.85	50	1.1	0.011
Arc 4	32.96	155	2.0	0.026
Arc 5	41.08	375	5.2	0.052
Arc 6	49.19	770	14.9	0.092
Arc 5	41.08	375	18.2	0.118
Arc 4	32.96	155	19.1	0.133
Arc 3	24.85	50	20.1	0.140
Arc 2	16.73	10	20.2	0.143
Arc 1	8.62	1	20.2	0.144
Dump	0.5		20.2	0.144

9.2.2 30 GeV ERL Options [Alex Bogacz]

One may think of an upgrade path from 30 to 50 GeV ERL, using the same 1/5 of the LHC circumference (5.4 km), footprint. In this scenario, each linac straight (front end) would initially be 'loaded' with 18 cryo-modules, forming two 5.21 GV linacs. One would also need to decrease the injector energy by factor of 5.21/8.11 The top ERL energy, after three passes, would reach 31.3 GeV. Then for the upgrade to 50 GeV, one would fill the remaining space in the linacs with additional 10 cryo-moduls each; 2.9 GV worth of RF in each linac. This way the energy ratios would be preserved for both 30 and 50 GeV ERL options, so that the same switch-yard geometry could be used. Finally, one would scale up the entire lattice; all magnets (dipoles and quads) by 8.11/5.21 ratio. If one wanted to stop at the 30 GeV option with no upgrade path, then the 1/12 of the LHC circumference (2.2 km) would be a viable footprint for the racetrack, featuring: two linacs, 533 m each, (18 cryo-modules) and arcs of 136 m radius. Again, assuming 0.32 GeV injection energy, the top ERL energy would reach 31.3 GeV.

9.2.3 Component Summary [Alex Bogacz]

This closing section will summarize active accelerator components: magnets (bends and quads) and RF cavities for the 50 GeV baseline ERL. The bends (both horizontal and vertical) are captured in Table 9.6, while the quadrupole magnets and RF cavities are collected in Table 9.7.

On would like to use a combined aperture (3-in-one) arc magnet design with 50 cm vertical separation between the three apertures, proposed by Attilo Milanese. That would reduce net arc bend count from 2112 to 704. As far as the Spr/Rec vertical bends are concerned, the design was optimized to include additional common bend separating two highest passes. So, there are total of 8 trapezoid B-com magnets, with second face tilted by 3 deg and large 10 cm vertical aperture, the rest are simple rectangular bends with specs from the summary Table 9.6.

Table 9.6: 50 GeV ERL - Dipole magnet count along with basic magnet parameters: Magnetic field - (B), Half-Gap - ($g/2$), Magnetic length - (L).

	Arc Dipoles (Hor.)				Spr/Rec Dipoles (Ver.)				'Dogleg' Dipoles (Hor.)			
Section	N	$B[T]$	$g/2[cm]$	$L[m]$	N	$B[T]$	$g/2[cm]$	$L[m]$	N	$B[T]$	$g/2[cm]$	$L[m]$
Arc 1	352	0.087	1.5	3	8	0.678	2	3	12	0.131	1.5	1
Arc 2	352	0.174	1.5	3	8	0.989	2	3	12	0.261	1.5	1
Arc 3	352	0.261	1.5	3	6	1.222	2	3	12	0.392	1.5	1
Arc 4	352	0.348	1.5	3	6	1.633	2	3	12	0.522	1.5	1
Arc 5	352	0.435	1.5	3	4	1.022	2	3	12	0.653	1.5	1
Arc 6	352	0.522	1.5	3	4	1.389	2	3	12	0.783	1.5	1
Total	2112				36				72			

Table 9.7: 50 GeV ERL - Quadrupole magnet and RF cavities count along with basic magnet/RF parameters: Magnetic field gradient - (G), Aperture radius - (a), Magnetic length - (L), Frequency - (f), Number of cells in RF cavity - ($cell$), RF Gradient - (G_{RF}).

	Quardupoles)				RF Cavities			
Section	N	$G[T/m]$	$a[cm]$	$L[m]$	N	$f[MHz]$	$cell$	$G_{\mathrm{RF}}[T/m]$
Linac 1	29	1.93	3	1	448	802	5	20
Linac 2	29	1.93	3	1	448	802	5	20
Arc 1	255	9.25	2.5	1				
Arc 2	255	17.67	2.5	1				
Arc 3	255	24.25	2.5	1	6	1604	9	30
Arc 4	255	27.17	2.5	1	6	1604	9	30
Arc 5	249	33.92	2.5	1	18	1604	9	30
Arc 6	249	40.75	2.5	1	30	1604	9	30
Total	1576				956			

9.3 Electron-Ion Scattering [John Jowett]

Besides colliding proton beams, the LHC also provides collisions of nuclear (fully-stripped ion) beams with each other (AA collisions) or with protons (pA). Either of these operating modes offers the possibility of electron-ion (eA) collisions in the LHeC configuration. In pA operation of the LHC the beams may be reversed (Ap) for some part of the operating time. Only one direction (ions in Beam 2) would provide eA collisions while the other would provide ep collisions at significantly reduced luminosity compared to the pp mode, since there would be fewer bunches of lower intensity.

Here we present luminosity estimates for collisions of electrons with $^{208}\mathrm{Pb}^{82+}$ nuclei, the species most commonly collided in the LHC. Other, lighter, nuclei are under consideration for future LHC operation [312].

9.4 Beam-Beam Interactions [Kevin Andre, Andrea Latina, Daniel Schulte]

9.4.1 Effect on the electron beam

9.4.2 Effect on the proton beam

9.5 Arc Magnets [Pierre Thonet, Cynthia Vallerand]

9.6 LINAC and SRF [Erk Jensen]

Each of the two main linacs has an overall length of 828.8 m and provides an acceleration of 8.114 GV. Each linac consists of 112 cryomodules, arranged in 28 units of 4 cryomodules with their focussing elements—each cryomodule contains four 5-cell cavities, optimized to operate with large beam current (up to 120 mA at the HOM frequencies). The operating temperature is 2 K; the cavities are based on modern SRF technology and are fabricated from bulk Nb sheets; they are described in detail in subsection 9.6.2 below. The nominal acceleration gradient is 19.73 MV/m.

In addition to the main linacs, the synchrotron losses in the arcs will make additional linacs necessary, referred to here as the "loss compensation linacs". These will have to provide different accelerations in the different arcs, depending on the energy of the beams as shown in Table 9.8. The quoted beam energies are at entry into the arc. Their natural placement would be at the end of the arcs just before the combiner, where the different energy beams are still separate. The largest of these linacs would have to compensate the SR losses at the highest energy, requiring a total acceleration of about 700 MV. The loss compensation linacs will be detailed in subsection 9.6.7 below.

Table 9.8: Synchroton radiation losses for the different arc energies

Arc number	Beam energy [GeV]	ΔE [MeV]
1	8.62	1
2	16.73	10
3	24.85	50
4	32.96	155
5	41.08	375
6	49.19	770

Through all arcs but arc 6, the beam passes twice, once while accelerated and once while decelerated. It is planned to operate these additional "loss compensation linacs" at 1603.2 MHz, which allows energy compensation of both the accelerated and the decelerated beam simultaneously. This subject will be discussed in detail in a subsequent section, 1.6.7.

9.6.1 Choice of Frequency [Frank Marhauser]

The RF frequency choice primarily takes into account the constraints of the LHC bunch repetition frequency, f_0, of 40.079 MHz, while allowing for a sufficiently high harmonic, h, for a flexible system. For an ERL with $n_{pass} = 3$ recirculating passes and in order to enable equal bunch spacing for the 3 bunches – though not mandatory – it was originally considered to suppress all harmonics that are not a multiple of $n_{pass} \cdot f_0 = 120.237$ MHz. Initial choices for instance were 721.42 MHz ($h = 18$) and 1322.61 MHz ($h = 33$) in consideration of the proximity to the frequencies used for state-of-the-art SRF system developments worldwide [462]. In synergy with other RF system developments at CERN though, the final choice was

801.58 MHz ($h = 20$), where the bunching between the 3 recirculating bunches can be made similar but not exactly equal. Note that this frequency is also very close to the 805 MHz SRF proton cavities operating at the Spallation Neutron Source (SNS) at ORNL, so that one could leverage from the experience in regard to cryomodule and component design at this frequency.

Furthermore, in the frame of an independent study for a 1 GeV CW proton linac, a capital plus operational cost optimization was conducted [463]. This optimization took into account the expenditures for cavities, cryomodules, the linac tunnel as well as the helium refrigerator expenses as a function of frequency and thus component sizes. Labor costs were included based on the existing SNS linac facility work breakdown structure. It was shown that capital plus operating costs could be minimized with a cavity frequency between 800 MHz and 850 MHz, depending also on the choice of the operating He bath temperature (1.8 K to 2.1 K). Clear benefit of operating in this frequency regime are the comparably small dynamic RF losses per installation length due to a relatively small BCS surface resistance as well as low residual resistance of the niobium at the operating temperature. This could be principally verified as part of the prototyping effort detailed in the next sub-section. Note that the cost optimum also favors cavities operating at rather moderate field levels (< 20 MV/m). This comes as a benefit in concern of field emission and associated potential performance degradations.

9.6.2 Cavity Prototype [Frank Marhauser]

Given the RF frequency of 801.58 MHz, JLab has collaborated with CERN, and consequently proposed a five-cell cavity design that was accepted for prototyping, see Fig. 9.9. The cavity shape has also been adopted for PERLE. Table 9.9 summarizes the relevant cavity parameters.

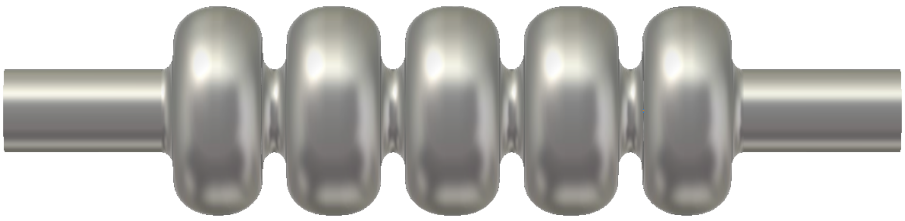

Figure 9.9: Bare 802 MHz five-cell cavity design (RF vacuum) with a 130 mm iris and beam tube aperture.

The cavity exhibits a rather large iris and beam tube aperture (130 mm) to consider beam-dynamical aspects such as HOM-driven multi-bunch instabilities. Despite the comparably large aperture, the ratio of the peak surface electric field, E_{pk}, respectively the peak surface magnetic field, B_{pk}, and the accelerating field, E_{acc}, are reasonably low, while the factor $R/Q \cdot G$ is kept reasonably high, concurrently to limit cryogenic losses. This is considered as a generically well 'balanced' cavity design [464]. The cavity cell shape also avoids that crucial HOMs will coincide with the main spectral lines (multiples of 801.58 MHz), while the specific HOM coupler development is pending.

Furthermore, as shown in Fig. 9.10 for the case of the bunch recombination pattern considered for PERLE originally, the much denser intermediate beam current lines (green) are not coinciding with cavity HOMs. Here the figure plots the real part of the beam-excited cavity monopole impedance spectrum up to 6 GHz, and denotes the power deposited at each spectral line (in Watt) for an injected beam current of 25 mA. For instance, the summation of the power in this spectral range results in a moderate 30 Watts. This covers the monopole modes with the highest impedances residing below the beam tube cutoff frequency. The HOM-induced heat has to be extracted from the cavity and shared among the HOM couplers attached to the cavity beam tubes. The fraction of the power escaping through the beam tubes above cutoff can be intercepted by beam line absorbers.

Table 9.9: Parameter table of the 802 MHz prototype five-cell cavity

Description	unit	parameters
Frequency	MHz	801.58
Number of cells		5
active length l_{act}	mm	917.9
loss factor	$\mathrm{V\,pC^{-1}}$	2.742
R/Q (linac convention)	Ω	523.9
$R/Q \cdot G$ per cell	Ω^2	28788
Cavity equator diameter	mm	327.95
Cavity iris diameter	mm	130
Beam tube inner diameter	mm	130
diameter ratio equator/iris		2.52
E_{peak}/E_{acc}		2.26
B_{peak}/E_{acc}	mT/(MV/m)	4.2
cell-to-cell coupling factor k_{cc}	%	3.21
$\mathrm{TE_{11}}$ cutoff frequency	GHz	1.35
$\mathrm{TM_{01}}$ cutoff frequency	GHz	1.77

Note that for Fig. 9.10 a single HOM-coupler end-group consisting of three scaled TESLA-type coaxial couplers was assumed to provide damping. Instead of coaxial couplers, waveguide couplers could be utilized, which for instance have been developed at JLab in the past for high current machines. These are naturally broadband and designed for high power capability, though some penalty is introduced as this will increase the complexity of the cryomodule. Ultimately, the aim is to efficiently damp the most parasitic longitudinal and transverse modes (each polarization). The evaluation of the total power deposition is important for LHeC to decide which HOM coupler technology is most appropriate to cope with the dissipated heat and whether active cooling of the couplers is a requirement.

Though the prototype efforts focused on the five-cell cavity development, JLab also produced single-cell cavities, i.e. one further Nb cavity and two OFE copper cavities. The former has been shipped to FNAL for N-doping/infusion studies, whereas the latter were delivered to CERN for Nb thin-film coating as a possible alternative to bulk Nb cavities. In addition, a copper cavity was built for low power bench measurements, for which multiple half-cells can be mechanically clamped together. Presently, a mock-up can be created with up to two full cells. This cavity has been produced in support of the pending HOM coupler development. Fig. 9.11 shows the ensemble of manufactured cavities resonating at 802 MHz.

Results for the Nb cavities - made from fine grain high-RRR Nb - were encouraging since both cavities reached accelerating fields, E_{acc}, slightly above 30 MV/m ultimately limited by thermal breakdown (quench). Moreover, the RF losses were rather small as a benefit of the relatively low RF frequency as anticipated. The residual resistance extracted from the measurement data upon cooldown of the cavity was $3.2\,\Omega \pm 0.8\,\Omega$. This resulted in unloaded quality factors, Q_0, well above 4×10^{10} at 2 K at low field levels, while Q_0-values beyond 3×10^{10} could be maintained for the five-cell cavity up to ∼27 MV/m (see Fig. 9.12). Only standard interior surface post-processing methods were applied including bulk buffered chemical polishing, high temperature vacuum annealing, light electropolishing, ultrapure high-pressure water rinsing, and a low temperature bake-out. While the vertical test results indicate generous headroom for a potential performance reduction once a cavity is equipped with all the ancillary components and installed in a cryomodule, clean cavity assembly procedure protocols must be established for the cryomodules to minimize the chance of introducing field-emitting particulates.

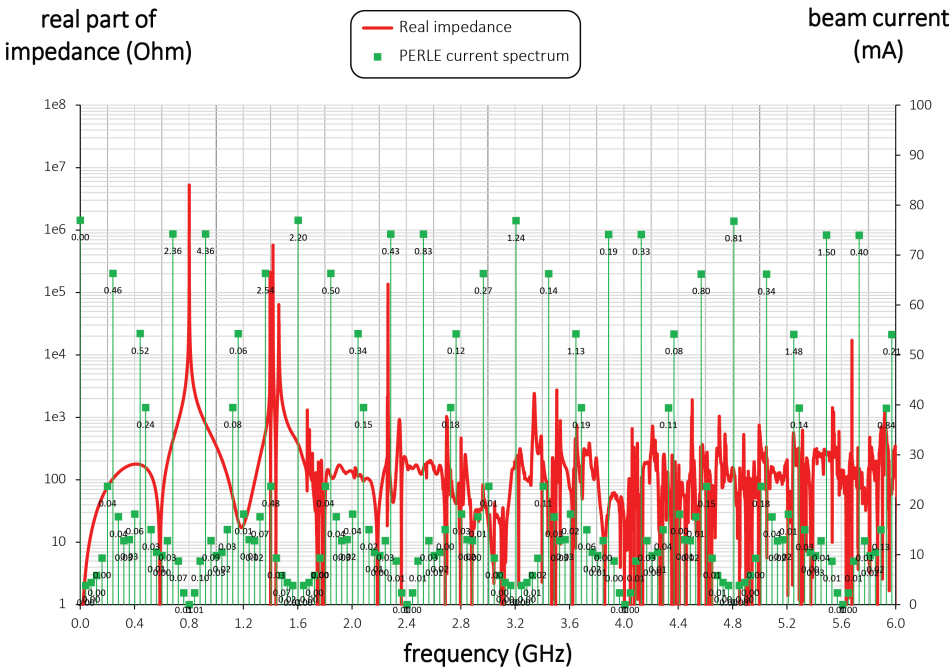

Figure 9.10: Real monopole impedance spectrum of the five-cell 802 MHz cavity prototype (red) together with the considered beam current lines (green) for the 3-pass PERLE machine (25 mA injected current). The numbers associated with the spectral lines denote the power dissipation (in Watt).

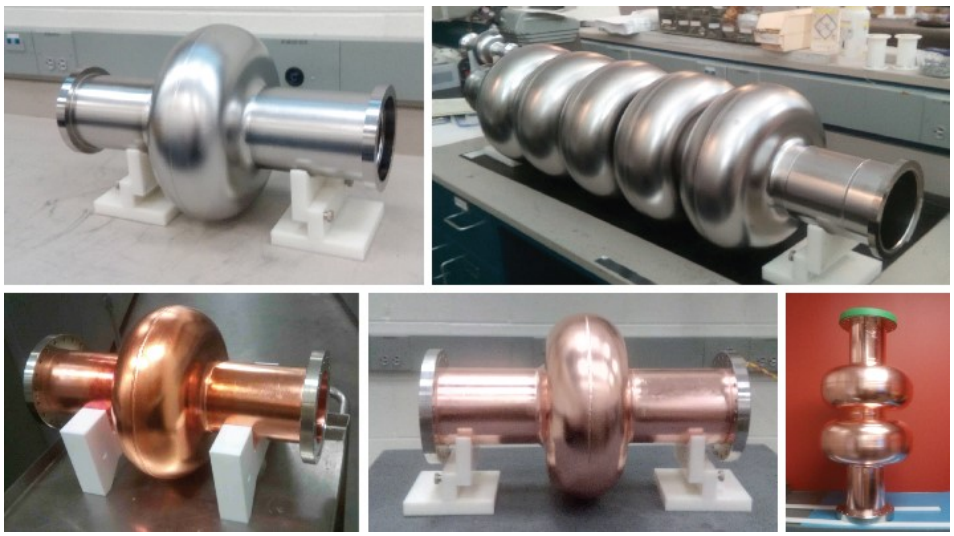

Figure 9.11: Ensemble of 802 MHz cavities designed and built at JLab for CERN. The Nb cavities have been tested vertically at 2 Kelvin in JLab's vertical test area.

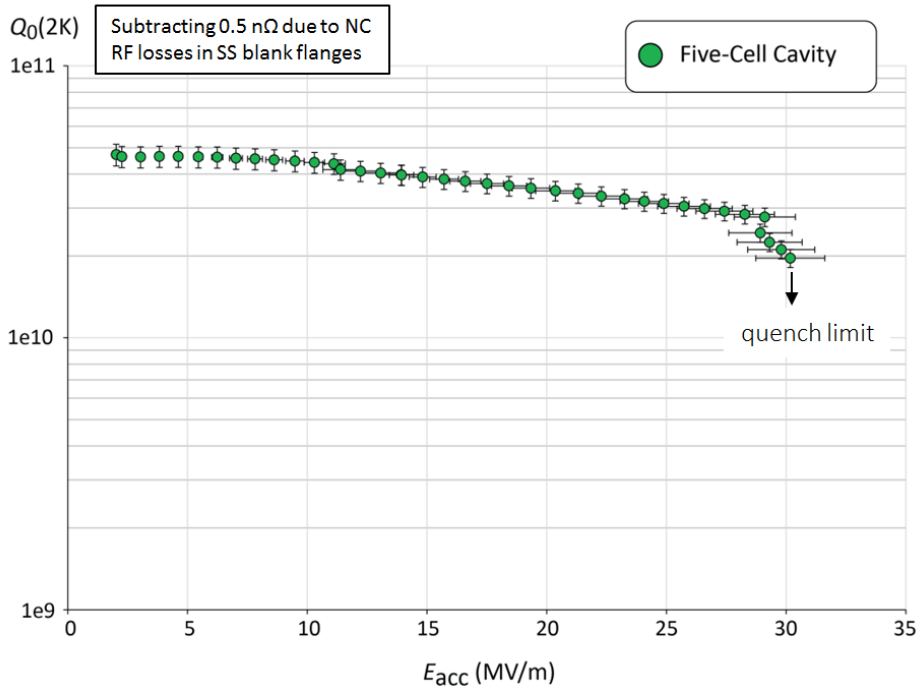

Figure 9.12: Vertical test result of the five-cell 802 MHz niobium cavity prototype.

9.6.3 Dressed Cavity Design [Sebastien Bousson]

9.6.4 Cavity-CryoModule [Gilles Olivier]

9.6.5 Sources [Boris Militsyn, Ben Hounsell, Matt Poelker]

Specification of electron sources

Operation of the LHeC with an electron beam, delivered by a full energy ERL imposes specific requirements on the electron source. It should deliver a beam with the charge and temporal structure required at the Interaction Point. Additionally as during acceleration in a high energy ERL both longitudinal and transverse emittances of the beam are increased due to Synchrotron Radiation (SR), the 6D emittance of the beam delivered by electron source should be small enough to mitigate this effect. The general specification of the electron source are shown in Table 9.10. Some parameters in this table such as RMS bunch length, uncorrelated energy spread and normalised transverse emittance are given on the basis of the requirements for the acceleration in ERL and to pre-compensate the effects of SR. The most difficult of the parameters to specify is injector energy. It should be as low as possible to reduce the unrecoverable power used to accelerate the beam before injection into the ERL while still being high enough to deliver short electron bunches with high peak current. Another constraint on the injection energy is the average energy and energy spread of the returned beam. The average energy cannot be less than the energy of electron source, but the maximum energy in the spectrum should not exceed 10 MeV the neutron activation threshold. An injection energy of 7 MeV is a reasonable compromise to meet this constraint.

The required temporal structure of the beam and the stringent requirements for beam emittance do not allow the use of conventional thermionic electron sources for the LHeC ERL without need for beam losses during the bunching process. While this option cannot completely be excluded as a source of unpolarised electrons. The requirement to deliver polarised beams leaves only one option available, electron sources

Table 9.10: General specification of the LHeC ERL electron injector.

Beam parameter	
Injection energy, MeV	7*
Bunch repetition rate, MHz	40.1
Average beam current, mA	20
Bunch charge, pC	500
RMS bunch length, mm	3
Normalised transverse emittance, π·mm·mrad	<6
Uncorrelated energy spread, keV	10
Beam polarisation	Unpolarised/Polarised

based on photoemission of electrons.

There are now four possible design of electron sources for delivering unpolarised beams and (potentially) three for delivering polarised beams:

1. A thermionic electron source with RF modulated grid or gate electrode with following (multi)stage compression and acceleration. The electron source could be either a DC electron gun or an RF electron source in this case. Although these sources are widely used in the injectors of IR FELs [465] their emittance is not good enough to meet the specification of the LHeC injector. Moreover, thermionic sources cannot deliver polarised electrons.

2. A VHF photoemission source. This is a type of normal conducting RF source which operates in the frequency range 160 MHz – 200 MHz. The relatively low frequency of these sources means that they are large enough that sufficient cooling can be provided to permit CW operation. This type of source has been developed for the new generation of CW FELs such as LCLS-II [466], SHINE [467] and European XFEL upgrade [468], but they have not yet demonstrated the average current required for the LHeC injector. The possibility of generating polarised electrons with this type of source has not investigated yet.

3. A superconducting RF photoemission source. This type of sources are under development for different applications such as an option for CW FEL's (ELBE [469], LCLS-II, European XFEL), as a basis of injectors for ERL's (bERLinPro) and for electron cooling (BNL). Though this type of sources has already demonstrated the possibility of delivering the average current, required for the LHeC with unpolarised beams (BNL), and has the potential for operation with GaAs type photocathodes (HZDR) which are required for delivery of polarised beams, the current technology of SRF photoelectron source cannot be considered as mature enough for use in the LHeC.

4. A DC photoemission source. In this type of source the electrons are accelerated immediately after emission by a potential difference between the source cathode and anode. This type of source is the most common for use in ERL injectors. It has been used in the projects which are already completed (JLAB, DL), is being used for ongoing projects (KEK, Cornell/CBeta [470]) and is planned to be used in new projects such as the LHeC prototype PERLE [471]. The technology of DC photoelectron sources is well-developed and has demonstrated the average current and beam emittance required for the LHeC ERL (Cornell). Another advantage of the photoelectron source with DC acceleration is the possibility of operation with GaAs photocathodes for delivering of polarised beam. Currently it's the only source, which can delivery of highly polarized electron beams with the current of up to 6 mA which is already in the range of LHeC specifications (JLab).

Based on this analysis at CDR stage we consider the use of DC photoelectron source as a basic option, keeping in mind that in the course of the injector development other types of electron sources may be considered, especially for providing of unpolarised beam.

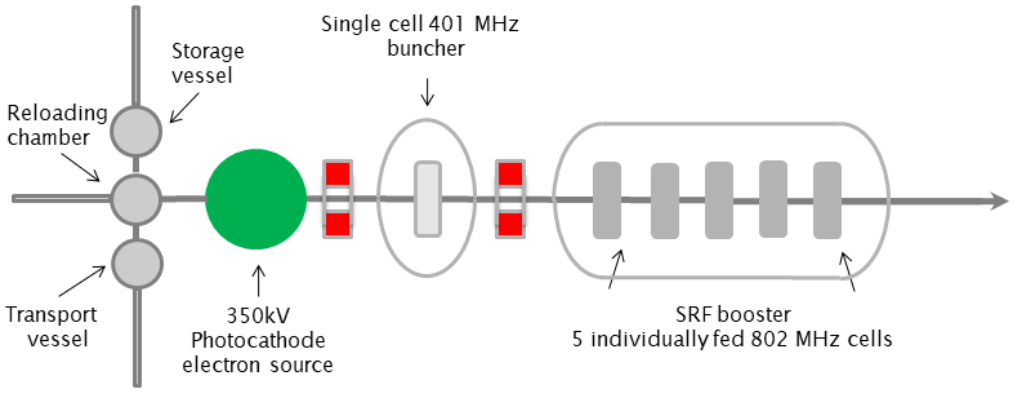

Figure 9.13: The layout of the unpolarised injector.

The injector layout follows the scheme depicted in Fig. 9.13. Its design will be similar to the unpolarised variant of the PERLE injector [471]. The electron source with DC acceleration delivers a CW beam with the required bunch charge and temporal structure. Immediately after the source is a focusing and bunching section consisting of two solenoids with a normal conducting buncher placed between them. The solenoids have two purposes. Firstly to control the transverse size of the space charge dominated beam which will otherwise rapidly expand transversely. This ensures that the beam will fit through all of the apertures in the injector beamline. Secondly the solenoids are used for emittance compensation to counter the space charge induced growth in the projected emittance. This is then followed by a superconducting booster linac. This accelerates the beam up to its injection energy, provides further longitudinal bunch compression and continues the emittance compensation process.

The DC electron source will have an accelerating voltage of 350 kV using a high quantum efficiency antimonide based photocathode such as Cs_2KSb. The photoinjector laser required for this cathode type will be a 532 nm green laser. There will be a load lock system to allow photocathodes to be replaced without breaking the source vacuum. This significantly reduces the down time required for each replacement which is a major advantage in a user facility such as the LHeC where maximising uptime is very important. The cathode electrode will be mounted from above similar to the Cornell [3] and KEK [472] sources. This electrode geometry makes the addition of a photocathode exchange mechanism much easier as photocathode can be exchanged through the back of the cathode electrode. In addition the cathode electrode will be shaped to provide beam focusing. An example of a Jefferson lab type electron source, with the cathode electrode mounted from behind, optimised for the requirements of the LHeC prototype PERLE can be seen in Fig. 9.14 [473].

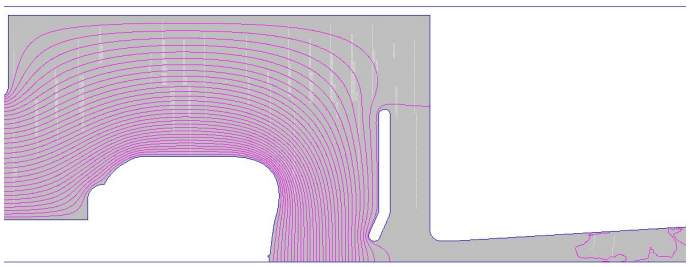

Figure 9.14: The optimised electrode geometry for PERLE. This is a Jefferson lab type gun and is optimised for both 350 kV and 220 kV operation.

The operational voltage of 350 kV for the source was chosen as practical estimate of what is achievable. A higher voltage would produce better performance but would be challenging to achieve in practice. The

highest operational voltage successfully achieved is 500 kV by the DC electron source that is used for the cERL injector [4]. However as shown in the following section 350 kV is sufficient to achieve the required beam quality. Fig. 9.14 shows configuration of electrodes in the PERLE electron source optimised for operation in two modes – at voltage 350 kV for unpolarised mode and 220 kV for polarised mode. In addition to the cathode electrode the source is also equipped with an anode electrode biased to few kV positive. The purpose of this electrode is to block back ion stream from low vacuum part of accelerator which can severe damage photocathodes.

The unpolarised variant of the PERLE injector [2] is shown in the previous section as it provides an example of the achievable parameters. The PERLE injector will have similar behaviour to the LHeC injector as it has the same layout but the electron source will be different as unlike PERLE the LHeC source only needs to perform in one operational mode. Beam dynamics in the injector up to the booster exit were simulated with ASTRA and optimised using the many objective optimisation algorithm NSGAIII. The target injection energy and bunch length were chosen as 7 MeV and 3 mm which are the required values for PERLE. A solution was selected from the results of the optimisation and is presented below. The transverse beam size and bunch length are kept small enough by the solenoid and buncher to ensure that there would be no issue with passing through the apertures or RF non-linearities. This can be seen in Fig. 9.15.

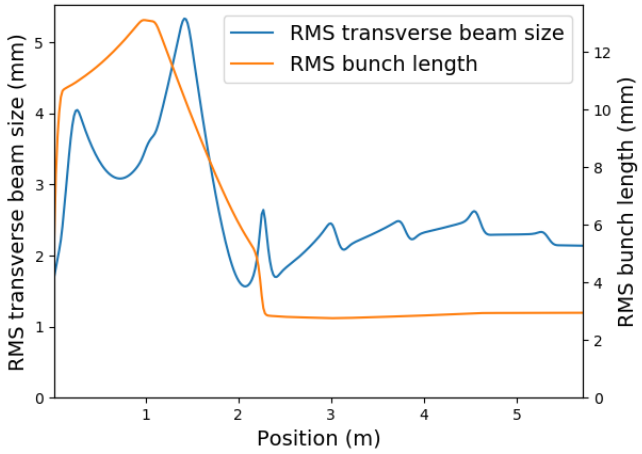

Figure 9.15: The rms beam sizes transversely and longitudinally as the bunch travels along the injector.

The behaviour of the emittances can be seen in Fig. 9.16.

The transverse emittance at the booster exit is 4 mm·mrad which meets the PERLE requirements and should be sufficient for the LHeC. This analysis shows that injector based on a high voltage DC electron source is capable of achieving the required transverse emittances for the LHeC at the necessary bunch charges.

Polarised electron source for ERL

Providing polarised electrons has always been challenging process, especially at relatively high average current as required for the LHeC. The only practically usable production mechanism of polarised electrons is the illumination of activated to Negative Electron Affinity (NEA) state GaAs based photocathodes with circularly polarised laser light. The vacuum requirements for these cathodes mean that this must be done in a DC electron source only. In the course of the last 30 years significant progress has been achieved in improving the performance of polarised electron sources. The maximum achievable polarisation has reached 90% and the maximum Quantum Efficiency (QE) of the photocathode at the laser wavelength of maximum polarisation has reached 6%. Meanwhile the implementation of a polarised electron source into the LHeC

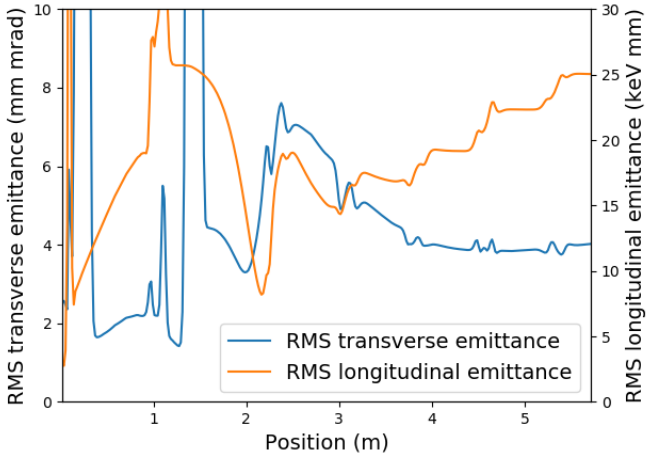

Figure 9.16: The emittances of the bunch as it travels along the injector.

remains a challenge as the practical operational charge lifetime of the GaAs based photocathode does not exceed few kC (JLAB) at an operational current of about 5 mA. In Fig. 9.17 a preliminary design of the LHeC polarised injector is shown.

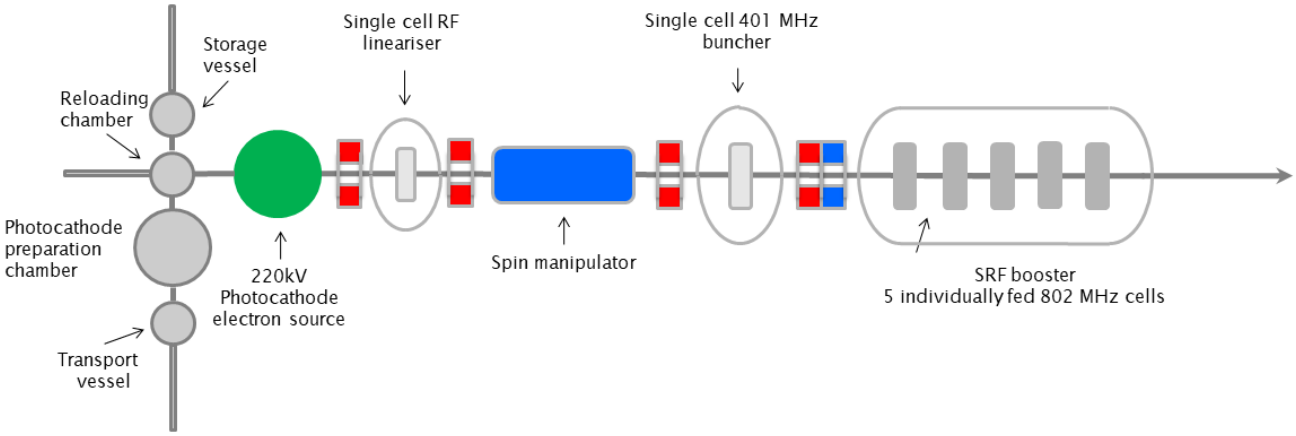

Figure 9.17: The layout of the polarised injector.

In general, the design of the polarised electrons injector is close to that of the unpolarised injector and is based on a DC electron source where a photocathode is illuminated by a pulsed laser beam. The choice of a DC source is dictated by the necessity of achieving extra high vacuum, with a pressure at a level of 10^{-12} mbar, in the photocathode area. This level of vacuum is neccesary for providing long lifetime of the photocathode. In order to reduce photocathode degradation caused by electron stimulated gas desorption accelerating voltage in the source is reduced to 220 kV. The main differences with unpolarised injector are the presence of a photocathode preparation system, permanently attached to the source, and a Wien filter based spin manipulator between the source and the buncher. In order to reduce depolarisation of the beam in the spin manipulator, caused by the space charge induced energy spread of the beam, an RF d is installed between the source and the spin manipulator. The injector is also equipped with a Mott polarimeter to characterise the polarisation of the beam delivered by the source.

An important consideration of the operation with interchangeable photocathodes is minimisation of the down time required for the photocathode exchange. It typically takes few hours to replace the photocathode and to characterise polarisation of the beam. For large facility like LHeC this is unacceptable. A practical

solution could be operation with 2 or more electron sources which operate in rotation. Another motivation for using several electron sources is the nonlinear dependence of photocathode charge lifetime on average beam current (JLAB), which reduces with increasing of the average current. In case of 3 electron sources 2 of them can be operated with half operation frequency 20.05 MHz in opposite phase delivering average current of 10 mA each, while the third is in stand by regime with freshly activated photocathode. The only time which is necessary to switch it on is the time required for rising the high voltage. Another advantage of using a 3 source scheme is the reduction of the average laser power deposited on the photocathode and as result relaxing requirements for the photocathode cooling. In order to implement a 3 source polarised electron injector, development of a deflection system which is able to merge the beams from different sources before the spin rotator is required.

Lasers for electron sources

In the proposed design of the LHeC injection system at least 2 lasers must be used. In the unpolarised electron injector, which is going to operate with antimionide-based photocathode, a laser with a wavelength of 532 nm is required. Typical initial QE of these photocathodes is 10% and for practical application reduction of QE up to 1% may be expected. For polarised electron source typical QE varies from 1% down to 0.1% and laser with a wavelength of 780 nm is required. The optimised parameters of the required lasers are summarised in Table 9.11. Laser temporal profile and spot size on the photocathode are given on the basis of source optimisation for operation at 350 kV for unpolarised regime and 220 kV for polarised.

Table 9.11: Parameters of the electron source drive laser.

Laser beam parameter	**unpolarised mode**	**polarised mode**
Laser wavelength, nm	532	780
Laser pulse repetition rate, MHz	40.1	
Laser pulse repetition rate, MHz		40.1
Energy in the single pulse at photocathode Qe=1%, μJ	0.12	
Average laser power at photocathode Qe=1%, W	4.7*	
Energy in the single pulse at photocathode Qe=0.1%, μJ		0.79
Average laser power at photocathode Qe=0.1%, W		32*
Laser pulse duration, ps FWHM	118	80
Laser pulse rise time, ps	3.2	3.2
Laser pulse fall time, ps	3.2	3.2
Spot diameter on the photocathode surface, mm	6.4	8
Laser spot shape on the photocathode surface	Flat top	

9.6.6 Injector [Oliver Bruening]

9.6.7 Compensation of Synchrotron Radiation Losses [Alex Bogacz]

Depending on energy, each arc exhibits factional energy loss due to the synchrotron radiation, which scales as γ^4/ρ^2 (see Equations 9.2). Arc-by-arc energy loss was previously summarized in Table 9.8. That energy loss has to be replenished back to the beam, so that at the entrance of each arc the accelerating and decelerating beams have the same energy. Before or after each arc, a matching section adjusts the optics from and to the linac. Adjacent to these, additional cells are placed, hosting the RF compensating sections. The compensation makes use of a second harmonic RF at 1603.2 MHz to replenish the energy loss for both the accelerating and the decelerating beams, therefore allowing them to have the same energy at the entrance of each arc, as shown in Figure 9.18.

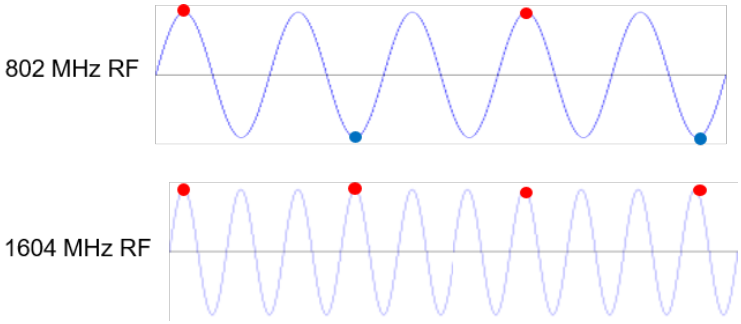

Figure 9.18: The second-harmonic RF restores the energy loss in both the accelerating and decelerating passes.

Parameters of the rf compensation cryomodules, shown in Table 9.12, have been extrapolated from the ILC cavity design, expecting that the higher frequency and lower gradient would support continuous operation.

Table 9.12: A tentative list of parameter for the compensating rf cryomodules extrapolated from the ILC design.

Frequency	1603.2 MHz
Gradient	30 MV/m
Design	Nine cells
Cells length	841 mm
Structure length	1 m
Cavity per cryomodule	6
Cryomodule length	6 m
Cryomodule voltage	150 MV

The compensating cryo-modules are placed into Linac 1 side of the racetrack, before the bending section of Arc 1, Arc 3, and Arc 5 and after the bending section of Arc 2, Arc 4, and Arc 6. This saves space on Linac 2 side to better fit the interaction point (IP) line and the bypasses. Note that with the current vertical separation of 0.5 m it will not be possible to stack the cryomodules on top of each other; therefore, they will occupy 36 m on the Arc 4 and Arc 6 side. Table 9.13 shows the energy loss for each arc and the corresponding synchrotron radiated power, along with number of cryomodules at 1603.2 MHz RF frequency required to replenish the energy loss.

Table 9.13: Arc-by-arc synchrotron radiated power and number of 2-nd harmonic RF cryomodules required to compensate energy loss.

Arc number	ΔE [MeV]	P [MW]	Cryomodules
1	1	0.03	0
2	10	0.5	0
3	50	2.5	1
4	155	7.8	1
5	375	18.7	3
6	770	38.5	5

and 18 m on the Arc3 and Arc 5 side of the racetrack. Each of the compensating cavities in Arc 5 needs to transfer up to 1 MW to the beam. Although a 1 MW continuous wave klystron are available [474], the cryomodule integration and protection system will require a careful design.

9.6.8 LINAC Configuration and Infrastructure [Erk Jensen]

Since the power supplied to the beam in the main linacs will be recovered, the average RF power requirements at 802 MHz are relatively small and determined by the needs to handle transients and microphonics.

The RF power required for the second-harmonic RF system however is substantial - it can be estimated from Table 9.8 with the nominal current of 20 mA:

9.7 Interaction Region [Emilia Cruz Alaniz, Kevin Andre', Bernhard Holzer, Roman Martin, Rogelio Tomas]

9.7.1 Layout [Emilia Cruz Alaniz, Roman Martin, Rogelio Tomas]

The basic principle of the Linac-Ring Interaction Region (IR) design remains unchanged and it is shown in Figure 9.19: the two proton beams are brought onto intersecting orbits by strong separation and recombination dipoles. A collision of the proton beams at the Interaction Point (IP) is avoided via timing. The large crossing angle keeps the long range beam-beam effect small and separates the beams enough to allow septum quadrupoles to focus only the colliding beam (the anti-clockwise rotating LHC beam – Beam 2). The non-colliding beam (the clockwise rotating LHC beam – Beam 1) is unfocused and passes the septum quadrupoles in a field free aperture. The electron beam is brought in with an even larger angle, partly sharing the field free aperture of the septum quadrupoles with the non-colliding beam. A weak dipole in the detector region bends the electron beam into head-on collisions with the colliding proton beam. The two proton beams are also exposed to the dipole field but, due to the large beam rigidity, they are barely affected. After the interaction point a dipole with opposite polarity separates the orbits of the electron and proton beam.

The high electron current (cfr. 9.1) required to approach the goal peak luminosity of $10^{34}\mathrm{cm}^{-2}\mathrm{s}^{-1}$ poses a potential problem for the interaction region (IR) as it increases the already high synchrotron radiation.

The ERL parameters are not the only major change the new IR design has to account for. The first design of the quadrupole septa featured a separation of 68 mm for the two proton beams. However, this design focused strongly on providing a field free region for the non-colliding beam. Unfortunately, this lead to a poor field quality for the strongly focused colliding beam. The first quadrupole Q1 was a half quadrupole design effectively acting as a combined function magnet with a dipole component of 4.45 T [475]. The sextupole field component was also prohibitively high. Consequently, a new design approach focusing on the field quality in the quadrupole aperture was necessary. Table 9.14 summarizes the parameters relevant for the interaction region design. It is noteworthy that the minimum separation of the two beams at the entrance of the first quadrupole Q1A increased from 68 mm to 106 mm requiring a stronger bending of the electron beam. This would increase the already high synchrotron radiation in the detector region even more. In order to compensate this increase, it was decided to increase L^* to 15 m, an approach that was shown to have a strong leverage on the emitted power [476].

The increased separation of the two proton beams, the longer L^* and the overall longer final focus triplet make longer and stronger separation and recombination dipoles necessary. The dipoles differ from the arc dipoles in that the magnetic field in both apertures has the same direction. Consequently the cross talk between both apertures is significant and the maximum reachable field is lower. The new geometry keeps the required field below 5.6 T. The required lengths and strength of these dipoles are listed in Table 9.15. It should be noted that the inter–beam distance is different for each of the five magnets per side, so each magnet will likely require an individual design. The design of the D1 dipoles is further complicated by the fact that an escape line for neutral collision debris traveling down the beam pipe will be necessary [452],

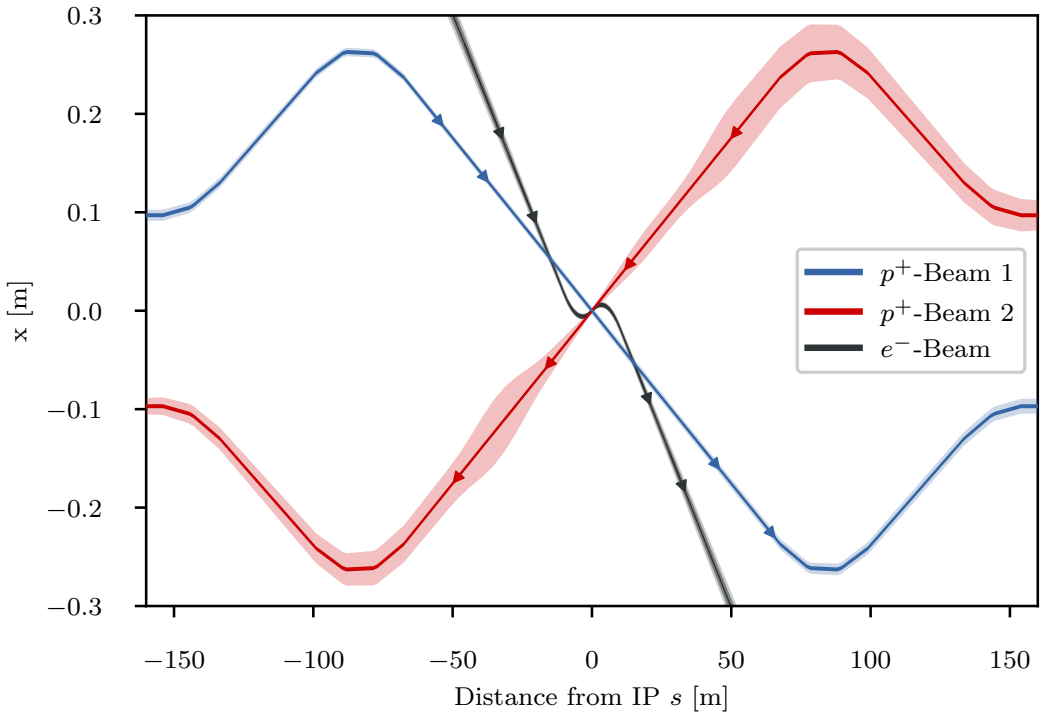

Figure 9.19: Geometry of the interaction region with 10σ envelopes.The electron beam is colliding with the focussed anti-clockwise rotating LHC beam (Beam 2) while the clockwise rotating LHC beam is unfocussed and passes the Interaction Region without interacting with the other two beams

Table 9.14: Parameters of the final focus quadrupole septa. The parameters of Q1A/B and Q2 are compatible with the Nb_3Sn based designs from [477] assuming the inner protective layer of Q2 can be reduced to 5 mm thickness.

Magnet	Gradient [T/m]	Length [m]	Free aperture radius [mm]
Q1A	252	3.5	20
Q1B	164	3.0	32
Q2 type	186	3.7	40
Q3 type	175	3.5	45

as well as a small angle electron tagger. These issues have not been addressed so far, further studies will require detailed dipole designs.

The first design of the LHeC interaction region featured detector dipoles occupying almost the entire drift space between the interaction point and first quadrupole. The approach was to have the softest synchrotron radiation possible to minimize the power. However, since the purpose of the dipoles is to create a spacial separation at the entrance of the first quadrupole, it is possible to make use of a short drift between dipole and quadrupole to increase the separation without increasing the synchrotron radiation power. A dipole length of $\frac{2}{3}L^*$ is the optimum in terms of synchrotron radiation power [478]. Compared to the full length dipole it reduces the power by 15.6 % at the cost of a 12.5 % higher critical energy. With an L^* of 15 m the optimum length of the detector dipoles is 10 m. A magnetic field of 0.21 T is sufficient to separate the electron and proton beams by 106 mm at the entrance of the first quadrupole. With these dipoles and an electron beam current of 20 mA at 49.19 GeV the total synchrotron radiation power is 38 kW with a critical energy of 283 keV to be compared with a power of 83 kW and a critical energy of 513 keV for the electron beam energy of 60 GeV. More detailed studies on the synchrotron radiation for different options

Table 9.15: Parameters of the separation and recombination dipoles. The respective interbeam distances are given for the magnet with the lowest value.

Magnet	Field strength [T]	Interbeam distance [mm]	Length [m]	Number
D1	5.6	≥ 496 mm	9.45	6
D2	4.0	≥ 194 mm	9.45	4
IP Dipole	0.21	-	10	-

and including a beam envelope for the electron beam can be found in Table .

A schematic layout of the LHeC interaction region with the dipoles discussed above is shown in Fig. 9.20. The corresponding beam optics will be discussed in the next Subsections.

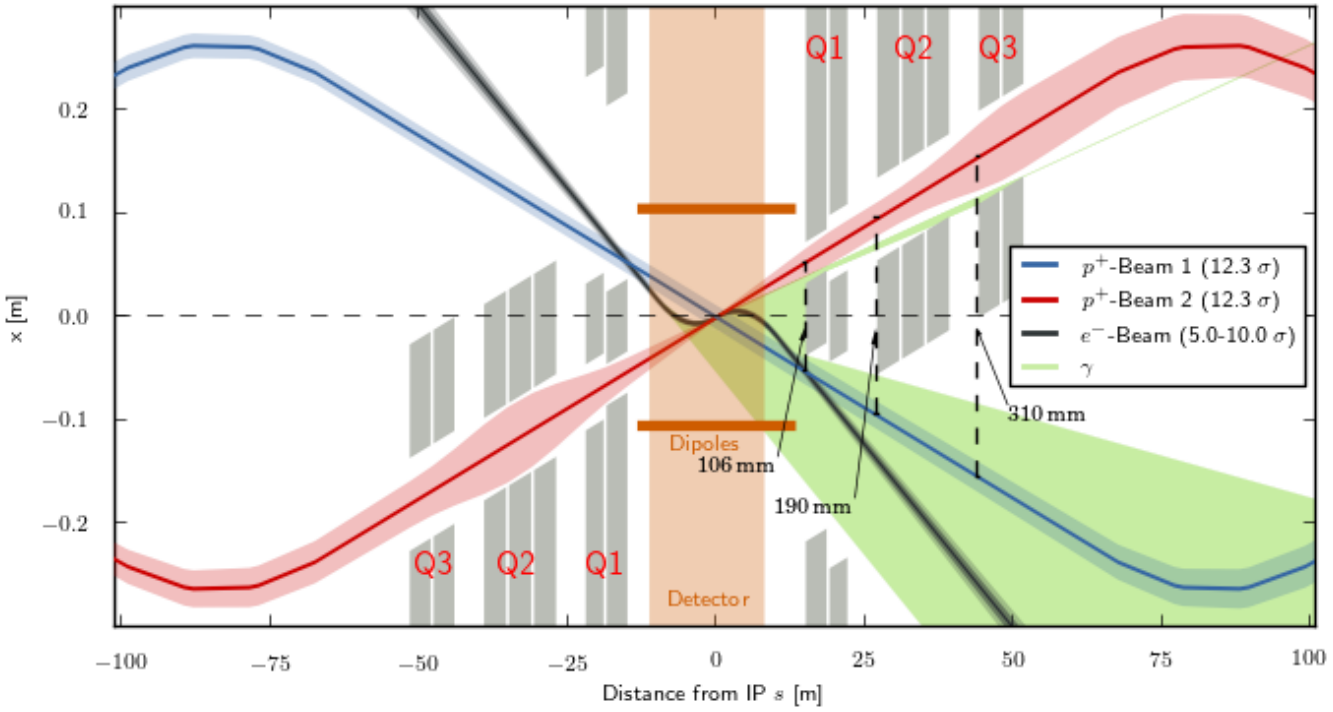

Figure 9.20: Schematic layout of the LHeC interaction region. The colliding proton beam and the electron beam are shown at collision energy while the non-colliding beam is shown at injection energy when its emittance is the largest.

9.7.2 Proton Optics [Emilia Cruz Alaniz]

As discussed above, the L^* was increased to 15 m in order to compensate the increased synchrotron radiation due to the larger separation. The final focus system is a triplet consisting of the quadrupoles Q1A and Q1B (see Table 9.14), three elements of the Q2 type and two of the Q3 type. Between the elements a drift space of 0.5 m was left to account for the magnet interconnects in a single cryostat. Between Q1 and Q2 as well as Q2 and Q3 a longer drift of 5 m is left for cold-warm transitions, Beam Position Monitors (BPMs) and vacuum equipment. Behind Q3, but before the first element of the recombination dipole D1, another 16 m of drift space are left to allow for the installation of non-linear correctors in case the need arises, as well as a local protection of the triplet magnets from asynchronous beam dumps caused by failures of the beam dump kickers (MKD) as discussed later.

As the recombination dipoles D1 and D2 for the LHeC interaction region require more space than the current ALICE interaction region, the quadrupoles Q4 and Q5 had to be moved further away from the IP. The position of Q6 is mostly unchanged but due to a need for more focusing the length was increased by replacing it with two elements of the MQM magnet class of LHC.

With the triplet quadrupole parameters provided in Table 9.14 we were able to match optics with a minimum β^* of 10 cm. The corresponding optics are shown in Fig. 9.21 and feature maximum β functions in the triplet in the order of 20 km. With these large β functions, the free apertures of the quadrupoles leave just enough space for a beam stay clear of $12.3\,\sigma$, the specification of the LHC. This is illustrated in Fig 9.21. However, since the LHeC is supposed to be incorporated in the HL-LHC lattice, this minimum beam stay clear requires specific phase advances from the MKD kicker to the protected aperture as detailed later. The large β functions not only drive the aperture need in the final focus system, but also the required chromaticity correction in the adjacent arcs. To increase the leverage of the arc sextupoles, the Achromatic Telescopic Squeezing scheme (ATS) developed for HL-LHC [479] was extended to the arc upstream of IP2 for the colliding beam (Beam 2) (see Fig. 9.22). This limited the optical flexibility in the matching sections of IR2, specifically of the phase advances between arc and IP2. As a consequence, the optical solution that has been found (Fig. 9.21) still has a residual dispersion of 15 cm at the IP and the polarities of the quadrupoles Q4 and Q5 on the left side of the IP break up the usual sequence of focusing and defocusing magnets. It needs to be studied whether this is compatible with the injection optics. The latest optics designs can be found in [480].

The free apertures given in Table 9.14 include a 10 mm thick shielding layer in Q1 and 5 mm in Q2 and Q3. This is necessary to protect the superconducting coils from synchrotron radiation entering the magnets as can be seen in Figure 9.20. The absorber must also protect the magnets from collision debris. Simulations of both synchrotron radiation and collision debris are yet to be conducted in order to confirm the feasibility of this design.

A separation between the two proton beams in time is currently foreseen, i.e. while the orbits of the two proton beams do cross, the bunches do not pass through the IP at the same time. This approach is complicated by the fact that the timing of the bunches in the other three interaction points should not be affected. The easiest way to accomplish this is by shifting the interaction point of LHeC by a quarter of a bunch separation, i.e. $6.25\,\text{ns} \times c \approx 1.87\,\text{m}$ upstream or downstream of the current ALICE IP. This will of course have an impact in the integration of the detector in the underground cavern [481], however it seems feasible [482].

The LHC protected aperture in the event of an asynchronous beam dump significantly depends on the phase advance between the MKD kicker and the local aperture protection [483]. This is due to the oscillation trajectory of bunches deflected during the kicker rise time. With a phase advance of 0° or 180° from the kicker to the protected aperture, a direct hit should be unlikely, so aperture bottlenecks should be close to that. For a beam stay clear of $12.3\,\sigma$ a phase advance of less than 30° from either 0° or 180° was calculated to be acceptable [483]. The major complication comes from the fact that not only the final focus system of LHeC, but also of the two main experiments ATLAS and CMS need to have to correct phase advances and since the phase advances between IP2 (LHeC) and IP1 (ATLAS) are locked in the achromatic telescopic squeezing scheme there are few degrees of freedom to make adaptations.

The Achromatic Telescopic Squeezing (ATS) scheme [479] is a novel optical solution proposed for the HL-LHC to strongly reduce the β^* while controlling the chromatic aberrations induced, among other benefits.

The principles of the ATS as implemented for the HL-LHC are as follows: first, in the presqueeze stage, a standard matching procedure is performed in the interaction regions to obtain a value of β^* which is achievable in terms of quadrupole strengths and chromaticity correction efficiency, in the case of HL-LHC this corresponds to IR1 and IR5. A further constraint at this point is to match the arc cell phase advance on the regions adjacent to the low β^* interaction regions to exactly $\pi/2$. Later, at the collision stage, the low

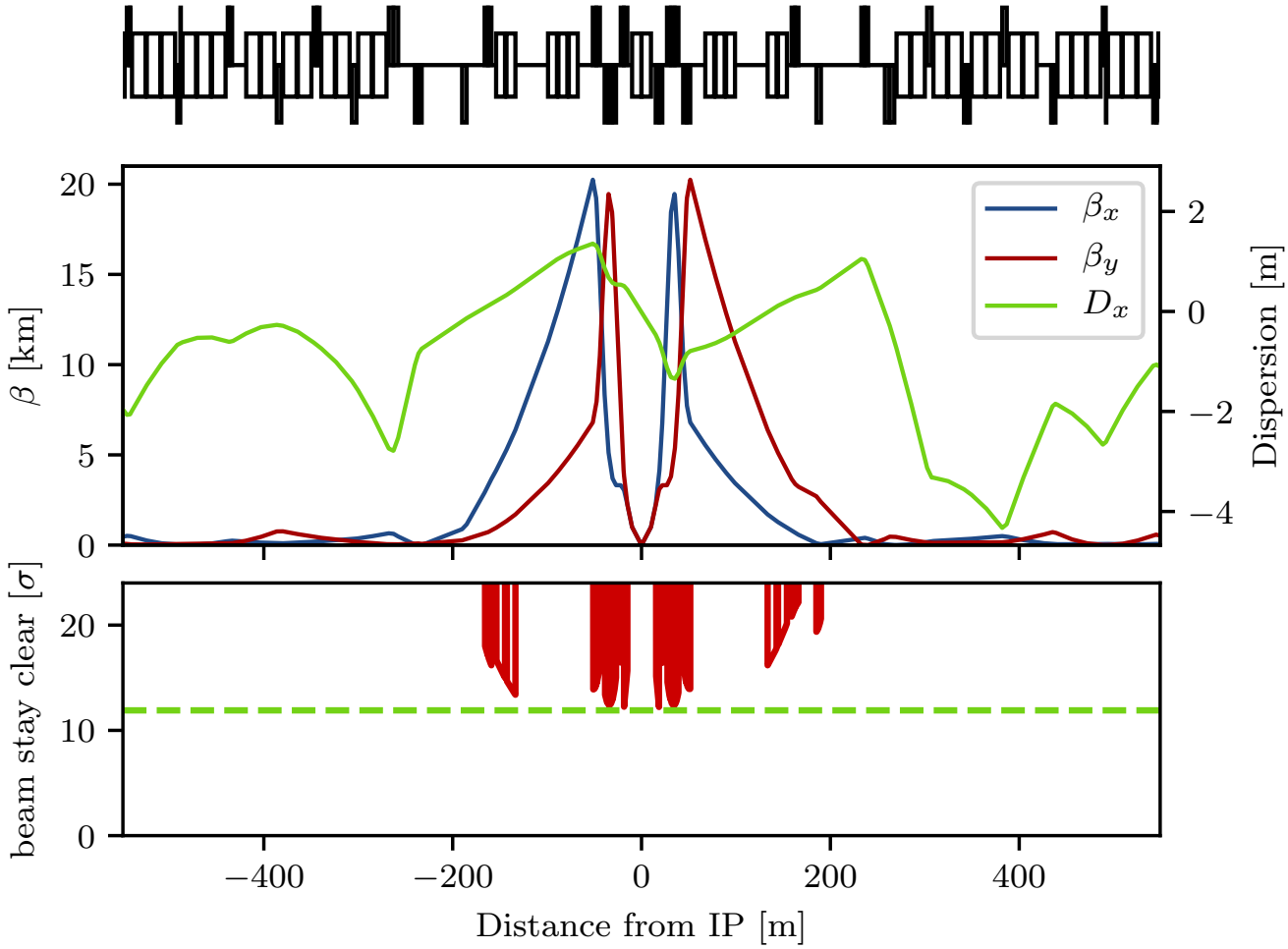

Figure 9.21: Optics (top) and beam stay clear (bottom) of the colliding beam with $\beta^* = 10\,\text{cm}$.

β^* insertions remain unchanged and instead the adjacent interaction regions contribute to the reduction of β^*, that is IR8 and IR2 for IR1, and IR4 and IR6 for IR5. The $\pi/2$ phase advance allows the propagation of β-waves in the arc. If phased correctly with the IP, these β-waves will reach their maximum at every other sextupoles, increasing the β function at their location at the same rate that the decrease in β^*. The increase of the β function at the location of the sextupoles will result in an increase of their efficiency, allowing the system to correct the high chromaticity produced by the high-β function in the inner triplet. This way, the ATS allows a further reduction of the β^* at the same time that correcting the chromaticity aberrations produced in the low β insertions.

Following the experience for HL-LHC, the ATS scheme was proposed for the LHeC project to overcome some of the challenges of this design in terms of limits in the quadrupole strengths of the interaction region and in the chromaticity correction.

A first integration of the LHeC IR into the HL-LHC lattice using the ATS scheme for the previous nominal case with $\beta^* = 10\,\text{cm}$ and $L^* = 10\,\text{m}$ was presented by extending the β wave into the arc 23 [476]. The flexibility of this design was later explored to study the feasibility of minimizing β^*, to increase the luminosity, and increasing L^*, to minimize the synchrotron radiation. It was found that increasing L^* to 15 m provided a good compromise but keeping the β^* to 10 cm.

The changes made to the HLLHCV1.3 lattice [484] to obtain the LHeC lattice and the detailed matching

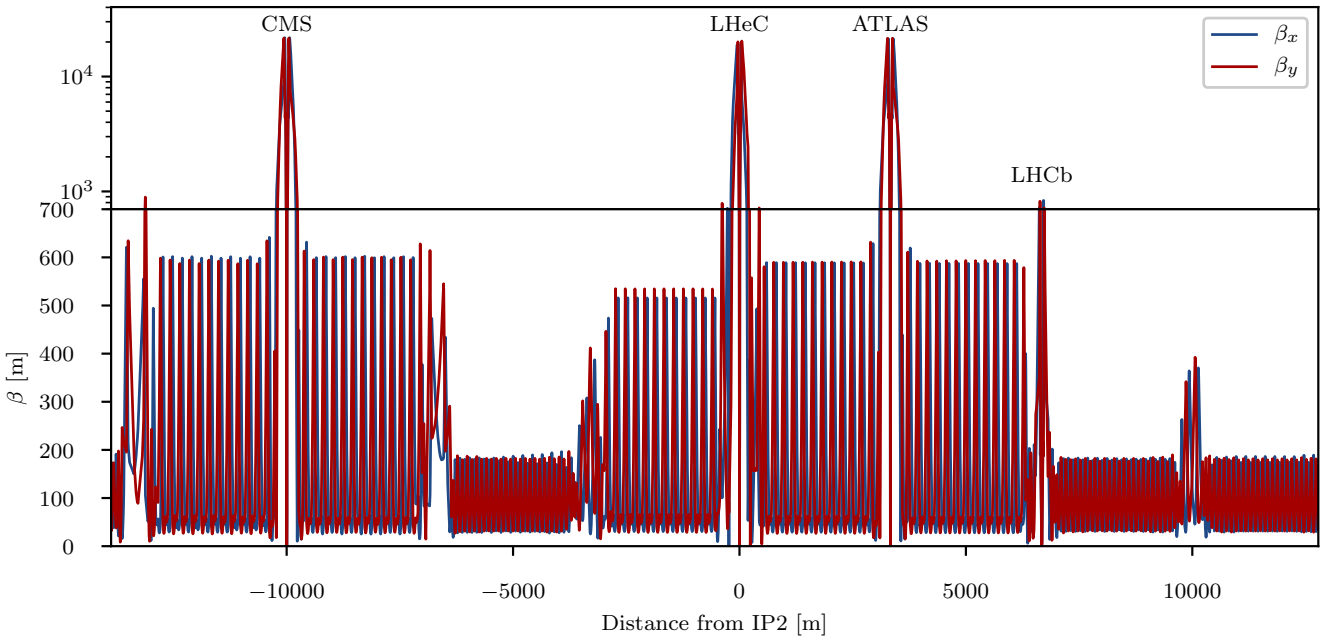

Figure 9.22: Optics of full ring of the colliding beam (Beam 2).

procedure are described in [485]. At the end of this process a lattice for the required collision optics in all IRs (β^*=15 cm for IR1 and IR5 and β^*=10 cm for IR2) has been obtained, with the appropriate corrections (crossing, dispersion, tune and chromaticity). The phases between the MKD kicker in IR6 and the different low β^* triplets were also checked, resulting in 15° from the horizontal for IR1, 22° for IR2 and 26° for IR5, therefore fulfilling the <30° requirement for all three IRs.

Similarly the chromaticity correction for the LHeC lattice further develops from the HL-LHC chromaticity correction scheme [485] allowing to correct the chromaticity for the case with $\beta^* = 10\,\text{cm}$ in IP2 within the available main sextupole strength. Lattices with β^*= 7, 8 and 9 cm and $L^* = 15$ m were also successfully matched in terms of both the β^* and the chromaticity correction. It must be noted however that these cases require a larger aperture in the inner triplet.

Dynamic aperture (DA) studies were performed to analyze the stability of the lattice designs using SixTrack [486] on a thin-lens version of the LHeC lattice at collision ($\beta^* = 0.15\,\text{m}$ in IP1 and IP5, $\beta^* = 10\,\text{cm}$ in IP2) over 10^5 turns with crossing angles on, 30 particles pairs per amplitude step of $2\,\sigma$, 5 angles in the transverse plane and a momentum offset of 2.7×10^{-4}. The energy was set to 7 TeV and the normalised emittance of the proton beam to $\epsilon = 2.5\,\mu\text{m}$. No beam-beam effects were included in this study.

Previous DA studies had been performed for an earlier version of the LHeC lattice [476]. These studies did not include triplet errors of either of the low-β interaction regions, as these errors were not available at that stage. These studies were updated for the newer version of the LHeC lattice described in the previous sections and included errors on the triplets of IR1 and IR5. For the case of IR2 errors tables for the new triplet are not yet available but it was estimated that the same field quality than the triplets for the HL-LHC IR can be achieved for these magnets, and therefore the same field errors were applied but adjusted to the LHeC triplet apertures.

The initial DA resulted in $7\,\sigma$ but following the example of HL-LHC and FCC studies [487] two further corrections were implemented: the use of non-linear correctors to compensate for the non linear errors in the LHeC IR, and the optimization of the phase advance between IP1 and IP5. With these corrections the DA was increased to $10.2\,\sigma$, above the target of $10\,\sigma$. The case for lower β^*, particularly for the case of

interest with $\beta^* = 7\,\text{cm}$ proved to be more challenging, as expected, when adding errors on the LHeC IR; however with the use of the latest corrections a DA of $9.6\,\sigma$ was achieved, that is not far off from the target. Fig. 9.23 shows the DA vs angle for both these cases. It is important to point out that the challenge for the β^*=7 cm case comes instead from the quadrupole aperture and gradient requirements, particularly in the first magnet.

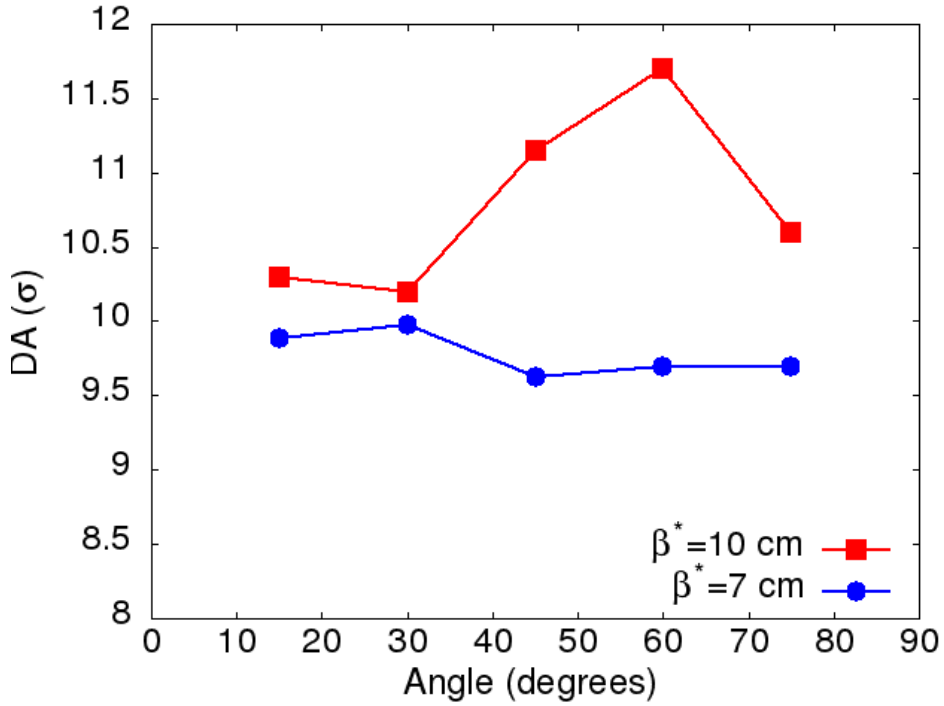

Figure 9.23: Dynamic aperture vs angle for 60 seeds for the LHeC lattice at collision for the cases $\beta^* = 10$ cm (red) and $\beta^* = 5$ cm in IP2.

β^* values lower than 10 cm require a completely different final focus system as the lower β^* means the beam size in the triplet will become larger. Larger apertures are required and consequently the gradients in the quadrupoles will decrease. However similar integrated focusing strengths will be required so the overall length of the triplet will increase. As this will in turn increase the β functions in the triplet further it is imperative to optimize the use of the available space. An example of available space is the drift between the detector region dipoles and the triplet magnets as shown in Fig. 9.24. The optimum dipole lengths in terms of synchrotron radiation power was determined to be $2/3 \cdot L^*$ so a drift of 5 m is left. Now it is immediately clear that this region cannot be occupied by a superconducting quadrupole septum as that would effectively decrease L^* and thus increase the synchrotron radiation power as a stronger separation is necessary. Instead it is thinkable that a normal conducting quadrupole septum can be built that either does not require a yoke or similar structure between the beams or has a very thin yoke, or a septum that has a very limited and controlled field in the region of the electron beam trajectory. In the later case it might even be used as part of the final focus system of the electron beam. Either way, it is clear that such a normal conducting septum must have a pole tip field way below the saturation limit of iron. The section on electron optics shows that a normal quadrupole of this kind can also have benefits in terms of synchrotron radiation, but studies remained to be done to make sure the parameters work for both cases. For our calculation a pole tip field of 1 T was assumed. For $\beta^* = 5\,\text{cm}$ an aperture radius of 20 mm is required at a distance of 14 m from the IP, resulting in a pole tip field of 50 T/m for the normal conducting septum called Q0. Possible ratios of apertures and gradients for the remaining triplet magnets were approximately based on the quadrupole parameters shown in Table 9.14, however these parameters would require a magnet design for confirmation. With the quadrupole parameters shown in Table 9.16 we were able to obtain triplet optics

that can accommodate a beam with a minimum β^* of 5 cm.

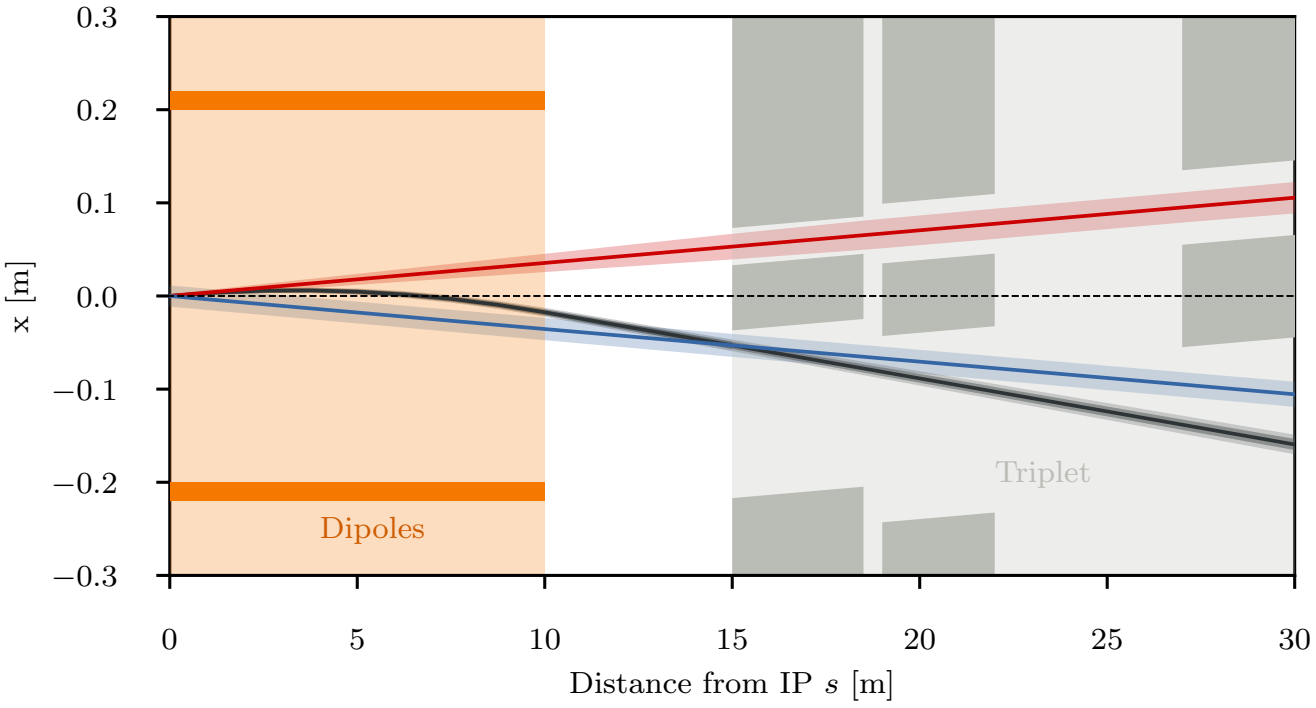

Figure 9.24: Empty space between the detector dipole and the superconducting quadrupoles of the final focus triplet.

Table 9.16: Parameters of the final focus quadrupole septa required to accommodate a β^* of 5 cm. The normal conducting quadrupole is called Q0 although it has the same polarity as Q1A/B.

Magnet	Gradient [T/m]	Length [m]	Aperture radius [mm]
Q0 (nc)	50	3.0	20
Q1A	110	3.5	27
Q1B	162	5.0	37
Q2	123	5.0	62
Q3	123	4.5	62

The corresponding optics are shown in Fig. 9.25. So from the triplet point of view it appears possible to reach lower β^*, however many assumptions need verification: First the magnetic design for the normal conducting quadrupole septum must be shown to be possible. If there is a residual field in the space of the electron beam trajectory, the impact on the electron beam and the synchrotron radiation power must be evaluated. The parameters of the modified superconducting triplet quadrupole septa, although scaled conservatively, must be confirmed. Furthermore the larger aperture radius of Q1 might require a larger separation at the entrance of Q1, increasing the synchrotron power that is already critical. Thus a full design of such magnets is required. Lastly, the interaction region must be integrated into the full ring to verify that chromaticity correction is possible. Studies in [485] that were conducted on the normal triplet without regard for aperture constraints suggest that a chromaticity correction is only possible for a β^* down to around 7 cm.

So far the optics of the final focus system featured asymmetrically powered triplets on the two sides of the IP. This is inherited from the ALICE final focus system where the aperture is shared and the antisymmetry guarantees the same optics for both beams and similar chromaticities in both horizontal and vertical planes.

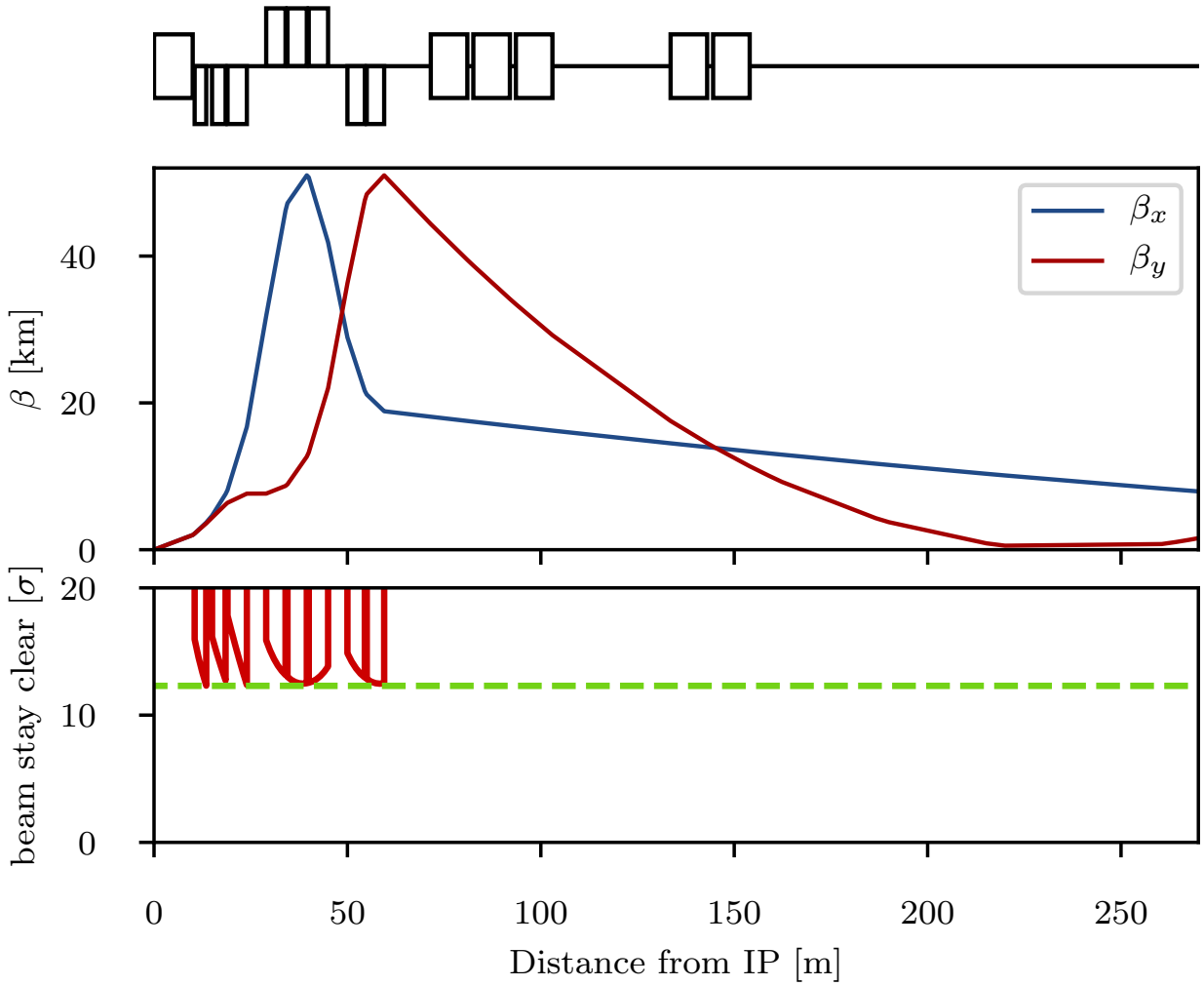

Figure 9.25: Optics (top) and beam stay clear (bottom) in the triplet region of colliding beam with $B^* = 5\,\text{cm}$.

In the LHeC final focus system however, the apertures of the quadrupoles are not shared between both beams, so the antisymmetry is not strictly necessary, although it eases the integration in the full ring. An alternative approach that is worth studying is a symmetric doublet. Doublets feature a large β function in one plane and a relatively low one in the other plane. Since the non-colliding proton beam is of no concern for LHeC it makes sense to create doublets on each side of the IP that have the peak β function in the horizontal plane as the chromaticity correction was limited in the vertical plane. Furthermore, in a doublet the integrated focusing strength needed is lower as fewer quadrupoles act against each other. This further reduces the chromaticity and should also reduce the overall length of the final focus system. With the space saved by the doublet it is possible to either shift the recombination dipoles D1 and D2 closer to the IP, reducing the needed integrated strengths, or even to increase L^* to further reduce the synchrotron radiation power and critical energy. In order to make best use of the available doublet quadrupole aperture, it is also thinkable to collide with flat beams. The main disadvantage of symmetric doublets is the breaking of the sequence of focusing and defocusing quadrupoles. As no changes should be made to the arcs, the left-right symmetry needs to be broken up again in one of the matching sections, either by introducing another quadrupole on one side of the IP, or by overfocusing the beam.

At collision energy the non-colliding beam has no optics specification within the straight section. Conse-

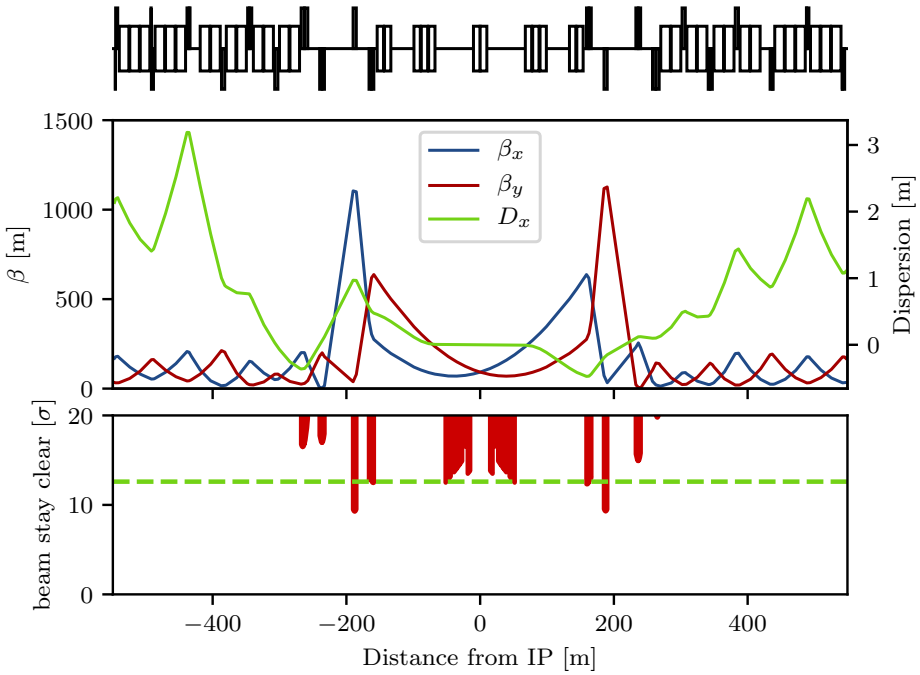

Figure 9.26: Optics (top) and beam stay clear of the non-colliding beam at injection energy. The Q5 quadrupole magnets on either side of the IP currently are aperture bottlenecks. It should be possible to mitigate this problem by replacing the magnets with longer, larger aperture magnets.

quently the optics should transfer the beam from the left arc to the right arc without hitting the aperture and at a specific phase advance. The same is true at injection energy, but with a larger emittance, making the satisfaction of the aperture constraint more difficult. Thus it is sufficient to find working injection optics, as no squeeze will be required for this beam. This approach of course will require some tuning as at least one arc will apply the ATS scheme at collision, but as the aperture constraint is less tight at higher energy there should be enough degrees of freedom available.

Finding injection optics appears trivial at first but is complicated by the fact that the distance between the IP and the first quadrupole magnet Q4 is larger than 159 m. A total distance of 318 m needs to be bridged without any focusing available. A solution has been found with $\beta^* = 92$ m and $\alpha^* = \pm 0.57$ with the required beam size in the quadrupole septa and Q4 [485]. The corresponding optics are shown in Fig. 9.26. For the magnets Q4 and Q5 LHC quadrupoles of the large aperture MQY type with 70 mm aperture diameter and a 160 T/m gradient were assumed. As can be seen in the aperture plot, the triplet quadrupole septa and Q4 are just below the minimum beam stay clear at injection of $12.6\,\sigma$ but it is expected that nominal aperture can be achieved With some minor optimization. However the Q5 magnets only have a beam stay clear of about $9.2\,\sigma$ with little chance of decreasing the beam size without increasing it both in Q4 and in the quadrupole septa. Consequently it will be necessary to use quadrupoles with apertures larger than 106 mm and make up for the lower gradient by increasing the length or by using Nb_3Sn technology. At injection energy the remaining magnets in the IR have strengths according to the HL-LHC specification and thus do not pose any problems. However the injection optics shown in Fig. 9.26 will require some changes during the ramp as Q4, Q5 and Q6 would become too strong at collision energy. This is not considered a problem though, as the emittance shrinking will ease the aperture requirements.

The non-colliding proton beam does not need to be focused and consequently passes the quadrupole septa of the colliding beam in the field free region.

The large angle of 7200 µrad between the two beams (compared to 590 µrad in the high luminosity IPs)

should suffice to mitigate long range beam-beam effects, considering that the shared aperture is only 30 m long as opposed to the main experiments where the shared aperture exceeds a length of 70 m.

9.7.3 Electron Optics [Kevin André, Bernhard Holzer]

First ideas of a possible layout and design of the Interaction Region IR between the LHeC lepton and proton beam have already been presented in [452]. Based on the principles explained there, a further optimisation of the beam separation scheme has been established, with the ultimate goal of lowest synchrotron radiation power and critical energy in the direct environment of the particle detector. Depending on the requests from the actual detector geometry and shielding, the flexibility of the new IR layout allows to optimise for either side.

The basic principle is - as before - based on the large ratio (approximately 140) of the proton to electron beam momentum (or beam rigidity, $B\rho = p/e$) that makes a magnetic field based separation scheme the straightforward solution to the problem, using effective dipole fields.

Boundary conditions are set however due to the limited longitudinal space, resulting from the distance of the first focusing elements of the proton lattice, located at L*=15m, and the need for sufficient transverse separation, defined by the technical design of this first proton quadrupole. The size of the two beams and - clear enough - the power of the emitted synchrotron radiation P_{syn} and the critical energy E_{crit} have to be taken into account in addition.

Equations 9.5 and 9.6 describe the well known dependencies of these two parameters on the beam energy $E_e = m_e c^2 \gamma$ and bending radius ρ.

$$P_{syn} = \frac{e^2 c}{6\pi\varepsilon_0} \frac{\gamma^4}{\rho^2}. \tag{9.5}$$

$$E_{crit} = \frac{3}{2} \frac{\hbar c \gamma^3}{\rho}. \tag{9.6}$$

The schematic layout of the original design of the electron interaction region shown in Fig. 9.20 is reproduced in Fig. 9.27a. The long dipole magnet B, used to deflect the electron beam, is embedded inside the detector structure which is ranging from -6 m to 4 m around the interaction point, extended by ± 1.65 m of muon chamber. Basic interaction region designs with and without chromaticity correction were presented [488, 489] but were not fully integrated in the ERL. The electron final quadrupoles were placed at 30 m from the IP [490], compatible with the proton layout described above. While this approach is straightforward, the only parameter that can be used to minimize the power of the emitted synchrotron radiaton is the length of the separator-dipole field [478]. In addition, the installation of the first focusing elements of the electron beam downstream of the triplet focussing the colliding proton beam leads to a considerable increase of the electron beam size in the separation plane.

Lattices including chromaticity correction had a significant length of 150 m. However, the whole straight section between Linac and arc is only 290 m long [452] and the IR design did not include a matching and splitting section or a focus system for the spent, outgoing electron beam. Without chromaticity correction in the electron final focus, aberrations at the IP decrease luminosity by about 20% [491].

Investigations have been launched to minimise critical energy and emitted synchrotron radiation power by reducing the separation in two main steps:

- introduce a compact mirror-plate half quadrupole (QNC) in front of Q1A (on the IP side) to focus the colliding proton beam and provide a field free region for the electron and non-interacting proton beam. This reduces the required bending field of the separation dipole B for the same separation at Q1A. In addition, the normal conducting magnet QNC will act as shielding of the superconducting

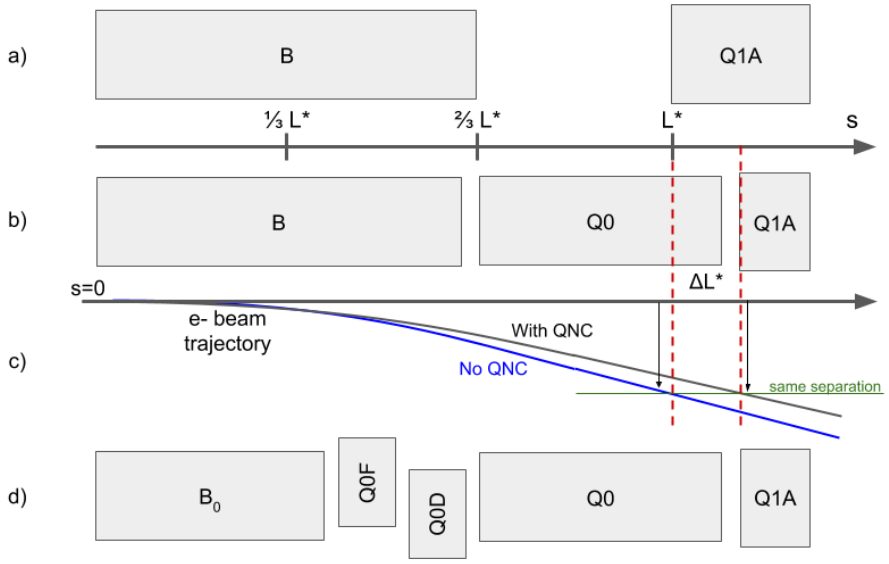

Figure 9.27: Separation scheme based on a long dipole magnet B (a) and improved layout using Q0, a normal conducting half-quadrupole as first focusing element of the proton beam (b). The last design features a doublet of off-centered quadrupoles to minimize the electron beam size at the entrance of Q1A (d).

triplet magnets that would otherwise be subject to direct synchrotron radiation. Additional shielding is foreseen, to protect the SC magnets and avoid as much as possible backshining to the detector. In addition, sufficient space will be provided to correct the vertical orbit and coupling of the electrons coming from the solenoid.

- reduce the beam size of the electron beam by a very early focusing of the beam. As positive side effect this leads to a considerable reduction of the chromaticity of the electron lattice.

The first step is sketched in Fig. 9.27b and the corresponding electron beam trajectory is shown in Fig. 9.27c.

The introduction of the mirror plate half quadrupole QNC allows to reduce the length of the Q1A quadrupole while conserving the total integrated gradient, therefore leaving the overall focusing properties of the proton lattice quasi untouched. The entry of Q1A is therefore moved away from the IP to relax the separation fields.

Scanning the Q1A entry position leads to either an optimum of the critical energy or to a minimum of the emitted synchrotron power. Both cases are shown in Fig. 9.28 and for each of them the new Q1A entry position has been determined. The power of the emitted radiation is reduced by up to 28%. The colliding proton beam, passing through this half quadrupole with a certain offset to guarantee sufficient beam stay clear, will receive a deflecting kick in the horizontal plane of about 90 µrad. It supports the dipole based beam separation, provided by the so-called D1 / D2 magnets in LHC, and will be integral part of the LHC design orbit.

The resulting beam optics of the protons differs only marginally from the original version and only a slight re-match is needed. However by carefully choosing the gradient of the new magnet the parameters of the superconducting proton quadrupoles are untouched and the phase advance at the end of the interaction region lattice is conserved in both planes.

Improved Electron lattice

A further improvement of the emitted synchrotron power and critical energy is obtained by introducing an early focusing scheme of the electrons, which leads to a reduced electron beam size and thus to softer

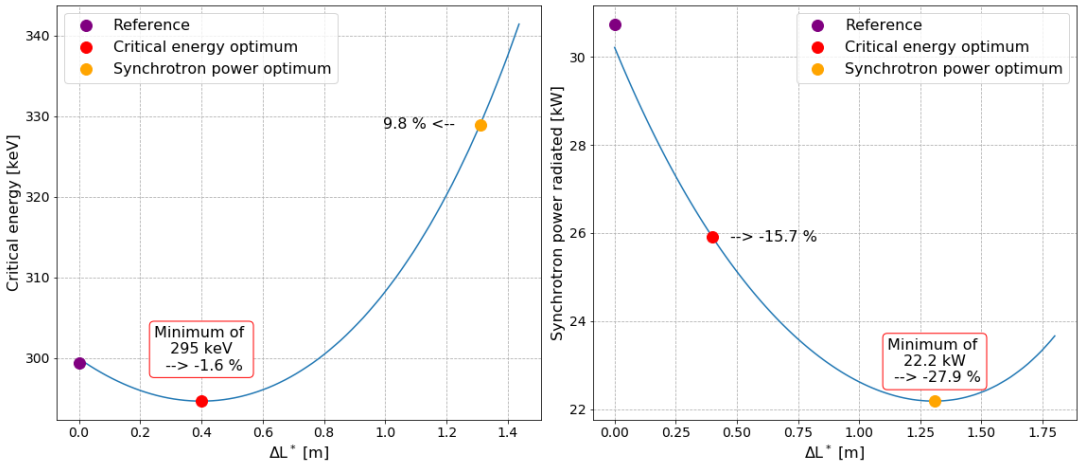

Figure 9.28: Improved critical energy and power of the synchrotron radiation for the half quadrupole based proton lattice. Left side: critical energy, right side: synchrotron radiation power. The horizontal axis refers to the shift ΔL^* of the position of the first proton superconducting magnet Q1A.

separation requirements.

The reduction of the electron beam size is obtained by installing a quadrupole doublet in the electron lattice between the separation dipole and the QNC (half-) quadrupole. A carefully matched focusing strength of this doublet will minimise the β function of the electrons at the location of Q1A. At the same time an effective dipole field, that is needed to maintain the separation of proton and electron beams, is provided by shifting the magnet centres of the doublet lenses off axis. The horizontal offset of these quadrupoles has been chosen to provide the same bending radius as the separation dipole, thus leading in first order to the same critical energy of the emitted light in all separation fields. A detailed calculation of the divergence of the photons, the geometry of the radiation fan and the position of the absorbers and collimators will be one of the essential next steps within the so-called machine-detector-interface considerations.

Fig. 9.27d shows the new layout – compared to the previous version. The doublet providing the early focusing of the electron beam is embedded in the separator dipole, i.e. it is positioned at $s = 6.3\,\mathrm{m}$ and acts in combination with the separation dipole. The quadrupole gradients have been chosen for optimum matching conditions of the electron beam and the transverse shift of the field centres provide the same separation dipole effect as used in the long dipole.

The early focusing of the electron beam allows for a softer separation of the beams, and leads therefore directly to a reduced critical energy E_{crit} and power P_{syn} of the emitted radiation. Fig. 9.29 shows the dependence of E_{crit} and P_{syn} on the β-function at $s = L^*$ for the electron optics for different values of the required electron beam stay-clear expressed in units of the electron beam size σ. The beam separation has been re-calculated and the critical energy and radiation power are plotted. The graphs include different assumptions for the beam size considered. Including orbit tolerances, a beam stay-clear of 20 σ is considered as the most relevant case, which refers to the red curve in the graph.

In order to provide a complete study with the lattice featuring the off-centered quadrupoles, the new interaction region has been embedded in between the high energy end of the acceleration part of the linac and the "arc 6" of the ERL, which marks the start of the energy recovery lattice. An optimum has been found for a beam optics with a beta function in the plane of the beam separation (i.e. horizontal) of $\beta_x = 90$ m at $L^* \approx 15\,\mathrm{m}$

An improvement of about 9 % for the critical energy and close to 25 % of the radiated power is obtained, if an electron beam optics with $\beta_x = 90\,\mathrm{m}$ at the entrance of Q1A is used. For this most promising case the

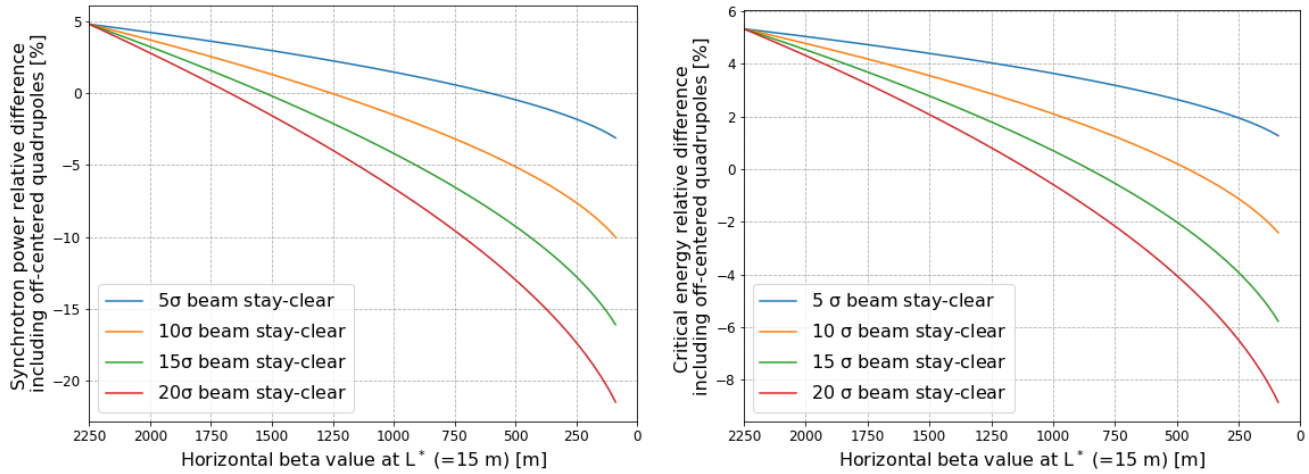

Figure 9.29: Relative difference with respect to the single dipole separation scheme for different values of the required beam stay-clear expressed in σ. Left : for the power of the emitted radiation, as function of the β-function of the electron beam at position s=15m. Left : for the critical energy of the emitted radiation, as function of the β-function of the electron beam at position s=15m. The early focusing of the electron beam allows for a much reduced separation field and thus to a reduced critical energy and power of the emitted radiation. The initial beta value is 2250 m.

matched beam optics is shown in Fig. 9.30.

The lower β-function of the electron beam at the focusing elements has the additional positive feature of reducing considerably the chromaticity of the new lattice, which is a crucial parameter for the performance of the energy recovery process. (Details are described below in the chapter on tracking calculations). Compared to the dipole based separation and a late focusing, Q' is reduced to a level of 13 % horizontally and to a level of 11 % in the vertical plane. The details are listed in Table 9.17. Furter studies will investigate the orbit correction scheme of the new IR, and an eventual interplay of the solenoid fringe field and the quadrupoles.

The influence of the electron doublet magnets on the proton optics is marginal - as can be expected due to the large difference in beam rigidity: If uncorrected, the electron doublet creates a distortion (a so-called beta-beat) of the proton optics of roughly 1%. Still it has been calculated and taken into account in the context of a re-match of the proton beam optics.

Table 9.17: Chromaticity of the dipole based separation scheme and the new lattice based on early focusing, off-axis quadrupole lenses.

	dipole based separation	early focusing scheme
ξ_x	-116	-15
ξ_y	-294	-32

Combining the two improvement factors, namely the effective lengthening of L^* due to the use of a half quadrupole in front of the superconducting triplet, and the early focusing scheme in the lattice of the electrons, leads to an overall improvement of the interaction region with respect to synchrotron radiation power and critical energy that is shown in Fig. 9.31. The overall improvement factor is plotted with reference to the baseline dipole separation design with originally $\beta = 2250$ m at the separation point s=L^*. Using a normal conducting half quadrupole in combination with the early focusing scheme, the power of the emitted synchrotron radiation is reduced by 48 % for an electron beam stay-clear of 20 σ.

The estimated synchrotron radiation power and critical energy for the different optimizations are plotted in Fig. 9.31 and the results are summarized in Table 9.18. Referring to a beam energy of 49.19 GeV and the

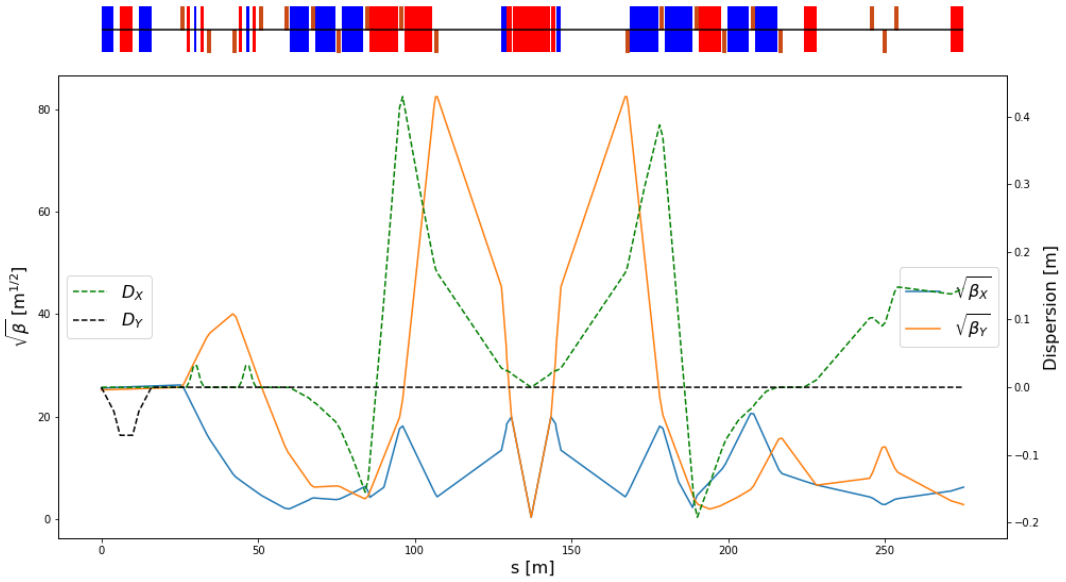

Figure 9.30: Electron beam optics for the new lattice including the early focusing scheme. The offset of the new doublet quadrupoles are chosen to provide the same separation field as in the dipole. The new optics is matched on the left side of the plot to the end of the acceleration linac. The right hand side is connected to arc 6, the beginning of the decelerating ERL part. At the position of the first superconducting proton magnet the β-function in the (horizontal) separation plane of the electron beam is reduced to 90 m for lowest possible synchrotron radiation load.

design current of 20 mA an overall power of 16.2 kW is emitted within one half of the interaction region.

Table 9.18: Synchrotron radiation power and critical energy for the different optimised separation schemes.

Optimum	Synchrotron Radiation		Critical energy	
	Radiation Power (kW)	Critical Energy (keV)	Radiation Power (kW)	Critical Energy (keV)
Reference design	30.8	300	30.8	300
Dipole length optimum	26.8	336	30.8	300
Half quadrupole optimum	22.2	331	26.1	295
Off-centered quadrupoles opti.	19.3	290	22.1	259
Half quad. + Off-centered quad. opti.	16.2	265	17.4	255

Depending on the boundary conditions imposed by the integration of the particle detector, one of the two optimum layouts can be chosen – or a combination of both, i.e. an overall minimum defined by critical energy and radiated power.

The basic main parameters of the proton mirror plate half quadrupole are summarized in Table 9.19 for the two optimum scenarios explained above: the optimum found for smallest synchrotron radiation power and the optimum for smallest critical energy of the emitted radiation. The values result from the optics studies of the previous sections. The presented gradients lead to a pole tip field of $B_p \approx 1.3\,\mathrm{T}$.

In both cases, the proton aperture radius has been chosen to include an orbit tolerance of 2 mm, a 10% tolerance on the beam size due to optics imperfections ($\beta-$ beating) and a beam size that corresponds to n=15 σ for a proton beam normalized emittance $\varepsilon_p = 2.50\mu m$. A value that is comfortably larger than the

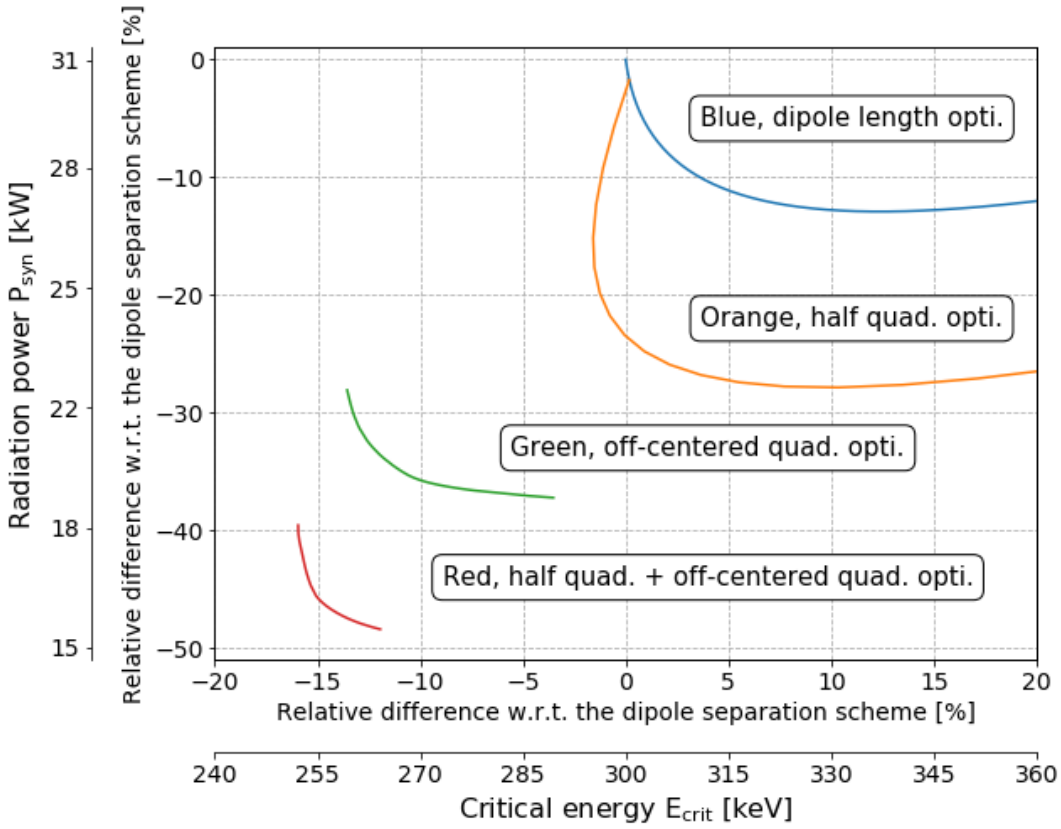

Figure 9.31: Relative differences with respect to the original single dipole separation scheme. The synchrotron radiated power is plotted as a function of the critical energy for different optimization results : only optimizing the dipole length (blue), only using a mirror quadrupole (orange), only using off-centered quadrupoles (green) and combining the mirror quadrupole with an earlier focusing (red).

requirements of the HL-LHC standard lattice. The injection proton optics has been taken into account and although it features a larger emittance it clearly fit in the aperture, see the red dashed line in Fig 9.32. The electron beam and the non-colliding proton beam will pass through the field free region delimited by the mirror plate.

The aperture requirements inside the half quadrupole are determined on one side by the colliding proton beam optics in the main aperture of the magnet. The beam separation scheme and optics of electron and non-colliding proton beam on the other side have to fit into the field free region beyond the mid plane of the mirror plate. As described below, a crossing angle of 7 mrad is assumed for the non-colliding protons. Fig. 9.32 illustrates these requirements. For the case of smallest synchrotron radiation power, the three beams are plotted at the entrance and exit of the quadrupole lens. For both proton beams the beam size shown in the graph corresponds to 15 sigma plus 2 mm orbit tolerance and 10 % beam size beating. Due

Table 9.19: Magnet gradient of the proposed half quadrupole for lowest synchrotron radiaton power and lowest critical energy. An aperture of 15 σ + 20% beta-beating + 2 mm orbit tolerances has been assumed.

	minimum synch. radiation power	minimum critical energy
$\gamma\varepsilon_p$ [mm.mrad]	2.50	2.50
Gradient [T/m]	48.2	50.7
Aperture radius [mm]	27.0	25.6
Length [m]	6.84	2.08

to the mini-beta optics the colliding proton beam fills nearly the given aperture of the magnet. The non-colliding proton beam follows a relaxed optics with very limited aperture need. The envelope of the electron beam is shown for 20 σ beam size in both transverse planes.

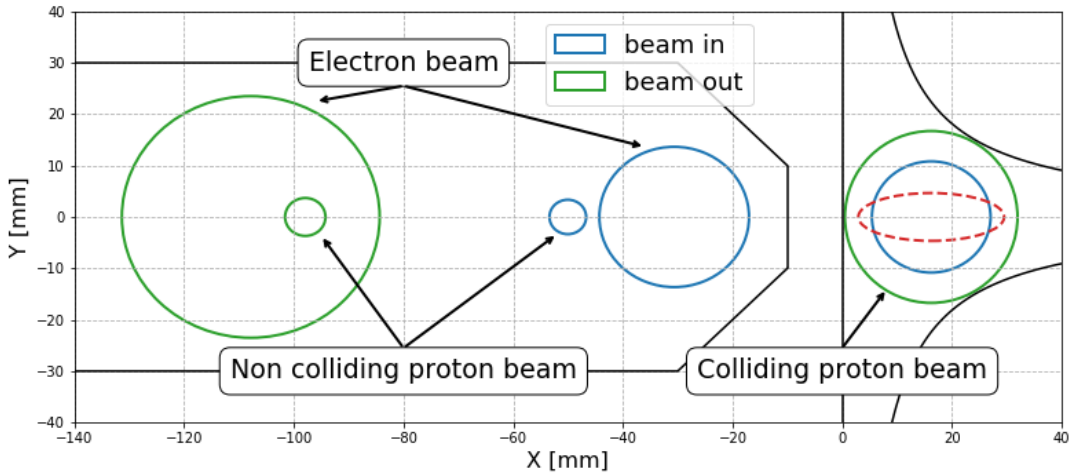

Figure 9.32: The position of the three beams at the entrance (blue) and exit (green) of the half quadrupole. The colliding proton beam is centered inside the main magnet aperture, while the second proton beam and the electrons are located in the field free region. The dashed red line represents the injection proton beam at the output of the half quadrupole.

In contrast to the proton half quadrupole, the doublet magnets of the early focusing scheme will house the three beams in one single aperture. In addition to the beam envelopes, the offset that has been chosen to provide the beam separation effect has to be taken into account and included in the aperture considerations. In Fig. 9.33 the situation is visualised. On the left side the first off-center quadrupole (powered as focusing lens) is presented. Following the field direction, the electron beam is offset towards the outer side of the ring (right side of the plot) as defined by the proton beam closed orbit. The right part of the figure shows the second quadrupole (powered as defocusing lens) with the electron beam offset shifted to the other direction. In order to provide sufficient aperture for the three beams, an elliptical shape has been chosen for the vacuum chamber. It defines enough space for the beam envelopes and the off-centre design trajectories. The black ellipses correspond to the beams at the entrance of the magnet while the red shapes represent the beams at the exit. From left to right the three beams are respectively the non colliding proton beam (tiny circles), electron beam (squeezed ellipses) and the colliding proton beam. As defined before we refer to a beam size of 20 σ in case of the electrons and 15 sigma plus beta-beating plus 2 mm orbit tolerance for the colliding and non-colliding proton beam.
In this context it should be pointed out that the non-colliding proton beam, travelling in the same direction as the electrons, is shifted in time by half the bunch spacing. While the projected beam envelopes in Fig. 9.33 and 9.32 seem to overlap in the transverse plane, they are well separated by 12.5 ns, corresponding to 3.75m, in the longitudinal direction.

The minimum required gradients and pole tip radius of the quadrupoles of the doublet are listed in Table 9.20. Following the increasing beam size after the IP, the two quadrupoles are optimised for sufficient free aperture for the collidng beams and their design orbits. Accordingly a different layout has been chosen for the magnets, to provide the best conditions for the radiation power and critical energy. An alternative approach has been studied, based on a single quadrupole design for both lenses of the doublet. While an optics solution still is possible, it does however not allow for minimum radiation power and sets more stringent requirements on the shielding and absorption of the synchrotron light fan.

The Fig. 9.35 shows the chromatic effect of the two lattice versions, as function of the momentum spread.

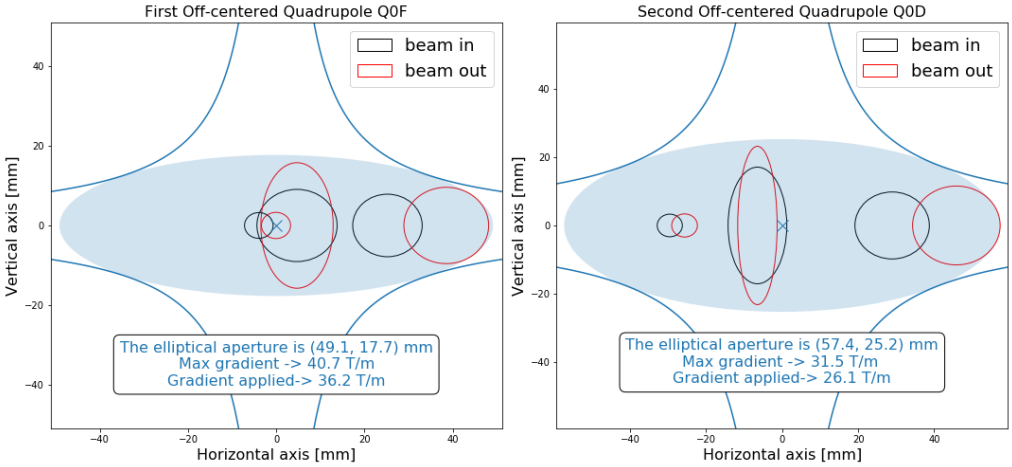

Figure 9.33: The position of the three beams at the entrance (black) and exit (red) of the electron doublet magnets. Following the internal convention, 15 σ plus 20% beta beating plus 2 mm orbit tolerances beam envelopes are chosen for the proton beams. The beam size of the electrons refer to 20 σ. From left to right the three beams are respectively the non colliding proton beam (tiny circles), electron beam (squeezed ellipses) and the colliding proton beam.

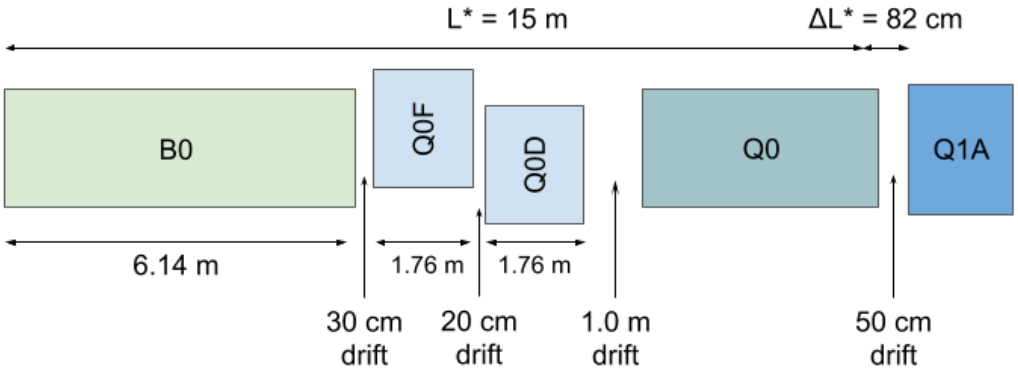

Figure 9.34: Possible optimized design featuring a 1.0 meter drift between the off-centered quadrupoles and the half quadrupole in order to leave space for shielding material.

The lattice based on a single dipole magnet and late focusing of the electron beam, shows an increase of the beta function of up 40% in the vertical plane for particles with a momentum deviation up to the design value of $\frac{\Delta p}{p} = 2.6 \times 10^{-4}$ (vertical cursor line in the graph) and a corresponding luminosity loss of 20% for those particles. The optimised design, based on the early focusing scheme, shows a much reduced chromatic effect and the resulting off-momentum beta-beating at the IP is limited to a few percent. As direct consequence the luminosity loss is well below the 1.5% level. A special local chromaticity correction scheme, therefore, dealing with the aberrations at IP, is thus not considered as necessary. Further studies will include the recirculation of the beam post-collision and the energy recovery performance and might nevertheless highlight the need of explicit sextupoles to mitigate the growing momentum spread through the deceleration process and to avoid beam losses.

Table 9.20: Magnet gradient and pole tip aperture of the quadrupoles of the doublet for the synchrotron power optimum

	Q0F	Q0D
$\gamma\varepsilon_e$ [mm.mrad]	50	50
$\gamma\varepsilon_p$ [mm.mrad]	2.50	2.50
Max. gradient [T/m]	36.2	26.1
Min. pole-tip radius [mm]	28.9	38.1
Length [m]	1.86	1.86

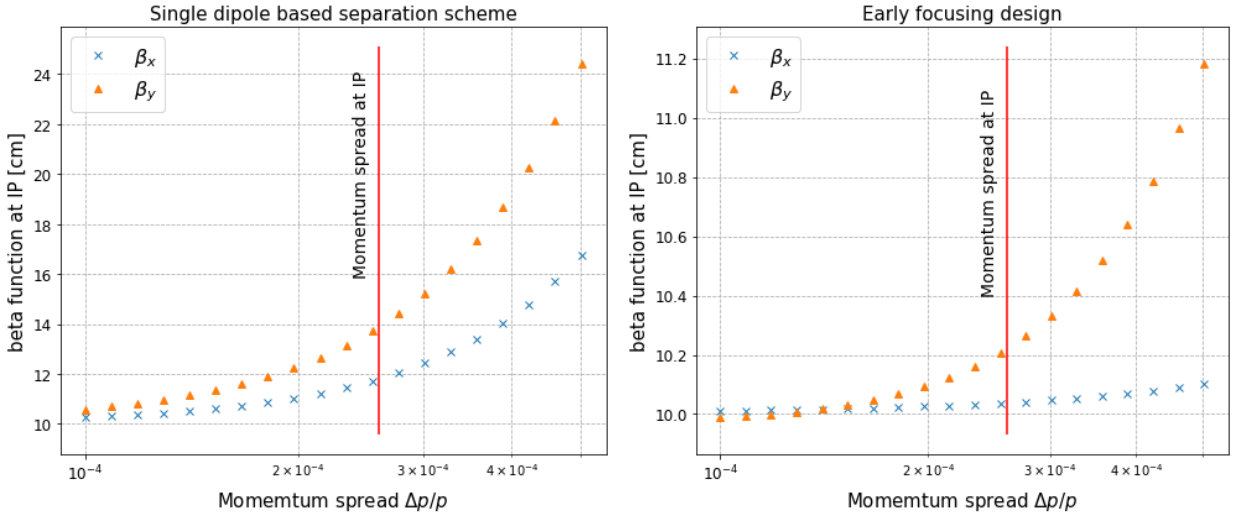

Figure 9.35: Beta function at the IP as a function of the momentum spread. Left : Situation for the single dipole based separation scheme. Right : With the design featuring an earlier focusing. The graphs show the increase of β^* due to the chromaticity of the lattice.

9.7.4 Interaction Region Magnet Design

[Stephan Russenschuck, Brett Parker, Kevin Andre', Bernhard Holzer]

Triplet Magnet Design

While the Q1 magnets remain in the range achievable with the well proven Nb-Ti superconductors, operated at 1.8 K, the Q2 magnets require Nb_3Sn technology. The working points on the load-line are given for both superconducting technologies in Fig. 9.37.

The thickness of a coil layer is limited by the flexural rigidity of the cable, which will make the coil-end design difficult. Therefore multi-layer coils must be considered. However, a thicker, multi-layer coil will increase the beam separation between the proton and the electron beams. The results of the field computation are given in Table 9.21. Because of the high iron saturation, the fringe fields in the electron beam channel are not negligible.

For the Nb_3Sn material we assume composite wire produced with the internal Sn process (Nb rod extrusions), [492]. The non-Cu critical current density is 2900 A/mm^2 at 12 T and 4.2 K. The filament size of 46 μm in Nb_3Sn strands give rise to higher persistent current effects in the magnet. The choice of Nb_3Sn would impose a considerable R&D and engineering design effort, which is however, not more challenging than other accelerator magnet projects, such as the HL-LHC.

Fig. 9.38 (right) shows the conceptual design of the mechanical structure of these magnets. The necessary prestress in the coil-collar structure, which must be high enough to avoid unloading at full excitation,

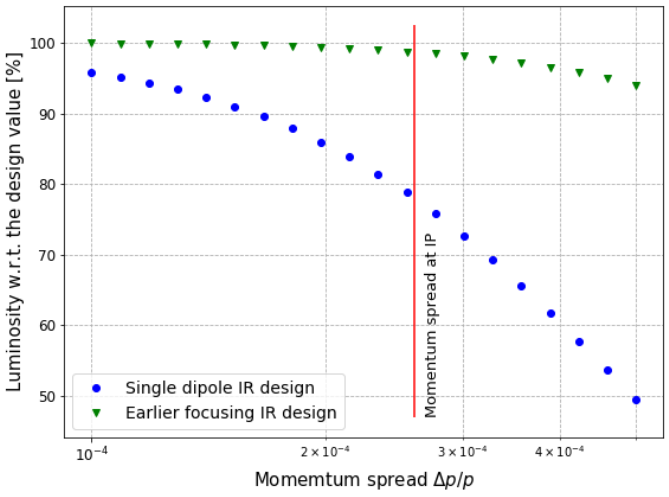

Figure 9.36: The resulting luminosity as a function of the momentum spread for the single dipole based separation scheme (blue circles) and the design featuring an earlier focusing (green triangles).

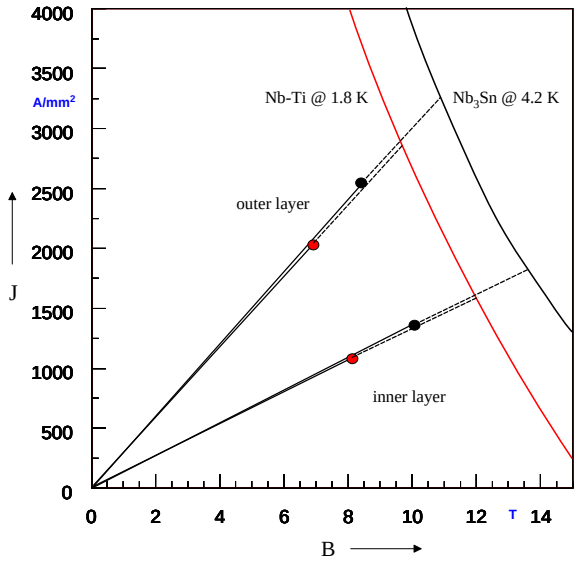

Figure 9.37: Working points on the load-line for both Nb-Ti and Nb_3Sn variants of Q1A.

cannot be exerted with the stainless-steel collars alone. Two interleaved sets of yoke laminations (a large one comprising the area of the yoke keys and a smaller, floating lamination with no structural function) provide the necessary mechanical stability of the magnet during cooldown and excitation. Preassembled yoke packs are mounted around the collars and put under a hydraulic press, so that the keys can be inserted. The sizing of these keys and the amount of prestress before the cooldown will have to be calculated using mechanical FEM programs. This also depends on the elastic modulus of the coil, which has to be measured with a short-model equipped with pressure gauges. Special care must be taken to avoid nonallowed multipole harmonics because the four-fold symmetry of the quadrupole will not entirely be maintained.

Table 9.21: SC = type of superconductor, g = field gradient, R = radius of the aperture (without coldbore and beam-screen), LL = percentage on the load line of the superconductor material, I_{nom} = operational current, S_{beam} = beam separation distance, B_{fringe} = fringe field in the aperture for the electron beam, g_{fringe} = gradient field in the aperture for the electron beam.

Magnet		Q1A	Q1B	Q2A	Q2B
SC		Nb-Ti	Nb_3Sn	Nb_3Sn	Nb3Sn
R	mm	20	32	40	45
I_{nom}	A				
g	T/m	252	164	186	175
LL	%				
S_{beam}	mm	?	?	?	?
B_{fringe}	T				
g_{fringe}	T/m				

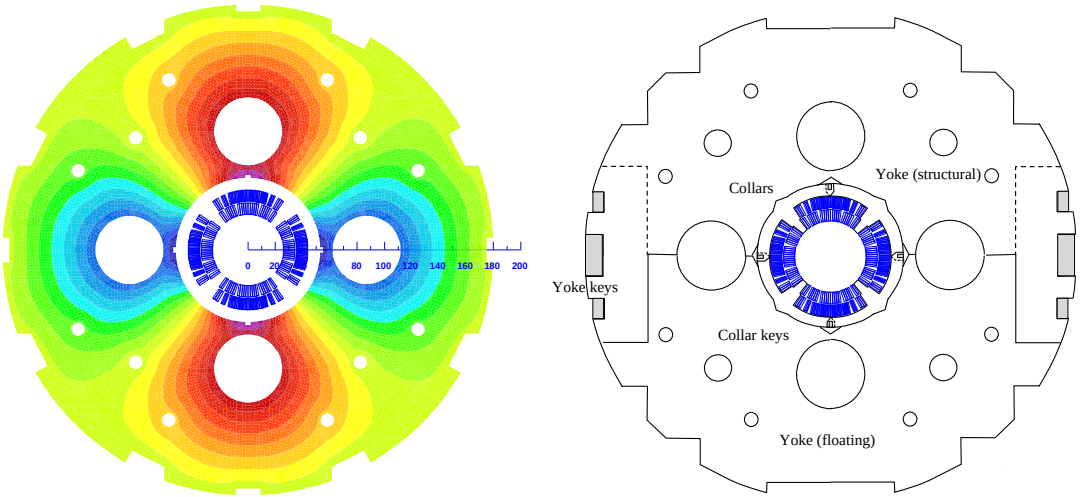

Figure 9.38: Conceptual design of the final focus septa. Left: Magnetic vector potential (field lines). Right: Sketch of the mechanical structure.

Normal-Conducting Magnet Design

The proposed mini-beta doublet of the electron lattice, providing an early focusing of the beam, and the normal conducting proton-half quadrupole are new magnet concepts. These have been studied conceptually to determine their technical feasibility. The geometry of the QNC magnet is shwon in Fig. 9.39 (left). Left of the mirror plate, the field free region will provide space for the electron beam and the non-colliding proton beam. The thickness of the mirror plate at the magnet mid-plane is 20 mm, allowing for sufficient mechanical stability at the minimal beam separation between the electron and proton beams.

Field calculations, using the magnet design code ROXIE [493] are presented in Fig. 9.39 (right). The achieved field gradient is 50 T/m for a current of 400 A, assuming a current density of 21.14 A/mm^2. This is in line with conductor geometries used for normal conducting magnets installed in the CERN injector complex, for example, ID: PXMQNDD8WC, which is rated at 860 A corresponding to 45.45 A/mm^2. A more comprehensive design study must also include a further reduction of the multipole field components.

The geometry of the Q0F and Q0D quadrupoles are given in Fig. 9.33 and the main specifications are provided in Table 9.20. A maximum magnetic field of 1.2 T at the pole tip is well within reach for a normal conducting quadrupole.

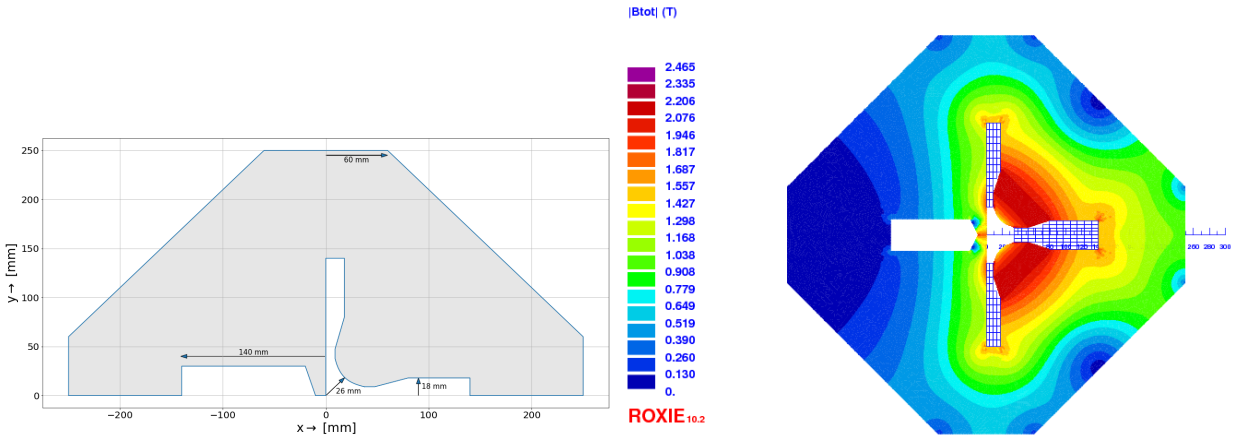

Figure 9.39: Left: Mechanical layout of the new half quadrupole for the proton beam. Right : Field distribution in the half quadrupole for the proton beam.

9.8 Civil Engineering [Alexandra Tudora, John Osborne]

Since the beginning of the LHeC concept, various shapes and sizes of the eh collider were studied around CERN region.The conceptual study report published in 2012 focused primarily on two main options, namely the RING-RING and the RING-LINAC options. For civil engineering, these options were studied taking into account geology, construction risks, land features as well as technical constrains and operation of the LHC. The Linac-Ring configuration was selected as preferred due to higher achievable luminosity. This chapter describes the civil engineering infrastructure required for an Energy Recovery Linac (ERL) injecting into the ALICE cavern at Point 2 LHC. Figure 9.40 shows three options of different sizes proposed for the ERL, represented as fractions of the LHC circumference. This chapter focuses on two of these options, specifically the 1/3 and 1/5 of the LHC circumference.

9.8.1 Placement and Geology

The proposed siting for the LHeC is in the North-Western part of the Geneva region at the existing CERN laboratory. The proposed Interaction Region is fully located within existing CERN land at LHC Point 2, close to the village of St.Genis, in France. The CERN area is extremely well suited to housing such a large project, with well understood ground conditions having several particle accelerators in the region for over 50 years. Extensive geological records exist from previous projects such as LEP and LHC and more recently, further ground investigations have been undertaken for the High-Luminosity LHC project. Any new underground structures will be constructed in the stable molasse rock at a depth of 100-150m in an area with very low seismic activity.

The LHeC is situated within the Geneva basin, a sub-basin of the large molassic plateau (Figure 9.41). The molasse formed from the erosion of the Alps and it is a weak sedimentary rock. It comprises of alternating layers of marls and sandstones (and formations of intermediate compositions), which show a high variety of strength parameters. The molasse is overlaid by the Quaternary glacial moraines. Figure 9.42 shows a simplified geological profile of the LHC. Although placed mainly within the molasse plateau, one sector of the LHC is situated in the Jura limestone.

The physical positioning of the LHeC has been developed based on the assumption that the maximum underground volume possible should be placed within the molasse rock and should avoid as much as possible any known geological faults or environmentally sensitive areas. Stable and dry, the molasse is considered a suitable rock type for TBM excavation. In comparison, CERN has experienced significant issues with the

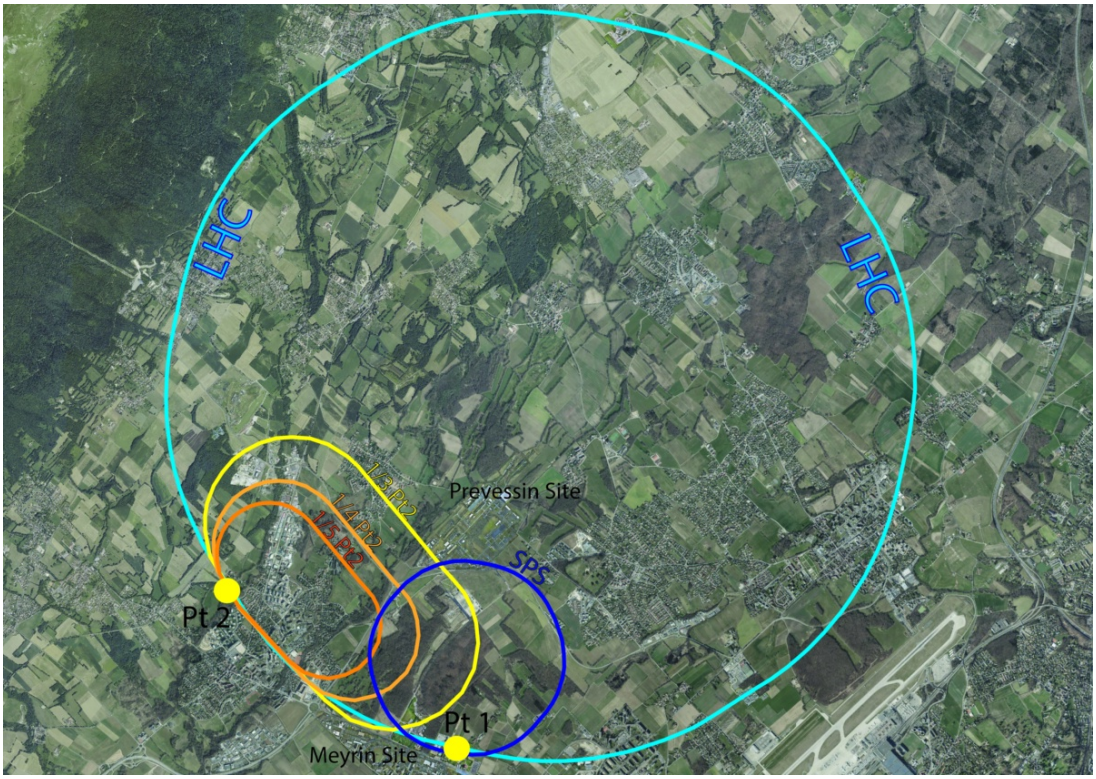

Figure 9.40: Racetrack options proposed for LHeC at Point 2 LHC

underground construction of sector 3-4 in the Jura limestone. There were major issues with water ingress at and behind the tunnel face. Another challenging factor for limestone is the presence of karsts. These are formed by chemical weathering of the rock and often they are filled with water and sediment, which can lead to infiltration and instability of the excavation.

The ERL will be positioned inside the LHC Ring, in order to ensure that new surface facilities are located on existing CERN land. The proposed underground structures for a Large Hadron electron Collider (LHeC) at high luminosity aiming for an electron beam energy of 60 GeV is shown in Figure 9.43. The LHeC tunnel will be tilted similarly to the LHC at a slope of 1.4% to follow a suitable layer of molasse rock.

9.8.2 Underground infrastructure

The underground structures proposed for LHeC option 1/3 LHC require a tunnel approximately 9 km long of 5.5m diameter, including two LINACs. Parallel to the main LINAC tunnels, at 10m distance apart, there are the RF galleries, each 1070m long. Waveguides of 1m diameter are connecting the RF galleries and LHeC main tunnel. These structures are listed in Table 9.22.

Two additional caverns, 25m wide and 50m long are required for cryogenics and technical services. These are connected to the surface via two 9m diameter access, provided with lifts to allow access for equipment and personnel.

Additional caverns are needed to house injection facilities and a beam dump. The underground structures proposed for LHeC option 1/5 LHC are the same as 1/3 options with the exception of the main tunnel which would be 5.4km long connected to RF galleries, each 830m long.

In addition to the new structures, the existing LHC infrastructure also requires modifications. To ensure connection between LHC and LHeC tunnels, the junction caverns UJ22 and UJ27 need to be enlarged (Figure

Figure 9.41: Simplified map of Swiss geology

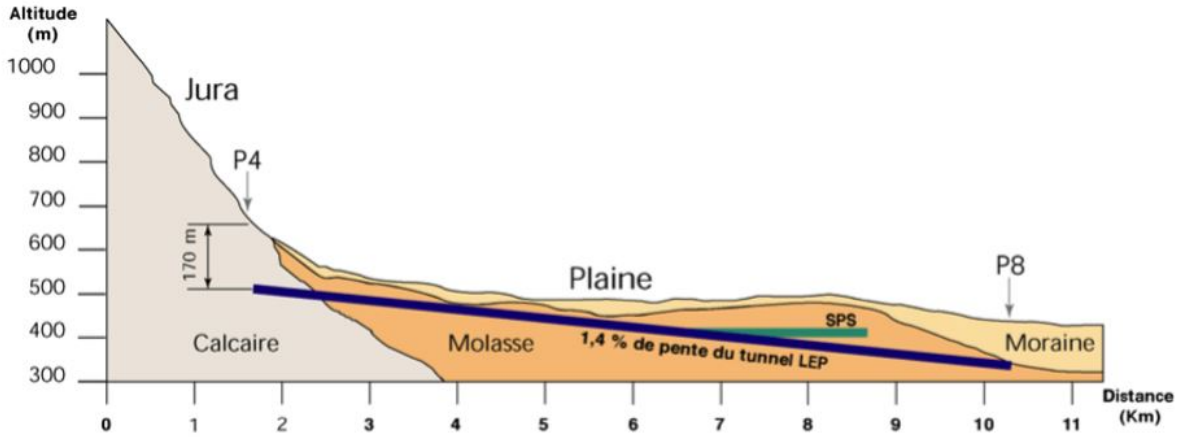

Figure 9.42: Geological profile of the LHC tunnel

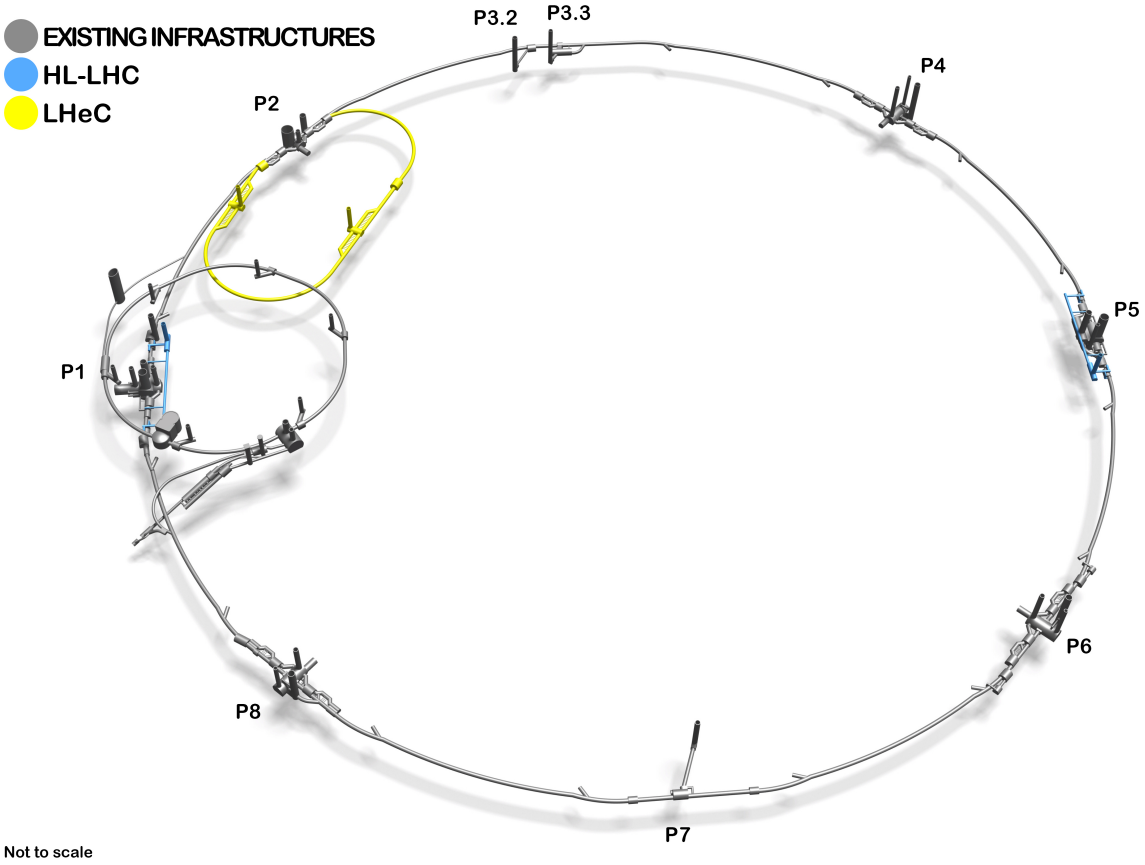

Figure 9.43: 3D Schematic showing proposed underground structures of LHeC (shwon in yellow). The HL-LHC structures are highlighted in blue.

Structures	Quantities	Length(m)	Span(m)
Machine tunnels	-	9091	5.5
Service caverns	2	50	25
Service shafts	2	80	9
Injection caverns	1	50	25
Dump cavern	1	90	16.8
Junction caverns	3	20	16.8
RF galleries	2	1070	5.5
Waveguide connections	50	10	1
Connection tunnels	4	10	3

Table 9.22: List of underground structures

9.44). Localised parts of the cavern and tunnel lining will be broken out to facilitate the excavation of the new spaces and the new connections, requiring temporary support.

Infrastructure works for LEP were completed in 1989, for which a design lifespan of 50 years was specified. If LHC is to be upgraded with a high energy, refurbishment, maintenance works are needed to re-use the existing infrastructure.

Shaft locations were chosen such that the surface facilities are located on CERN land. The scope for surface sites is still to be defined. New facilities are envisaged for housing technical services such as cooling and ventilation, cryogenics and electrical distribution.

9.8.3 Construction Methods

A Tunnel Boring Machines (TBM) should be utilised for the excavation of the main tunnel to achieve the fastest construction. When ground conditions are good and the geology is consistent, TBMs can be two to four times faster than conventional methods. A shielded TBM could be employed, with pre-cast segmental lining, and injection grouting behind the lining.

For the excavation of the shafts, caverns and connection tunnels, conventional technique could be used. Similar construction methods as for HL-LHC, for example using roadheaders and rockbreakers, can be adopted for LHeC. Some of these machinery could be seen in Figures 9.45 and 9.46 showing the excavation works at point 1 HL-LHC. One main constraint that dictated what equipment to be used for the HL-LHC excavation, was the vibration limit. Considering the sensitivity of the beamline, diesel excavators have been modified and equipped with an electric motor in order to reduce vibrations that could disrupt LHC operation. A similar equipment could also be needed for LHeC if construction works are carried out during operation of the LHC.

Existing boreholes data around IP2 shows that the moraines layer can be 25-35m deep before reaching the molasse. Temporary support of the excavation, for example using diaphragm walls is recommended. Once reaching a stable ground in dry conditions, common excavation methods can be adopted, for example using a hydraulic hammer and rockbreakers. The shaft lining will consist of a primary layer of shortcrete with rockbolts and an in-situ reinforced concrete secondary lining, with a waterproofing membrane in between the two linings.

9.8.4 Cost estimate

A detailed cost estimate was prepared for a 9.1km ERL located at Point 2 of LHC, using the same measure prices as for FCC. More recently for LHeC, the cost figures were adapted to fit the smaller version, the

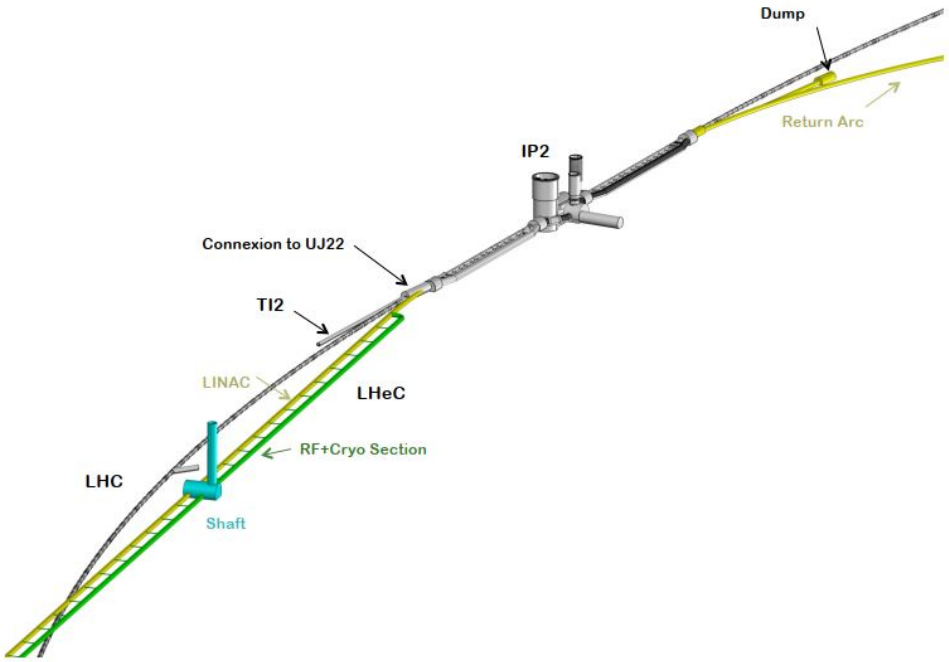

Figure 9.44: ERL injection area into IP2 and junction cavern

Figure 9.45: Excavator with hydraulic cutting heads being used at HL-LHC Point 1

Figure 9.46: Rockbreaker used for cavern excavation at HL-LHC Point 1

5.4km racetrack at point 2 (option 1/5 LHC).

The civil engineering costs amount to about 25% of the total project costs. In particular, for a 9.1km ERL (1/3 LHC option) the civil engineering was estimated to 386 MCHF and for a 5.4km configuration (1/5LHC) the costs is 289 MCHF. These estimates include the fees for preliminary design, approvals and tender documents (12%), site investigations (2%) and contractor's profit (3%). The costs mentioned do not include surface structures. Where possible, existing surface infrastructure will be re-used.

Chapter 10

Technology of ERL and PERLE [Alex Bogacz, Walid Kaabi]

10.1 Energy Recovery Linac Technology - Status and Prospects [Chris Tennant]

10.1.1 Introduction

In instances where high beam power is required, the concept of energy recovery presents an attractive solution. Energy recovering linacs (ERLs) are a class of novel accelerators which are uniquely qualified to meet the demands for a wide variety of applications by borrowing features from traditional architectures to generate linac quality beams with near storage ring efficiency [494]. After acceleration through a linac section, the electrons in an ERL are returned 180° out of phase with respect to the radio frequency (RF) accelerating field for energy recovery. The beam deposits energy into cavity fields, which can then accelerate newly injected bunches, thereby effectively canceling the beam loading effects of the accelerated beam. Therefore ERLs can accelerate very high average currents with only modest amounts of RF power. Because the beam is constantly being renewed, it never reaches an equilibrium state. Consequently this provides flexibility to manipulate the phase space and tailor the beam properties for a specific application. Further, since the energy of the decelerated beam is approximately equal to the injection energy, the dump design becomes considerably easier.

10.1.2 ERL Applications

Historically, nearly all ERLs built and operated were used to drive a free-electron laser (FEL). The requirement for high peak current bunches necessitated bunch compression and handling the attendant beam dynamical challenges. In recent years, ERLs have turned from being drivers of light sources toward applications for nuclear physics experiments, Compton backscattering sources and strong electron cooling. Unlike an FEL, these latter use cases require long, high charge bunches with small energy spread. Where once a short bunch length was the key performance metric, now there is a premium on maintaining a small correlated energy spread (with a commensurately long bunch).

10.1.3 Challenges

Energy recovery linacs are not without their own set of challenges. In the following sections a brief survey of some of the most relevant are given. These include collective effects, such as space charge, the multipass beam breakup (BBU) instability, coherent synchrotron radiation (CSR) and the microbunching instability (μBI),

beam dynamic issues such as halo, the interaction of the beam with the RF system and other environmental impedances as well as issues related to common transport lines.

Space Charge The role of space charge forces (both transverse and longitudinal) often dictate many operational aspects of the machine. Maintaining beam brightness during the low energy injection stage is vitally important. In addition to the low energy, ERL injectors must also preserve beam quality through the merger system that directs the beam to the linac axis. Once injected into the linac, the beam energy at the front end is often still low enough that space charge forces cannot be neglected. Just as important is the longitudinal space charge (LSC) force which manifests itself by an energy spread asymmetry about the linac on-crest phase [495]. The LSC wake acts to accelerate the head of the bunch while decelerating the tail. Operating on the rising part of the waveform leads to a decrease in the correlated energy spread, while accelerating on the falling side leads to an increase. These observations inform where acceleration, and how the longitudinal match, is performed.

Beam Breakup Instability The beam breakup instability is initiated when a beam bunch passes through an RF cavity off-axis, thereby exciting dipole higher-order modes (HOMs). The magnetic field of an excited mode deflects following bunches traveling through the cavity. Depending on the details of the machine optics, the deflection produced by the mode can translate into a transverse displacement at the cavity after recirculation. The recirculated beam induces, in turn, an HOM voltage which depends on the magnitude and direction of the beam displacement. Thus, the recirculated beam completes a feedback loop which can become unstable if the average beam current exceeds the threshold for stability [496]. Beam breakup is of particular concern in the design of high average current ERLs utilizing superconducting RF (SRF) technology. If not sufficiently damped by the HOM couplers, dipole modes with quality factors several orders of magnitude higher than in normal conducting cavities can exist, providing a threat for BBU to develop. For single pass ERLs, beam optical suppression techniques – namely, interchanging the horizontal and vertical phase spaces to break the feedback loop between the beam and the offending HOM – are effective at mitigating BBU [497].

Coherent Synchrotron Radiation Coherent synchrotron radiation poses a significant challenge for accelerators utilizing high brightness beams. When a bunch travels along a curved orbit, fields radiated from the tail of the bunch can overtake and interact with the head. Rather than the more conventional class of head-tail instabilities where the tail is affected by the actions of the head, CSR is a tail-head instability. The net result is that the tail loses energy while the head gains energy leading to an undesirable redistribution of particles in the bunch. Because the interaction takes place in a region of dispersion, the energy redistribution is correlated with the transverse positions in the bend plane and can lead to projected emittance growth. While there has been much progress in recent years to undo the effects of CSR in the bend plane with an appropriate choice of beam optics [498], it is more difficult to undo the gross longitudinal distortion caused by the CSR wake. This is particularly true in applications where the intrinsic energy spread is small and/or where the effect can accumulate over multiple recirculations. One possible mitigation is shielding the CSR wake using an appropriately sized beam pipe [499].

Microbunching Instability Microbunching develops when an initial density modulation, either from shot noise or from the drive laser, is converted to energy modulations through short-range wakefields such as space charge and CSR. The energy modulations are then transformed back to density modulations through the momentum compaction of the lattice. Danger arises when a positive feedback is formed and the initial modulations are enhanced. This phenomenon has been studied extensively, both theoretically and experimentally, in bunch compressor chicanes [500, 501]. Only recently has there been a concerted effort to study the microbunching instability in recirculating arcs [502, 503, 504]. Because the beam is subject to

space charge and/or CSR throughout an ERL, density modulations can be converted to energy modulations. And because of the native momentum compaction of the lattice (in arcs, spreaders/recombiners, chicanes, etc.) those energy modulations may be converted back to density modulations. Therefore, ERLs offer potentially favorable conditions for seeding the microbunching instability, which requires careful attention in the early design stages.

Halo Halo is defined as the relatively diffuse and potentially irregularly distributed components of beam phase space that can reach large amplitudes. It is of concern because ERL beams are manifestly non-Gaussian and can have beam components of significant intensity beyond the beam core [505]. Though sampling large amplitudes, halo responds to the external focusing of the accelerator transport system in a predictable manner. It is therefore not always at large spatial amplitude, but will at some locations instead be small in size but strongly divergent. Halo can therefore present itself as "hot spots" in a beam distribution, and thus may be thought of as a lower-intensity, co-propagating beam that is mismatched to the core beam focusing, timing, and energy. Beam loss due to halo scraping is perhaps the major operational challenge for higher-power ERLs. Megawatt-class systems must control losses at unshielded locations to better than 100 parts-per-million to stay within facility radiation envelopes. Scaling to 100 MW suggests that control must be at the part-per-million level. This has been demonstrated – but only at specific locations within an ERL [506].

RF Transients Dynamic loading due to incomplete energy recovery is an issue for all ERLs [507]. In some machines it is due to unintentional errors imposed on the energy recovered beam; for instance, path length errors in large-scale systems. In other machines, such as high power ERL-based FEL drivers, it is done intentionally. In cases where there is the potential for rapid changes in the relative phase of the energy recovered beam, dynamic loading would be difficult to completely control using fast tuners. In such cases adequate headroom in the RF power will have to be designed into the system. These transient beam-loading phenomena are widely unrecognized and/or neglected. RF drive requirements for an ERL are often viewed as "minimal", because in steady-state operation the recovered beam notionally provides RF power for acceleration. It has however been operationally established that RF drive requirements for ERLs are defined not by the steady-state, but rather by beam transients and environmental/design factors such as microphonics [508]. As a result, the RF power required for stable ERL operation can differ dramatically from naïve expectations.

Wakefields and Interaction of Beam with Environment As with other system architectures intended to handle high-brightness beams, ERLs can be performance-limited by wakefield effects. Not only can beam quality be compromised by interaction of the beam with environmental impedances, there is also significant potential for localized power deposition in beamline components. Resistive wall and RF heating have proven problematic during ERL operation in the past [509]. Extrapolation of this experience to higher bunch charges and beam powers leads to serious concern regarding heating effects. Careful analysis and management of system component impedances is required.

Multi-turn, Common Transport Future systems must evolve to utilize multiple turns; it is a natural cost optimization method [510] and multi-turn systems can in principle provide performance equal to that of 1-pass up/down ERLs at significantly lower cost. In addition to the use of multiple turns, cost control motivates use of extended lengths of common transport, in which both accelerated and recovered passes are handled simultaneously using the same beam lines. This presents unique challenges for high energy ERLs, like LHeC in particular, where energy loss due to synchrotron radiation cannot be ignored and causes an energy mismatch for common transport lines. But addressing these challenges will open up exciting new opportunities for ERLs. In addition to PERLE and LHeC, a multi-turn ERL design from Daresbury

illustrates the manner in which the cost/complexity optimum lies toward shorter linacs, more turns, and multiple beams in fewer beam lines [511]. This also drives the use of multiple turns in stacking rings for hadron cooling; the more turns the cooling beam can be utilized, the lower the current required from the driver ERL, which mitigates challenges associated with source lifetime [512].

10.1.4 ERL Landscape

One way to view the current state of ERLs globally is the so-called "ERL landscape" shown in Fig. 10.1 [513]. Every data point represents a machine that demonstrated energy recovery and is positioned in (maximum) energy and (average) current parameter space. For clarity, the plot is restricted to continuous-wave (CW), SRF-based ERLs only and includes legacy machines, those under construction and currently in operation as well as the LHeC and PERLE (proposed). The size of the marker is indicative of the charge per bunch while a black line around the marker indicates it was/is a "true ERL". That is, where the beam power exceeds the installed RF power (they are represented in the plot by the three FEL drivers that were designed, built, commissioned and operated at Jefferson Laboratory).

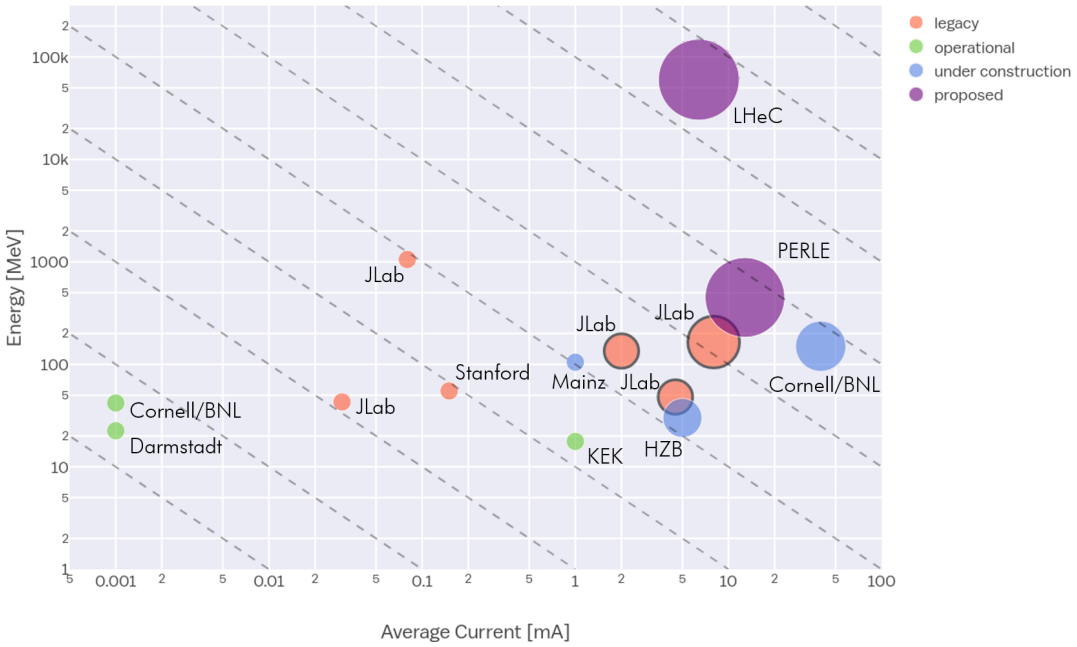

Figure 10.1: The "ERL landscape", where data points are restricted to CW, SRF-based ERLs. The dashed lines represent lines of constant beam power – starting from 10 W in the lower left and going to 10 GW in the upper right. Note that both axes use a log scale.

A cursory look at Fig. 10.1 illustrates several of the challenges facing the next generation of ERLs. While getting from the current state-of-the-art to the LHeC requires only a modest increase in average current, it requires a significant increase in bunch charge and addressing the consequent collective effects [514]. Most significantly, however, is the leap in energy from systems that have operated in the 100 MeV range to several tens of GeV. Note that PERLE is strategically positioned to address incremental changes in both average current, bunch charge and energy. As such, it provides a convenient test bed facility to address the issues described previously [515]. Several ERLs are still in the nascent stages and as they ramp up beam power, will also be valuable in advancing the state-of-the-art. For instance, though it uses a Fixed Field Alternating Gradient (FFAG) arc, the Cornell/Brookhaven ERL Test Accelerator (CBETA) will address multi-turn energy recovery for the first time in an SRF system [516]. Note that with only minor modifications Jefferson Laboratory's Continuous Electron Beam Accelerator Facility (CEBAF) could be operated with multi-pass

energy recovery at several GeV using common transport with the same topology as LHeC (i.e. bisected linacs of equal energy gain with arcs vertically separated by energy using spreaders and recombiners) [517].

10.2 PERLE [Walid Kaabi]

Chapter 11

Experimentation at the LHeC [Paul Newman, Peter Kostka]

11.1 Introduction [Paul Newman]

We should start with a summary of the CDR-2012. Based on that we can continue (the same structuring as the CDR-12) to describe the differences/changes.

11.2 Novel Detector Design Considerations [Peter]

Compared to year 2012 the physics program of LHeC at the CERN LHC accelerator complex has been extended/broadened (see chapters [ref.]) and as consequence the refined requirements on physics cross section accessibility supported by detector setup. The detector design specifically is ask for higher accuracy/resolution in space, energy and momentum measurement, allowing isolation of jets, charged as well as neutral particle productions, strongly and weakly interacting. The linear-ring (electron-proton) arrangement adopting the novel ERL-design for the electron acceleration part (described in chapter [ref.]) can reach high luminosities and electron-beam currents allowing the access of new levels for electron-hadron physics study at power consumption levels still kept within tolerable limits.

The kinematics, an unbalanced forward particle/jet production (in direction of incoming proton), impose consequences on detector design with higher requirements in forward direction at low azimuthal angles θ especially. As described in (chapter [ref.]) a dipole bends the electron beam into head-on collisions with the colliding proton beam and after the interaction point a dipole with opposite polarity separates the orbits of the electron and proton beam. Those weak bending dipoles have to be placed near to the beam line but outside of the tracker and electromagnetic calorimeter radius. The resulting synchrotron radiation fan has to be given free space and the beam pipe geometry has to follow the expanding radiation. The synchrotron background radiation require an advanced detector layout such that all components can tolerate the additional load.

11.3 Main Detector Elements

Fig. 11.1

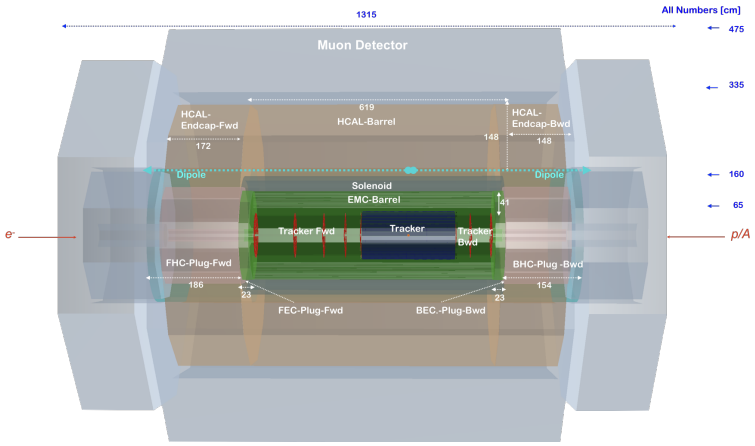

Figure 11.1: Side view of a LHeC concept detector designed using the DD4hep framework [ref.] with essential measures. The Si-tracker is surrounded by the Electromagnet-Barrel (ECAL-Barrel) and Electromagnet-forward/backward-Plug calorimeters using tungsten (forward) and lead (backward) absorber material and Si-based sensitive readout in both cases. The experiment solenoid is placed between the ECAL-Barrel and Hadronic-Barrel calorimeter (HCAL-Barrel) and housed in a cryostat common with a weak dipole which bends the electron beam into head-on collisions with the colliding proton beam and after the interaction point a dipole with opposite polarity separates the orbits of the electron and proton beam. The steering dipoles extend over the full length of the HCAL-Barrel and HCAL-Plug-forward/backward. The Hadronic Calorimeters Barrel/Endcaps are based on steel structures as absorbing material (of ATLAS type [ref.]) and close the outer field of the central solenoid. The Muon Detector builds an envelope of all other parts of the main LHeC detector.

11.3.1 Magnets [Hermann ten Kate]

Fig. 11.2

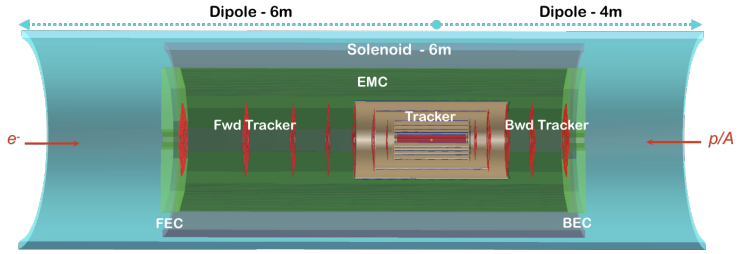

Figure 11.2: The experiment solenoid and the electron-beam steering dipoles enclosing the electromagnetic calorimeters and the tracker setup completely. In case of a cold solution for the EMC (discussed in [ref.]) this barrel electromagnetic calorimeter will be mounted inside the magnet cryostat of the solenoid and dipoles additionally.

Fig. 11.3

11.3.2 Machine-Detector Interface, Beam Pipe and Radiation [Peter Kostka]

Fig. 11.4

11.3.3 Inner Tracking [Peter Kostka]

Fig. 11.5

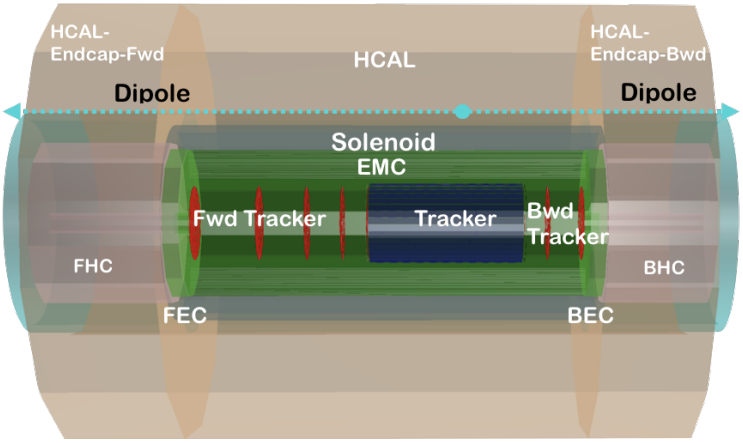

Figure 11.3: The barrel HCAL, the HCAL-Endcap-Fwd/Bwd and the plug hadronic calorimeters in forward/backward direction (FHC, BHC) are placed outside of the solenoidal field.

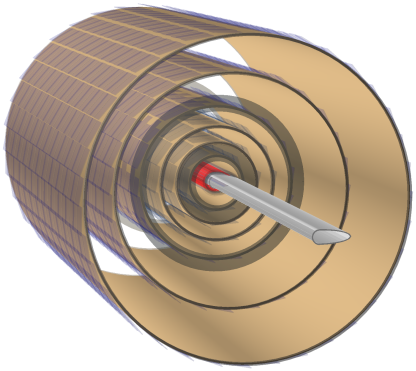

Figure 11.4: The circular-elliptical beam pipe is surrounded by the first layer of the barrel tracker following the shape of the beam pipe as close as possible. The barrel tracker is formed by one layer of pixel-wafers, three layers of macro-pixel and strip-sensors, respectively (see table [ref.]).

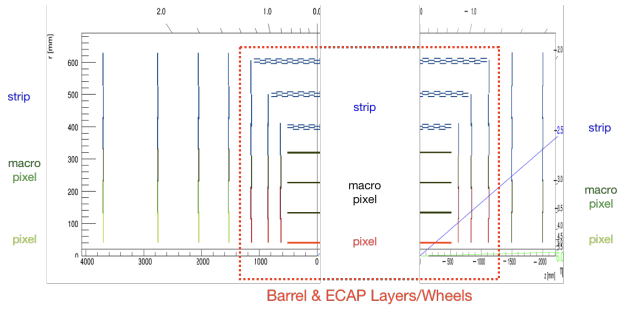

Figure 11.5: Schematic view of the tracker subdivided in forward and backward part. Both parts have been optimised using the tklayout program [ref.]. The layers/wheels forming the barrel part are enclosed by the red-dotted box. The innermost pixel layers are colored red, the macro-pixel layers are coded light and dark green and blue indicate the strip sensors for barrel and fwd/bwd wheel mount, respectively. All types of sensor modules used are summarised in table [ref.].

Fig. 11.6

Sensor Overview								
Sensorname	sensorType	numStripsAcross	numSegments	numROCX	numROCY	sensorLayout	numSensors	sensorThickness [mm]
Pixel_BRL0_module0	pixel	512	1370	1	3	mono	1	0.1
Pixel_InnerFwd_module0	pixel	1352	1522	3	3	mono	1	0.1
Pixel_InnerFwd_module1	pixel	1442	1007	3	2	mono	1	0.1
Pixel_Fwd_module0	pixel	2067	1800	4	4	mono	1	0.1
Pixel_Fwd_module1	pixel	1514	1000	3	2	mono	1	0.1
MacroPixel_module0	macroPixel	1536	256	3	1	mono	1	0.1
MacroPixel_InnerFwd_module0	macroPixel	1480	258	3	1	mono	1	0.1
MacroPixel_Fwd_module0	macroPixel	1531	250	3	1	mono	1	0.1
Strip_Fwd_module	strip	3072	10	6	10	mono	1	0.2
Strip_Outer_module	strip	3072	2	6	2	mono	1	0.2

Sensor Mount for Barrel Layers and Wheel Rings (from lower to higher Radii)				
Barrel Layers	ECAP Wheel1 - Ring Structure	ECAP Wheel2 - Ring Structure	ECAP Wheel3 - Ring Structure	FWD/BWD Wheels - Ring Structure
Pixel_BRL0_module0	Pixel_InnerFwd_module0	Pixel_InnerFwd_module0	Pixel_InnerFwd_module0	Pixel_Fwd_module0
MacroPixel_module0	Pixel_InnerFwd_module1	Pixel_InnerFwd_module1	Pixel_InnerFwd_module1	Pixel_Fwd_module1
MacroPixel_module0	MacroPixel_InnerFwd_module0	MacroPixel_InnerFwd_module0	MacroPixel_InnerFwd_module0	MacroPixel_Fwd_module0
MacroPixel_module0	Strip_Fwd_module	Strip_Fwd_module	Strip_Fwd_module	Strip_Fwd_module
Strip_Outer_module		Strip_Fwd_module	Strip_Fwd_module	Strip_Fwd_module
Strip_Outer_module			Strip_Fwd_module	Strip_Fwd_module
Strip_Outer_module				

Figure 11.6: All types of sensor modules used for the tracker are summarised.

Table 11.1: LHeC Tracker

Tracker_{LHeC} [1]	Inner Barrel			ECAP			Fwd Tracker			Bwd Tracker			Total
	pix	pix_m	strip	pix	pix_m	strip	pix	pix_m	strip	pix	pix_m	strip	
$\eta_{max/min}$	±3.3	±2.1	±1.4	±4.1/1.8	±2.4/1.5	±2./1.	5.3/2.6	3.5/2.2	3.1/1.6	-4./-2.6	-2.9/-2.2	-2.5/-1.6	5.3/-4.6
$\#\text{Layers}_{Barrel}$	1	3	3										
#Rings				2	1	1-3	2	1	3	2	1	3	
#Modules/Sensors	320	4420	3352	192	192	552	144	144	560	36	36	140	10088
Total Si area $[m^2]$	0.3	4.6	17.6	0.8	1.0	3.3	0.6	0.7	3.9	0.2	0.2	1.0	34,2
#Read-out-Channels [M]	224.5	1738	20.6	322.4	36.6	17.0	323.9	55.1	17.2	81.0	13.8	4.3	2854.4
$\sigma^{r-\phi}$ $[\mu m]$	7.5	9.5	9.5	7.5-9.5	9.5	9.5	7.5-9.5	9.5	9.5	7.5-9.5	9.5	9.5	
σ^{z} $[\mu m]$	15	115	2.9k	15-30	115-2.9k	2.9k	15-30	115-2.9k	2.9k	15-30	115-2.9k	2.9k	
average X_0/Λ_I [%]	7.2 / 2.2			3.0 / 1.0			2.5 / 0.8			0.9 / 0.3			
Beam pipe inclusive													35 / 23

[1] Based on tklayout calculations [ref.]

Fig. 11.7

Fig. 11.8

Fig. 11.9

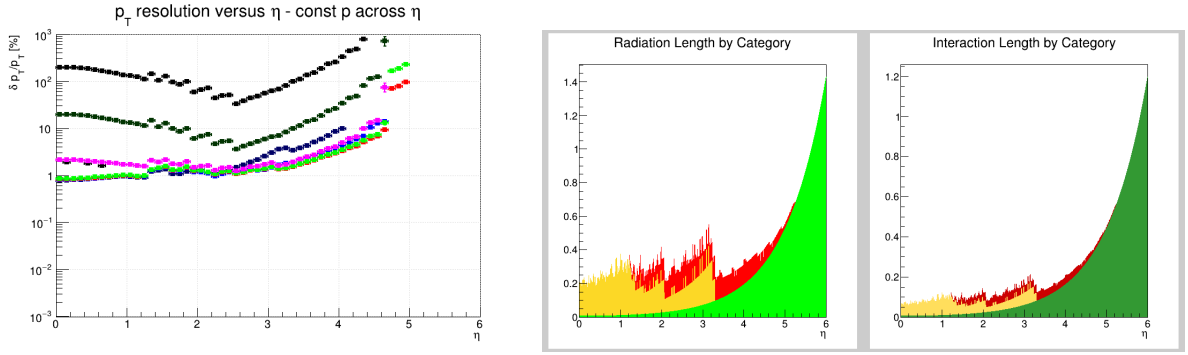

Figure 11.7: Left figure: Shows the transversal momentum $\mathbf{p_t}$ track resolution for several constant momentum **P** across pseudo-rapidity η (active+pasive material included - 2.5mm thick beam pipe).
The color coding for particle momenta P in GeV: 0.1 (Black), 1 (DarkBlue), 2 (Blue), 5 (Red), 10 (Green), 100 (Magenta), 1000 (DarkGreen), 10000 (Black).
Right figures: The radiation and interaction length dependence on η for categories (color coded): barrel modules (yellow), Endcap modules (red), beam pipe (green)

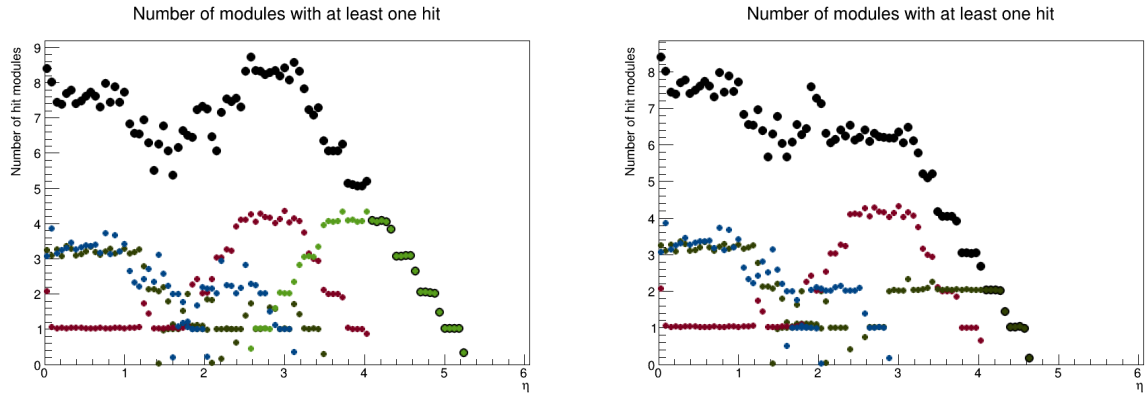

Figure 11.8: Left figure: shown is the number of modules/wafers with at least one hit versus the pseudo rapidity η for the forward tracker
Right figure: the similar picture for the for backward tracker.
Color coding: Module Type Red - **pixel** / light-Green and dark-Green - **macro-pixel** / Blue - srip / Black - SUM

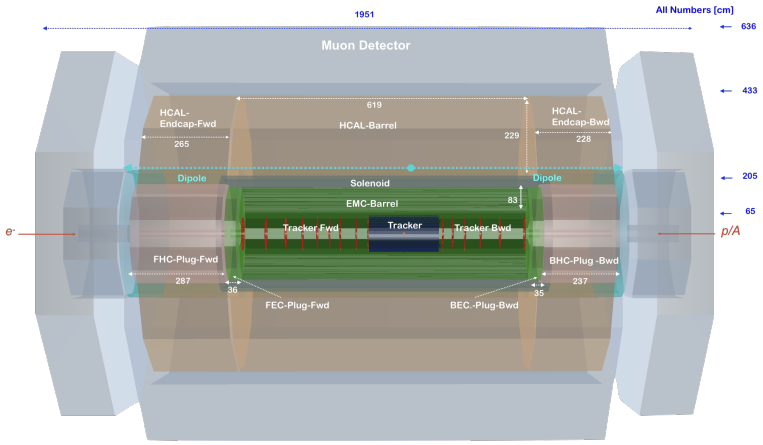

Figure 11.9: Side view of a lowE-FCCeh (E_p = 20TeV) concept detector designed using the DD4hep framework [ref.] showing essential measures. The principal layout is similar to the LHeC detector. As well as the choice of materials (warm version). The experiment solenoid is placed again between the ECAL-Barrel and Hadronic-Barrel calorimeter (HCAL-Barrel) and housed in a cryostat common with the beam steering dipoles extending over the full length of the HCAL-Barrel and HCAL-Plug-forward/backward. The sizes has been chosen such that the solenoid/dipoles and ECAL-Barrel systems as well as the whole tracker serve also after an upgrade of beam energy to E_p = 50TeV and an upgrade of detector accordingly.

Table 11.2: LHeC Main Calorimeter Properties

Calo$_{LHeC}$ [*Readout,Absorber*]	**FHC** [*Si,W*]	**FEC** [*Si,W*]	**EMC** [*Sci,Pb*]	**HCAL** [*Sci,Fe*]			**BEC** [*Si,Pb*]	**BHC** [*Si,Cu*]
	Plug Fwd	Plug Fwd	Barrel	Ecap Fwd	Barrel	Ecap Bwd	Plug Bwd	Plug Bwd
$\eta_{max/min}$	5.5/1.9	5.1/2.0	2.4/-1.4	1.9/1.0	1.6/-0.7	-1.5/-1.0	-4.4/-4.5	-4.5/-5.0
[1] σ_E/E [%]	51.8/5.4	17.8/1.4	12.4/1.9	49.3/4.7	48.23/5.6	49.9/4.8	14.4/2.8	49.5/7.9
Λ_I / X_0	$\Lambda_I = 9.6$	$X_0 = 48.8$	$X_0 = 30.2$	$\Lambda_I = 10.0$	$\Lambda_I = 7.3$	$\Lambda_I = 8.7$	$X_0 = 30.8$	$\Lambda_I = 9.2$

[1] **GEANT4** simulation based fits using crystal ball function

11.3.4 Calorimetry [Peter Kostka]

11.3.5 Muon Detector [Alessandro Polini]

11.4 Central Detector Performance [Peter Kostka]

11.5 Forward and Backward Detectors [Paul Newman]

11.6 Detector Installation and Infrastructure [Andrea Gaddi]

Table 11.3: lowE-FCCeh Main Calorimeter Properties

Calo FCC^{eh}_{lowE} $[Readout, Absorber]$	**FHC** $[Si,W]$	**FEC** $[Si,W]$	**EMC** $[Sci,Pb]$	**HCAL** $[Sci,Fe]$			**BEC** $[Si,Pb]$	**BHC** $[Si,Cu]$
	Plug Fwd	Plug Fwd	Barrel	Ecap Fwd	Barrel	Ecap Bwd	Plug Bwd	Plug Bwd
$\eta_{max/min}$	5.8/1.8	5.4/1.8	2.8/-1.7	2.0/0.8	1.6/0.8	-1.4/-1.8	-5.1/-5.2	-5.2/-5.6
[1] σ_E/E [%]	61.9/0.5	26.5/0.4	12.6/1.1	49.3/4.7	42.4/4.2	49.6/4.8	24.7/0.4	46.7/4.4
Λ_I / X_0	$\Lambda_I = 15.5$	$X_0 = 84.7$	$X_0 = 66.2$	$\Lambda_I = 15.4$	$\Lambda_I = 11.3$	$\Lambda_I = 13.3$	$X_0 = 50.2$	$\Lambda_I = 14.7$

[1] **GEANT4** simulation based fits using crystal ball function

Chapter 12

Conclusions [Oliver Bruening, Max Klein]

12.1 Summary [Max Klein]

12.2 Timeline and Future Project Development [Oliver Bruening]

Bibliography

[1] LHeC Study Group Collaboration, J. L. Abelleira Fernandez *et al.*, *J. Phys.* G39 (2012) 075001, arXiv:1206.2913.

[2] O. Bruening, *FCC-ACC-RPT-XXXX* (2018) .

[3] A. Bogacz, *Talk at ERL Workshop, Berlin* (2019) .

[4] FCC Collaboration, A. Abada *et al.*, *Eur. Phys. J. ST* 228 (2019) 755–1107.

[5] LHeC, PERLE Collaboration, O. Bruening and M. Klein, *J. Phys.* G46 (2019) 123001.

[6] F. Bordry, M. Benedikt, O. Bruning, J. Jowett, L. Rossi, D. Schulte, S. Stapnes and F. Zimmermann, arXiv:1810.13022.

[7] J. Butterworth *et al.*, *J. Phys.* G43 (2016) 023001, arXiv:1510.03865.

[8] J. Rojo *et al.*, *J. Phys.* G42 (2015) 103103, arXiv:1507.00556.

[9] R. Abdul Khalek, S. Bailey, J. Gao, L. Harland-Lang and J. Rojo, arXiv:1906.10127.

[10] T. J. Hobbs, B.-T. Wang, P. M. Nadolsky and F. I. Olness, *PoS* DIS2019 (2019) 247, arXiv:1907.00988.

[11] B.-T. Wang, T. J. Hobbs, S. Doyle, J. Gao, T.-J. Hou, P. M. Nadolsky and F. I. Olness, *Phys. Rev.* D98 (2018) 094030, arXiv:1803.02777.

[12] R. D. Ball, V. Bertone, M. Bonvini, S. Marzani, J. Rojo and L. Rottoli, *Eur. Phys. J.* C78 (2018) 321, arXiv:1710.05935.

[13] xFitter Developers' Team Collaboration, H. Abdolmaleki *et al.*, *Eur. Phys. J.* C78 (2018) 621, arXiv:1802.00064.

[14] M. Bonvini and S. Marzani, *Phys. Rev. Lett.* 120 (2018) 202003, arXiv:1802.07758.

[15] M. Klein, "Future Deep Inelastic Scattering with the LHeC," in *From My Vast Repertoire ...: Guido Altarelli's Legacy*, A. Levy, S. Forte and G. Ridolfi (eds.), pp. 303–347. 2019. arXiv:1802.04317.

[16] NNPDF Collaboration, R. Abdul Khalek, J. J. Ethier and J. Rojo, *Eur. Phys. J.* C79 (2019) 471, arXiv:1904.00018.

[17] A. M. Cooper-Sarkar and K. Wichmann, *Phys. Rev.* D98 (2018) 014027, arXiv:1803.00968.

[18] xFitter Developers' Team Collaboration, H. Abdolmaleki *et al.*, arXiv:1907.01014.

[19] ATLAS Collaboration, G. Aad *et al.*, *Phys. Rev. Lett.* 109 (2012) 012001, arXiv:1203.4051.

[20] ATLAS Collaboration, M. Aaboud *et al.*, *Eur. Phys. J.* C77 (2017) 367, arXiv:1612.03016.

[21] ATLAS Collaboration, G. Aad *et al.*, *JHEP* 05 (2014) 068, arXiv:1402.6263.

[22] CMS Collaboration, S. Chatrchyan *et al.*, *JHEP* 02 (2014) 013, arXiv:1310.1138.

[23] S. J. Brodsky, D. S. Hwang and I. Schmidt, *Phys. Lett.* B530 (2002) 99–107, arXiv:hep-ph/0201296.

[24] C. Lorce and B. Pasquini, *Int. J. Mod. Phys. Conf. Ser.* 20 (2012) 84–91, arXiv:1208.3065.

[25] C. Lorce, B. Pasquini, X. Xiong and F. Yuan, *Phys. Rev.* D85 (2012) 114006, arXiv:1111.4827.

[26] H1 Collaboration, F. D. Aaron *et al.*, *Eur. Phys. J.* C67 (2010) 1–24, arXiv:0911.5678.

[27] H1 Collaboration, V. Andreev *et al.*, *Eur. Phys. J.* C77 (2017) 791, arXiv:1709.07251.

[28] D. Britzger *et al.*, *Eur. Phys. J.* C79 (2019) 845, arXiv:1906.05303.

[29] H1, ZEUS Collaboration, H. Abramowicz *et al.*, *Eur. Phys. J.* C75 (2015) 580, arXiv:1506.06042.

[30] P. Azzi *et al.*, *CERN Yellow Rep. Monogr.* 7 (2019) 1–220, arXiv:1902.04070.

[31] Particle Data Group Collaboration, M. Tanabashi *et al.*, *Phys. Rev.* D98 (2018) 030001.

[32] J. R. Ellis, E. Gardi, M. Karliner and M. A. Samuel, *Phys. Lett.* B366 (1996) 268–275, arXiv:hep-ph/9509312.

[33] M. Gell-Mann and F. E. Low, *Phys. Rev.* 95 (1954) 1300–1312.

[34] S. J. Brodsky and P. Huet, *Phys. Lett.* B417 (1998) 145–153, arXiv:hep-ph/9707543.

[35] S. J. Brodsky and X.-G. Wu, *Phys. Rev.* D85 (2012) 034038, arXiv:1111.6175. [Erratum: Phys. Rev.D86,079903(2012)].

[36] S. J. Brodsky and X.-G. Wu, *Phys. Rev. Lett.* 109 (2012) 042002, arXiv:1203.5312.

[37] S. J. Brodsky and L. Di Giustino, *Phys. Rev.* D86 (2012) 085026, arXiv:1107.0338.

[38] M. Mojaza, S. J. Brodsky and X.-G. Wu, *Phys. Rev. Lett.* 110 (2013) 192001, arXiv:1212.0049.

[39] S. J. Brodsky, M. Mojaza and X.-G. Wu, *Phys. Rev.* D89 (2014) 014027, arXiv:1304.4631.

[40] S. J. Brodsky and X.-G. Wu, *Phys. Rev.* D86 (2012) 054018, arXiv:1208.0700.

[41] X.-G. Wu, Y. Ma, S.-Q. Wang, H.-B. Fu, H.-H. Ma, S. J. Brodsky and M. Mojaza, *Rept. Prog. Phys.* 78 (2015) 126201, arXiv:1405.3196.

[42] X.-G. Wu, J.-M. Shen, B.-L. Du, X.-D. Huang, S.-Q. Wang and S. J. Brodsky, *Prog. Part. Nucl. Phys.* 108 (2019) 103706, arXiv:1903.12177.

[43] S. J. Brodsky, G. P. Lepage and P. B. Mackenzie, *Phys. Rev.* D28 (1983) 228.

[44] S.-Q. Wang, S. J. Brodsky, X.-G. Wu, J.-M. Shen and L. Di Giustino, *Phys. Rev.* D100 (2019) 094010, arXiv:1908.00060.

[45] S. Brandt, C. Peyrou, R. Sosnowski and A. Wroblewski, *Phys. Lett.* 12 (1964) 57–61.

[46] E. Farhi, *Phys. Rev. Lett.* 39 (1977) 1587–1588.

[47] G. Parisi, *Phys. Lett.* 74B (1978) 65–67.

[48] J. F. Donoghue, F. E. Low and S.-Y. Pi, *Phys. Rev.* D20 (1979) 2759.

[49] T. Gehrmann, N. Häfliger and P. F. Monni, *Eur. Phys. J.* C74 (2014) 2896, arXiv:1401.6809.

[50] M. Dasgupta and G. P. Salam, *J. Phys.* G30 (2004) R143, arXiv:hep-ph/0312283.

[51] A. Gehrmann-De Ridder, T. Gehrmann, E. W. N. Glover and G. Heinrich, *Phys. Rev. Lett.* 99 (2007) 132002, arXiv:0707.1285.

[52] S. Weinzierl, *Phys. Rev. Lett.* 101 (2008) 162001, arXiv:0807.3241.

[53] ALEPH Collaboration, A. Heister *et al.*, *Eur. Phys. J.* C35 (2004) 457–486.

[54] DELPHI Collaboration, J. Abdallah *et al.*, *Eur. Phys. J.* C29 (2003) 285–312, arXiv:hep-ex/0307048.

[55] OPAL Collaboration, G. Abbiendi *et al.*, *Eur. Phys. J.* C40 (2005) 287–316, arXiv:hep-ex/0503051.

[56] L3 Collaboration, P. Achard *et al.*, *Phys. Rept.* 399 (2004) 71–174, arXiv:hep-ex/0406049.

[57] SLD Collaboration, K. Abe *et al.*, *Phys. Rev.* D51 (1995) 962–984, arXiv:hep-ex/9501003.

[58] A. Gehrmann-De Ridder, T. Gehrmann, E. W. N. Glover and G. Heinrich, *JHEP* 05 (2009) 106, arXiv:0903.4658.

[59] S. Weinzierl, *Phys. Rev.* D80 (2009) 094018, arXiv:0909.5056.

[60] C. J. Pahl, *Untersuchung perturbativer und nichtperturbativer Struktur der Momente hadronischer Ereignisformvariablen mit den Experimenten JADE und OPAL*. PhD thesis, Munich, Max Planck Inst., 2007. http://nbn-resolving.de/urn:nbn:de:bvb:91-diss-20070906-627360-1-2.

[61] I. I. Balitsky and L. N. Lipatov, *Sov. J. Nucl. Phys.* 28 (1978) 822–829. [Yad. Fiz.28,1597(1978)].

[62] E. A. Kuraev, L. N. Lipatov and V. S. Fadin, *Sov. Phys. JETP* 45 (1977) 199–204. [Zh. Eksp. Teor. Fiz.72,377(1977)].

[63] L. N. Lipatov, *Sov. Phys. JETP* 63 (1986) 904–912. [Zh. Eksp. Teor. Fiz.90,1536(1986)].

[64] V. S. Fadin and L. N. Lipatov, *Phys. Lett.* B429 (1998) 127–134, arXiv:hep-ph/9802290.

[65] M. Ciafaloni and G. Camici, *Phys. Lett.* B430 (1998) 349–354, arXiv:hep-ph/9803389.

[66] J. Blumlein and A. Vogt, *Phys. Rev.* D58 (1998) 014020, arXiv:hep-ph/9712546.

[67] D. A. Ross, *Phys. Lett.* B431 (1998) 161–165, arXiv:hep-ph/9804332.

[68] Y. V. Kovchegov and A. H. Mueller, *Phys. Lett.* B439 (1998) 428–436, arXiv:hep-ph/9805208.

[69] E. Levin, *Nucl. Phys.* B545 (1999) 481–504, arXiv:hep-ph/9806228.

[70] N. Armesto, J. Bartels and M. A. Braun, *Phys. Lett.* B442 (1998) 459–469, arXiv:hep-ph/9808340.

[71] M. Ciafaloni, *Nucl. Phys.* B296 (1988) 49–74.

[72] B. Andersson, G. Gustafson and J. Samuelsson, *Nucl. Phys.* B467 (1996) 443–478.

[73] J. Kwiecinski, A. D. Martin and P. J. Sutton, *Z. Phys.* C71 (1996) 585–594, arXiv:hep-ph/9602320.

[74] J. Kwiecinski, A. D. Martin and A. M. Stasto, *Phys. Rev.* D56 (1997) 3991–4006, arXiv:hep-ph/9703445.

[75] G. P. Salam, *JHEP* 07 (1998) 019, arXiv:hep-ph/9806482.

[76] M. Ciafaloni, D. Colferai and G. P. Salam, *JHEP* 10 (1999) 017, arXiv:hep-ph/9907409.

[77] M. Ciafaloni, D. Colferai and G. P. Salam, *Phys. Rev.* D60 (1999) 114036, arXiv:hep-ph/9905566.

[78] M. Ciafaloni, D. Colferai, D. Colferai, G. P. Salam and A. M. Stasto, *Phys. Lett.* B576 (2003) 143–151, arXiv:hep-ph/0305254.

[79] M. Ciafaloni, D. Colferai, G. P. Salam and A. M. Stasto, *Phys. Lett.* B587 (2004) 87–94, arXiv:hep-ph/0311325.

[80] M. Ciafaloni, D. Colferai, G. P. Salam and A. M. Stasto, *Phys. Rev.* D68 (2003) 114003, arXiv:hep-ph/0307188.

[81] M. Ciafaloni, D. Colferai, G. P. Salam and A. M. Stasto, *JHEP* 08 (2007) 046, arXiv:0707.1453.

[82] G. Altarelli, R. D. Ball and S. Forte, *Nucl. Phys.* B575 (2000) 313–329, arXiv:hep-ph/9911273.

[83] G. Altarelli, R. D. Ball and S. Forte, *Nucl. Phys.* B599 (2001) 383–423, arXiv:hep-ph/0011270.

[84] G. Altarelli, R. D. Ball and S. Forte, *Nucl. Phys.* B621 (2002) 359–387, arXiv:hep-ph/0109178.

[85] G. Altarelli, R. D. Ball and S. Forte, *Nucl. Phys.* B674 (2003) 459–483, arXiv:hep-ph/0306156.

[86] G. Altarelli, R. D. Ball and S. Forte, *Nucl. Phys.* B799 (2008) 199–240, arXiv:0802.0032.

[87] R. S. Thorne, *Phys. Rev.* D64 (2001) 074005, arXiv:hep-ph/0103210.

[88] A. Sabio Vera, *Nucl. Phys.* B722 (2005) 65–80, arXiv:hep-ph/0505128.

[89] M. Bonvini, S. Marzani and T. Peraro, *Eur. Phys. J.* C76 (2016) 597, arXiv:1607.02153.

[90] V. Bertone, S. Carrazza and J. Rojo, *Comput. Phys. Commun.* 185 (2014) 1647–1668, arXiv:1310.1394.

[91] M. Bonvini, S. Marzani and C. Muselli, *JHEP* 12 (2017) 117, arXiv:1708.07510.

[92] R. Gandhi, C. Quigg, M. H. Reno and I. Sarcevic, *Phys. Rev.* D58 (1998) 093009, arXiv:hep-ph/9807264.

[93] IceCube Collaboration, M. G. Aartsen *et al.*, *JINST* 12 (2017) P03012, arXiv:1612.05093.

[94] J. Kwiecinski, A. D. Martin and A. M. Stasto, *Phys. Rev.* D59 (1999) 093002, arXiv:astro-ph/9812262.

[95] IceCube Collaboration, M. G. Aartsen *et al.*, *Nature* 551 (2017) 596–600, arXiv:1711.08119.

[96] T. K. Gaisser, *Cosmic rays and particle physics*. 1990. http://www.cambridge.org/uk/catalogue/catalogue.asp?isbn=0521326672.

[97] IceCube Collaboration, M. G. Aartsen *et al.*, *Phys. Rev. Lett.* 113 (2014) 101101, arXiv:1405.5303.

[98] G. Gelmini, P. Gondolo and G. Varieschi, *Phys. Rev.* D61 (2000) 056011, arXiv:hep-ph/9905377.

[99] A. Bhattacharya, R. Enberg, Y. S. Jeong, C. S. Kim, M. H. Reno, I. Sarcevic and A. Stasto, *JHEP* 11 (2016) 167, arXiv:1607.00193.

[100] A. Accardi *et al.*, *Eur. Phys. J.* A52 (2016) 268, arXiv:1212.1701.

[101] A. V. Belitsky, X.-d. Ji and F. Yuan, *Phys. Rev.* D69 (2004) 074014, arXiv:hep-ph/0307383.

[102] N. N. Nikolaev and B. G. Zakharov, *Z. Phys.* C49 (1991) 607–618. [,733(1990)].

[103] N. Nikolaev and B. G. Zakharov, *Z. Phys.* C53 (1992) 331–346.

[104] N. N. Nikolaev and B. G. Zakharov, *J. Exp. Theor. Phys.* 78 (1994) 598–618. [Zh. Eksp. Teor. Fiz.105,1117(1994)].

[105] N. N. Nikolaev, B. G. Zakharov and V. R. Zoller, *Z. Phys.* A351 (1995) 435–446.

[106] A. H. Mueller, *Nucl. Phys.* B415 (1994) 373–385.

[107] A. H. Mueller and B. Patel, *Nucl. Phys.* B425 (1994) 471–488, arXiv:hep-ph/9403256.

[108] U. Amaldi and K. R. Schubert, *Nucl. Phys.* B166 (1980) 301–320.

[109] S. Munier, A. M. Stasto and A. H. Mueller, *Nucl. Phys.* B603 (2001) 427–445, arXiv:hep-ph/0102291.

[110] N. Armesto and A. H. Rezaeian, *Phys. Rev.* D90 (2014) 054003, arXiv:1402.4831.

[111] H. Kowalski and D. Teaney, *Phys. Rev.* D68 (2003) 114005, arXiv:hep-ph/0304189.

[112] H. Kowalski, L. Motyka and G. Watt, *Phys. Rev.* D74 (2006) 074016, arXiv:hep-ph/0606272.

[113] G. Watt and H. Kowalski, *Phys. Rev.* D78 (2008) 014016, arXiv:0712.2670.

[114] Y. Hatta, B.-W. Xiao and F. Yuan, *Phys. Rev. Lett.* 116 (2016) 202301, arXiv:1601.01585.

[115] T. Altinoluk, N. Armesto, G. Beuf and A. H. Rezaeian, *Phys. Lett.* B758 (2016) 373–383, arXiv:1511.07452.

[116] H. Mantysaari, N. Mueller and B. Schenke, *Phys. Rev.* D99 (2019) 074004, arXiv:1902.05087.

[117] F. Salazar and B. Schenke, *Phys. Rev.* D100 (2019) 034007, arXiv:1905.03763.

[118] H. MÃ€ntysaari and B. Schenke, *Phys. Rev. Lett.* 117 (2016) 052301, arXiv:1603.04349.

[119] H. MÃ€ntysaari and B. Schenke, *Phys. Rev.* D94 (2016) 034042, arXiv:1607.01711.

[120] H. MÃ€ntysaari and B. Schenke, *Phys. Lett.* B772 (2017) 832–838, arXiv:1703.09256.

[121] H. Mantysaari and B. Schenke, *Phys. Rev.* D98 (2018) 034013, arXiv:1806.06783.
[122] J. Cepila, J. G. Contreras and J. D. Tapia Takaki, *Phys. Lett.* B766 (2017) 186–191, arXiv:1608.07559.
[123] D. Bendova, J. Cepila and J. G. Contreras, *Phys. Rev.* D99 (2019) 034025, arXiv:1811.06479.
[124] M. Krelina, V. P. Goncalves and J. Cepila, *Nucl. Phys.* A989 (2019) 187–200, arXiv:1905.06759.
[125] H1 Collaboration, C. Adloff *et al.*, *Z. Phys.* C76 (1997) 613–629, arXiv:hep-ex/9708016.
[126] ZEUS Collaboration, J. Breitweg *et al.*, *Eur. Phys. J.* C1 (1998) 81–96, arXiv:hep-ex/9709021.
[127] V. N. Gribov, *Sov. Phys. JETP* 29 (1969) 483–487. [Zh. Eksp. Teor. Fiz.56,892(1969)].
[128] J. C. Collins, *Phys. Rev.* D57 (1998) 3051–3056, arXiv:hep-ph/9709499. [Erratum: Phys. Rev.D61,019902(2000)].
[129] A. Berera and D. E. Soper, *Phys. Rev.* D53 (1996) 6162–6179, arXiv:hep-ph/9509239.
[130] L. Trentadue and G. Veneziano, *Phys. Lett.* B323 (1994) 201–211.
[131] N. Armesto, P. R. Newman, W. Slominski and A. M. Stasto, *Phys. Rev.* D100 (2019) 074022, arXiv:1901.09076.
[132] H1 Collaboration Collaboration, A. Aktas *et al.*, *Eur.Phys.J.* C48 (2006) 715–748, arXiv:hep-ex/0606004.
[133] ZEUS Collaboration Collaboration, S. Chekanov *et al.*, *Nucl.Phys.* B816 (2009) 1–61, arXiv:0812.2003.
[134] H1 Collaboration Collaboration, F. Aaron *et al.*, *Eur.Phys.J.* C72 (2012) 2074, arXiv:1203.4495.
[135] H1, ZEUS Collaboration, F. D. Aaron *et al.*, *Eur. Phys. J.* C72 (2012) 2175, arXiv:1207.4864.
[136] ZEUS Collaboration, S. Chekanov *et al.*, *Nucl. Phys.* B713 (2005) 3–80, arXiv:hep-ex/0501060.
[137] H1 Collaboration, A. Aktas *et al.*, *Eur. Phys. J.* C48 (2006) 749–766, arXiv:hep-ex/0606003.
[138] ZEUS Collaboration Collaboration, S. Chekanov *et al.*, *Nucl.Phys.* B831 (2010) 1–25, arXiv:0911.4119.
[139] H1 Collaboration, F. Aaron *et al.*, *Eur.Phys.J.* C71 (2011) 1578, arXiv:1010.1476.
[140] V. N. Gribov and L. N. Lipatov, *Sov. J. Nucl. Phys.* 15 (1972) 675–684. [Yad. Fiz.15,1218(1972)].
[141] V. N. Gribov and L. N. Lipatov, *Sov. J. Nucl. Phys.* 15 (1972) 438–450. [Yad. Fiz.15,781(1972)].
[142] G. Altarelli and G. Parisi, *Nucl. Phys.* B126 (1977) 298–318.
[143] Y. L. Dokshitzer, *Sov. Phys. JETP* 46 (1977) 641–653. [Zh. Eksp. Teor. Fiz.73,1216(1977)].
[144] J. C. Collins and W.-K. Tung, *Nucl. Phys.* B278 (1986) 934.
[145] R. S. Thorne and W. K. Tung, arXiv:0809.0714.
[146] J. F. Owens, *Phys. Rev.* D30 (1984) 943.
[147] M. Gluck, E. Reya and A. Vogt, *Z. Phys.* C53 (1992) 651–656.
[148] R. S. Thorne and R. G. Roberts, *Phys. Rev.* D57 (1998) 6871–6898, arXiv:hep-ph/9709442.
[149] O. Bruning, J. Jowett, M. Klein, D. Pellegrini, D. Schulte and F. Zimmermann, .
[150] S. J. Brodsky, G. F. de Teramond, H. G. Dosch and J. Erlich, *Phys. Rept.* 584 (2015) 1–105, arXiv:1407.8131.
[151] G. F. de Teramond, H. G. Dosch and S. J. Brodsky, *Phys. Rev.* D87 (2013) 075005, arXiv:1301.1651.
[152] V. de Alfaro, S. Fubini and G. Furlan, *Nuovo Cim.* A34 (1976) 569.
[153] G. Veneziano, *Nuovo Cim.* A57 (1968) 190–197.
[154] A. Deur, S. J. Brodsky and G. F. de Teramond, *Prog. Part. Nucl. Phys.* 90 (2016) 1–74, arXiv:1604.08082.
[155] G. Grunberg, *Phys. Lett.* 95B (1980) 70. [Erratum: Phys. Lett.110B,501(1982)].
[156] J. D. Bjorken, *Phys. Rev.* 148 (1966) 1467–1478.
[157] A. Deur *et al.*, *Phys. Rev. Lett.* 93 (2004) 212001, arXiv:hep-ex/0407007.
[158] A. Deur, Y. Prok, V. Burkert, D. Crabb, F. X. Girod, K. A. Griffioen, N. Guler, S. E. Kuhn and N. Kvaltine, *Phys. Rev.* D90 (2014) 012009, arXiv:1405.7854.
[159] A. Deur *et al.*, *Phys. Rev.* D78 (2008) 032001, arXiv:0802.3198.
[160] S. J. Brodsky and H. J. Lu, *Phys. Rev.* D51 (1995) 3652–3668, arXiv:hep-ph/9405218.
[161] S. J. Brodsky, G. F. de Teramond and A. Deur, *Phys. Rev.* D81 (2010) 096010, arXiv:1002.3948.
[162] A. Deur, S. J. Brodsky and G. F. de Teramond, *Phys. Lett.* B750 (2015) 528–532, arXiv:1409.5488.
[163] S. J. Brodsky, G. F. de Téramond, A. Deur and H. G. Dosch, *Few Body Syst.* 56 (2015) 621–632, arXiv:1410.0425.
[164] A. Deur, V. Burkert, J.-P. Chen and W. Korsch, *Phys. Lett.* B650 (2007) 244–248, arXiv:hep-ph/0509113.
[165] A. Deur, V. Burkert, J. P. Chen and W. Korsch, *Phys. Lett.* B665 (2008) 349–351, arXiv:0803.4119.
[166] S. J. Brodsky, *J. Phys. Conf. Ser.* 1137 (2019) 012027.

[167] G. P. Lepage and S. J. Brodsky, *Phys. Lett.* 87B (1979) 359–365.

[168] A. V. Efremov and A. V. Radyushkin, *Phys. Lett.* 94B (1980) 245–250.

[169] S. J. Brodsky, G. F. De Téramond and H. G. Dosch, *Phys. Lett.* B729 (2014) 3–8, arXiv:1302.4105.

[170] S. J. Brodsky, *Few Body Syst.* 57 (2016) 703–715, arXiv:1601.06328.

[171] R. S. Sufian, G. F. de Téramond, S. J. Brodsky, A. Deur and H. G. Dosch, *Phys. Rev.* D95 (2017) 014011, arXiv:1609.06688.

[172] HLFHS Collaboration, G. F. de Teramond, T. Liu, R. S. Sufian, H. G. Dosch, S. J. Brodsky and A. Deur, *Phys. Rev. Lett.* 120 (2018) 182001, arXiv:1801.09154.

[173] T. Gutsche, V. E. Lyubovitskij, I. Schmidt and A. Vega, *Phys. Rev.* D91 (2015) 114001, arXiv:1501.02738.

[174] T. Gutsche, V. E. Lyubovitskij and I. Schmidt, *Phys. Rev.* D94 (2016) 116006, arXiv:1607.04124.

[175] H. G. Dosch, G. F. de Teramond and S. J. Brodsky, *Phys. Rev.* D91 (2015) 085016, arXiv:1501.00959.

[176] S. J. Brodsky, G. F. de Téramond, H. G. Dosch and C. Lorcé, *Int. J. Mod. Phys.* A31 (2016) 1630029, arXiv:1606.04638.

[177] M. Nielsen, S. J. Brodsky, G. F. de Téramond, H. G. Dosch, F. S. Navarra and L. Zou, *Phys. Rev.* D98 (2018) 034002, arXiv:1805.11567.

[178] G. F. de Teramond, H. G. Dosch and S. J. Brodsky, *Phys. Rev.* D91 (2015) 045040, arXiv:1411.5243.

[179] ANDY Collaboration, L. C. Bland *et al.*, arXiv:1909.03124.

[180] A. H. Mueller, *Nucl. Phys.* B335 (1990) 115–137.

[181] S. Carrazza, S. Forte, Z. Kassabov, J. I. Latorre and J. Rojo, *Eur. Phys. J.* C75 (2015) 369, arXiv:1505.06736.

[182] H. Paukkunen and P. Zurita, *JHEP* 12 (2014) 100, arXiv:1402.6623.

[183] J. Rojo and F. Caola, "Parton distributions and small-x QCD at the Large Hadron Electron Collider," in *Proceedings, 17th International Workshop on Deep-Inelastic Scattering and Related Subjects (DIS 2009): Madrid, Spain, April 26-30, 2009*, p. 222, Science Wise Publ. Science Wise Publ., Berlin, Germany, 2009. arXiv:0906.2079.

[184] R. Abdul Khalek, S. Bailey, J. Gao, L. Harland-Lang and J. Rojo, *Eur. Phys. J.* C78 (2018) 962, arXiv:1810.03639.

[185] J. Bartels, K. J. Golec-Biernat and H. Kowalski, *Phys. Rev.* D66 (2002) 014001, arXiv:hep-ph/0203258.

[186] K. J. Golec-Biernat and S. Sapeta, *Phys. Rev.* D74 (2006) 054032, arXiv:hep-ph/0607276.

[187] K. Golec-Biernat and S. Sapeta, *JHEP* 03 (2018) 102, arXiv:1711.11360.

[188] J. Gao, L. Harland-Lang and J. Rojo, *Phys. Rept.* 742 (2018) 1–121, arXiv:1709.04922.

[189] S. Forte, E. Laenen, P. Nason and J. Rojo, *Nucl. Phys.* B834 (2010) 116–162, arXiv:1001.2312.

[190] V. Bertone, R. Gauld and J. Rojo, *JHEP* 01 (2019) 217, arXiv:1808.02034.

[191] S. L. Glashow, *Nucl. Phys.* 22 (1961) 579.

[192] S. Weinberg, *Phys. Rev. Lett.* 19 (1967) 1264.

[193] S. Weinberg, *Phys. Rev. Lett.* 27 (1971) 1688.

[194] S. Weinberg, *Phys. Rev.* D5 (1972) 1412.

[195] A. Salam and J. C. Ward, *Phys. Lett.* 13 (1964) 168.

[196] P. W. Higgs, *Phys. Lett.* 12 (1964) 132.

[197] P. W. Higgs, *Phys. Rev. Lett.* 13 (1964) 508.

[198] F. Englert and R. Brout, *Phys. Rev. Lett.* 13 (1964) 321.

[199] H1 Collaboration, A. Aktas *et al.*, *Phys. Lett.* B632 (2006) 35, arXiv:hep-ex/0507080.

[200] ZEUS Collaboration, H. Abramowicz *et al.*, *Phys. Rev.* D93 (2016) 092002, arXiv:1603.09628.

[201] H1 Collaboration, V. Andreev *et al.*, *Eur. Phys. J.* C78 (2018) 777, arXiv:1806.01176.

[202] M. Klein and T. Riemann, *Z. Phys.* C24 (1984) 151.

[203] M. Böhm and H. Spiesberger, *Nucl. Phys.* B294 (1987) 1081.

[204] D. Yu. Bardin, C. Burdik, P. C. Khristova and T. Riemann, *Z. Phys.* C42 (1989) 679.

[205] W. Hollik, D. Yu. Bardin, J. Blümlein, B. A. Kniehl, T. Riemann and H. Spiesberger, "Electroweak parameters at HERA: Theoretical aspects," in *Workshop on physics at HERA Hamburg, Germany, October 29-30, 1991*, p. 923. 1992.

[206] M. Böhm and H. Spiesberger, *Nucl. Phys.* B304 (1988) 749.

[207] D. Yu. Bardin, K. C. Burdik, P. K. Khristova and T. Riemann, *Z. Phys.* C44 (1989) 149.

[208] A. Sirlin, *Phys. Rev.* D22 (1980) 971.

[209] M. Bohm, H. Spiesberger and W. Hollik, *Fortsch. Phys.* 34 (1986) 687–751.

[210] W. F. L. Hollik, *Fortsch. Phys.* 38 (1990) 165.

[211] H1 Collaboration, F. D. Aaron *et al.*, *JHEP* 09 (2012) 061, arXiv:1206.7007.

[212] D. Britzger and M. Klein, *PoS* DIS2017 (2018) 105.

[213] M. Botje, *Comput. Phys. Commun.* 182 (2011) 490, arXiv:1005.1481.

[214] M. Botje, arXiv:1602.08383.

[215] H. Spiesberger, "EPRC: A program package for electroweak physics at HERA," in *Future physics at HERA. Proceedings, Workshop, Hamburg, Germany, September 25, 1995-May 31, 1996. Vol. 1, 2.* 1995.

[216] H1 Collaboration, V. Andreev *et al.*, *Eur. Phys. J.* C75 (2015) 65, arXiv:1406.4709.

[217] G. Cowan, K. Cranmer, E. Gross and O. Vitells, *Eur. Phys. J.* C71 (2011) 1554, arXiv:1007.1727. [Erratum: Eur. Phys. J. C73 (2013) 2501].

[218] CDF, D0 Collaboration, T. E. W. Group, arXiv:1204.0042.

[219] ALEPH, DELPHI, L3, OPAL, LEP Electroweak Collaboration, S. Schael *et al.*, *Phys. Rept.* 532 (2013) 119–244, arXiv:1302.3415.

[220] ATLAS Collaboration, M. Aaboud *et al.*, *Eur. Phys. J.* C78 (2018) 110, arXiv:1701.07240. [Erratum: Eur. Phys. J.C78,no.11,898(2018)].

[221] Particle Data Group Collaboration, M. Tanabashi *et al.*, "2019 Update of the Review of Particle Physics," in *ref. [31] and online at pdglive.lbl.gov.*

[222] J. de Blas, M. Ciuchini, E. Franco, S. Mishima, M. Pierini, L. Reina and L. Silvestrini, *JHEP* 12 (2016) 135, arXiv:1608.01509.

[223] J. Haller, A. Hoecker, R. Kogler, K. Mönig, T. Peiffer and J. Stelzer, *Eur. Phys. J.* C78 (2018) 675, arXiv:1803.01853.

[224] MuLan Collaboration, V. Tishchenko *et al.*, *Phys. Rev.* D87 (2013) 052003, arXiv:1211.0960.

[225] M. Schott, "Global EW fits: experimental and theoretical issues," Talk presented at the Ultimate Precision at Hadron Colliders, Sarclay, France, 2019.

[226] ALEPH, DELPHI, L3, OPAL, SLD, LEP Electroweak Working Group, SLD Electroweak Group, SLD Heavy Flavour Group Collaboration, S. Schael *et al.*, *Phys. Rept.* 427 (2006) 257–454, arXiv:hep-ex/0509008.

[227] D0 Collaboration, V. M. Abazov *et al.*, *Phys. Rev.* D84 (2011) 012007, arXiv:1104.4590.

[228] CDF, D0 Collaboration, T. A. Aaltonen *et al.*, *Phys. Rev.* D97 (2018) 112007, arXiv:1801.06283.

[229] LHCb Collaboration, R. Aaij *et al.*, *JHEP* 11 (2015) 190, arXiv:1509.07645.

[230] ATLAS Collaboration, T. A. collaboration, .

[231] CMS Collaboration, A. M. Sirunyan *et al.*, *Eur. Phys. J.* C78 (2018) 701, arXiv:1806.00863.

[232] J. Erler, "Global fits of the SM parameters," in *7th Large Hadron Collider Physics Conference (LHCP 2019) Puebla, Puebla, Mexico, May 20-25, 2019.* 2019. arXiv:1908.07327.

[233] J. Erler and M. Schott, *Prog. Part. Nucl. Phys.* 106 (2019) 68–119, arXiv:1902.05142.

[234] K. Hagiwara, S. Ishihara, R. Szalapski and D. Zeppenfeld, *Phys. Rev.* D48 (1993) 2182–2203.

[235] K. Hagiwara, S. Ishihara, R. Szalapski and D. Zeppenfeld, *Phys. Lett.* B283 (1992) 353–359.

[236] A. De Rujula, M. B. Gavela, P. Hernandez and E. Masso, *Nucl. Phys.* B384 (1992) 3–58.

[237] S. S. Biswal, M. Patra and S. Raychaudhuri, arXiv:1405.6056.

[238] I. T. Cakir, O. Cakir, A. Senol and A. T. Tasci, *Acta Phys. Polon.* B45 (2014) 1947, arXiv:1406.7696.

[239] U. Baur and D. Zeppenfeld, *Nucl. Phys.* B325 (1989) 253–274.

[240] U. Baur, B. A. Kniehl, J. A. M. Vermaseren and D. Zeppenfeld, "Single W and Z production at LEP / LHC," in *ECFA Large Hadron Collider Workshop, Aachen, Germany, 4-9 Oct 1990: Proceedings.2.*, pp. 956–966. 1990.

[241] U. Baur, J. A. M. Vermaseren and D. Zeppenfeld, *Nucl. Phys.* B375 (1992) 3–44.

[242] R. Li, X.-M. Shen, K. Wang, T. Xu, L. Zhang and G. Zhu, *Phys. Rev.* D97 (2018) 075043, arXiv:1711.05607.

[243] M. Köksal, A. A. Billur, A. Gutiérrez-Rodríguez and M. A. Hernández-Ruíz, arXiv:1910.06747.

[244] A. Gutiérrez-Rodríguez, M. Köksal, A. A. Billur and M. A. Hernández-Ruíz, arXiv:1910.02307.

[245] CMS Collaboration, A. M. Sirunyan *et al.*, *Phys. Lett.* B772 (2017) 21–42, arXiv:1703.06095.

[246] CMS Collaboration, A. M. Sirunyan *et al.*, arXiv:1907.08354.

[247] S. Villa, *Nucl. Phys. Proc. Suppl.* 142 (2005) 391–396, arXiv:hep-ph/0410208. [,391(2004)].

[248] S. Dutta, A. Goyal, M. Kumar and B. Mellado, *Eur. Phys. J.* C75 (2015) 577, arXiv:1307.1688.

[249] A. O. Bouzas and F. Larios, *Phys. Rev.* D88 (2013) 094007, arXiv:1308.5634.

[250] S. Ovyn, X. Rouby and V. Lemaitre, arXiv:0903.2225.

[251] CMS Collaboration, V. Khachatryan *et al.*, *JHEP* 06 (2014) 090, arXiv:1403.7366.

[252] H. Sun, *PoS* DIS2018 (2018) 167.

[253] CMS Collaboration, V. Khachatryan *et al.*, *Phys. Lett.* B736 (2014) 33–57, arXiv:1404.2292.

[254] J. A. Aguilar-Saavedra, *Acta Phys. Polon.* B35 (2004) 2695–2710, arXiv:hep-ph/0409342.

[255] J. Charles *et al.*, *Phys. Rev.* D91 (2015) 073007, arXiv:1501.05013.

[256] I. Turk Cakir, A. Yilmaz, H. Denizli, A. Senol, H. Karadeniz and O. Cakir, *Adv. High Energy Phys.* 2017 (2017) 1572053, arXiv:1705.05419.

[257] O. Cakir, A. Yilmaz, I. Turk Cakir, A. Senol and H. Denizli, *Nucl. Phys.* B944 (2019) 114640, arXiv:1809.01923.

[258] H. Sun and X. Wang, *Eur. Phys. J.* C78 (2018) 281, arXiv:1602.04670.

[259] FCC Collaboration, A. Abada *et al.*, *Eur. Phys. J.* C79 (2019) 474.

[260] J. A. Aguilar-Saavedra and T. Riemann, "Probing top flavor changing neutral couplings at TESLA," in *5th Workshop of the 2nd ECFA - DESY Study on Physics and Detectors for a Linear Electron - Positron Collider Obernai, France, October 16-19, 1999*, pp. 2428–2450. 2001. arXiv:hep-ph/0102197. http://www-library.desy.de/cgi-bin/showprep.pl?LC-TH-2001-067. [,2428(2001)].

[261] Top Quark Working Group Collaboration, K. Agashe *et al.*, "Working Group Report: Top Quark," in *Proceedings, 2013 Community Summer Study on the Future of U.S. Particle Physics: Snowmass on the Mississippi (CSS2013): Minneapolis, MN, USA, July 29-August 6, 2013*. 2013. arXiv:1311.2028. http://www.slac.stanford.edu/econf/C1307292/docs/Top-21.pdf.

[262] B. Coleppa, M. Kumar, S. Kumar and B. Mellado, *Phys. Lett.* B770 (2017) 335–341, arXiv:1702.03426.

[263] S. Atag and B. Sahin, *Phys. Rev.* D73 (2006) 074001.

[264] G. R. Boroun, *Phys. Lett.* B744 (2015) 142–145, arXiv:1503.01590.

[265] S. J. Brodsky, P. Hoyer, C. Peterson and N. Sakai, *Phys. Lett.* 93B (1980) 451–455.

[266] S. J. Brodsky, A. Kusina, F. Lyonnet, I. Schienbein, H. Spiesberger and R. Vogt, *Adv. High Energy Phys.* 2015 (2015) 231547, arXiv:1504.06287.

[267] S. J. Brodsky and S. Gardner, *Phys. Rev. Lett.* 116 (2016) 019101, arXiv:1504.00969.

[268] G. F. de Teramond and S. J. Brodsky, *Phys. Rev. Lett.* 102 (2009) 081601, arXiv:0809.4899.

[269] SELEX Collaboration, A. Ocherashvili *et al.*, *Phys. Lett.* B628 (2005) 18–24, arXiv:hep-ex/0406033.

[270] K. O. Mikaelian, M. A. Samuel and D. Sahdev, *Phys. Rev. Lett.* 43 (1979) 746.

[271] S. J. Brodsky and R. W. Brown, *Phys. Rev. Lett.* 49 (1982) 966.

[272] R. W. Brown, K. L. Kowalski and S. J. Brodsky, *Phys. Rev.* D28 (1983) 624. [Addendum: Phys. Rev.D29,2100(1984)].

[273] M. A. Samuel and J. H. Reid, *Prog. Theor. Phys.* 76 (1986) 184.

[274] European Muon Collaboration, J. J. Aubert *et al.*, *Phys. Lett.* 123B (1983) 275–278.

[275] CHORUS Collaboration, G. Onengut *et al.*, *Phys. Lett.* B632 (2006) 65–75.

[276] J. Gomez *et al.*, *Phys. Rev.* D49 (1994) 4348–4372.

[277] New Muon Collaboration, P. Amaudruz *et al.*, *Nucl. Phys.* B441 (1995) 3–11, arXiv:hep-ph/9503291.

[278] NuTeV Collaboration, M. Tzanov *et al.*, *Phys. Rev.* D74 (2006) 012008, arXiv:hep-ex/0509010.

[279] New Muon Collaboration, M. Arneodo *et al.*, *Nucl. Phys.* B441 (1995) 12–30, arXiv:hep-ex/9504002.

[280] New Muon Collaboration, M. Arneodo *et al.*, *Nucl. Phys.* B481 (1996) 3–22.

[281] European Muon Collaboration, J. Ashman *et al.*, *Z. Phys.* C57 (1993) 211–218.

[282] New Muon Collaboration, M. Arneodo *et al.*, *Nucl. Phys.* B481 (1996) 23–39.

[283] New Muon Collaboration, P. Amaudruz *et al.*, *Nucl. Phys.* B371 (1992) 3–31.

[284] J. P. Berge *et al.*, *Z. Phys.* C49 (1991) 187–224.

[285] M. Arneodo, *Phys. Rept.* 240 (1994) 301–393.

[286] D. F. Geesaman, K. Saito and A. W. Thomas, *Ann. Rev. Nucl. Part. Sci.* 45 (1995) 337–390.

[287] K. J. Eskola, P. Paakkinen, H. Paukkunen and C. A. Salgado, *Eur. Phys. J.* C77 (2017) 163, arXiv:1612.05741.

[288] C. A. Salgado *et al.*, *J. Phys.* G39 (2012) 015010, arXiv:1105.3919.

[289] K. J. Golec-Biernat and M. Wusthoff, *Phys. Rev.* D59 (1998) 014017, arXiv:hep-ph/9807513.

[290] L. Frankfurt, V. Guzey and M. Strikman, *Phys. Rept.* 512 (2012) 255–393, arXiv:1106.2091.

[291] F. Gelis, E. Iancu, J. Jalilian-Marian and R. Venugopalan, *Ann. Rev. Nucl. Part. Sci.* 60 (2010) 463–489, arXiv:1002.0333.

[292] Y. V. Kovchegov and E. Levin, *Camb. Monogr. Part. Phys. Nucl. Phys. Cosmol.* 33 (2012) 1–350.

[293] B. L. Ioffe, V. S. Fadin and L. N. Lipatov, *Quantum chromodynamics: Perturbative and nonperturbative aspects*, vol. 30. Cambridge Univ. Press, 2010. http://www.cambridge.org/de/knowledge/isbn/item2710695.

[294] J. Collins, *Camb. Monogr. Part. Phys. Nucl. Phys. Cosmol.* 32 (2011) 1–624.

[295] J. C. Collins, D. E. Soper and G. F. Sterman, *Adv. Ser. Direct. High Energy Phys.* 5 (1989) 1–91, arXiv:hep-ph/0409313.

[296] H. Paukkunen, *Nucl. Phys.* A967 (2017) 241–248, arXiv:1704.04036.

[297] H. Paukkunen, *PoS* HardProbes2018 (2018) 014, arXiv:1811.01976.

[298] K. J. Eskola, H. Paukkunen and C. A. Salgado, *JHEP* 04 (2009) 065, arXiv:0902.4154.

[299] D. de Florian, R. Sassot, P. Zurita and M. Stratmann, *Phys. Rev.* D85 (2012) 074028, arXiv:1112.6324.

[300] K. Kovarik *et al.*, *Phys. Rev.* D93 (2016) 085037, arXiv:1509.00792.

[301] H. Khanpour and S. Atashbar Tehrani, *Phys. Rev.* D93 (2016) 014026, arXiv:1601.00939.

[302] H. Paukkunen and C. A. Salgado, *JHEP* 07 (2010) 032, arXiv:1004.3140.

[303] K. Kovarik, I. Schienbein, F. I. Olness, Y. Yu, C. Keppel, J. G. Morfin, J. F. Owens and T. Stavreva, *Phys. Rev. Lett.* 106 (2011) 122301, arXiv:1012.0286.

[304] H. Paukkunen and C. A. Salgado, *Phys. Rev. Lett.* 110 (2013) 212301, arXiv:1302.2001.

[305] N. Armesto, *J. Phys.* G32 (2006) R367–R394, arXiv:hep-ph/0604108.

[306] K. J. Eskola, P. Paakkinen and H. Paukkunen, *Eur. Phys. J.* C79 (2019) 511, arXiv:1903.09832.

[307] N. Armesto, H. Paukkunen, J. M. Penín, C. A. Salgado and P. Zurita, *Eur. Phys. J.* C76 (2016) 218, arXiv:1512.01528.

[308] A. Kusina, F. Lyonnet, D. B. Clark, E. Godat, T. Jezo, K. Kovarik, F. I. Olness, I. Schienbein and J. Y. Yu, *Eur. Phys. J.* C77 (2017) 488, arXiv:1610.02925.

[309] N. Armesto, A. Capella, A. B. Kaidalov, J. Lopez-Albacete and C. A. Salgado, *Eur. Phys. J.* C29 (2003) 531–540, arXiv:hep-ph/0304119.

[310] N. Armesto, A. B. Kaidalov, C. A. Salgado and K. Tywoniuk, *Eur. Phys. J.* C68 (2010) 447–457, arXiv:1003.2947.

[311] S. J. Brodsky, I. Schmidt and J.-J. Yang, *Phys. Rev.* D70 (2004) 116003, arXiv:hep-ph/0409279.

[312] Z. Citron *et al.*, "Future physics opportunities for high-density QCD at the LHC with heavy-ion and proton beams," in *HL/HE-LHC Workshop: Workshop on the Physics of HL-LHC, and Perspectives at HE-LHC Geneva, Switzerland, June 18-20, 2018*. 2018. arXiv:1812.06772.

[313] M. Klein, *EPJ Web Conf.* 112 (2016) 03002.

[314] J. Blumlein and M. Klein, "Kinematics and resolution at future e p colliders," in *1990 DPF Summer Study on High-energy Physics: Research Directions for the Decade (Snowmass 90) Snowmass, Colorado, June 25-July 13, 1990*, pp. 549–551. 1990.

[315] LHeC study Group Collaboration, H. Paukkunen, *PoS* DIS2017 (2018) 109, arXiv:1709.08342.

[316] E. C. Aschenauer, S. Fazio, M. A. C. Lamont, H. Paukkunen and P. Zurita, *Phys. Rev.* D96 (2017) 114005, arXiv:1708.05654.

[317] LHCb Collaboration, R. Aaij *et al.*, *JHEP* 10 (2017) 090, arXiv:1707.02750.

[318] LHCb Collaboration, R. Aaij *et al.*, *Phys. Rev.* D99 (2019) 052011, arXiv:1902.05599.

[319] K. J. Eskola, I. Helenius, P. Paakkinen and H. Paukkunen, arXiv:1906.02512.

[320] I. Helenius, K. J. Eskola and H. Paukkunen, *JHEP* 09 (2014) 138, arXiv:1406.1689.

[321] J. Pumplin, D. Stump, R. Brock, D. Casey, J. Huston, J. Kalk, H. L. Lai and W. K. Tung, *Phys. Rev.* D65 (2001) 014013, arXiv:hep-ph/0101032.

[322] N. Armesto, "Nuclear pdfs." 2nd FCC Physics Workshop (CERN, January 15th-19th 2018), 2018.

[323] N. Armesto, *PoS* HardProbes2018 (2019) 123.

[324] S. Alekhin *et al.*, *Eur. Phys. J.* C75 (2015) 304, arXiv:1410.4412.

[325] T. Lappi and H. Mantysaari, *Phys. Rev.* C87 (2013) 032201, arXiv:1301.4095.

[326] A. J. Baltz, *Phys. Rept.* 458 (2008) 1–171, arXiv:0706.3356.

[327] C. Marquet, M. R. Moldes and P. Zurita, *Phys. Lett.* B772 (2017) 607–614, arXiv:1702.00839.

[328] L. L. Frankfurt and M. I. Strikman, *Phys. Lett.* B382 (1996) 6–12.

[329] H. Kowalski, T. Lappi, C. Marquet and R. Venugopalan, *Phys. Rev.* C78 (2008) 045201, arXiv:0805.4071.

[330] A. H. Mueller and H. Navelet, *Nucl. Phys.* B282 (1987) 727–744.

[331] M. Deak, F. Hautmann, H. Jung and K. Kutak, *Eur. Phys. J.* C72 (2012) 1982, arXiv:1112.6354.

[332] J. L. Albacete and C. Marquet, *Phys. Rev. Lett.* 105 (2010) 162301, arXiv:1005.4065.

[333] T. Lappi and H. Mantysaari, *Nucl. Phys.* A908 (2013) 51–72, arXiv:1209.2853.

[334] A. Stasto, S.-Y. Wei, B.-W. Xiao and F. Yuan, *Phys. Lett.* B784 (2018) 301–306, arXiv:1805.05712.

[335] A. van Hameren, P. Kotko, K. Kutak, C. Marquet, E. Petreska and S. Sapeta, *JHEP* 12 (2016) 034, arXiv:1607.03121. [Erratum: JHEP02,158(2019)].

[336] CMS Collaboration, V. Khachatryan *et al.*, *JHEP* 09 (2010) 091, arXiv:1009.4122.

[337] S. Schlichting and P. Tribedy, *Adv. High Energy Phys.* 2016 (2016) 8460349, arXiv:1611.00329.

[338] C. Loizides, *Nucl. Phys.* A956 (2016) 200–207, arXiv:1602.09138.

[339] B. Schenke, *Nucl. Phys.* A967 (2017) 105–112, arXiv:1704.03914.

[340] P. Romatschke, *Eur. Phys. J.* C77 (2017) 21, arXiv:1609.02820.

[341] ATLAS Collaboration, T. A. collaboration, .

[342] A. Badea, A. Baty, P. Chang, G. M. Innocenti, M. Maggi, C. Mcginn, M. Peters, T.-A. Sheng, J. Thaler and Y.-J. Lee, *Phys. Rev. Lett.* 123 (2019) 212002, arXiv:1906.00489.

[343] ZEUS Collaboration, arXiv:1912.07431.

[344] J. D. Bjorken, S. J. Brodsky and A. Scharff Goldhaber, *Phys. Lett.* B726 (2013) 344–346, arXiv:1308.1435.

[345] S. D. Glazek, S. J. Brodsky, A. S. Goldhaber and R. W. Brown, *Phys. Rev.* D97 (2018) 114021, arXiv:1805.08847.

[346] CMS Collaboration, S. Chatrchyan *et al.*, *Phys. Lett.* B724 (2013) 213–240, arXiv:1305.0609.

[347] CMS Collaboration, V. Khachatryan *et al.*, *Phys. Lett.* B765 (2017) 193–220, arXiv:1606.06198.

[348] P. A. M. Dirac, *Rev. Mod. Phys.* 21 (1949) 392–399.

[349] S. J. Brodsky, H.-C. Pauli and S. S. Pinsky, *Phys. Rept.* 301 (1998) 299–486, arXiv:hep-ph/9705477.

[350] D. Ashery, *Nucl. Phys. Proc. Suppl.* 161 (2006) 8–14, arXiv:hep-ex/0511052. [,8(2005)].

[351] G. Bertsch, S. J. Brodsky, A. S. Goldhaber and J. F. Gunion, *Phys. Rev. Lett.* 47 (1981) 297.

[352] L. Frankfurt, G. A. Miller and M. Strikman, *Phys. Rev.* D65 (2002) 094015, arXiv:hep-ph/0010297.

[353] S. J. Brodsky, C.-R. Ji and G. P. Lepage, *Phys. Rev. Lett.* 51 (1983) 83.

[354] S. J. Brodsky and A. H. Mueller, *Phys. Lett.* B206 (1988) 685–690.

[355] S. J. Brodsky, I. A. Schmidt and G. F. de Teramond, *Phys. Rev. Lett.* 64 (1990) 1011.

[356] S. J. Brodsky and H. J. Lu, *Phys. Rev. Lett.* 64 (1990) 1342.

[357] S. J. Brodsky, I. Schmidt and S. Liuti, arXiv:1908.06317.

[358] S. Buddenbrock, A. S. Cornell, Y. Fang, A. Fadol Mohammed, M. Kumar, B. Mellado and K. G. Tomiwa, *JHEP* 10 (2019) 157, arXiv:1901.05300.

[359] W. Liu, H. Sun, X. Wang and X. Luo, *Phys. Rev.* D92 (2015) 074015, arXiv:1507.03264.

[360] X. Wang, H. Sun and X. Luo, *Adv. High Energy Phys.* 2017 (2017) 4693213, arXiv:1703.02691.

[361] ATLAS Collaboration, M. Aaboud *et al.*, *Phys. Rev.* D98 (2018) 032002, arXiv:1805.03483.

[362] CMS Collaboration, V. Khachatryan *et al.*, *JHEP* 02 (2017) 079, arXiv:1610.04857.

[363] J. Hernandez-Sanchez, O. Flores-Sanchez, C. G. Honorato, S. Moretti and S. Rosado, *PoS* CHARGED2016 (2017) 032, arXiv:1612.06316.

[364] S. P. Das, J. Hernandez-Sanchez, S. Moretti and A. Rosado, arXiv:1806.08361.

[365] H. Sun, X. Luo, W. Wei and T. Liu, *Phys. Rev.* D96 (2017) 095003, arXiv:1710.06284.

[366] G. Azuelos, H. Sun and K. Wang, *Phys. Rev.* D97 (2018) 116005, arXiv:1712.07505.

[367] C. Mosomane, M. Kumar, A. S. Cornell and B. Mellado, *J. Phys. Conf. Ser.* 889 (2017) 012004, arXiv:1707.05997.

[368] L. Delle Rose, O. Fischer and A. Hammad, *Int. J. Mod. Phys.* A34 (2019) 1950127, arXiv:1809.04321.

[369] CMS Collaboration, A. M. Sirunyan *et al.*, *JHEP* 06 (2018) 127, arXiv:1804.01939. [Erratum: JHEP03,128(2019)].

[370] CMS Collaboration, C. Collaboration, .

[371] S. P. Das, J. Hernández-Sánchez, S. Moretti, A. Rosado and R. Xoxocotzi, *Phys. Rev.* D94 (2016) 055003, arXiv:1503.01464.

[372] S. P. Das and M. Nowakowski, *Phys. Rev.* D96 (2017) 055014, arXiv:1612.07241.

[373] S. S. Biswal, R. M. Godbole, B. Mellado and S. Raychaudhuri, *Phys. Rev. Lett.* 109 (2012) 261801, arXiv:1203.6285.

[374] I. T. Cakir, O. Cakir, A. Senol and A. T. Tasci, *Mod. Phys. Lett.* A28 (2013) 1350142, arXiv:1304.3616.

[375] M. Kumar, X. Ruan, R. Islam, A. S. Cornell, M. Klein, U. Klein and B. Mellado, *Phys. Lett.* B764 (2017) 247–253, arXiv:1509.04016.

[376] H. Hesari, H. Khanpour and M. Mohammadi Najafabadi, *Phys. Rev.* D97 (2018) 095041, arXiv:1805.04697.

[377] Y.-L. Tang, C. Zhang and S.-h. Zhu, *Phys. Rev.* D94 (2016) 011702, arXiv:1508.01095.

[378] S. Liu, Y.-L. Tang, C. Zhang and S.-h. Zhu, *Eur. Phys. J.* C77 (2017) 457, arXiv:1608.08458.

[379] D. Curtin, K. Deshpande, O. Fischer and J. Zurita, *JHEP* 07 (2018) 024, arXiv:1712.07135.

[380] G. Azuelos, M. D'Onofrio, S. Iwamoto and K. Wang, arXiv:1912.03823.

[381] C. Han, R. Li, R.-Q. Pan and K. Wang, *Phys. Rev.* D98 (2018) 115003, arXiv:1802.03679.

[382] S. Kuday, *J. Korean Phys. Soc.* 64 (2014) 1783–1787, arXiv:1304.2124.

[383] R.-Y. Zhang, H. Wei, L. Han and W.-G. Ma, *Mod. Phys. Lett.* A29 (2014) 1450029, arXiv:1401.4266.

[384] X.-P. Li, L. Guo, W.-G. Ma, R.-Y. Zhang, L. Han and M. Song, *Phys. Rev.* D88 (2013) 014023, arXiv:1307.2308.

[385] J. A. Evans and D. Mckeen, arXiv:1803.01880.

[386] D. Curtin, K. Deshpande, O. Fischer and J. Zurita, *Phys. Rev.* D99 (2019) 055011, arXiv:1812.01568.

[387] S. Antusch and O. Fischer, *JHEP* 05 (2015) 053, arXiv:1502.05915.

[388] S. Antusch, E. Cazzato and O. Fischer, *Int. J. Mod. Phys.* A32 (2017) 1750078, arXiv:1612.02728.

[389] S. Antusch, O. Fischer and A. Hammad, arXiv:1908.02852.

[390] A. Das, S. Jana, S. Mandal and S. Nandi, *Phys. Rev.* D99 (2019) 055030, arXiv:1811.04291.

[391] ATLAS Collaboration, G. Aad *et al.*, arXiv:1905.09787.

[392] S. Antusch, E. Cazzato and O. Fischer, *Phys. Lett.* B774 (2017) 114–118, arXiv:1706.05990.

[393] DELPHI Collaboration, P. Abreu *et al.*, *Z. Phys.* C74 (1997) 57–71. [Erratum: Z. Phys.C75,580(1997)].

[394] MEG Collaboration, J. Adam *et al.*, *Phys. Rev. Lett.* 110 (2013) 201801, arXiv:1303.0754.

[395] S. Jana, N. Okada and D. Raut, arXiv:1911.09037.

[396] L. Duarte, G. A. González-Sprinberg and O. A. Sampayo, *Phys. Rev.* D91 (2015) 053007, arXiv:1412.1433.

[397] L. Duarte, G. Zapata and O. A. Sampayo, *Eur. Phys. J.* C78 (2018) 352, arXiv:1802.07620.

[398] S. Mondal and S. K. Rai, *Phys. Rev.* D93 (2016) 011702, arXiv:1510.08632.

[399] M. Lindner, F. S. Queiroz, W. Rodejohann and C. E. Yaguna, *JHEP* 06 (2016) 140, arXiv:1604.08596.

[400] S. Mondal and S. K. Rai, *Phys. Rev.* D94 (2016) 033008, arXiv:1605.04508.

[401] B. Holdom, *Phys. Lett.* 166B (1986) 196–198.

[402] M. D'Onofrio, O. Fischer and Z. S. Wang, arXiv:1909.02312.

[403] LHCb Collaboration, R. Aaij *et al.*, *Phys. Rev. Lett.* 120 (2018) 061801, arXiv:1710.02867.

[404] S. Heeba and F. Kahlhoefer, arXiv:1908.09834.

[405] C.-X. Yue, M.-Z. Liu and Y.-C. Guo, *Phys. Rev.* D100 (2019) 015020, arXiv:1904.10657.

[406] I. T. Cakir, A. Senol and A. T. Tasci, *Mod. Phys. Lett.* A29 (2014) 1450021, arXiv:1301.2617.

[407] I. A. Sarmiento-Alvarado, A. O. Bouzas and F. Larios, *J. Phys.* G42 (2015) 085001, arXiv:1412.6679.

[408] H. Denizli, A. Senol, A. Yilmaz, I. Turk Cakir, H. Karadeniz and O. Cakir, *Phys. Rev.* D96 (2017) 015024, arXiv:1701.06932.

[409] S. Behera, R. Islam, M. Kumar, P. Poulose and R. Rahaman, *Phys. Rev.* D100 (2019) 015006, arXiv:1811.04681.

[410] HFLAV Collaboration, Y. S. Amhis *et al.*, arXiv:1909.12524.

[411] J. C. Pati and A. Salam, *Phys. Rev.* D10 (1974) 275–289. [Erratum: Phys. Rev.D11,703(1975)].

[412] S. Davidson, D. C. Bailey and B. A. Campbell, *Z. Phys.* C61 (1994) 613–644, arXiv:hep-ph/9309310.

[413] J. Zhang, C.-X. Yue and Z.-C. Liu, *Mod. Phys. Lett.* A33 (2018) 1850039.

[414] S. Mandal, M. Mitra and N. Sinha, *Phys. Rev.* D98 (2018) 095004, arXiv:1807.06455.

[415] Y.-J. Zhang, L. Han and Y.-B. Liu, *Phys. Lett.* B768 (2017) 241–247.

[416] Y.-B. Liu, *Nucl. Phys.* B923 (2017) 312–323, arXiv:1704.02059.

[417] L. Han, Y.-J. Zhang and Y.-B. Liu, *Phys. Lett.* B771 (2017) 106–112.

[418] A. Ozansoy, V. Ar? and V. Çetinkaya, *Adv. High Energy Phys.* 2016 (2016) 1739027, arXiv:1607.04437.

[419] A. Caliskan, *Adv. High Energy Phys.* 2017 (2017) 4726050, arXiv:1706.09797.

[420] A. Caliskan and S. O. Kara, *Int. J. Mod. Phys.* A33 (2018) 1850141, arXiv:1806.02037.

[421] Y. O. Günayd?n, M. Sahin and S. Sultansoy, *Acta Phys. Polon.* B49 (2018) 1763, arXiv:1707.00056.

[422] M. Sahin, *Acta Phys. Polon.* B45 (2014) 1811, arXiv:1302.5747.

[423] Y. C. Acar, U. Kaya, B. B. Oner and S. Sultansoy, *J. Phys.* G44 (2017) 045005, arXiv:1605.08028.

[424] A. Michel and M. Sher, *Phys. Rev.* D100 (2019) 095011, arXiv:1909.10627.

[425] G. R. Boroun, *Chin. Phys.* C41 (2017) 013104, arXiv:1510.02914.

[426] G. R. Boroun, B. Rezaei and S. Heidari, *Int. J. Mod. Phys.* A32 (2017) 1750197, arXiv:1606.02864.

[427] H.-Y. Bi, R.-Y. Zhang, H.-Y. Han, Y. Jiang and X.-G. Wu, *Phys. Rev.* D95 (2017) 034019, arXiv:1612.07990.

[428] K. He, H.-Y. Bi, R.-Y. Zhang, X.-Z. Li and W.-G. Ma, *J. Phys.* G45 (2018) 055005, arXiv:1710.11508.

[429] H.-Y. Bi, R.-Y. Zhang, X.-G. Wu, W.-G. Ma, X.-Z. Li and S. Owusu, *Phys. Rev.* D95 (2017) 074020, arXiv:1702.07181.

[430] N. Armesto and E. Scomparin, *Eur. Phys. J. Plus* 131 (2016) 52, arXiv:1511.02151.

[431] W. Busza, K. Rajagopal and W. van der Schee, *Ann. Rev. Nucl. Part. Sci.* 68 (2018) 339–376, arXiv:1802.04801.

[432] P. Romatschke and U. Romatschke, *Relativistic Fluid Dynamics In and Out of Equilibrium*. Cambridge Monographs on Mathematical Physics. Cambridge University Press, 2019. arXiv:1712.05815. https://www.cambridge.org/academic/subjects/physics/theoretical-physics-and-mathematical-physics/relativistic-fluid-dynamics-and-out-equilibrium-and-applications-relativistic-nuclear-collisions?format=HB&isbn=9781108483681.

[433] Y. Mehtar-Tani, J. G. Milhano and K. Tywoniuk, *Int. J. Mod. Phys.* A28 (2013) 1340013, arXiv:1302.2579.

[434] A. Andronic *et al.*, *Eur. Phys. J.* C76 (2016) 107, arXiv:1506.03981.

[435] D. d'Enterria, A. Morsch and P. Crochet (eds.), *Proceedings, 9th International Conference on Hard and Electromagnetic Probes of High-Energy Nuclear Collisions: Hard Probes 2018 (HP2018)*, vol. HardProbes2018, SISSA. SISSA, 2018. https://pos.sissa.it/345.

[436] H. A. Andrews *et al.*, arXiv:1808.03689.

[437] ALICE Collaboration, B. B. Abelev *et al.*, *Phys. Lett.* B734 (2014) 314–327, arXiv:1311.0214.

[438] H. Song, S. A. Bass, U. Heinz, T. Hirano and C. Shen, *Phys. Rev. Lett.* 106 (2011) 192301, arXiv:1011.2783. [Erratum: Phys. Rev. Lett.109,139904(2012)].

[439] H. Niemi, K. J. Eskola and R. Paatelainen, *Phys. Rev.* C93 (2016) 024907, arXiv:1505.02677.

[440] J. Liu, C. Shen and U. Heinz, *Phys. Rev.* C91 (2015) 064906, arXiv:1504.02160. [Erratum: Phys. Rev.C92,no.4,049904(2015)].

[441] B. Schenke, P. Tribedy and R. Venugopalan, *Phys. Rev. Lett.* 108 (2012) 252301, arXiv:1202.6646.

[442] J.-Y. Ollitrault, A. M. Poskanzer and S. A. Voloshin, *Phys. Rev.* C80 (2009) 014904, arXiv:0904.2315.

[443] STAR Collaboration, J. Adams *et al.*, *Phys. Rev.* C72 (2005) 014904, arXiv:nucl-ex/0409033.

[444] STAR Collaboration, B. I. Abelev *et al.*, *Phys. Rev.* C79 (2009) 034909, arXiv:0808.2041.

[445] CMS Collaboration, A. M. Sirunyan *et al.*, arXiv:1905.01486.

[446] V. Guzey and M. Zhalov, *JHEP* 10 (2013) 207, arXiv:1307.4526.

[447] J. G. Contreras, *Phys. Rev.* C96 (2017) 015203, arXiv:1610.03350.

[448] V. Guzey and M. Klasen, *Eur. Phys. J.* C79 (2019) 396, arXiv:1902.05126.

[449] ATLAS Collaboration, M. Aaboud *et al.*, *Phys. Rev. Lett.* 121 (2018) 212301, arXiv:1806.08708.

[450] ATLAS Collaboration, M. Aaboud *et al.*, *Phys. Rev.* C100 (2019) 034903, arXiv:1901.10440.

[451] R. Aaij *et al.*, "Expression of Interest for a Phase-II LHCb Upgrade: Opportunities in flavour physics, and beyond, in the HL-LHC era," CERN-LHCC-2017-003, CERN, Geneva, Feb 2017. http://cds.cern.ch/record/2244311.

[452] J. L. Abelleira Fernandez *et al.*, *Journal of Physics G: Nuclear and Particle Physics* 39 (2012) 075001. https://doi.org/10.1088/0954-3899/39/7/075001.

[453] O. Brüning, "Accelerator design." Presented at the lhec workshop, June 2015.

[454] A. Klein, M. and. Stocchi, "PERLE: A High Power Energy Recovery Facility for Europe A contribution to the Update of the European Strategy on Particle Physics," CERN-ACC-NOTE-2018-0086, CERN, Geneva, 2018.

[455] I. Apollinari, G. and. Bejar Alonso, O. Brüning, P. Fessia, M. Lamont, L. Rossi and L. Tavian, "High-Luminosity Large Hadron Collider (HL-LHC), Technical Design Report V.0.1," CERN-2017-007-M, CERN, Geneva, 2017.

[456] D. S. D. Pellegrini, A. Latina and S. Bogacz, *Phys. Rev. ST-AB* 121004 (2015) .

[457] S. B. et al, *ICFA Beam Dynamics Newsletter* 71 (2017) 135–144.

[458] G. Hoffstaetter and I. Bazarov, *Phys. Rev. ST-AB* 7 (2004) .

[459] , *Reference Design* (2012) . www.jlab.org/physics/GeV/accelerator.

[460] D. Pellegrini, *Ph.D. Thesis, EPFL, Switzerland* (2016) .

[461] J. Schwinger, *Report No. LBNL-39088,* (1996) .

[462] R. Calaga and E. Jensen, "A Proposal for an ERL Test Facility at CERN," in *Proceedings, 4th International Particle Accelerator Conference (IPAC 2013): Shanghai, China, May 12-17, 2013*, p. WEPWO049. 2013. http://JACoW.org/IPAC2013/papers/wepwo049.pdf.

[463] F. Marhauser, "Cost Rationales for an SRF Proton Linac," in *Proceedings, 5th International Particle Accelerator Conference (IPAC 2014): Dresden, Germany, June 15-20, 2014*, p. THPME053. 2014. http://jacow.org/IPAC2014/papers/thpme053.pdf.

[464] F. Marhauser, "Recent results on a multi-cell 802 mhz bulk nb cavity." Presented at fcc week 2018, https://indico.cern.ch/event/656491/contributions/2932251/attachments/1629681/2597650/5_cell_Cavity_Marhauser.pdf, 2018.

[465] A. T. H.P. Bluem, D. Dowell and L. Young, "High brightness thermionic electron gun performance," in *Proceedings of ERL2011*, pp. 30–35. Association for Computing Machinery, Tsukuba, Japan, 2011. https://accelconf.web.cern.ch/AccelConf/ERL2011/papers/proceed.pdf.

[466] F. Sannibale, K. Baptiste, C. Cork, J. Corlett, M. Decool, S. D. Santis, M. Dickinson, L. Doolittle, J. Doyle, J. Feng, D. Filippetto, D. Gibson, S. Giermann, G. Harris, G. Huang, M. Johnson, M. K. andT. Kramasz, S. Kwiatkowski, D. Leitner, R. Lellinger, R. Li, C. Mitchell, V. Moroz, J. Nasiatka, W. Norum, H. Padmore, C. Pagani, G. Portmann, H. Qian, H. Rasool, J. Schmerge, D. Sertore, D. Syversrud, T. Vecchione, M. Vinco, S. Virostek, R. Wells, F. Zhou and M. Zolotorev, "The vhf-gun, the lbnl high-brightness electron photo-injector for mhz-class repetition-rate applications∗," in *High-Brightness Sources and Light-Driven Interactions*, p. ET1A.1. Optical Society of America, 2016. http://www.osapublishing.org/abstract.cfm?URI=EUVXRAY-2016-ET1A.1.

[467] Z. Wang, Q. Gu, G. Wang and M. Zhao, "Injector Physics Design at SHINE," in *Proc. 10th International Particle Accelerator Conference (IPAC'19), Melbourne, Australia, 19-24 May 2019*, no. 10 in International Particle Accelerator Conference, pp. 1801–1803. JACoW Publishing, Geneva, Switzerland, Jun. 2019. http://jacow.org/ipac2019/papers/tuprb053.pdf. https://doi.org/10.18429/JACoW-IPAC2019-TUPRB053.

[468] G. Shu, Y. Chen, S. Lal, H. Qian, H. Shaker and F. Stephan, "FIRST DESIGN STUDIES OF A NC CW RF GUN FOR EUROPEAN XFEL," in *Proc. 10th International Particle Accelerator Conference (IPAC'19), Melbourne, Australia, 19-24 May 2019*, no. 10 in International Particle Accelerator Conference, pp. 1698–1701. JACoW Publishing, Geneva, Switzerland, Jun. 2019. http://jacow.org/ipac2019/papers/tuprb010.pdf. https://doi.org/10.18429/JACoW-IPAC2019-TUPRB010.

[469] J. Teichert, A. Arnold, H. BÃŒttig, M. Justus, T. Kamps, U. Lehnert, P. Lu, P. Michel, P. Murcek, J. Rudolph, R. Schurig, W. Seidel, H. Vennekate, I. Will and R. Xiang, *Nuclear Instruments and Methods in Physics Research Section A: Accelerators, Spectrometers, Detectors and Associated Equipment* 743 (2014) 114 – 120. http://www.sciencedirect.com/science/article/pii/S016890021400014X.

[470] B. Dunham, J. Barley, A. Bartnik, I. Bazarov, L. Cultrera, J. Dobbins, G. Hoffstaetter, B. Johnson, R. Kaplan, S. Karkare, V. Kostroun, Y. Li, M. Liepe, X. Liu, F. Loehl, J. Maxson, P. Quigley, J. Reilly, D. Rice, D. Sabol, E. Smith, K. Smolenski, M. Tigner, V. Vesherevich, D. Widger and Z. Zhao, *Applied Physics Letters* 102 (2013) 034105, https://doi.org/10.1063/1.4789395. https://doi.org/10.1063/1.4789395.

[471] B. Hounsell, W. Kaabi, M. Klein, B. Militsyn and C. Welsch, "Optimisation of the PERLE injector," in *Proceedings, ERL19*. 2019.

[472] N. Nishimori, R. Nagai, S. Matsuba, R. Hajima, M. Yamamoto, T. Miyajima, Y. Honda, H. Iijima, M. Kuriki and M. Kuwahara, *Applied Physics Letters* 102 (2013) 234103, https://doi.org/10.1063/1.4811158. https://doi.org/10.1063/1.4811158.

[473] B. Hounsell, W. Kaabi, M. Klein, B. Militsyn, T. Noakes and C. Welsch, "Re-optimisation of the ALICE Gun Upgrade Design for the 500-pC Bunch Charge Requirements of PERLE," in *Proceedings, 10th International Particle Accelerator Conference (IPAC2019): Melbourne, Australia, May 19-24, 2019*, p. TUPTS066. 2019.

[474] A. Zaltsman and R. Lambiase, *Proceedings of the 24-th Particle Accelerator Conference, PAC-2011, TUP125* (2011) .

[475] B. Parker, "Latest Developments and Progress on the IR magnet design." presented at the LHeC and FCC-eh Workshop, Sept 2017.

[476] E. Cruz-Alaniz, D. Newton, R. Tomás and M. Korostelev, *Phys. Rev. ST Accel. Beams* 18 (2015) 111001. https://link.aps.org/doi/10.1103/PhysRevSTAB.18.111001.

[477] B. Parker, "Superconducting Magnet Concepts for Electron Hadron Collider IRs." Presented at the electrons for the lhc - lhec/fcceh and perle workshop, Sept 2018.

[478] R. Martin and R. Tomás Garcia, "Length optimization of the detector region dipoles in LHeC and FCC-eh," CERN-ACC-2018-0042, CERN, Geneva, Oct 2018. http://cds.cern.ch/record/2644892.

[479] S. Fartoukh, *Phys. Rev. ST Accel. Beams* 16 (2013) 111002. https://link.aps.org/doi/10.1103/PhysRevSTAB.16.111002.

[480] "Lattice repository." https://gitlab.cern.ch/lhec-optics/lhec-lattice, 2019.

[481] A. Gaddi, "Installation Issues of eh Detectors (LHC and FCC)." Presented at the lhec and fcc-eh workshop, Sept 2017.

[482] A. Gaddi. Private communication, Jan 2019.

[483] R. Bruce, C. Bracco, R. De Maria, M. Giovannozzi, S. Redaelli, R. Tomás Garcia, F. M. Velotti and J. Wenninger, "Updated parameters for HL-LHC aperture calculations for proton beams," CERN-ACC-2017-0051, CERN, Geneva, Jul 2017. https://cds.cern.ch/record/2274330.

[484] R. De Maria *et al.*, "HLLHCV1.3 Optics repository." http://lhc-optics.web.cern.ch/lhc-optics/HLLHCV1.3/.

[485] E. Cruz-Alaniz, R. Martin and R. Tomás, "LHeC optics with $\beta^* = 10$ cm and $L^* = 15$ m," CERN-XXX-2019-XXX, CERN, Geneva, 2019.

[486] Sixtrack web site: http://sixtrack.web.cern.ch/SixTrack/.

[487] E. Cruz-Alaniz, J. L. Abelleira, L. van Riesen-Haupt, A. Seryi, R. Martin and R. Tomás, "Methods to increase the dynamic aperture of the fcc-hh lattice," in *Proc. of International Particle Accelerator Conference (IPAC'18), Vancouver, Canada, 2018*, no. 1 in International Particle Accelerator Conference, pp. 3593–3596. JACoW, Geneva, Switzerland, May 2018. https://accelconf.web.cern.ch/AccelConf/ipac2018/papers/thpak145.pdf.

[488] F. Zimmermann *et al.*, "Interaction-Region Design Options for a Linac-Ring LHeC," in *Proc. of International Particle Accelerator Conference (IPAC'10), Kyoto, Japan, May 23-28, 2010*, no. 1 in International Particle Accelerator Conference, pp. 1605–1607. JACoW, Geneva, Switzerland, May 2010. http://accelconf.web.cern.ch/AccelConf/IPAC10/papers/tupeb037.pdf.

[489] J. L. Abelleira, H. Garcia, R. Tomás and F. Zimmermann, "Final-Focus Optics for the LHeC Electron Beam Line," in *Proc. of International Particle Accelerator Conference (IPAC'12), New Orleans, Louisiana, USA, May 20-25, 2012*, no. 1 in International Particle Accelerator Conference, pp. 1861–1863. JACoW, Geneva, Switzerland, May 2012. http://accelconf.web.cern.ch/AccelConf/IPAC10/papers/tupeb037.pdf.

[490] G. Arduini *et al.*, "Energy frontier DIS at CERN: the LHeC and the FCCeh, PERLE." https://pos.sissa.it/316/183/pdf.

[491] R. Tomás, "LHeC interaction region." Presented at dis 2012 workshop, https://indico.cern.ch/event/153252/contributions/1396962/attachments/160393/226540/SLIDES.pdf, 2012.

[492] P. et al., *IEEE Transactions on Applied Superconductivity* (2003) .

[493] S. Russenschuck, *Field computation for accelerator magnets: analytical and numerical methods for electromagnetic design and optimization*. Wiley, Weinheim, 2010. https://cds.cern.ch/record/1221810.

[494] C. Tennant, "Energy Recovery Linacs," in *Challenges and Goals for Accelerators in the XXI Century*, O. Brüning and S. Myers (eds.). World Scientific, 2016.

[495] C. Tennant, "Progress at the Jefferson Laboratory FEL," in *Particle accelerator. Proceedings, 23rd Conference, PAC'09, Vancouver, Canada, May 4-8, 2009*, p. TH3PBI03. 2010. http://www1.jlab.org/Ul/publications/view_pub.cfm?pub_id=8641.

[496] G. H. Hoffstaetter and I. V. Bazarov, *Phys. Rev. ST Accel. Beams* 7 (2004) 054401. https://link.aps.org/doi/10.1103/PhysRevSTAB.7.054401.

[497] D. R. Douglas, K. C. Jordan, L. Merminga, E. G. Pozdeyev, C. D. Tennant, H. Wang, T. I. Smith, S. Simrock, I. V. Bazarov and G. H. Hoffstaetter, *Phys. Rev. ST Accel. Beams* 9 (2006) 064403. https://link.aps.org/doi/10.1103/PhysRevSTAB.9.064403.

[498] S. Di Mitri, M. Cornacchia and S. Spampinati, *Phys. Rev. Lett.* 110 (2013) 014801. https://link.aps.org/doi/10.1103/PhysRevLett.110.014801.

[499] M. G. Fedurin, D. Kayran, V. Yakimenko, A. V. Fedotov, V. Litvinenko and P. Muggli, *Conf. Proc.* C110328 (2011) 1677–1679.

[500] S. Heifets, G. Stupakov and S. Krinsky, *Phys. Rev. ST Accel. Beams* 5 (2002) 064401. https://link.aps.org/doi/10.1103/PhysRevSTAB.5.064401.

[501] Z. Huang and K.-J. Kim, *Phys. Rev. ST Accel. Beams* 5 (2002) 074401. https://link.aps.org/doi/10.1103/PhysRevSTAB.5.074401.

[502] S. Di Mitri and M. Cornacchia, *EPL (Europhysics Letters)* 109 (2015) 62002. https://app.dimensions.ai/details/publication/pub.1064226665.

[503] C.-Y. Tsai, D. Douglas, R. Li and C. Tennant, *Phys. Rev. Accel. Beams* 19 (2016) 114401. https://link.aps.org/doi/10.1103/PhysRevAccelBeams.19.114401.

[504] C.-Y. Tsai, S. Di Mitri, D. Douglas, R. Li and C. Tennant, *Phys. Rev. Accel. Beams* 20 (2017) 024401. https://link.aps.org/doi/10.1103/PhysRevAccelBeams.20.024401.

[505] D. Douglas *et al.* Jefferson Laboratory Technical Note 12-017, 2012.

[506] R. Alarcon *et al.*, *Phys. Rev. Lett.* 111 (2013) 164801. https://link.aps.org/doi/10.1103/PhysRevLett.111.164801.

[507] T. Powers and C. Tennant, "Implications of incomplete energy recovery in srf-based energy recovery linacs," in *Proceedings of the 2007 ICFA Workshop on Energy Recovery Linacs, Daresbury, UK*, p. 75. 2007.

[508] T. Powers, "Control of Microphonics for Narrow Control Bandwidth Cavities," Talk presented at the 2017 International Conference on RF Superconductivity, Lanzhou, China, 2017.

[509] S. Benson *et al.*, *Conf. Proc.* C070625 (2007) 79.

[510] T. Powers, "Optimization of SRF Linacs," in *Proceedings of the 2013 International Conference on RF Superconductivity, Paris, France*, p. 830. 2013.

[511] P. Williams, "A Staged, Multi-User X-Ray Free Electron Laser and Nuclear Physics Facility based on a Multi-Pass Recirculating Superconducting CW Linac," in *Proc. Future Light Sources 2018, Shanghai.* 2018.

[512] S. Benson *et al.*, "Development of a Bunched-Beam Electron Cooler for the Jefferson Lab Electron-Ion Collider," in *Proceedings, 9th International Particle Accelerator Conference (IPAC 2018), Vancouver, BC Canada*, p. MOPMK015. 2018.

[513] C. Tennant. https://userweb.jlab.org/~tennant/.

[514] C. Tennant, "Analysis of the Baseline PERLE Lattice," Jefferson Laboratory Technical Note 18-031, 2018.

[515] D. Douglas *et al.*, ""Why PERLE?" Historical Context and Technological Motivation," Jefferson Laboratory Technical Note 18-014, 2018.

[516] G. H. Hoffstaetter *et al.*, "CBETA Design Report, Cornell-BNL ERL Test Accelerator," 2017. arXiv:1706.04245.

[517] T. Satogata *et al.*, "ER@CEBAF: A test of 5-pass energy recovery at CEBAF," Program Advisory Committee Proposal, June 2016.